OPTICAL AND ELECTROCHEMICAL BIOSENSING

EDITED BY: Junjie Zhu, Renyun Zhang, Tingting Zheng and Cheng Ma
PUBLISHED IN: Frontiers in Chemistry

frontiers Research Topics

ISSN 1664-8714
ISBN 978-2-83250-094-1
DOI 10.3389/978-2-83250-094-1

About Frontiers

Frontiers is more than just an open-access publisher of scholarly articles: it is a pioneering approach to the world of academia, radically improving the way scholarly research is managed. The grand vision of Frontiers is a world where all people have an equal opportunity to seek, share and generate knowledge. Frontiers provides immediate and permanent online open access to all its publications, but this alone is not enough to realize our grand goals.

Frontiers Journal Series

The Frontiers Journal Series is a multi-tier and interdisciplinary set of open-access, online journals, promising a paradigm shift from the current review, selection and dissemination processes in academic publishing. All Frontiers journals are driven by researchers for researchers; therefore, they constitute a service to the scholarly community. At the same time, the Frontiers Journal Series operates on a revolutionary invention, the tiered publishing system, initially addressing specific communities of scholars, and gradually climbing up to broader public understanding, thus serving the interests of the lay society, too.

Dedication to Quality

Each Frontiers article is a landmark of the highest quality, thanks to genuinely collaborative interactions between authors and review editors, who include some of the world's best academicians. Research must be certified by peers before entering a stream of knowledge that may eventually reach the public - and shape society; therefore, Frontiers only applies the most rigorous and unbiased reviews.
Frontiers revolutionizes research publishing by freely delivering the most outstanding research, evaluated with no bias from both the academic and social point of view. By applying the most advanced information technologies, Frontiers is catapulting scholarly publishing into a new generation.

What are Frontiers Research Topics?

Frontiers Research Topics are very popular trademarks of the Frontiers Journals Series: they are collections of at least ten articles, all centered on a particular subject. With their unique mix of varied contributions from Original Research to Review Articles, Frontiers Research Topics unify the most influential researchers, the latest key findings and historical advances in a hot research area! Find out more on how to host your own Frontiers Research Topic or contribute to one as an author by contacting the Frontiers Editorial Office: frontiersin.org/about/contact

OPTICAL AND ELECTROCHEMICAL BIOSENSING

Topic Editors:
Junjie Zhu, Nanjing University, China
Renyun Zhang, Mid Sweden University, Sweden
Tingting Zheng, East China Normal University, China
Cheng Ma, Yangzhou University, China

Citation: Zhu, J., Zhang, R., Zheng, T., Ma, C., eds. (2022). Optical and Electrochemical Biosensing. Lausanne: Frontiers Media SA.
doi: 10.3389/978-2-83250-094-1

Table of Contents

frontiers | Frontiers in Chemistry

TYPE Editorial
PUBLISHED 17 August 2022
DOI 10.3389/fchem.2022.964825

OPEN ACCESS

EDITED BY
Huangxian Ju,
Nanjing University, China

REVIEWED BY
Robert Sandulescu,
Iuliu Haţieganu University of Medicine and Pharmacy, Romania
Neso Sojic,
Université de Bordeaux, France
Nicole J. Jaffrezic-Renault,
Université Claude Bernard Lyon 1, France

*CORRESPONDENCE
Cheng Ma,
chengma@nju.edu.cn
Tingting Zheng,
ttzheng@chem.ecnu.edu.cn
Renyun Zhang,
renyun.zhang@miun.se
Jun-Jie Zhu,
jjzhu@nju.edu.cn

SPECIALTY SECTION
This article was submitted to Analytical Chemistry, a section of the journal Frontiers in Chemistry

RECEIVED 09 June 2022
ACCEPTED 28 July 2022
PUBLISHED 17 August 2022

CITATION
Ma C, Zheng T, Zhang R and Zhu J-J (2022), Editorial: Optical and electrochemical biosensing. *Front. Chem.* 10:964825. doi: 10.3389/fchem.2022.964825

Editorial: Optical and electrochemical biosensing

Cheng Ma[1]*, Tingting Zheng[2]*, Renyun Zhang[3]* and Jun-Jie Zhu[4]*

[1]School of Chemistry and Chemical Engineering, Yangzhou University, Yangzhou, Jiangsu, China, [2]School of Chemistry and Molecular Engineering, East China Normal University, Shanghai, China, [3]Department of Natural Sciences, Mid Sweden University, Sundsvall, Sweden, [4]State Key Laboratory of Analytical Chemistry for Life Science, School of Chemistry and Chemical Engineering, Nanjing University, Nanjing, Jiangsu, China

KEYWORDS

biosensing, optical analysis, electrochemical analysis, photoelectrochemistry, microscopy

Editorial on the Research Topic
Optical and electrochemical biosensing

It is a great opportunity for us to organize the important Research Topic "*Optical and electrochemical biosensing*" that highlights the recent developments emerging in biosensing field. This Research Topic is here to help with a Research Topic of articles and reviews that cover recent optical and electrochemical biosensing technologies. Although many transduction approaches are available for biosensors, optical and electronic signals are still two important pillars of analysis. This Research Topic collects three articles on optical sensing and four articles on electrochemical sensing. In addition, some interconnection techniques between optical and electrochemical signals, such as photoelectrochemical sensor, demonstrated the merits of minimum intercross inference between input and output signals. The reviews are encouraged to cover the last 3 years developments so that readers can catch up on the most up to date trends in this Research Topic. Therefore, two reviews are included in the Research Topic to summary recent developments in analytical probes such as DNAzyme and metal graphitic nanocapsules. These reviews will also offer a convenient way for junior researchers to quickly understand a field.

Optical biosensing is one of the most important pillars in measurement science. By using light intensity, spectroscopy and microscopy, a fruitful source of information can be obtained from different aspects. The three articles on optical sensing in this Research Topic have chosen different fluorescent probes (gold nanocluster, organic molecules and quantum dots, respectively) for biosensing. The analytical targets range from neurotransmitters, ClO^-, and glycoproteins on cell membranes. The most powerful information with optical output is its spatial resolution that enables the direct observation of the distribution of targets in cellular compartments. For example, the ferroptosis-induced ClO^- was mapped by using mitochondrial-targeted ratiometric fluorescent probe in confocal fluorescence microscope. Abundant groups in organic fluorescent molecules possess great flexibility in designing targeted units and reactions units. Thus, the recognition group p-methoxyphenol and

mitochondrial-targeted group benzimidazole are integrated into the probe. Another fluorescence imaging strategy is to use fluorescence resonance energy transfer (FRET). A short distance between quantum dots and gold nanoparticles is controlled by the hybridization of aptamer and ssRNA. But antigen CD133 on the cell membrane competitively replaced ssRNA and bound to aptamer, releasing the gold nanoparticles and recovering the fluorescence signal. Thus, lung cancer cells can be determined by the FRET aptasensor using confocal imaging.

Electrochemical biosensing is another important issue in this Research Topic. Compared with fluorescence analysis, electrochemical techniques generally have a simple setup and higher sensitivity. The modified materials on electrode surface largely determined the performance of these electrochemical sensors. As we can see, the four collected articles about electrochemical sensors have emphasized the design of modified materials, including graphene, carbon nanotube, metal-organic frameworks. These materials not only fabricate conductive interface for electron transfer, but also act as vehicles for other nanomaterials such as noble metal nanoparticles. The combination of electrocatalytic materials and DNA amplification techniques further improves the sensitivity and limit of detection. For example, G-quatruplex-hemin hybridization chain reaction nanowire acted as a mimicking DNAzyme to assist the cycle amplification of electrochemical signals. Some biomarkers released by cells can also be detected by the nanomaterial-modified electrode.

In addition to individually used optical or electrochemical biosensors, interconnection techniques between optical and electrochemical signals demonstrate the unique advantages by separating input and output signals. Photoelectrochemical sensors attracted great attentions in recent years due to its low background. The semiconductor heterostructure plays a key role in the performance of photoelectrochemical signal sensitivity. Thus, novel bismuth-based semiconductors were used to fabricate photoelectrochemical interface for the detection of L-Cys. Compared with other analytical methods, photoelectrochemical analysis generally has a wide linear range and a low limit of detection. In addition to original articles, two reviews on DNAzyme and metal graphitic nanocapsules are included in this Research Topic. DNAzyme-based biosensor for the detection of uranyl is an important tool for monitoring the processes in nuclear technology. Diverse signal outputting strategies like fluorescence, colorimetry, surface-enhanced Raman scattering and electrochemistry are fully discussed in the realm of DNAzyme biosensing. In addition, the encapsulation of metal NPs is one of the most effective strategies to promote their stability for biosensing. Metal graphitic nanocapsules are excellent nanoprobes in many analytical methods. By using the properties of metal core and graphene shell, the Raman signal of graphene and catalytic activity of H_2O_2 in colorimetry analysis can be used in various biosensing.

I remember that every day writing at least five grateful things can increase the base level of happiness. Therefore, I would like to thank 1) our editorial team that informed the potential authors and put efforts on review processes, 2) the *Frontiers in Chemistry* staff that did excellent and professional works for publication in a timely manner, 3) the reviewers whose professional advice helped improve the quality of every publication, 4) the authors that contributed their efforts to develop new analytical techniques and summarize the recent progress, 5) our funding agencies that supported the financial cost in all experiments. It is both meaningful and pleasurable to complete this Research Topic and I appreciate if it is useful to our potential readers.

Author contributions

All authors listed have made a substantial, direct, and intellectual contribution to the work and approved it for publication.

Funding

We acknowledge financial support by the National Natural Science Foundation of China (Grants 21904063), the Natural Science Foundation of Jiangsu Province (Grant BK20190279).

Acknowledgments

We gratefully thank all authors and reviewers that participated in this Research Topic in "*Optical and Electrochemical Biosensing*." Many thanks to editorial support from Frontiers in Chemistry throughout the publication process.

Conflict of interest

The authors declare that the research was conducted in the absence of any commercial or financial relationships that could be construed as a potential conflict of interest.

The handling editor HJ declared a shared affiliation with the author JZ at the time of review.

Publisher's note

frontiers in Chemistry

ORIGINAL RESEARCH
published: 11 March 2022
doi: 10.3389/fchem.2022.856003

Direct Electrodeposition of Bimetallic Nanostructures on Co-Based MOFs for Electrochemical Sensing of Hydrogen Peroxide

Yixuan Xie[1], Xianhua Shi[1], Linxi Chen[1], Jing Lu[2], Xiange Lu[1], Duanping Sun[1,2]* and Luyong Zhang[1,3]**

[1]Center for Drug Research and Development, Guangdong Provincial Key Laboratory of Pharmaceutical Bioactive Substances, Guangdong Pharmaceutical University, Guangzhou, China, [2]National and Local United Engineering Lab of Druggability and New Drugs Evaluation, School of Pharmaceutical Sciences, Sun Yat-Sen University, Guangzhou, China, [3]New Drug Screening Center, Jiangsu Center for Pharmacodynamics Research and Evaluation, China Pharmaceutical University, Nanjing, China

Hydrogen peroxide (H_2O_2) is the most significant reactive oxygen species in biological systems. Here, we reported an electrochemical sensor for the detection of H_2O_2 on the basis of bimetallic gold-platinum nanoparticles (Au_3Pt_7 NPs) supported by Co-based metal organic frameworks (Co-MOFs). First, Au_3Pt_7 NPs, with optimal electrocatalytic activity and accessible active surface, can be deposited on the surface of the Co-MOF–modified glassy carbon electrodes (Au_3Pt_7/Co-MOFs/GCE) by one-step electrodeposition method. Then, the electrochemical results demonstrated that the two-dimensional (2D) Co-MOF nanosheets as the supporting material displayed better electrocatalytic properties than the 3D Co-MOF crystals for reduction of H_2O_2. The fabricated Au_3Pt_7/2D Co-MOF exhibited high electrocatalytic activity, and the catalytic current was linear with H_2O_2 concentration from 0.1 μM to 5 mM, and 5–60 mM with a low detection limit of 0.02 μM (S/N = 3). The remarkable electroanalytical performance of Au_3Pt_7/2D Co-MOF can be attributed to the synergistic effect of the high dispersion of the Au_3Pt_7 NPs with the marvelous electrochemical properties and the 2D Co-MOF with high-specific surface areas. Furthermore, this sensor has been utilized to detect H_2O_2 concentrations released from the human Hela cells. This work provides a new method for improving the performance of electrochemical sensors by choosing the proper support materials from diverse crystal morphology materials.

Keywords: electroanalysis, bimetallic nanoparticles, electrochemical sensor, hydrogen peroxide, cancer cells

OPEN ACCESS

Edited by:
Junjie Zhu,
Nanjing University, China

Reviewed by:
Maoguo Li,
Anhui Normal University, China
Qin Xu,
Yangzhou University, China

****Correspondence:***
Xiange Lu
lxe_0103@sina.com
Duanping Sun
sundp@gdpu.edu.cn
Luyong Zhang
lyzhang@cpu.edu.cn

Specialty section:
This article was submitted to Analytical Chemistry, a section of the journal Frontiers in Chemistry

Received: *16 January 2022*
Accepted: *09 February 2022*
Published: *11 March 2022*

Citation:
Xie Y, Shi X, Chen L, Lu J, Lu X, Sun D and Zhang L (2022) Direct Electrodeposition of Bimetallic Nanostructures on Co-Based MOFs for Electrochemical Sensing of Hydrogen Peroxide. Front. Chem. 10:856003. doi: 10.3389/fchem.2022.856003

INTRODUCTION

Hydrogen peroxide (H_2O_2), as one of the most significant reactive oxygen species (ROS), commonly exists in biological processes as a ubiquitous intracellular messenger or receptor signaling in various cells (Ushio-Fukai et al., 1999). On the one hand, H_2O_2 was considered as a toxic by-product during the process of aerobic metabolism (Rhee et al., 2005). On the other hand, some serious human diseases will be triggered by an abnormal concentration level of H_2O_2 (Trachootham et al., 2009; Yang et al., 2011), including myocardial infarct (Griendling, 2004), Alzheimer's disease (Markesbery, 1997), aging (Giorgio et al., 2007; Hayyan et al., 2016), and cancers (Jorgenson et al., 2013).

Therefore, developing an accurate and sensitive detection method to monitor the H_2O_2 concentration at the cellular level is vital and urgent for future clinic diagnosis and cancer treatment (Dong et al., 2019a). Until now, various analytical technologies have been utilized to detect H_2O_2, such as fluorescence (Ren et al., 2016; Ma et al., 2017), chemiluminescence (Yuan and Shiller, 1999; Xie and Huang, 2011), spectrophotometry (Yu et al., 2017), chromatography (Gimeno et al., 2015), and electrochemistry. Compared with the established analytical methods, the electrochemical sensing technique is a promising approach to attain dynamic analysis of H_2O_2 concentration for its outstanding properties, specifically high sensitivity, good selectivity, simple operation, and low cost.

Electrochemical sensors for testing H_2O_2 can be subdivided into natural enzymes and nanomaterial-based artificial enzymes (nanozymes)–based sensors. The natural enzymes were known as peroxidases, such as horseradish peroxidase (Sun et al., 2004). The enzyme-based electrochemical sensors have been widely utilized in electroanalysis for the advantage of specificity and fast response to the target substance. However, natural enzymes are restricted to their inherent weaknesses, including the uncontrollable deactivation and hardship in purification (Wang et al., 2018). Therefore, to overcome the shortages of natural enzymes, nanozymes have been taken into consideration as robust alternatives. Until now, a series of nanomaterials have been proved to possess intrinsic peroxidase-mimicking catalytic properties (Wu et al., 2019), including noble metals, metal oxides, and carbon-based nanomaterials (Wei and Wang, 2013).

Among various enzyme mimics, bimetallic nanoparticles (NPs) have been widely employed to fabricate electrochemical biosensors. It usually performed better electrocatalytic properties than its monometallic counterparts (Iyyamperumal et al., 2013; Li et al., 2020; Yang et al., 2021). As previously reported, the properties of electrons can be improved by the synergistic effects of each monometallic nanomaterials (Renner et al., 2006). However, few limitations are constraining the further application of these bimetallic particles-based electrochemical sensors: 1) it is usually a challenge to meet the satisfactory sensitivity of the living cells detection; and 2) their thermodynamic instability and tendency to aggregate, owing to their high surface free energy (Wang et al., 2019).

These disadvantages can be improved by immobilizing metal NPs in/on supporting structures. Recently, metal organic frameworks (MOFs) formed by the self-assembly of organic ligands and metal ions (Batten et al., 2013) have drawn extensive attention as supporting materials because of their inherent advantages (Furukawa et al., 2013). Among various MOFs, Co-based MOFs were widely used in fabricating electrochemical sensors as supporting material (Dong et al., 2019b). According to the previous research, the zeolite imidazolate framework (ZIF)–67 which compounded of the imidazole-based organic linkers and transition metal (Co) displaying a desirable 3D structure rhombic dodecahedron morphology, and it has been widely utilized for fabricating the 3D Co-MOF–modified electrodes. Lu et al. (2020) constructed a novel electrochemical sensor with the help of 3D Co-MOF to load artificial enzymes Ag nanostructures. Recently, two-dimensional (2D) Co-MOF has drawn extensive attention as supporting material in fabricating electrochemical sensors. The meso-tetra-(4-carboxyphenyl)–substituted porphyrins (TCPP) is the excellent ligand for the constructing 2D MOF due to their tetragonal symmetry and rigid structure (Zhao et al., 2018a). When the TCPP ligands connect with Co^{2+}, 2D Co-MOF nanosheets was formed. Four Co paddle-wheel metal nodes link one TCPP ligand. These TCPP linked ultrasmall 2D metalloporphyrinic MOF nanosheets have been used to fabricating electrochemical sensors for electrochemical catalyzing and sensing applications (Zhao et al., 2015). For example, Huang et al. (2017) reported a novel sensor for catalyzing the cascade reactions. The electrochemical sensor was fabricated by peroxidase mimics material Au NPs and artificial glucose oxidase, ultrasmall 2D metalloporphyrinic MOF nanomaterial. Ma et al. (2019) reported a novel electrochemical sensor fabricated by TCPP-based 2D Cu-MOF nanosheets and Ag NPs. Because of the smaller size and more accessible active sites (Xu et al., 2016; Zhao et al., 2018b), 2D Co-MOF may combine other functionalized materials better than 3D bulk MOF crystals (Tan et al., 2017; Liu et al., 2020). However, which morphology of MOF can perform better in loading artificial enzymes that still need more exploration?

In this work, our experiments first tried to answer whether AuPt NPs are a much better catalyst for H_2O_2 reduction reaction than either Au or Pt NPs. Then, we evaluated the electrocatalytic activity of 3D and 2D Co-MOF–modified electrodes, figuring out the influences of morphology for a supporting material. During the electrodeposition process with a negative voltage, AuPt NPs can be easily reduced from the solution adhering to the surface of the working electrode steadily (Wirtz and Martin, 2003). After comparing a series ration of Au NPs and Pt NPs with (V:V = 1:9, 3:7, 5:5, 7:3, and 9:1), a novel sensor was constructed which bimetallic Au_3Pt_7 NPs decorated on the 2D Co-MOF–modified glassy carbon electrode (Au_3Pt_7/2D Co-MOFs/GCE) by electrodeposition. This high-performance electrochemical sensor was successfully utilized to monitor H_2O_2 concentration in real-time, and it performed a desirable property for tracing H_2O_2 in human cancer samples. **Scheme 1** illustrated the detecting process of in suit analyzing of H_2O_2 secreted from Hela cells with drug stimulation by electrochemical sensor.

EXPERIMENTAL

Reagents and Apparatus

The reagents and apparatus were provided in detail in the Supporting Information.

Synthesis of 2D and 3D Co-MOF

In this work, two kinds of pristine Co-MOF materials were prepared according to the published method with some improvements (Zhao et al., 2015; Sun et al., 2020).

Preparation of the Modified Electrodes

First, 0.3 and 0.05 μM alumina slurries were used to polished the bare GCE (3 mm in diameter), until it shows mirror-like luster. Second, the electrodes were ultrasonicated in ultrapure water, ethanol, and ultrapure water. Last, nitrogen steam was used to dry the electrodes. A volume of 5 μl (2 mg/ml) of crystal ink of 2D Co-MOFs and 3D Co-MOFs were dropped on the GCE surface (the

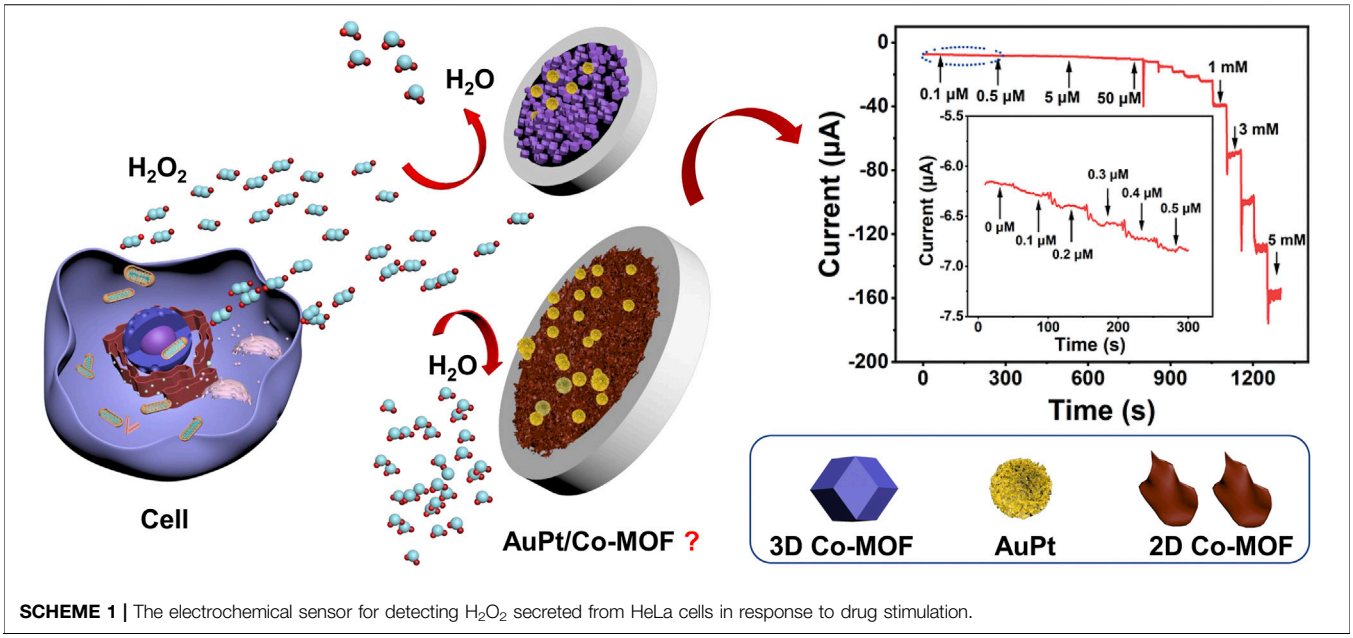

SCHEME 1 | The electrochemical sensor for detecting H_2O_2 secreted from HeLa cells in response to drug stimulation.

modified electrode was labeled as 2D Co-MOFs/GCE and 3D Co-MOFs/GCE), respectively. Then, the electrodes were air-dried at room temperature. After that, $HAuCl_4$ (1.0 mM) and H_2PtCl_4 (1.0 mM) were mixed with the different volume ratio. The Co-MOFs/GCE was immersed in the mixed $HAuCl_4$ and H_2PtCl_4 solution. AuPt NPs were grown on the surface of the modified electrodes by electrodepositing at −0.2 V (vs. Ag/AgCl). Last, two pristine Co-MOF–supported electrodes were fabricated, and these modified electrodes were washed by ultrapure water.

Measuring H_2O_2 Secreted From Hela Cells

In the electrochemical experiments at the cellular level, 10 mM phosphate-buffered saline (PBS) with N_2-saturating (pH 7.0) was utilized as the electrolyte to collect the living Hela cells. The details of Hela cells culturing condition were listed in the Supporting Information. With the help of cyclic voltammogram (CV) measurement and amperometric I-t experiment, the redox characteristics of the fabricated electrodes Au_3Pt_7/2D Co-MOF/GCE were fully approved and the I-t experiment potential was kept at −0.5 V.

Before the analyzing experiments, the cultured cells were gently washed twice with PBS. Then, 3 ml of PBS was added into the Hela cells culture dish, and 400 μM ascorbic acid (AA) was injected into the dish to stimulate the cells releasing H_2O_2. With the amperometric technique, the current response for H_2O_2 detection was recorded.

RESULTS AND DISCUSSION

Characterization of Noble Metal Nanostructures

Here, we fabricated a bimetallic electrochemical sensor on the basis of Au_3Pt_7 NPs for H_2O_2 detection by CV measurements. Scanning electron microscopy (SEM) were employed to characterize the Au NPs, Pt NPs, and Au_3Pt_7 NPs. **Figure 1A** showed the SEM image of Au NPs that dispersedly immobilizing on the electrode. The Au NPs were of spheroidal nature, the average diameter of Au NPs was almost 20 nm. As recorded in the CV curves of **Figure 1B**, with different time of electrodeposition, the Au NP–modified electrodes showed an increased catalytic ability to H_2O_2, and the best catalytic response was obtained at 120 s. **Figure 1C** exhibited the histograms of the reduction peak current value of different electrodeposition time (t = 30, 60, 90, 120, and 150 s). The detection signal of H_2O_2 increased following the electrodeposition time, increasing until the electrochemical signal achieves a peak value of 120 s. Then, the current signal declined with continually increasing the electrodeposition time. The SEM image of Pt NPs is shown in **Figure 1D**, and the Pt NPs were of spheroidal nature, showing an average size of ~50 nm. **Figures 1E,F** demonstrate the CV curves with different electrodeposition time of Pt NPs. The peak current increased from 30 to 120 s and dropped down until 150 s. The result demonstrated that, with the electrodeposition time increased to 120 s, the detection signal of H_2O_2 reduction achieved a peak value. Therefore, 120 s was chosen to be the suitable electrodeposition time of synthesized Au_3Pt_7 NPs. As shown in **Figure 1G**, the SEM image of Au_3Pt_7 NPs was distributed sparsely on the surface of GCE electrode, where a uniform NP structure with nearly 100 nm exists. **Figures 1H,I** depict the volume ratio of AuPt NPs (3:7), presenting the best catalytic ability to H_2O_2 with the different volume ratio of AuPt NPs (V:V = 1:9, 3:7, 5:5, 7:3, and 9:1). Au_3Pt_7 NPs was selected as the optimum nanozyme for fabricating the novel electrochemical sensors. From the results above, metal NPs all gain high catalytic abilities to H_2O_2, especially the Au_3Pt_7 bimetallic NPs, and the phenomenon may come from the several reasons as follows: 1) electrodeposition provided a considerable route for its low cost,

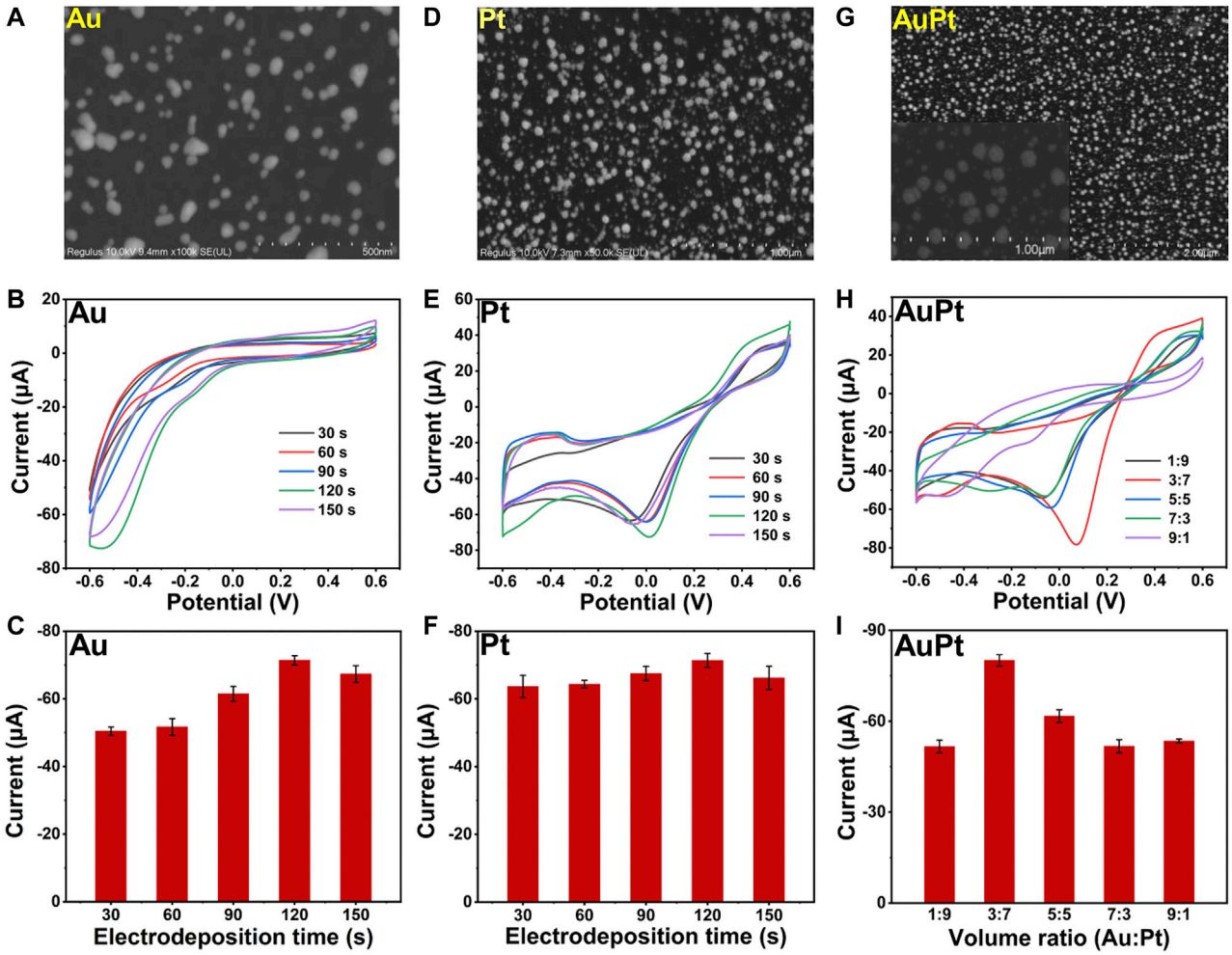

FIGURE 1 | (A) SEM images of Au NPs. **(B,C)** The CV curves and histograms of reduction peak current responses of Au/GCE for 2 mM H_2O_2 with different electrodeposition time (t = 30, 60, 90, 120, and 150 s) (n = 3). **(D)** SEM images of Pt NPs. **(E,F)** The CV curves and histograms of reduction peak current responses of Pt/GCE for 2 mM H_2O_2 with different electrodeposition time (t = 30, 60, 90, 120, and 150 s) (n = 3). **(G)** SEM images of Au_3Pt_7 NPs. **(H,I)** The CV curves and histograms of reduction peak current responses of Au_3Pt_7/GCE for 2 mM H_2O_2 with different volume ratio of Au NPs : Pt NPs (1:9, 3:7, 5:5, 7:3, and 9:1).

immediate modification, stable current signal, and simple construction; and 2) Au_3Pt_7 NPs combining the advantages the high catalytic ability of the Pt NPs and the stability of Au NPs. Therefore, the electrochemical catalytic capability and the selectivity of Au_3Pt_7 have been improved (Sun et al., 2017; Yu et al., 2018).

Characterization of Pristine 3D and 2D Co-MOF

The morphology analysis of 2D and 3D Co-MOF was investigated by SEM, transmission electron microscopy (TEM), powder X-ray diffraction (XRD), X-ray photoelectron spectroscopy (XPS), and Fourier transform infrared (FT-IR) spectroscopy. As **Supplementary Figure S1** shown, the collected products of pristine Co-MOF exhibited a powder-like 3D Co-MOF that was purple and 2D Co-MOF that was brown, matching with the previous report. **Figure 2A** shows the SEM image of 3D Co-MOF, which displays a 3D structure rhombic dodecahedron crystalline morphology with the uniform size of nearly 500 nm. **Figure 2B** reveals the 2D Co-MOF with a sheet-like structure. The crumpled and wrinkled surface indicates its ultrathin property. The TEM image supported 2D Co-MOF with a thin nanosheet structure and confirmed the structure shown in the SEM image. **Figures 2C,D** reveal the XRD patterns of the 3D Co-MOF and 2D Co-MOF. **Figure 2E** shows the chemical composition and states of the Co-MOF. As indicated from the two lines of XPS data, there were two main peaks of approximately 780 and 796 eV for 3D and 2D Co-MOF products, respectively, corresponding to Co $2p_{3/2}$ and Co $2p_{1/2}$ that are derived from Co^{2+}. The two broad peaks at 786.0 and 802.8 eV were satellite peaks, matching well with the reported data. Then, for further investigating of the prepared pristine MOFs, FT-IR spectroscopic studies are shown in **Figure 2F**, and the characteristic absorption peak of 3D Co-MOF and 2D Co-MOF nanosheet appeared at nearly 716, 770, and 1,025 cm^{-1}.

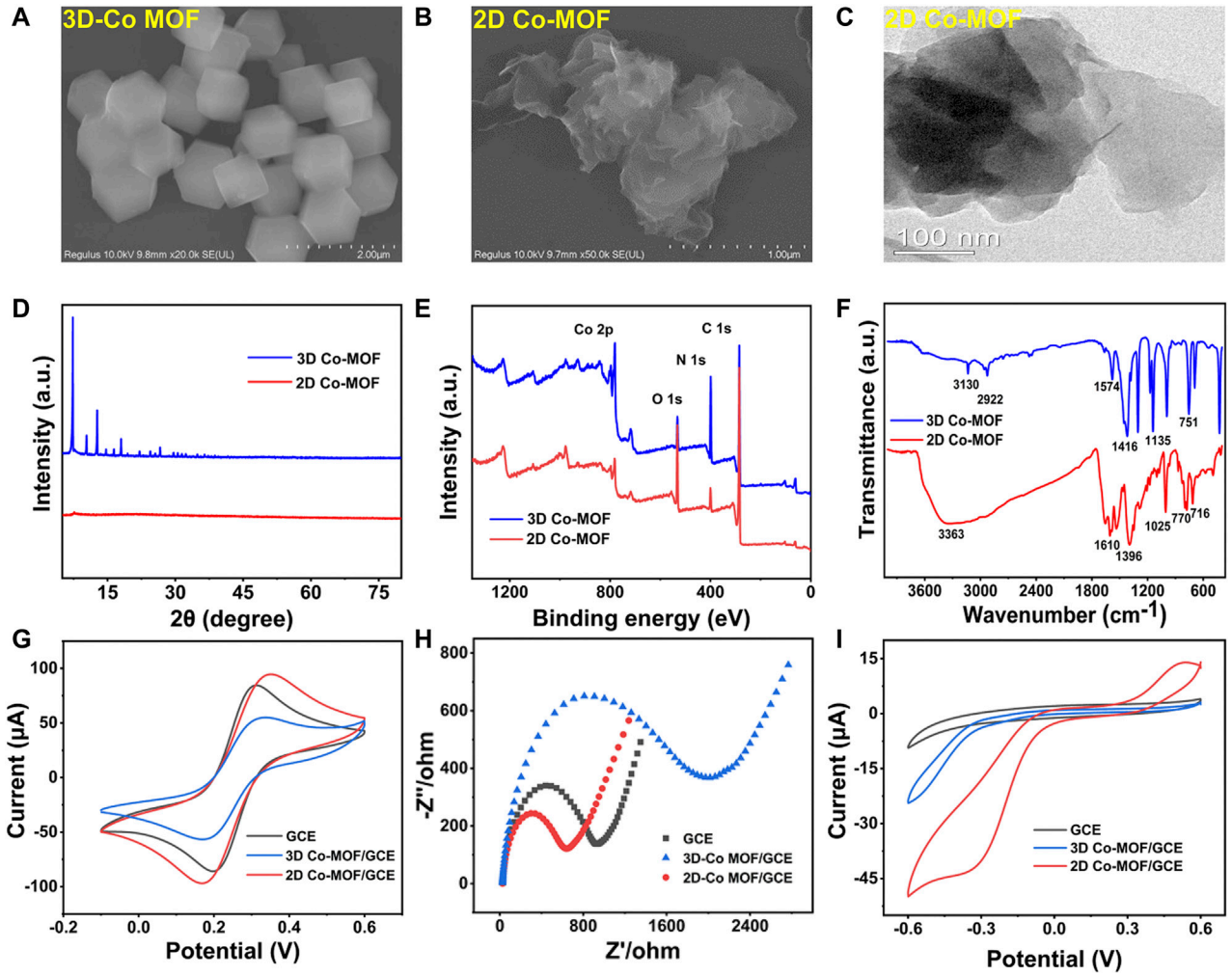

FIGURE 2 | SEM images of **(A)** 3D Co-MOF and **(B)** 2D Co-MOF. **(C)** TEM images of 2D Co-MOF. **(D)** XRD patterns of 3D Co-MOF and 2D Co-MOF. **(E)** XPS survey scan of 3D Co-MOF and 2D Co-MOF. **(F)** The FTIR spectra of 3D Co-MOF and 2D Co-MOF. **(G,H)** CV curves and EIS curves of GCE, 3D Co-MOF/GCE, and 2D Co-MOF/GCE in 5.0 mM $K_3Fe(CN)_6/K_4Fe(CN)_6$ solution containing 0.1 M KCl (amplitude 10 mV, impedance spectral frequency 0.1~10^5 Hz). **(I)** CV curves of GCE, 3D Co-MOF/GCE and 2D Co-MOF/GCE in 100 mM PBS solution containing 10 mM H_2O_2 at a scan rate of 100 mV/s.

These three peaks can prove the existing of skeleton vibration absorption peak of the porphyrin ring (Bai et al., 2019). The peak approximately 1,396 cm^{-1} is related to the stretching vibration of C=N. Besides, the peaks at 1,128 and 1,610 cm^{-1} are generated by the vibration of the benzene ring skeleton outside the pyrrole ring. The absorption peak at 1,700 cm^{-1} can be attributed to the C=O vibration of the carboxyl group on the benzene ring. These results demonstrated that the pristine Co-MOF products had been successfully synthesized.

The examination of CV and electrochemical impedance spectroscopy (EIS) characterized that the pristine Co-MOF of two morphologies was decorated on the surface of the surface of GCE. The electrochemical study of the fabricated sensor in 5 mM $K_3Fe(CN)_6/K_4Fe(CN)_6$. As shown in **Figures 2G,H**, the electrochemical performances of the interfacial of the modified electrodes have been tested by CV and EIS. For the bare GCE, a couple of reversible redox peaks was observed, and the current signals of 3D Co-MOF and 2D Co-MOF–modified electrodes (2D Co-MOF/GCE) were decreased. Moreover, the diffusion-limited process of the electrons was showed in the Nyquist plots. The semicircle diameter displaying the charge transfer resistance (R_{ct}) of the modified GCE electrodes. The picture of EIS showed the bad conductivity of the pristine 3D Co-MOF. The Rct of 2D Co-MOF/GCE was close to 800 Ω, and the Rct of 3D Co-MOF/GCE was close to 1,700 Ω. Three-dimensional Co-MOF performed worse than the bare GCE in electrical conductivity properties. Without interlayer interactions and electron confinement, 2D Co-MOF performed better than 3D Co-MOF and bare GCE. As shown in **Figure 2I** by using the CV technique, the electrocatalytic activity of the selected two pristine Co-MOF for H_2O_2 reduction was evident, indicating the current signal of the 2D Co-MOF/GCE closed to 50 μA, the 3D Co-MOF/GCE closed to 23 μA, and the bare GCE was 8 μA. These results illustrated that Co-MOF materials had little influence in the

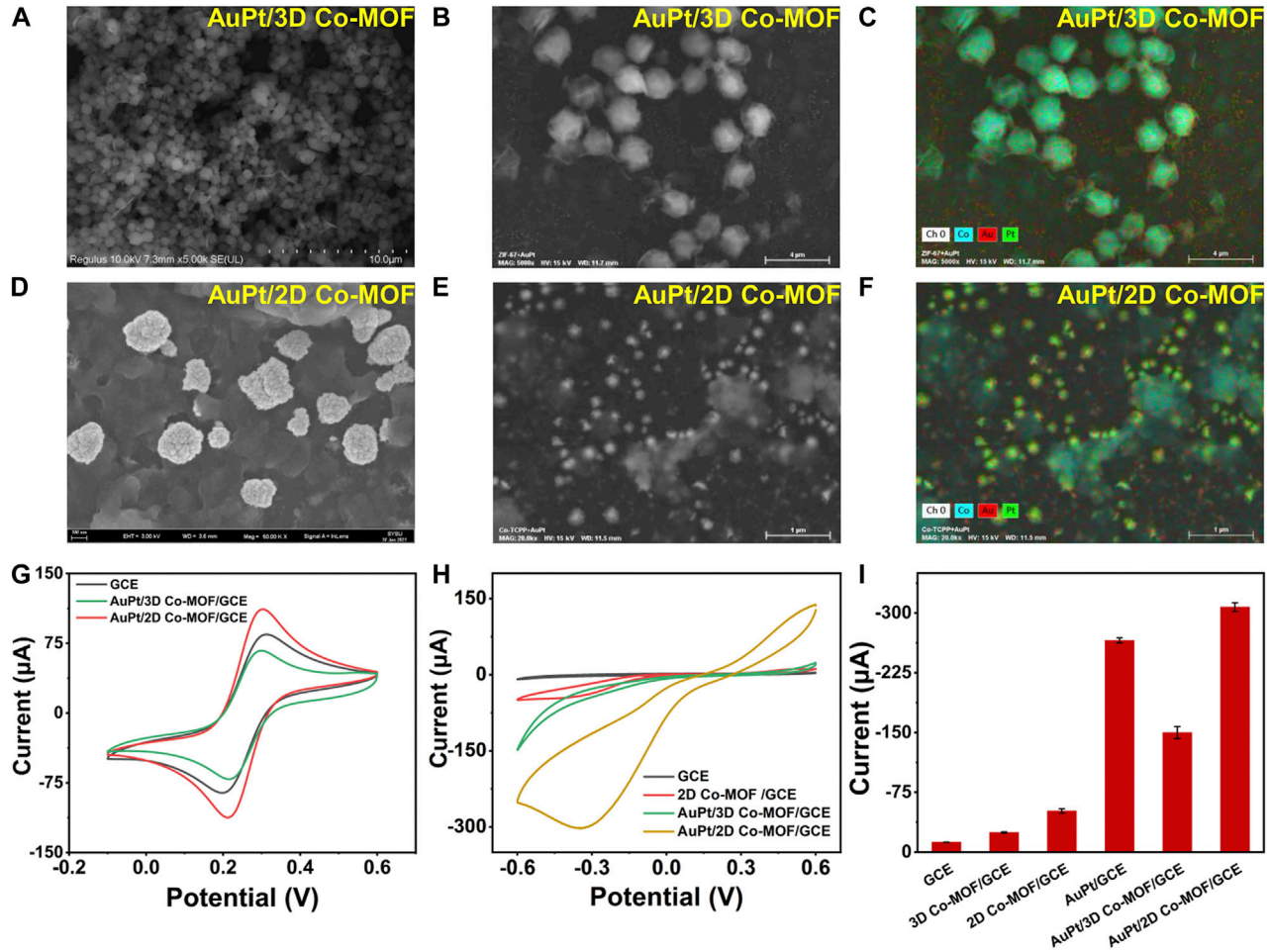

FIGURE 3 | (A,B) SEM images of 3D Co-MOF. **(C)** EDS mapping analysis of Au_3Pt_7/3D Co-MOF/GCE. **(D,E)** SEM images of Au_3Pt_7/2D Co-MOF/GCE. **(F)** EDS mapping analysis of Au_3Pt_7/2D Co-MOF/GCE. **(G)** CV curves of GCE, Au_3Pt_7/3D Co-MOF/GCE, and Au_3Pt_7/2D Co-MOF/GCE in 5.0 mM $K_3Fe(CN)_6/K_4Fe(CN)_6$ solution containing 0.1 M KCl (amplitude 10 mV, impedance spectral frequency 0.1~10^5 Hz). **(H)** CV curves of GCE, 2D Co-MOF/GCE, Au_3Pt_7/3D Co-MOF/GCE, and Au_3Pt_7/2D Co-MOF/GCE in 100 mM PBS solution containing 10 mM H_2O_2 at a scan rate of 100 mV/s. **(I)** Histograms of GCE, 3D Co-MOF/GCE, 2D Co-MOF/GCE, Au_3Pt_7/GCE, Au_3Pt_7/3D Co-MOF/GCE, and Au_3Pt_7/2D Co-MOF/GCE in 0.1 M PBS containing 10 mM H_2O_2.

catalytic activity for H_2O_2 reduction in 100 mM PBS solution containing 10 mM H_2O_2, which can be ignored after the noble metal depositing on the Co-MOF–modified electrodes.

Characterization of Au_3Pt_7 NP-Modified Co-MOF Electrodes

After figuring out the optimum volume ratio of Au_3Pt_7/GCE for H_2O_2 detection, the influence of the supporting materials was investigated. Electrodepositing Au_3Pt_7 NPs on Co-MOF/GCE, the morphology of Au_3Pt_7/3D Co-MOF/GCE and Au_3Pt_7/2D Co-MOF/GCE was observed by SEM measurements. Moreover, the CV measurement results exhibited that 2D Co-MOF performed better in supporting that Au_3Pt_7 NPs showed the best electrocatalytic activity to reduce H_2O_2. As **Figures 3A,B** reveal, Au_3Pt_7 NPs immobilized on the 3D Co-MOF sparsely with an average size of 100 nm. The corresponding EDS spectrum verified the existence of Co, Au, and Pt elements, as shown in **Figure 3C** and **Supplementary Figure S2**. The pictures of SEM clarified that the Au_3Pt_7 NPs located on the 2D Co-MOF/GCE uniformly (**Figures 3D,E**). The result of EDS element analysis clearly characterized the Au_3Pt_7 NPs combining on the nanosheet 2D Co-MOF. The Co, Au, and Pt elements can be observed distinctly in **Figure 3F** and **Supplementary Figure S3**. The result supported that the Au_3Pt_7/2D Co-MOF/GCE was synthesized successfully. The small Au_3Pt_7 NPs attached better to the 2D Co-MOF nanosheet layers than these were attached to 3D Co-MOF. The redox peak current was increased due to the excellent conductivity of the Au_3Pt_7 NPs.

Operating in the solution of 5 mM $K_3Fe(CN)_6/K_4Fe(CN)_6$, in **Figure 3G**, after Au_3Pt_7 NPs depositing on two morphologies of pristine Co-MOF–modified electrodes, the gap between the cathodic and anodic peaks of the CV curves has been narrower, and the peak current of Au_3Pt_7 Co-MOF/GCE and Au_3Pt_7 2D Co-MOF/GCE was increased. Comparing with the conventional 3D Co-MOF, the 2D Co-MOF nanosheets

possessed a larger surface area, smaller diffusion barrier, and more accessible active sites for the substrate molecules (Li et al., 2018). As shown in **Figure 3H**, compared with the peak current of the pristine 2D Co-MOF–modified electrode, the current signal of the Au_3Pt_7/Co-MOF/GCE prominent increased, indicating that the H_2O_2 can be catalyzed effectively by the presence of Au_3Pt_7 NPs. Preliminarily, the 2D Co-MOF with the better affinity for locating the Au_3Pt_7 NPs was inferred. Two-dimensional MOF nanosheets possess unique advantages, such as their large surface area can facilitate the contact of substrate molecules with the active sites on their surface with minimal diffusion barriers (Huang et al., 2017), thus improving their performance in catalysis and sensing applications (Wang et al., 2016). **Figure 3I** illustrates the peak current of 10 mM H_2O_2 to electrodes modified by different materials. The sequence of the peak current increases as follows: GCE < 3D Co-MOF/GCE < 2D Co-MOF/GCE < Au_3Pt_7/3D Co-MOF/GCE < Au_3Pt_7/GCE < Au_3Pt_7/2D Co-MOF/GCE. The sequence indicated the 2D Co-MOF as supporting materials combining the Au_3Pt_7 NPs as the compound nanozymes can help get the best electrocatalytic activity to reduce H_2O_2.

These results are mainly attributed by the 2D Co-MOF with a highly porous structure and more accessible electroactive sites for adsorbing more Au_3Pt_7 NPs than the 3D Co-MOF. On the basis of the Randled–Sevcik equation, the electroactive surface area of different modified electrodes was calculated $Ip = (2.69 \times 10^5) AD^{1/2}n^{3/2}\gamma^{1/2}C$, where Ip is the peak current (A); A refers to the effective surface area of the electrode (cm^2), D means the diffusion coefficient for $[Fe(CN)6]^{3-/4-}$(6.7×10^{-6} cm^2s^{-1}), n is the number of transition electrons of $[Fe(CN)6]^{3-/4-}$ ($n = 1$), γ means the scan rate (V/s), and C is the concentration of the redox reactant (5×10^{-6} mol cm^{-3}). The effective surface area of Au_3Pt_7/2D Co-MOF/GCE was determined to be 0.143 cm^2, which is nearly 1.5 times higher than that of bare GCE (0.09 cm^2). However, the effective surface area of Au_3Pt_7/3D Co-MOF/GCE was determined to be 0.085 cm^2, indicating the lousy conductivity of the 3D Co-MOF. Therefore, Au_3Pt_7/2D Co-MOF/GCE was selected to carry on the further electrocatalytic performance.

Electrochemical Performance of Au_3Pt_7/2D Co-MOF/GCE

The sensitivity of Au_3Pt_7/2D Co-MOF/GCE was verified in 10 ml of PBS solution with different concentrations of H_2O_2 (2, 4, 6, 8, and 10 mM) (**Supplementary Figure S4A**). The reduction peak current increased following the increase of H_2O_2 concentrations from 0 to 10 mM. The electrochemical signal was plotted, and a good linear relationship was revealed in **Supplementary Figure S4B**. These consequences preliminarily illuminated that the fabricated electrode possessed a good response for H_2O_2 reduction. **Supplementary Figure S5A** displays the effect of scan rates and the charge transport behavior of electrode Au_3Pt_7/2D Co-MOF/GCE that have been investigated, with the help of the $[Fe(CN)_6]^{3-/4-}$redox probe. The CV curves revealed that both the catholic and anodic peak currents were enhanced with increasing scan rates from 50 to 700 mV/s. Furthermore, the current signal responses exhibited a proportional to the square root of the scan rates (**Supplementary Figure S5B**). The good linear relationship illustrated fast electron transfer kinetics with a typical diffusion-controlled process.

Amperometric Measurement of H_2O_2

For meeting the sensitivity of demonstrating H_2O_2 concentration at the cellular level, the suitable detecting potential of the fabricated electrode Au_3Pt_7/2D Co-MOFs/GCE needs to be obtained. The amperometric responses were recorded in different potentials from −0.2 to −0.6 V. With the potential increase, the current responses were enhanced under successive injection of 0.4 mM H_2O_2, and the solution was stirred continuously at 250 rpm. The highest response showed in the potentials −0.6 V, but the signal noise of the background currents was too larger to be ignored. On the basis of the above results, −0.5 V was selected as the optimal working potential in the following determination (**Supplementary Figure S6**).

The amperometric measurement was employed to evaluate the detection sensitivity of Au_3Pt_7/2D Co-MOFs/GCE for the reduction of H_2O_2. With the successive injection of different H_2O_2 concentrations into 10 ml of PBS at the optimum potential of −0.5 V. **Figure 4A** describes the current response for the low concentration of H_2O_2. A typical amperometric plot was exhibited of injecting H_2O_2 per 50 s. The insets of **Figure 4A** show that the current response was achieved at 0.1 μM. The result means that the electrochemical sensor had a good sensitivity response for H_2O_2 at a low concentration. **Figure 4B** reveals the linear regions from 0.1 μM to 5 mM and the linear regression was I (μA) = −31.77C (mM) −0.16695 (R^2 = 0.999) with the sensitivities of 236.1 μA mM^{-1} cm^{-2}. The amperometric plot of 5–60 mM was shown in **Figures 4C,D**, discovering the liner regression of high concentration of H_2O_2, which was I (μA) = −24.98C (mM) −73.26 (R^2 = 0.997) with the sensitivities of 174.6 μA mM^{-1} cm^{-2} (the sensitivities were calculated by dividing the slope of the linear regression equation by the geometric surface area of the bare GCE). In addition, the low detection limit (LOD) was calculated to be 0.02 μM (S/N = 3). The Au_3Pt_7/2D Co-MOF/GCE presented a good electrochemical catalytic activity for H_2O_2 with an extended linear range and a lower LOD.

Selectivity, Reproducibility, and Stability of Au_3Pt_7/2D Co-MOF/GCE

The selectivity of Au_3Pt_7/2D Co-MOF/GCE for H_2O_2 was evaluated by injecting the relevant species successively. As shown in **Figures 4E,F**, there was no obvious current signal when following adding different substances, including 5 mM L-AA, 5 mM DL-alanine, 5 mM glucose, 5 mM lactic acid, 5 mM citric acid, 5 mM Lysine acid, and 5 mM KCl, NaCl, and Na_2SO_4. However, an apparent electrochemical signal was observed when a low concentration of H_2O_2 (0.5 μM) was added into the same solvent system. These results indicated that the H_2O_2 sensor possessed high selectivity for H_2O_2.

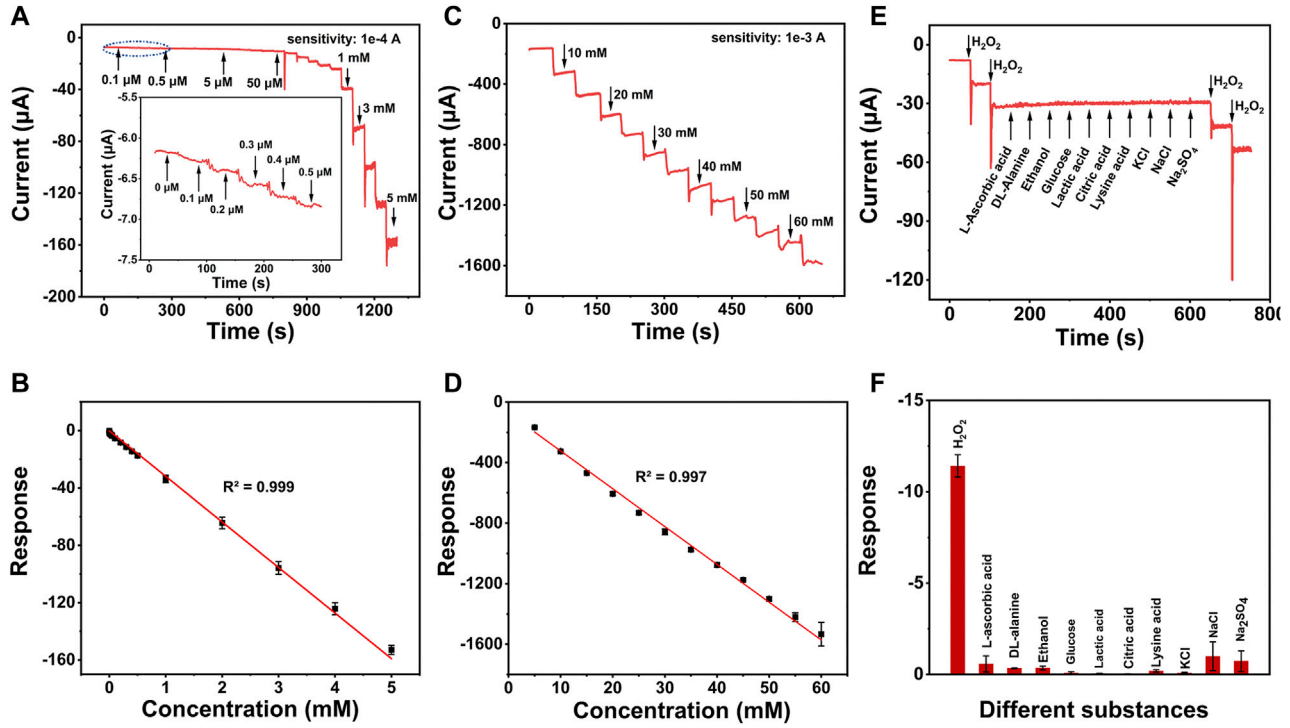

FIGURE 4 | (A) Amperometric responses of Au_3Pt_7/2D Co-MOF/GCE with the successive addition of low concentration of H_2O_2. **(B)** The linear relationships of the response current of Au_3Pt_7/2D Co-MOF/GCE with the H_2O_2 concentrations from 0.1 μM to 5 mM (R^2 = 0.999) and **(C)** amperometric responses of Au_3Pt_7/2D Co-MOF/GCE with the successive addition of high concentration of H_2O_2. **(D)** The linear relationships of from 5 to 60 mM (R^2 = 0.997). **(E)** Amperometric responses of 5 mM L-ascorbic acid, DL-alanine, ethanol, glucose, lactic acid, citric acid, lysine acid, KCl, NaCl, Na_2SO_4, and 0.5 mM H_2O_2 in PBS solution at an applied potential of −0.5 V. **(F)** Histograms of different substances.

The stability of the H_2O_2 sensor was investigated. The peak current of CV curves was displayed in **Supplementary Figures S7A,B** after 7 days, the signal of peak currents only decreased to 93.3%, which presented the excellent stability of the Au_3Pt_7/2D Co-MOF/GCE. The same sensor recorded five successive CV measurements. The response current signals shown in **Supplementary Figure S8** were almost unchanged with a relative standard deviation of 3.5%, which suggested the excellent repeatability of the electrode. The relevant electrode materials for the electrochemical sensing of H_2O_2 displayed in **Table 1**. The novel electrode Au_3Pt_7/2D Co-MOF/GCE exhibited an acceptable electrochemical catalytic activity for H_2O_2 with an extended linear range and a lower LOD.

TABLE 1 | Comparison of the different H_2O_2 sensors in detection performance.

Working electrode	Linear range (μM)	LOD (μM)	References
AgAuPt/ITO	4–4,000	2	Peng et al. (2015)
Pt@Au/NWEs	0.15–3.2	0.12	Liu et al. (2017)
ZIF-67-Au@Pt/GCE	0.8–3,000	0.08	Wang et al. (2021)
MoS_2-Au@Pt/GCE	10–19,070	0.39	Zhou et al. (2017)
PB/Pt@Pd/ITO	0.4–2,247	0.10	Zhu et al. (2019)
Pt@Au/EDA/GCE	1–450	0.18	Li et al. (2013)
Au_3Pt_7/2D Co-MOF/GCE	0.1–5,000 5,000–60,000	0.02	This work

ITO, indium tin oxide; NWEs, nanowire electrodes; EDA, ethylenediamine ($C_2H_8N_2$)

Real-Time Determination of H_2O_2 Released From Hela Cells

Hela cells have been elected as the model cell to estimate weather the sensitivity of the novel electro-sensor Au_3Pt_7/Co-TCPP/GCE could meet the need of evaluating H_2O_2 secreted from actual samples. Before the electrochemical detecting, dehydrogenate (DHE) staining was applied for preliminary analyzing the intracellular H_2O_2 of Hela cells. As the fluorescence image depicting, the intracellular concentration of H_2O_2 was kept at a low level before AA stimulation (**Figure 5A**). After the treatment with AA (400 μM), the level of endogenous H_2O_2 concentration increased apparently (**Figure 5B**). The DHE fluorescence photographs proved that H_2O_2 of Hela cells indeed motivated by AA.

The amperometric technique was utilized to analyze H_2O_2 at the cellular level with the potential of −0.5 V. AA was injected into the dish as a stimulant to boost the H_2O_2 secreted from the Hela cells. After the injection of 400 μM AA solution into the system without cell, there was a negligible current response. However, an obvious electrochemical current signal was observed when the same drug injected into the system

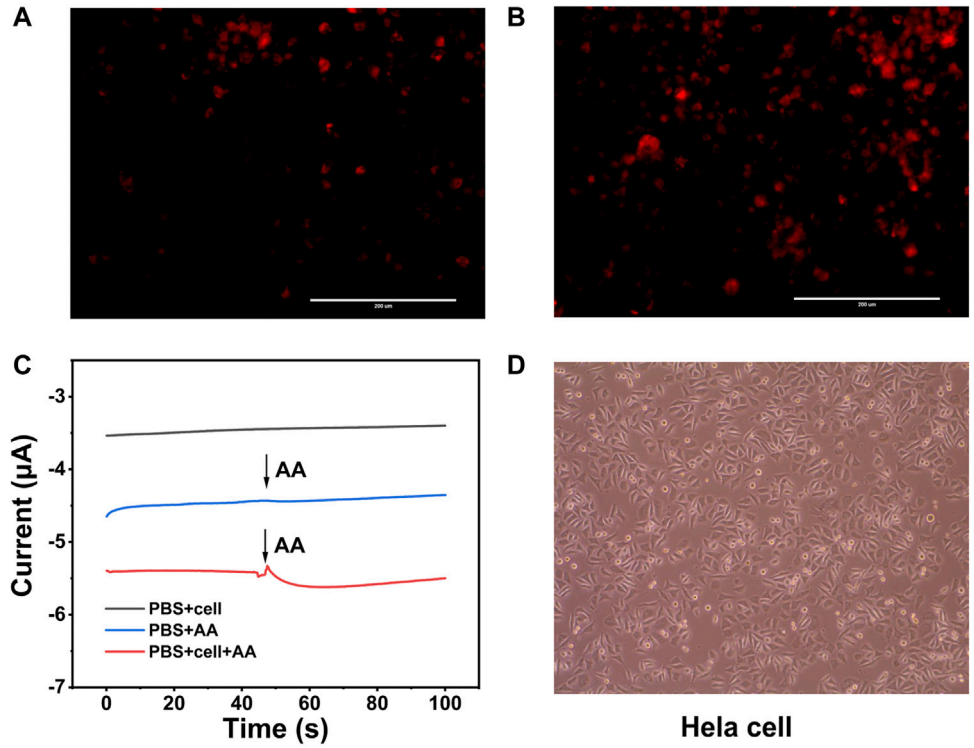

FIGURE 5 | (A) DHE fluorescence image of Hela cells without stimulation by AA (400 μM). **(B)** Hela cells stimulated by AA (400 μM). **(C)** Current responses of Hela cells without and with AA (400 μM) stimulations at an applied potential of −0.5 V. **(D)** Bright images of Hela cells after electrochemical detection.

contained the Hela cells at the same concentration. The current value was calculated to be 204 nA, which corresponded to 0.12 μM H_2O_2 (**Figure 5C**). Bright images of Hela cells revealed that the modified electrodes and the electrochemical detection were harmless to the cells, and the morphology and viability of the living cells were similar to those without stimulating (**Figure 5D**). These results supported that Au_3Pt_7/2D Co-MOF/GCE could meet the need of the intracellular H_2O_2 *in situ* detection.

CONCLUSION

In conclusion, we have fabricated an enzyme-free electrochemical sensor for the real-time detection of H_2O_2 released from cells. We discovered that bimetallic Au_3Pt_7 NPs showed much higher electrocatalytic activity than pure Au NPs or Pt NPs toward H_2O_2 detection. Because of the ultrathin nanosheet structural features, 2D Co-MOF showed a better supporting ability than the 3D Co-MOF. Benefitting from the microplate structures of 2D Co-MOF and the high catalytic ability of Au_3Pt_7 NPs, we constructed a novel electrochemical biosensor on the basis of the Au_3Pt_7 NPs deposited on the 2D Co-MOF/GCE for the first time. The fabricated Au_3Pt_7/2D Co-MOF/GCE exhibited high electrocatalytic activity, fast response, and good sensitivity toward H_2O_2 reduction. The linear range of the Au_3Pt_7/2D Co-MOFs/GCE provided to H_2O_2 appealing in 0.1 μM–5 mM and 5–60 mM and exhibited a LOD of 0.02 μM (S/N = 3). These characters enable the real-time quantification of H_2O_2 secreted from Hela cancer cells under drug stimulation. This work provided a new method for improving the detection performance by changing the supporting materials of different crystalline morphologies. For future electrochemical sensors, more efforts will be made in cell adhesion/growth on the surface of the electrodes to get excellent sensitivity *in situ* detection of H_2O_2 or other disease biomarkers.

DATA AVAILABILITY STATEMENT

The original contributions presented in the study are included in the article/**Supplementary Material**, further inquiries can be directed to the corresponding authors.

AUTHOR CONTRIBUTIONS

This study was conceived and supervised by DS, XL, and LZ. Synthesis, structural characterization, and electrochemical measurements were performed by YX, XS, and LC. The analysis of all data was done by YX and XS. The original draft was written by YX. The manuscript was revised by DS, JL, and LZ.

All authors contributed to the article and approved the submitted version.

FUNDING

This work was supported by the National Natural Science Foundation of China (82003710), the Natural Science Foundation of Guangdong Province (2020A1515010075), the Project of Educational Commission of Guangdong Province (2021ZDZX 2012), and the Foundation from Guangdong Traditional Medicine Bureau (20201194).

ACKNOWLEDGMENTS

We thank all members of laboratory for their technical support and academic discussions.

SUPPLEMENTARY MATERIAL

The Supplementary Material for this article can be found online at: https://www.frontiersin.org/articles/10.3389/fchem.2022.856003/full#supplementary-material

REFERENCES

Bai, W., Li, S., Ma, J., Cao, W., and Zheng, J. (2019). Ultrathin 2D Metal-Organic Framework (Nanosheets and Nanofilms)-Based xD-2D Hybrid Nanostructures as Biomimetic Enzymes and Supercapacitors. *J. Mater. Chem. A.* 7 (15), 9086–9098. doi:10.1039/c9ta00311h

Batten, S. R., Champness, N. R., Chen, X.-M., Garcia-Martinez, J., Kitagawa, S., Öhrström, L., et al. (2013). Terminology of Metal-Organic Frameworks and Coordination Polymers (IUPAC Recommendations 2013). *Pure Appl. Chem.* 85 (8), 1715–1724. doi:10.1351/pac-rec-12-11-20

Dong, Y., Duan, C., Sheng, Q., and Zheng, J. (2019b). Preparation of Ag@zeolitic Imidazolate Framework-67 at Room Temperature for Electrochemical Sensing of Hydrogen Peroxide. *Analyst* 144 (2), 521–529. doi:10.1039/c8an01641k

Dong, Z., Yang, Z., Hao, Y., and Feng, L. (2019a). Fabrication of H2O2-Driven Nanoreactors for Innovative Cancer Treatments. *Nanoscale* 11 (35), 16164–16186. doi:10.1039/c9nr04418c

Furukawa, H., Cordova, K. E., O'Keeffe, M., and Yaghi, O. M. (2013). The Chemistry and Applications of Metal-Organic Frameworks. *Science* 341 (6149), 1230444. doi:10.1126/science.1230444

Gimeno, P., Bousquet, C., Lassu, N., Maggio, A.-F., Civade, C., Brenier, C., et al. (2015). High-performance Liquid Chromatography Method for the Determination of Hydrogen Peroxide Present or Released in Teeth Bleaching Kits and Hair Cosmetic Products. *J. Pharm. Biomed. Anal.* 107, 386–393. doi:10.1016/j.jpba.2015.01.018

Giorgio, M., Trinei, M., Migliaccio, E., and Pelicci, P. G. (2007). Hydrogen Peroxide: a Metabolic By-Product or a Common Mediator of Ageing Signals? *Nat. Rev. Mol. Cel Biol.* 8 (9), 722–728. doi:10.1038/nrm2240

Griendling, K. K. (2004). Novel NAD(P)H Oxidases in the Cardiovascular System. *Heart* 90 (5), 491–493. doi:10.1136/hrt.2003.029397

Hayyan, M., Hashim, M. A., and AlNashef, I. M. (2016). Superoxide Ion: Generation and Chemical Implications. *Chem. Rev.* 116 (5), 3029–3085. doi:10.1021/acs.chemrev.5b00407

Huang, Y., Zhao, M., Han, S., Lai, Z., Yang, J., Tan, C., et al. (2017). Growth of Au Nanoparticles on 2D Metalloporphyrinic Metal-Organic Framework Nanosheets Used as Biomimetic Catalysts for Cascade Reactions. *Adv. Mater.* 29 (32), 1700102. doi:10.1002/adma.201700102

Iyyamperumal, R., Zhang, L., Henkelman, G., and Crooks, R. M. (2013). Efficient Electrocatalytic Oxidation of Formic Acid Using Au@Pt Dendrimer-Encapsulated Nanoparticles. *J. Am. Chem. Soc.* 135 (15), 5521–5524. doi:10.1021/ja4010305

Jorgenson, T. C., Zhong, W., and Oberley, T. D. (2013). Redox Imbalance and Biochemical Changes in Cancer. *Cancer Res.* 73 (20), 6118–6123. doi:10.1158/0008-5472.Can-13-1117

Li, S., Liu, X., Chai, H., and Huang, Y. (2018). Recent Advances in the Construction and Analytical Applications of Metal-Organic Frameworks-Based Nanozymes. *Trac Trends Anal. Chem.* 105, 391–403. doi:10.1016/j.trac.2018.06.001

Li, Y., Hou, L., Liu, Z., Lu, W., Zhao, M., Xiao, H., et al. (2020). A Sensitive Electrochemical MUC1 Sensing Platform Based on Electroactive Cu-MOFs Decorated by AuPt Nanoparticles. *J. Electrochem. Soc.* 167(7), þ2158–2161. doi:10.1149/1945-7111/ab88b9

Li, Y., Lu, Q., Wu, S., Wang, L., and Shi, X. (2013). Hydrogen Peroxide Sensing Using Ultrathin Platinum-Coated Gold Nanoparticles with Core@shell Structure. *Biosens. Bioelectron.* 41, 576–581. doi:10.1016/j.bios.2012.09.027

Liu, C.-S., Li, J., and Pang, H. (2020). Metal-organic Framework-Based Materials as an Emerging Platform for Advanced Electrochemical Sensing. *Coord. Chem. Rev.* 410, 213222. doi:10.1016/j.ccr.2020.213222

Liu, Y., Zhang, Y., Hua, H., and Li, Y. (2017). Fabrication of Single Pt@Au Nanowire Electrodes for Monitoring Hydrogen Peroxide Released from Living Cells. *RSC Adv.* 7 (70), 44552–44558. doi:10.1039/c7ra08085a

Lu, J., Hu, Y., Wang, P., Liu, P., Chen, Z., and Sun, D. (2020). Electrochemical Biosensor Based on Gold Nanoflowers-Encapsulated Magnetic Metal-Organic Framework Nanozymes for Drug Evaluation with *In-Situ* Monitoring of H2O2 Released from H9C2 Cardiac Cells. *Sensors Actuators B: Chem.* 311, 127909. doi:10.1016/j.snb.2020.127909

Ma, J., Bai, W., and Zheng, J. (2019). Non-enzymatic Electrochemical Hydrogen Peroxide Sensing Using a Nanocomposite Prepared from Silver Nanoparticles and Copper (II)-porphyrin Derived Metal-Organic Framework Nanosheets. *Microchim. Acta* 186 (7), 482. doi:10.1007/s00604-019-3551-1

Ma, Y., Cen, Y., Sohail, M., Xu, G., Wei, F., Shi, M., et al. (2017). A Ratiometric Fluorescence Universal Platform Based on N, Cu Codoped Carbon Dots to Detect Metabolites Participating in H2O2-Generation Reactions. *ACS Appl. Mater. Inter.* 9 (38), 33011–33019. doi:10.1021/acsami.7b10548

Markesbery, W. R. (1997). Oxidative Stress Hypothesis in Alzheimer's Disease. *Free Radic. Biol. Med.* 23 (1), 134–147. doi:10.1016/s0891-5849(96)00629-6

Peng, Y., Yan, Z., Wu, Y., and Di, J. (2015). AgAuPt Nanocages for Highly Sensitive Detection of Hydrogen Peroxide. *RSC Adv.* 5 (11), 7854–7859. doi:10.1039/c4ra13653e

Ren, M., Deng, B., Wang, J.-Y., Kong, X., Liu, Z.-R., Zhou, K., et al. (2016). A Fast Responsive Two-Photon Fluorescent Probe for Imaging H2O2 in Lysosomes with a Large Turn-On Fluorescence Signal. *Biosens. Bioelectron.* 79, 237–243. doi:10.1016/j.bios.2015.12.046

Renner, F. U., Stierle, A., Dosch, H., Kolb, D. M., Lee, T.-L., and Zegenhagen, J. (2006). Initial Corrosion Observed on the Atomic Scale. *Nature* 439 (7077), 707–710. doi:10.1038/nature04465

Rhee, S. G., Kang, S. W., Jeong, W., Chang, T.-S., Yang, K.-S., and Woo, H. A. (2005). Intracellular Messenger Function of Hydrogen Peroxide and its Regulation by Peroxiredoxins. *Curr. Opin. Cel Biol.* 17 (2), 183–189. doi:10.1016/j.ceb.2005.02.004

Sun, D., Cai, C., Li, X., Xing, W., and Lu, T. (2004). Direct Electrochemistry and Bioelectrocatalysis of Horseradish Peroxidase Immobilized on Active Carbon. *J. Electroanalytical Chem.* 566 (2), 415–421. doi:10.1016/j.jelechem.2003.11.055

Sun, D., Yang, D., Wei, P., Liu, B., Chen, Z., Zhang, L., et al. (2020). One-step Electrodeposition of Silver Nanostructures on 2D/3D Metal-Organic Framework ZIF-67: Comparison and Application in Electrochemical Detection of Hydrogen Peroxide. *ACS Appl. Mater. Inter.* 12 (37), 41960–41968. doi:10.1021/acsami.0c11269

Sun, Y., Luo, M., Meng, X., Xiang, J., Wang, L., Ren, Q., et al. (2017). Graphene/Intermetallic PtPb Nanoplates Composites for Boosting Electrochemical Detection of H2O2 Released from Cells. *Anal. Chem.* 89 (6), 3761–3767. doi:10.1021/acs.analchem.7b00248

Tan, C., Cao, X., Wu, X.-J., He, Q., Yang, J., Zhang, X., et al. (2017). Recent Advances in Ultrathin Two-Dimensional Nanomaterials. *Chem. Rev.* 117 (9), 6225–6331. doi:10.1021/acs.chemrev.6b00558

Trachootham, D., Alexandre, J., and Huang, P. (2009). Targeting Cancer Cells by ROS-Mediated Mechanisms: a Radical Therapeutic Approach? *Nat. Rev. Drug Discov.* 8 (7), 579–591. doi:10.1038/nrd2803

Ushio-Fukai, M., Alexander, R. W., Akers, M., Yin, Q., Fujio, Y., Walsh, K., et al. (1999). Reactive Oxygen Species Mediate the Activation of Akt/protein Kinase B by Angiotensin II in Vascular Smooth Muscle Cells. *J. Biol. Chem.* 274 (32), 22699–22704. doi:10.1074/jbc.274.32.22699

Wang, H., Chen, W., Chen, Q., Liu, N., Cheng, H., and Li, T. (2021). Metal-organic Framework (MOF)-Au@Pt Nanoflowers Composite Material for Electrochemical Sensing of H2O2 in Living Cells. *J. Electroanalytical Chem.* 897, 115603. doi:10.1016/j.jelechem.2021.115603

Wang, N., Sun, Q., and Yu, J. (2019). Ultrasmall Metal Nanoparticles Confined within Crystalline Nanoporous Materials: a Fascinating Class of Nanocatalysts. *Adv. Mater.* 31 (1), 1803966. doi:10.1002/adma.201803966

Wang, Q., Wei, H., Zhang, Z., Wang, E., and Dong, S. (2018). Nanozyme: an Emerging Alternative to Natural Enzyme for Biosensing and Immunoassay. *Trac Trends Anal. Chem.* 105, 218–224. doi:10.1016/j.trac.2018.05.012

Wang, Y., Zhao, M., Ping, J., Chen, B., Cao, X., Huang, Y., et al. (2016). Bioinspired Design of Ultrathin 2D Bimetallic Metal-Organic-Framework Nanosheets Used as Biomimetic Enzymes. *Adv. Mater.* 28 (21), 4149–4155. doi:10.1002/adma.201600108

Wei, H., and Wang, E. (2013). Nanomaterials with Enzyme-like Characteristics (Nanozymes): Next-Generation Artificial Enzymes. *Chem. Soc. Rev.* 42 (14), 6060–6093. doi:10.1039/c3cs35486e

Wirtz, M., and Martin, C. R. (2003). Template-fabricated Gold Nanowires and Nanotubes. *Adv. Mater.* 15 (5), 455–458. doi:10.1002/adma.200390106

Wu, J., Wang, X., Wang, Q., Lou, Z., Li, S., Zhu, Y., et al. (2019). Nanomaterials with Enzyme-like Characteristics (Nanozymes): Next-Generation Artificial Enzymes (II). *Chem. Soc. Rev.* 48 (4), 1004–1076. doi:10.1039/c8cs00457a

Xie, J., and Huang, Y. (2011). Co3O4 Nanoparticles-Enhanced Luminol Chemiluminescence and its Application in H2O2 and Glucose Detection. *Anal. Methods* 3 (5), 1149–1155. doi:10.1039/c1ay05103b

Xu, R., Wang, Y., Duan, X., Lu, K., Micheroni, D., Hu, A., et al. (2016). Nanoscale Metal-Organic Frameworks for Ratiometric Oxygen Sensing in Live Cells. *J. Am. Chem. Soc.* 138 (7), 2158–2161. doi:10.1021/jacs.5b13458

Yang, J.-C., Lu, M.-C., Lee, C.-L., Chen, G.-Y., Lin, Y.-Y., Chang, F.-R., et al. (2011). Selective Targeting of Breast Cancer Cells through ROS-Mediated Mechanisms Potentiates the Lethality of Paclitaxel by a Novel Diterpene, Gelomulide K. *Free Radic. Biol. Med.* 51 (3), 641–657. doi:10.1016/j.freeradbiomed.2011.05.012

Yang, S., Han, G., Chen, Q., Yu, L., Wang, P., Zhang, Q., et al. (2021). Au-Pt Nanoparticle Formulation as a Radiosensitizer for Radiotherapy with Dual Effects. *Ijn* Vol. 16, 239–248. doi:10.2147/ijn.S287523

Yu, M., Zhao, K., Zhu, X., Tang, S., Nie, Z., Huang, Y., et al. (2017). Development of Near-Infrared Ratiometric Fluorescent Probe Based on Cationic Conjugated Polymer and CdTe/CdS QDs for Label-free Determination of Glucose in Human Body Fluids. *Biosens. Bioelectron.* 95, 41–47. doi:10.1016/j.bios.2017.03.065

Yu, Y., Yu, C., Niu, Y., Chen, J., Zhao, Y., Zhang, Y., et al. (2018). Target Triggered Cleavage Effect of DNAzyme: Relying on Pd-Pt Alloys Functionalized Fe-MOFs for Amplified Detection of Pb2+. *Biosens. Bioelectron.* 101, 297–303. doi:10.1016/j.bios.2017.10.006

Yuan, J., and Shiller, A. M. (1999). Determination of Subnanomolar Levels of Hydrogen Peroxide in Seawater by Reagent-Injection Chemiluminescence Detection. *Anal. Chem.* 71 (10), 1975–1980. doi:10.1021/ac981357c

Zhao, M., Huang, Y., Peng, Y., Huang, Z., Ma, Q., and Zhang, H. (2018a). Two-dimensional Metal-Organic Framework Nanosheets: Synthesis and Applications. *Chem. Soc. Rev.* 47 (16), 6267–6295. doi:10.1039/c8cs00268a

Zhao, M., Wang, Y., Ma, Q., Huang, Y., Zhang, X., Ping, J., et al. (2015). Ultrathin 2D Metal-Organic Framework Nanosheets. *Adv. Mater.* 27 (45), 7372–7378. doi:10.1002/adma.201503648

Zhao, W., Peng, J., Wang, W., Liu, S., Zhao, Q., and Huang, W. (2018b). Ultrathin Two-Dimensional Metal-Organic Framework Nanosheets for Functional Electronic Devices. *Coord. Chem. Rev.* 377, 44–63. doi:10.1016/j.ccr.2018.08.023

Zhou, J., Zhao, Y., Bao, J., Huo, D., Fa, H., Shen, X., et al. (2017). One-step Electrodeposition of Au-Pt Bimetallic Nanoparticles on MoS 2 Nanoflowers for Hydrogen Peroxide Enzyme-free Electrochemical Sensor. *Electrochimica Acta* 250, 152–158. doi:10.1016/j.electacta.2017.08.044

Zhu, D., Zuo, J., Tan, L., Pang, H., and Ma, H. (2019). Enzymeless Electrochemical Determination of Hydrogen Peroxide at a Heteropolyanion-Based Composite Film Electrode. *New J. Chem.* 43 (2), 1053–1062. doi:10.1039/c8nj04570d

Conflict of Interest: The authors declare that the research was conducted in the absence of any commercial or financial relationships that could be construed as a potential conflict of interest.

Publisher's Note: All claims expressed in this article are solely those of the authors and do not necessarily represent those of their affiliated organizations or those of the publisher, the editors, and the reviewers. Any product that may be evaluated in this article, or claim that may be made by its manufacturer, is not guaranteed or endorsed by the publisher.

frontiers | Frontiers in Chemistry

ORIGINAL RESEARCH
published: 06 April 2022
doi: 10.3389/fchem.2022.858107

Ultrasensitive Detection of Ochratoxin A With a Zeolite Imidazolate Frameworks Composite–Based Electrochemical Aptasensor

Xiao Ni[1], *Yuyan Zhang*[1], *Chuhan Xue*[2] *and Xiaojun Chen*[1,3]*

[1]College of Chemistry and Molecular Engineering, Nanjing Tech University, Nanjing, China, [2]Shanghai Pudong New District Jincai High School, Shanghai, China, [3]Jiangsu Key Laboratory of Molecular Biology for Skin Diseases and STIs, Nanjing, China

Ochratoxin A (OTA) is a harmful mycotoxin, which is mainly secreted by *Penicillium* and *Aspergillus* species. In this work, an electrochemical aptasensor is presented for OTA detection based on Au nanoparticles (AuNPs) modified zeolite imidazolate frameworks (ZIFs) ZIF-8 platform and duplex-specific nuclease (DSN) triggered hybridization chain reaction (HCR) signal amplification. G-quadruplex-hemin assembled HCR nanowire acted as a nicotinamide adenine dinucleotide (NADH) oxidase and an HRP-mimicking DNAzyme. Besides, thionine (Thi) was enriched as a redox probe for signal amplification in this pseudobienzyme electrocatalytic system. Under the optimal conditions, the analytical response ranged from 1 to 10^7 fg ml^{-1} with a detection limit of 0.247 fg ml^{-1}. Furthermore, the aptasensor was proven to be applied in real wheat samples with a recovery between 96.8 and 104.2%, illustrating the potential prospects in practical detection.

Keywords: zeolite imidazolate frameworks (ZIF-8), electrochemical aptasensors, mycotoxin, ochratoxin A (OTA), signal amplification strategy

OPEN ACCESS

Edited by:
Cheng Ma,
Yangzhou University, China

Reviewed by:
Sha Yu,
Xi'an University of Architecture and Technology, China
Qin Xu,
Yangzhou University, China

***Correspondence:**
Xiaojun Chen
chenxj@njtech.edu.cn

Specialty section:
This article was submitted to Analytical Chemistry, a section of the journal Frontiers in Chemistry

Received: *19 January 2022*
Accepted: *14 February 2022*
Published: *06 April 2022*

Citation:
Ni X, Zhang Y, Xue C and Chen X (2022) Ultrasensitive Detection of Ochratoxin A With a Zeolite Imidazolate Frameworks Composite–Based Electrochemical Aptasensor. Front. Chem. 10:858107. doi: 10.3389/fchem.2022.858107

INTRODUCTION

Ochratoxin is one of the secondary metabolism substances of ochra and penicillium fungi, which includes seven types of homologous structure compounds. Under the classification of WHO's International Agency for Research on Cancer, ochratoxin A (OTA) is known as the highest-toxic-ranking category, marking as Level 2B carcinogen (Lee and Ryu, 2017). It can threaten the health of most mammalian species in liver, kidneys, and immune system. OTA contamination occurs in most crop types, such as corn and wheat, and causes accumulation in livestock (Lee and Ryu, 2015). Besides, due to the high chemical stability, OTA rarely has quantity loss in the transportation and storage or lower risk of toxic hazards through additional manufacturing procedures (Abrunhosa et al., 2002). Hence, OTA can even be found in people's body since they eat the contaminated food (García-Campaña et al., 2012). Fully taking into account the potential toxicity, firm standards for residue harmful substance have been established by European regulators and the maximum content of OTA in both farm and sideline products shall not exceed 10 μg kg^{-1}. In general, the concentration of OTA often demonstrates low levels especially in the early stage. With the increase in health consciousness, associated research for detection of OTA in foodstuff has garnered particular attention.

Up to now, the universal analysis for OTA detection is largely concentrated in advanced instrumental methods, including high-performance liquid chromatography (HPLC), HPLC-fluorescence detector (HPLC-FLD), ELISA, and immunochromatographic assay (Pittet and

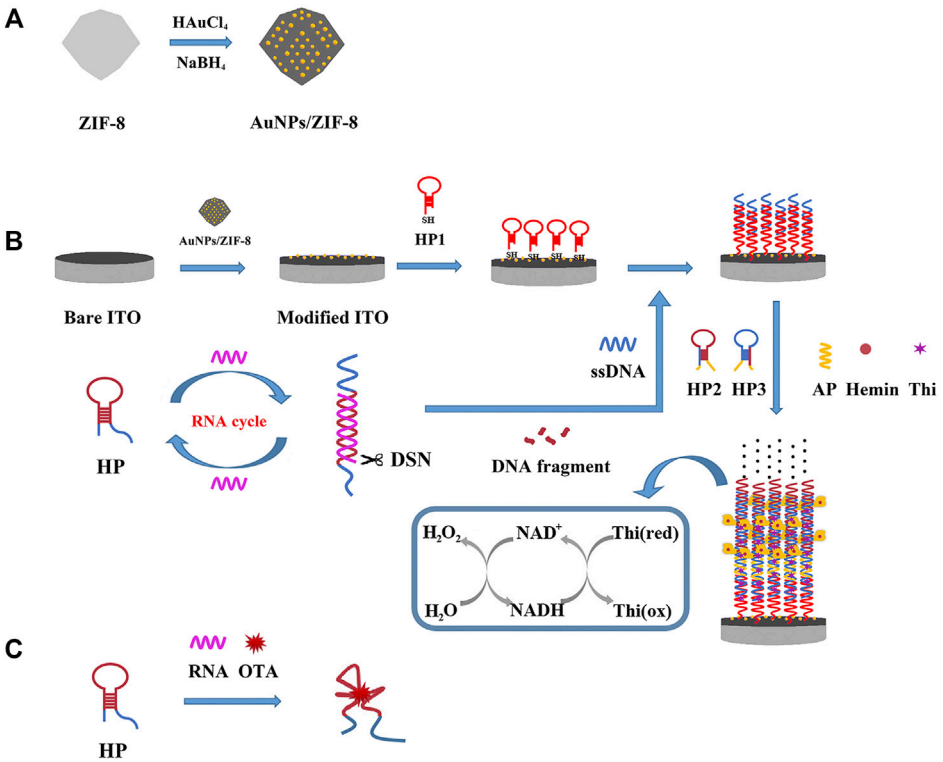

SCHEME 1 | Schematic illustration of the principle of the electrochemical aptasensor: **(A)** fabrication of the AuNPs/ZIF-8, **(B)** DSN-assisted signal amplification strategy in the absence of OTA, and **(C)** selective recognition of HP with OTA.

Royer, 2002; Cho et al., 2005; Giovannoli et al., 2014; Zhang et al., 2017; Sun Zhichang et al., 2018; Armstrong-Price et al., 2020). Although these chromatography and immunoassays have high precision and are selective during external interference, there still exist inescapable disadvantages such as high-cost expenses, complicated operation requirements and strict experimental conditions, and difficulty to conduct field testing. Therefore, the upcoming challenge is to have higher sensitivity and cost reduction advantages in OTA detection to realize application in practice. Compared with the aforementioned methods, electrochemical methods are preferable due to the low cost and short response, and are suitable for miniaturization in practical applications. Thereafter, various electrochemical biosensors for OTA have arisen, mainly involving immunosensors, capacitance biosensors, photo-electrochromic biosensors, aptasensors, etc. (Chen et al., 2012; Bougrini et al., 2016; Duan et al., 2017; Ying et al., 2018). Among them, the electrochemical aptasensors have been attracting more and more attention since they combine the advantages of electrochemical methods and aptamers.

Alternatively, aptamers have a favorable ascendancy in stability, affinity, and output, which make them obtain very high commercial availability (Cheow and Han, 2011; Han et al., 2012). Ever since the first time it was reported that the aptamer was applied for OTA detection by Cruz-Aguado's team (Cruz-Aguado and Penner, 2008), diverse OTA electrochemical aptasensors have been widely introduced. Hairpin-DNA aptamer toward OTA was first reported by Zhang et al. with an analytical response varying from 1.0 to 20 pg ml^{-1} (Zhang et al., 2012). Moreover, one recent work proposed a new model of OTA aptasensor, based on self-assembly between SH-aptamer and gold layer deposition, allowing to show wide-dynamic-range capabilities (1×10^{-5}–10 nM). Researchers also applied the aptasensor to investigate OTA in red wine samples (Yang et al., 2019). Although the sensitivity of these sensors has fulfilled OTA detection with a low content, development of novel aptasensors from various angles is still imperative.

To further make the best use of electrochemical aptasensors, electrode materials are crucial to enhance the sensitivity and stability. A series of nanomaterials were introduced to bring larger active surface and higher electrical conductivity for amplifying the response to weak signals (Manna and Raj, 2018). Metal-organic frameworks (MOFs), characteristic of high crystalline structure, have shown extensive application prospect in catalysis, medical science, biological toxicity testing, etc. (Wang P.-L. et al., 2019). However, bare MOFs did worse in constructing electrochemical aptasensors as they often conduct electricity poorly. Therefore, various MOF composites with metal nanoparticles, carbon nanostructures, and conductive polymers have been assembled for a wide application in electrochemical field (Zhang et al., 2020). In addition, zeolitic imidazolate frameworks (ZIFs) belonging to

TABLE 1 | Oligonucleotides used in this work

Oligonucleotide	Sequence (from 5′ to 3′)
HP	HS-C6- TTT TTT GAT CGG GTG TGG GTG GCG TAA AGG GAG CAT CGG ATC AAT CCG TCG AGC AGA GTT CCA TGT GTA GAT AGC TTA
HP1	HS-C6- CCA TGT GTA GAT CAG ACT ATT CGA TTA AGC TAT CTA CAC ATG G
HP2	AGG GCG GGT GGG TGT TTA AGT TGG AGA ATT GTA CTT AAA CAC CTT CTT CTT GGG T
HP3	TGG GTC AAT TCT CCA ACT TAA ACT AGA AGA AGG TGT TTA AGT TGG GTA GGG CGG G
AP	AAC TCT GCT CGA CGG ATT AGA AGA AGG TGT TTA AGT
RNA	U CCG AUG CUC CCU UUA CGC CAC CCA CAC CCG AUC

Note: The red font in HP is the OTA aptamer. Letters of the same color (blue, green, and brown) are respectively complementary to each other. The stem part in HP, HP1, HP2, and HP3 was marked with underlines.

one of those prove to have special structure of zeolite, which is characteristic of both thermal and chemical stability (Keskin, 2011). Because of the aforementioned advantages, ZIFs composite was used as a carrier in this work to load biomaterials. At present, the quest for ZIF-based aptasensors is still under way (Hao et al., 2019; Salandari-Jolge et al., 2021), and significantly, few of them have been applied in aspect of OTA detection.

With this idea in mind, a heterogeneous composite of Au nanoparticles (AuNPs)/ZIF-8 was selected and served as a conductive platform for supporting and sensing, by implanting ultrafine AuNPs into the highly regular ZIF-8 while the dodecahedral structure was unchanged. At the same time, in attempt to boost the number of recycling oligonucleotides for signal amplification, duplex-specific nuclease (DSN) was adopted. It can identify and digest DNA strand from a DNA/RNA hybrid to free RNA and achieving recovery (Qiu et al., 2015). The schematic illustration of this work is displayed in **Scheme 1**. In the absence of OTA, hairpin aptamer (HP) hybridized with RNA strand, which had an unmatched ssDNA on 3′-end. DNA strand in the duplex can be shorn by DSN to release RNA and trigger more cycles of DSN reaction. A short strand named ssDNA could be released to open HP1 assembled on the electrode, which initiated a HCR on the AuNPs/ZIF-8 modified electrode surface. The remaining parts in HP2 and HP3 combined with Hemin molecules to form G-quadruplex-hemin DNAzymes. In the catalytic reaction, thionine (Thi) was adopted as a redox probe and nicotinamide adenine dinucleotide (NADH) worked as coenzyme to further amplify the electrochemical signal (Yuan et al., 2014). Otherwise, with certain amount of OTA, HP tended to interact with OTA while RNA strands are released. HP/OTA failed to release ssDNA and trigger the subsequent HCR reactions, and then a weaker redox signal was recorded in comparison with circumstances when no OTA exists. In this perspective, the relationship between OTA content (C_{OTA}) and current signal has a negative linear correlation instead of a linear one.

EXPERIMENTAL

Materials and Instrumentation

Zinc (II) nitrate hexahydrate [$Zn(NO_3)_2{\cdot}6H_2O$], 2-methyl imidazole (2-MI), and sodium borohydride ($NaBH_4$) were purchased from Aladdin. Chloroauric acid hydrated ($HAuCl_4{\cdot}4H_2O$) was obtained from Beijing HWRK. NADH, Thi, and hemin were obtained from Aldrich. Bovine serum albumin (BSA) and Tris (2-carboxyethyl) phosphine hydrochloride (TCEP-HCl) were purchased from Baoman Biotech. Co., Ltd. Phosphoric acid buffer solution (PBS, 0.1 M, pH 7.0) was prepared by regulating the amount of Na_2HPO_4 and NaH_2PO_4 and used as electrolyte. PBS containing 5.0 mM $[Fe(CN)_6]^{3-/4-}$ was used for cyclic voltammetry (CV) and electrochemical impedance spectroscopy (EIS) analysis. Hemin solution was prepared by 0.15 mM hemin, 0.25 mM HEPES, 0.20 mM KCl, 2 mM NaCl, and 1 mM DMSO. OTA was obtained from PriboLab. DSN and the buffer were obtained from Evrogen. All functional group-modified oligonucleotides were purified by Sangon Biotechnology Co., Ltd. Indium tin oxide (ITO)–coated electrodes (coating thickness 180 ± 25 nm, sheet resistance <15 U/cm^2) were purchased from Kaivo Electronic Components Co., Ltd. All reagents were prepared with ultrapure water. All other chemicals were analytical grade and used without further purification. The oligonucleotide sequences are listed in **Table 1**.

Electrochemical measurements including differential pulse voltammetry (DPV), CV, and EIS were conducted on a CHI 660E electrochemical workstation (Chenhua Instrument). The morphology of the nanostructures was investigated by scanning electron microscopy (SEM; Zeiss Sigma 300) and transmission electron microscope (TEM; JEOL JEM-F200). Elemental mapping and energy dispersive spectrometry (EDS) were characterized on TEM (Hitachi S4800). The X-ray diffraction (XRD) pattern was recorded in the 2θ scan range from 5 to 40° using Cu Kα radiation with wavelength (λ) of 0.154 nm. Fourier-transform infrared resonance (FTIR) spectra were conducted on a Nicolet iS5 (Thermo Fisher Scientific) instrument using KBr pellet method. The chemical states were measured by X-ray photoelectron spectroscopy (XPS; Thermo Kalpha). The nitrogen adsorption–desorption isotherms were recorded by a gas sorption analyzer (ASAP2460), and the specific surface area was estimated by Barrett–Emmett–Teller (BET) theory. Agarose gel electrophoresis (AGE) analysis was conducted in 1× TAE buffer under 120 V for 40 min, in which the concentration of agarose was 2%. The gel stained by ethidium bromide (EB) was then separated to have images under gel imaging system (Bio-

Rad). The 50–500 bp DNA Ladder (Solarbio) was used as marker to analyze DNA bands.

Synthesis of ZIF-8

ZIF-8 was prepared according to a previous literature with a slight adjustment (Torad et al., 2013). Then 1 mmol $Zn(NO_3)_2{\cdot}6H_2O$ and 8 mmol 2-MI were respectively added to 10 ml methanol to form two clear solutions. They were then mixed into one beaker and let stand overnight for stratification. The white precipitated ZIF-8 was prepared in steps of methanol washing and vacuum drying.

Synthesis of AuNPs/ZIF-8

AuNPs/ZIF-8 was prepared according to a previous report (Wang Y. et al., 2019). ZIF-8 (0.2 g) was taken and 20 ml of 10 mM $HAuCl_4$ solution was added into a 50-ml beaker. To guarantee sufficient reaction, the solution was first ultrasonicated for 10 min and stirred vigorously for another 12 h. Then, 0.2 M $NaBH_4$ solution was quickly added and stirred for another 30 min. The resulting AuNPs/ZIF-8 was prepared in steps of water washing and vacuum drying.

Fabrication of AuNPs/ZIF-8 Modified Electrode

First, ITO electrode underwent ultrasonic cleaning in acetone and then successively treated with ethanol and distilled water, and then dried with nitrogen for further use. A region of space for electrochemical testing was confined to a 3-mm-diameter circular controlled by tape punching. Then, 10 μl of 1 mg ml^{-1} AuNPs/ZIF-8 dispersion was obtained and dribbled on the electrode surface. It was left to stand under room ambience to dry naturally and then stored at 4°C, which was designated as AuNPs/ZIF-8/ITO.

Process of Aptasensing

Before aptasensing, 20 μl of HP, HP1, HP2, or HP3 solution with a concentration of 4 μM was brought to a 95°C thermostatic water bath for 5 min and then cooled down to room temperature prior to use. Significantly, since HP and HP1 are –SH group modified, to reduce the formation of disulfide bond, per 100 μl of solution was added with 0.1 μl of 100 mM TCEP-HCl after activation. All DNA sequences were diluted with PBS and RNA sequence was diluted with TE buffer. Twenty microliters of different concentrations of HP1 was immersed on the AuNPs/ZIF-8/ITO surface at room temperature for 2 h. In this procedure, thiolated HP1 bound to the electrode surface via Au–S bonding. After that, the electrode was rinsed with distilled water and then incubated with 0.25 wt.% BSA solution for 30 min to block the residue active sites on electrode surface.

After that, the electrode was immersed in 20 μl of mixture (containing 7 μl of 2 μM HP, 1 μl of OTA with different concentrations, 1 μl of 10× DSN buffer, 1 μl of 2 μM RNA, and 0.1 U DSN) and reacted at 50°C for 30 min. This process was aimed at activating DSN and cleaving DNA–RNA duplex. Then, 10 μl of 2× DSN STOP solution was added for another 5 min. At this time, the released DNA had been digested and ssDNA had been generated. A part of HP1 strands on electrode surface could hybrid with ssDNA after incubating with the aforementioned mixture at room temperature. After thoroughly rinsed with PBS, the ssDNA/HP1/AuNPs/ZIF-8/ITO electrode was incubated with 10 μl mixture containing 1 μM HP2, HP3, and AP, 0.25 mM Thi, and 0.15 mM hemin to initiate HCR reaction (Sun Xiaofan et al., 2018). After the incubation, the hemin/G-quadruplex came to generate and acted as a horseradish peroxidase (HRP) mimicking enzyme for NADH oxidation to NAD^+ with the aid of dissolved O_2. During this process, Thi worked as an electron mediator and a dramatically amplified current signal could be observed. DPV measurements were carried out in 10 ml PBS and the addition of NADH was 3 mM. The potential range came between −0.4 and 0 V.

RESULTS AND DISCUSSION

Characterization of AuNPs/ZIF-8

Surface functional groups and formation of zinc nuclear imidazole coordination polymer were observed by FTIR spectra. As depicted in **Figure 1A**, both precursor ZIF-8 (curve b) and AuNPs/ZIF-8 (curve c) showed a C=N stretching vibration at 600 cm^{-1} and an aliphatic C–H stretch at 3,129 and 2,929 cm^{-1}, which is caused by methyl and imidazole ring of imidazole ligands (Yang et al., 2015; Zhang et al., 2011). Besides, the band at 400 cm^{-1} is characterized by Zn–N stretch, demonstrating that Zn^{2+} was coordinated with N atom in the imidazole ring, and the structure of the ligand was intact (Zhang et al., 2016). Compared with FTIR spectra of imidazole ligands (curve a), observations cannot be made at 1,845 or 2,648 cm^{-1}, which should be credited with N–H vibration and the N–H–N hydrogen bond absorption. The disappearance of the two strong bands shows the deprotonation of 2-methyl imidazole in the preparation process. It is known that there are no characteristic peaks for Au in the IR region and the analyzed FTIR result of AuNPs/ZIF-8 coincides well with that conclusion (Wang, Y., et al., 2019).

XRD patterns also authenticated the preparation of ZIF-8 and AuNPs/ZIF-8, as illustrated in **Figure 1B**. The presence of diffraction peaks with high intensity demonstrated that the synthesized products all had a crystalline structure. The characteristic peaks at 7.4°, 10.4°, 12.3°, 16.5°, 18.1°, and 26.8° corresponded to the crystal plane of (011), (002), (112), (013), (222), and (134) belonging to ZIF-8, which is consistent with previous reports (Park et al., 2006). In addition, the sharp peaks appearing at 7.4° and 12.3° indicated that the synthesized ZIF-8 structure was highly crystalline. Shown as the red curve in **Figure 1B**, after encapsulation of AuNPs, the main diffraction peaks of ZIF-8 remained unchanged, which can be attributed to the small sizes and high dispersion of AuNPs (Zhang et al., 2018).

The structure and morphology of ZIF-8 and AuNPs/ZIF-8 were characterized by TEM and SEM, respectively. As seen in **Figures 2A,B**, typical uniform rhombic dodecahedron shape of ZIF-8 was preserved entirely after AuNP modification, and the particle size was found to increase from 65 nm (**Figure 2C**) to 80 nm (**Figure 2D**). Since AuNPs were produced *in situ* on the

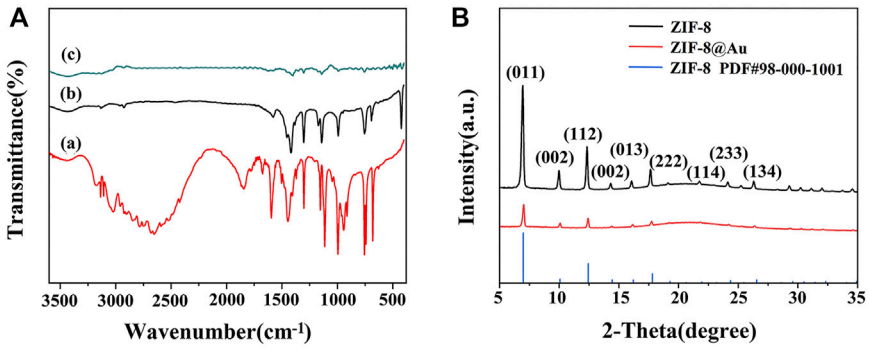

FIGURE 1 | (A) FTIR spectra of (a) 2-MI, (b) ZIF-8, and (c) AuNPs/ZIF-8. **(B)** XRD patterns of ZIF-8 and AuNPs/ZIF-8.

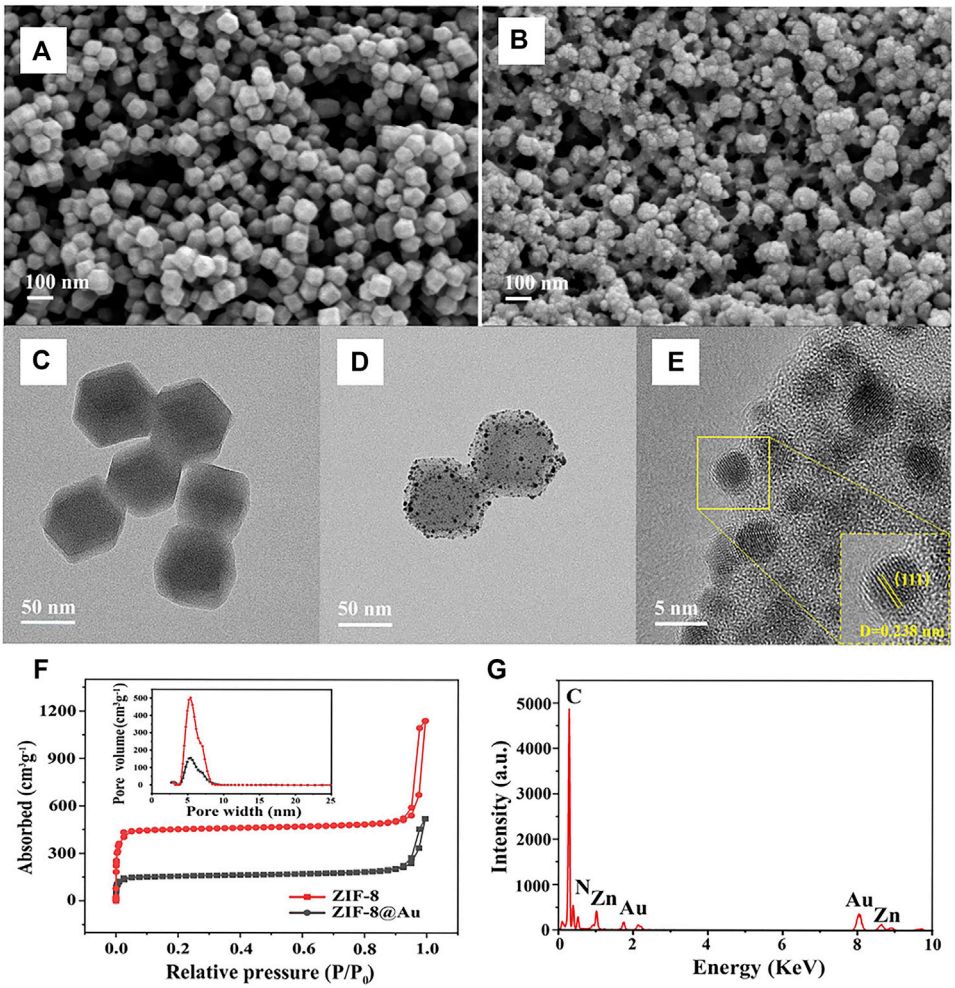

FIGURE 2 | SEM images of **(A)** ZIF-8 and **(B)** AuNPs/ZIF-8. TEM images of the **(C)** ZIF-8 and **(D)** AuNPs/ZIF-8. **(E)** HRTEM image of AuNPs/ZIF-8. **(F)** N_2 adsorption–desorption isotherms of ZIF-8 and AuNPs/ZIF-8 (inset: pore size distribution). **(G)** EDS spectrum of AuNPs/ZIF-8.

surface of ZIF-8 particles, some AuNPs uniformly scattered over the surface of ZIF-8 particles and others were implanted inside of ZIF-8, as seen in **Figures 2D,E**. To evaluate the pore structure and surface area before and after AuNPs interspersing into ZIF-8, N_2 adsorption–desorption isotherms were performed (**Figure 2F**). According to the IUPAC classification, two hysteresis loops of

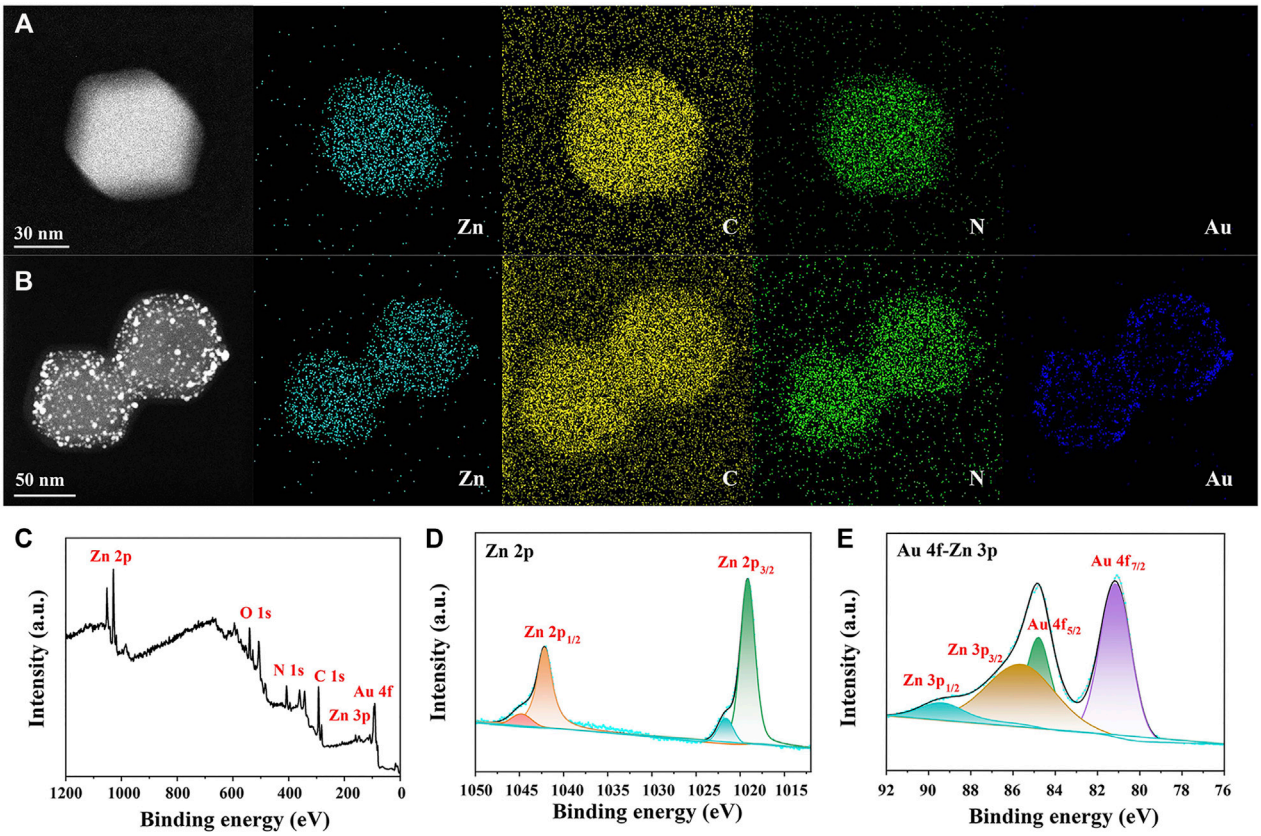

FIGURE 3 | EDS mapping of **(A)** ZIF-8 and **(B)** AuNPs/ZIF-8. **(C)** XPS survey spectrum, high-resolution XPS spectra of **(D)** Zn 2p and **(E)** Au 4f-Zn 3p of AuNPs/ZIF-8.

Type-I were observed, indicating the presence of microporous structure of ZIF-8 and AuNPs/ZIF-8 materials (Sun et al., 2019). The surface area of AuNPs/ZIF-8 was calculated to be 628.8 ± 2 m^2 g^{-1}, which was much smaller than that of ZIF-8 (1,880.1 ± 2 m^2 g^{-1}). The pore size of AuNPs/ZIF-8 (5.38 nm) was a little smaller than that of the parent ZIF-8 (5.42 nm), and the total pore volume also decreased by about 68%. The result illustrated that AuNPs have implanted into the pores of ZIF-8 (Li Ying et al., 2021). Meanwhile, TEM images of **Figure 2D** demonstrated the uniform distribution of AuNPs into ZIF-8 surface, which was further confirmed in **Figure 2E**. The EDS result of **Figure 2G** verified the existence of Zn, C, N, and Au elements in an AuNPs/ZIF-8 singular particle.

Elementary mapping was also applied for confirming AuNP distribution in AuNPs/ZIF-8. Compared with **Figure 3A** of ZIF-8, uniformly distributed AuNPs could be observed on ZIF-8 surface (blue dots in **Figure 3B**). As shown in **Figure 3C**, XPS measurements were conducted to determine the valance states of different atoms in AuNPs/ZIF-8. In **Figure 3D**, the high-resolution Zn 2p spectrum in AuNPs/ZIF-8 split into doublet peaks due to the spin–orbit coupling effect, corresponding to Zn $2p_{1/2}$ and Zn $2p_{3/2}$. Meanwhile, Zn 2p spectrum was deconvoluted into four peaks, which were assigned to Zn–N (1,019.22 eV, 1,042.16 eV) and Zn–O (1,021.69 eV, 1,044.63 eV), respectively, which indicated the presence of +2 oxidation state of Zn (Tuncel and Ökte, 2021). As shown in **Figure 3E**, the XPS spectrum of Au 4f overlapped with that of Zn 3p, which could be deconvoluted into four peaks of Au $4f_{7/2}$ at 81.18 eV, Au $4f_{5/2}$ at 84.80 eV, Zn $3p_{3/2}$ at 85.64 eV, and Zn $3p_{1/2}$ at 89.63 eV, respectively (Gao et al., 2020). It can be noted that the intensity of Au was lower than that of Zn^{2+}, which can be attributed to the sub-participation of AuNPs, and the obtained results were consistent with EDS analysis (**Figure 2G**).

Feasibility of the Amplification Strategy

To characterize the stepwise modification process of the aptasensor, EIS at each immobilization step was recorded as shown in **Figure 4A**. Curve a represented the impedance spectrum of ITO, with an electron transfer resistance (R_{et}) value around 135.2 Ω. When the AuNPs/ZIF-8 was modified onto the ITO surface, the diameter of semicircle (curve b) decreased since external AuNPs helped enhance the interface electron transfer. After the modification of HP1 through Au–S bond, R_{et} value increased from 96.7 to 133.6 Ω (curve c), which can be explained that the negative-charged HP1 electrostatically repulsed the negative-charged electrochemical probe of $[Fe(CN)_6]^{3-/4-}$, decreasing the electron transfer rate from $[Fe(CN)_6]^{3-/4-}$ to electrode surface. A larger semicircle

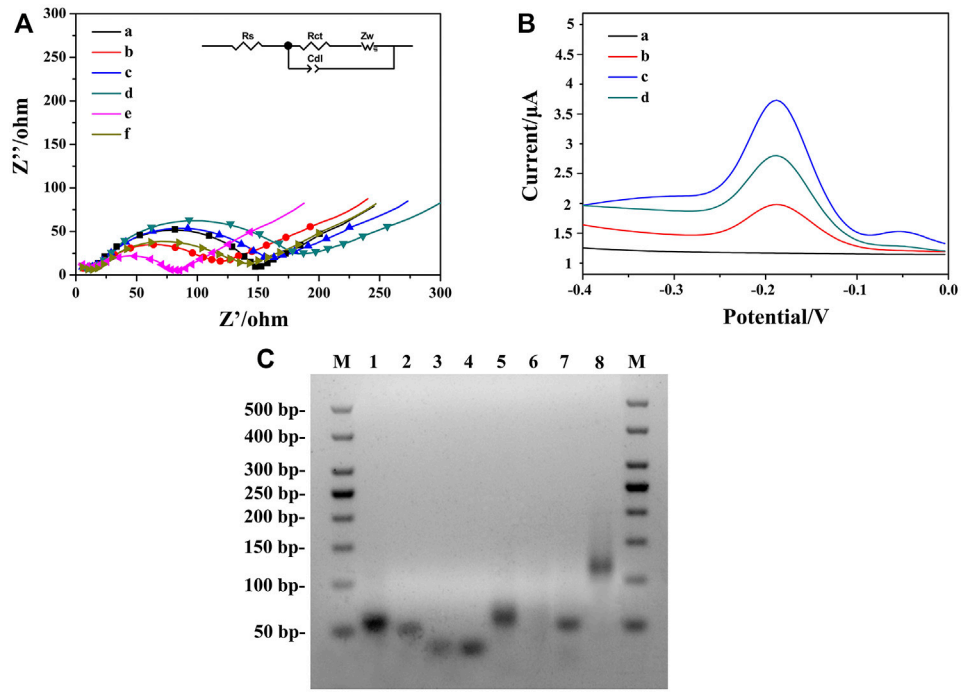

FIGURE 4 | (A) Nyquist plots of different modified electrodes were recorded in PBS containing 5.0 mM $[Fe(CN)_6]^{3-/4-}$: (a) bare ITO, (b) AuNPs/ZIF-8/ITO, (c) HP1/AuNPs/ZIF-8/ITO, (d) BSA/HP1/AuNPs/ZIF-8/ITO, (e) ssDNA/HP1/AuNPs/ZIF-8/ITO, (f) HCR/ssDNA/HP1/AuNPs/ZIF-8/ITO. **(B)** DPV signals in PBS at (a) ssDNA/HP1/AuNPs/ZIF-8/ITO, (b) HCR/ssDNA/HP1/AuNPs/ZIF-8/ITO with Thi, (c) solution b added with NADH, Thi, and hemin, (d) HCR/ssDNA/HP1/AuNPs/ZIF-8/ITO formed after the addition of 10^3 fg ml^{-1} OTA. **(C)** The AGE characterization. Lane M: DNA marker, lanes 1–4: HP, HP1, HP2, and HP3, respectively; lane 5: HP/RNA; lane 6: solution 5 added with DSN; lane 7: ssDNA/HP1; lane 8: ssDNA/HP1/HCR.

domain was displayed after the electrode was blocked with 0.25% BSA (curve d). Curve e depicts the hybridization of ssDNA with HP1, by unfolding HP1 from hairpin rigid structure to liner flexible structure, with a very small R_{et} value around 71 Ω. The decrease of R_{et} can be explained in terms of steric effects caused by structural changes of chains. As for electrode treating with HCR, a further increased R_{et} was observed because the exponential negatively charged nucleic acids immobilized onto the sensing interface (Wang X. et al., 2019). According to the characterization of impedance spectra, each step of fabrication was successfully conducted and HCR/ssDNA/HP1/AuNPs/ZIF-8/ITO was proved to be well assembled. The fitted R_{et} values were calculated based on the equivalent circuit, which consisted of four main elements: electrolyte solution resistance (R_s), R_{et}, the double layer capacitance (C_{dl}), and Warburg impedance (Z_w) (inset part in **Figure 4A**).

Feasibility of the strategy employed for amplifying signals was verified by DPV with different modified electrodes under diverse detection conditions. **Figure 4B** illustrates the DPV responses of different aptasensors. Curve a corresponded to ssDNA/HP1/AuNPs/ZIF-8/ITO electrode in PBS, in which no visible DPV signals could be seen. It indicated that there was no electrochemical probe Thi on the electrode surface at this time. After HCR structure formed on the electrode surface, Thi could be electrostatically adsorbed on HCR, arousing a low current response (curve b) mainly due to the insulating nature of oligonucleotides. When hemin/G-quadruplex DNAzyme formed with the participation of hemin, an obviously increased peak current was obtained in the presence of 3.0 mM NADH (curve c) due to the synergistic catalytic effect between DNAzyme and NADH. The obtained current was about 2.6 times of that in curve b, illustrating enhanced signal amplification. For comparison, in the presence of 10^3 fg ml^{-1} target OTA, a weaker DPV signal (curve d) was recorded since the strong affinity between HP and OTA caused less ssDNA to be released.

To further evaluate the feasibility of the aptasensor, AGE analysis was conducted by DNA electrophoresis on various stages of samples (Bai et al., 2021). As shown in **Figure 4C**, lanes 1 to 4 corresponded to HP, HP1, HP2, and HP3, and four bright bands could be observed respectively. In the absence of OTA, HP hybridized with RNA, which gave a good explanation for a bright band in lane 5, and the height was a little higher than that of HP. After adding DSN in duplex HP/RNA, HP was digested while ssDNA was released. No obvious band was observed in lane 6, which might be explained by the fact that single-stranded ssDNAs with much smaller molecular weights were hard to detect in electrophoresis analysis. Lanes 7 and 8 corresponded to ssDNA/HP1 and ssDNA/HP1/HCR, two bright bands that illustrated the hybridization among ssDNA, HP1, AP, HP2, and HP3 was successful. In addition, lane 7 was found to be a little higher than lane 2, which can be attributed to the

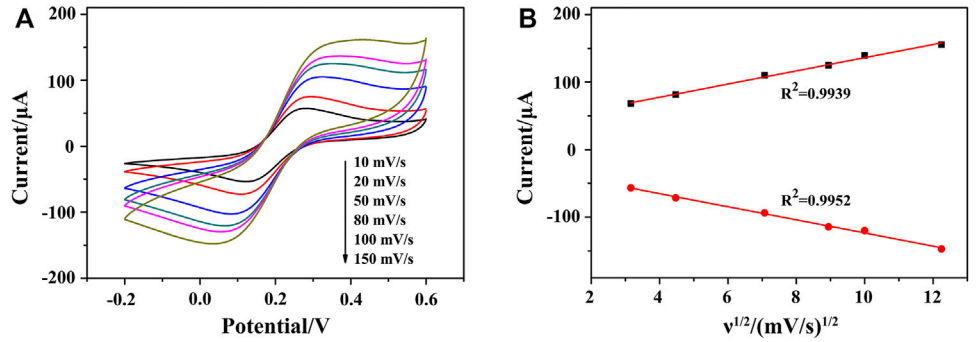

FIGURE 5 | (A) CVs of HP1/AuNPs/ZIF-8/ITO at the scan rate of 10, 20, 50, 80, 100, and 150 mV s^{-1} (from internal to external) in PBS solution containing 5.0 mM $[Fe(CN)_6]^{3-/4-}$, respectively. **(B)** The corresponding plot of peak current *vs*. $v^{1/2}$.

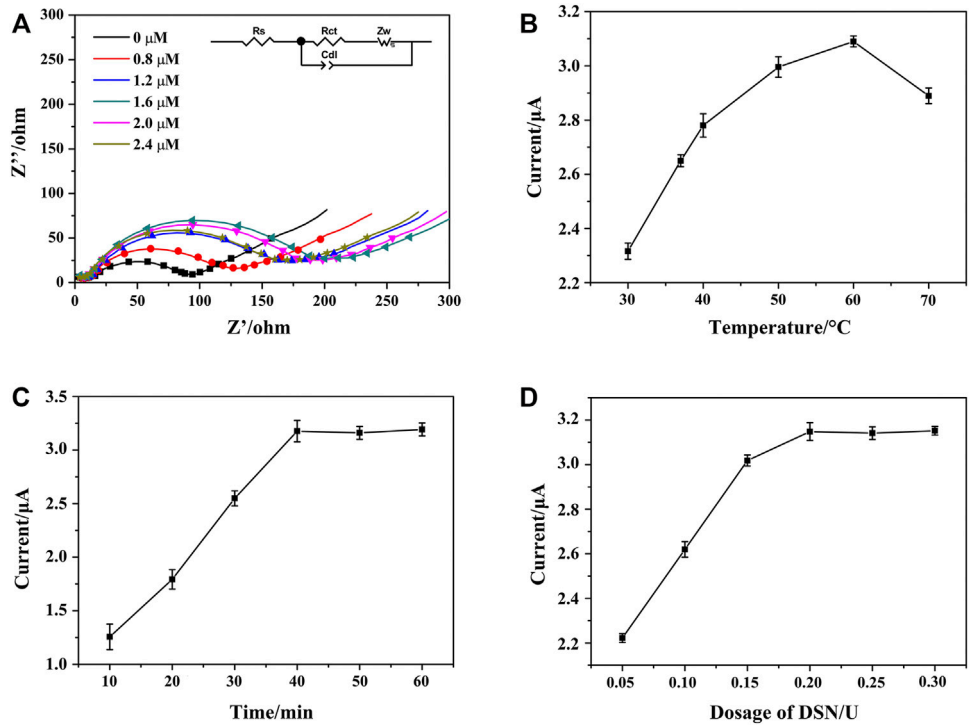

FIGURE 6 | (A) Nyquist plots of HP1/AuNPs/ZIF-8/ITO immobilized with different concentrations of HP1, which recorded in PBS containing 5.0 mM $[Fe(CN)_6]^{3-/4-}$. Effects of DSN catalytic nicking reaction parameters of **(B)** reaction temperature, **(C)** reaction time, and **(D)** DSN dosage on the peak current of HCR/ssDNA/HP1/AuNPs/ZIF-8/ITO in the presence of NADH and Thi, respectively.

combination of ssDNA and HP1. Lane 8 was the highest band in this image, illustrating the large molecule nature of HCR structure. Therefore, the AGE result fully confirmed the strong interactions among these sequences and the feasibility of the sensing strategy in this work.

Kinetic Study of the Modified Electrode

To study the kinetic principle of the electrochemical process, CV curves were recorded at different scan rates (v) from 10 to 150 mV s^{-1}. As shown in **Figure 5A**, CV curves displayed good symmetry at different scanning rates accompanying with a significant pair of redox peaks, in which $[Fe(CN)_6]^{3-/4-}$ worked as the oxidation–reduction probe. By deducing the relationship between redox peak currents and the square root of scan rate ($v^{1/2}$), a linear relationship can be acquired, indicating a diffusion-controlled electrochemical process. It meant that a fast electron transfer occurs between the $Fe(CN)_6^{4-}$ and the electrode surface, demonstrating an excellent conductivity of AuNPs/ZIF-8 and a uniform distribution of AuNPs in pores of ZIF-8 (**Figure 5B**).

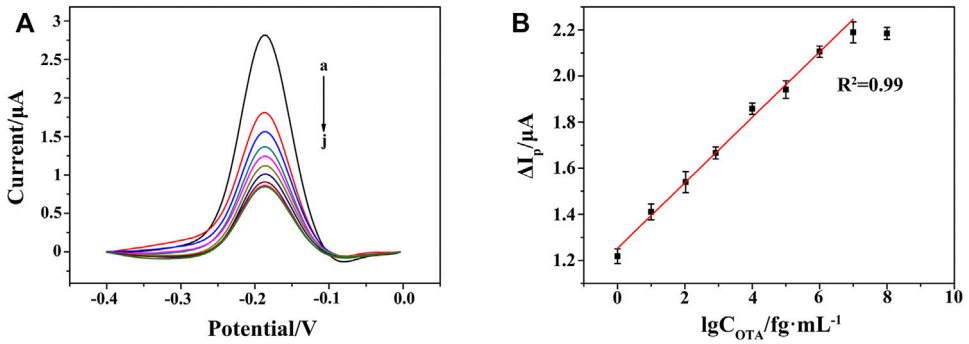

FIGURE 7 | (A) DPV responses at the HCR/ssDNA/HP1/AuNPs/ZIF-8/ITO with varying concentrations of OTA from 0 to 10^7 fg ml^{-1} (curves a to j: 0, 1 fg ml^{-1}, 10 fg ml^{-1}, 10^2 fg ml^{-1}, 10^3 fg ml^{-1}, 10^4 fg ml^{-1}, 10^5 fg ml^{-1}, 10^6 fg ml^{-1}, 10^7 fg ml^{-1}, 10^8 fg ml^{-1}). **(B)** Linear relationship between the peak current change and the logarithm of OTA concentration from 1 to 10^7 fg ml^{-1}.

Optimization of Experimental Parameters

To improve the performance of the aptasensor, the reaction parameters of HP1 concentration, DSN dosage, DSN cleaving temperature, and reaction time were investigated by EIS and DPV techniques (Li Xiaoyan et al., 2021; Peng et al., 2018; Zhang et al., 2019). As shown in **Figure 6A**, along with the concentration of HP1 that increased from 0 to 2.4 μM, the detected R_{et} value of HP1/AuNPs/ZIF-8/ITO increased accordingly and the largest value appeared at 1.6 μM. If the immobilized HP1 exceeded 1.6 μM, the R_{et} value seemed decreased a little, which might be ascribed to the excessive HP1 that could not link the limited active sites on AuNPs/ZIF-8/ITO surface. It meant that 1.6 μM of HP1 immobilization was saturated on electrode surface.

DSN could cleave HP in heteroduplex of HP/RNA and thus release the RNA strand for amplification cycle. The reaction temperature, time, and DSN dosage are important for the optimal performance of DSN catalytic reaction, which should be studied and discussed. To maximize the effect of DSN catalysis, reaction time and DSN dosage were fixed at 60 min and 0.3 U, respectively. The peak currents of HCR/ssDNA/HP1/AuNPs/ZIF-8/ITO in the presence of NADH and Thi were recorded. As **Figure 6B** illustrates, peak current successively increased when the reaction temperature rose from 30 to 60°C, since more and more ssDNA could be released after DSN catalysis. However, the current was observed to decrease at 70°C, which might be due to less stability of DSN and HP/RNA heteroduplex at a higher temperature. In addition, the peak current was found to be increased along with the reaction time that was prolonged from 10 to 40 min, and then reached a plateau. Similarly, the peak current was also found to reach a maximum and steady value at the DSN dosage of 0.2 U. It meant that 40 min of reaction time at 60°C and 0.2 U of DSN dosage were sufficient for the enzyme catalyzed nicking reaction.

Quantitative Determination of OTA

Under the optimal conditions, the performance of the aptasensor was evaluated in terms of sensitivity and dynamic response range. In the absence of OTA, the DPV current of Thi was recorded as I_0. In the presence of OTA, the high infinity of OTA with its aptamer led to the decrease in the amount of HP/RNA, and thus the corresponding current response of Thi (I) became lower. A gradual reduction of DPV current was observed after adding OTA from 1 to 10^7 fg ml^{-1} (**Figure 7A**). As shown in **Figures 7A,B**, good linearity between the peak current change ($\Delta I_p = I_0 - I$) and the logarithm of OTA concentration was obtained, with a linear equation of $\Delta I_p/\mu A = 0.14\ lgC_{OTA}/fg\ ml^{-1} + 1.25$ ($n = 5$, $R^2 = 0.99$). The limit of detection was evaluated to be 0.247 fg ml^{-1} according to 3 σ principle. Compared with the performance of previously reported OTA aptasensors, as listed in **Table 2**, the proposed aptasensor exhibited a wide linear range by eight orders of magnitude with a low detection limit. The advantages of our work were ascribed to six aspects: 1) the controllable and perfect structured ZIF-8 provided rich active sites and a large surface area for DNA strands modification; 2) the *in situ* implantation of AuNPs significantly enhanced the electron transfer rate; 3) DSN was used for selective digestion of DNA strand in DNA/RNA hybrid, providing a good chance for designing a RNA recycled amplification strategy; 4) the G-quadruplex-hemin assembled HCR nanowire acted as an NADH oxidase to assist the concomitant formation of H_2O_2 in the presence of dissolved O_2; 5) meanwhile, the G-quadruplex-hemin assembled HCR nanowire acted as an HRP-mimicking DNAzyme to catalyze the reduction of the produced H_2O_2; 6) with the redox probe Thi as electron mediator, the pseudobienzyme electrocatalytic system combined with the aptamer recognition strategy endowed a dramatically amplified electrochemical aptasensing performance.

Selectivity and OTA Detection in Real Samples

To evaluate the selectivity of the constructed OTA aptasensing strategy, 10^3 fg ml^{-1} of zearalenone (ZEN), aflatoxin B1 (AFB1), aflatoxin B2 (AFB2), and the mixture of the aforementioned interfering substances were tested as the normal interferents toward OTA. Herein, blank solution without OTA and 10^3 fg ml^{-1} of OTA were set as control samples. It could be seen that a significantly decreased peak current was obtained in 10^3 fg ml^{-1} of OTA solution, while the peak currents detected in interferents were similar to that in blank solution, as could be seen in **Figure 8**. It could be demonstrated that there is a high selectivity of this OTA

TABLE 2 | Comparisons of analytical performances of different OTA aptasensors

Signal amplification mode	Liner range (fg ml^{-1})	Detection limit (fg ml^{-1})	Ref
RCA	5 × 10^4–10^8	104	Hao et al. (2020)
Exo III-assisted cycling	1–10^5	0.25	Huang et al. (2020)
Exo I + silver metallized aptamer	10^3–10^8	700	Suea-Ngam et al. (2019)
G-quadruplex-hemin	10^4–10^8	4,280	Shen et al. (2017)
Restriction endonuclease	10^3–2 × 10^4	400	Zhang et al. (2012)
HCR-restriction endonuclease-aided DNA walker	10–10^7	3.3	Wang et al. (2021)
"DSN + G-quadruplex-hemin" dual-enzyme	1–10^7	0.247	This work

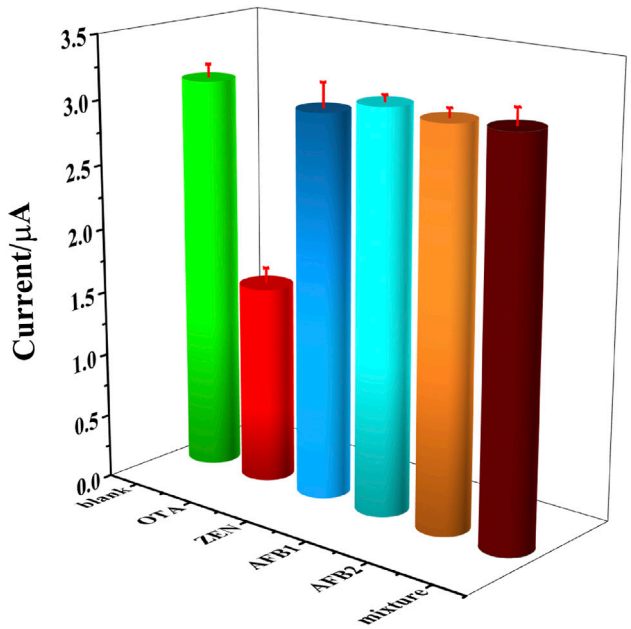

FIGURE 8 | DPV currents recorded in blank solution, 10^3 fg ml^{-1} of OTA, ZEN, AFB1, AFB2 and the mixture of above interfering substance, respectively.

TABLE 3 | The recovery determination in real wheat flour samples

Sample	Added (fg ml^{-1})	Found (fg ml^{-1})	Recovery (%)	RSD (%)
1	102	99.8	99.8	1.6
2	105	9.68 × 104	96.8	5.9
3	108	1.042 × 108	104.2	3.0

aptasensor, which was owing to the high affinity between aptamer and OTA.

The performance of the aptasensor was further evaluated in some OTA real samples. Wheat flour (5 g) purchased from the market was added into 20 ml of acetonitrile–water (v/v = 9:1) mixture, and the supernatant was collected for use after centrifugation and filtration. Wheat extract was diluted with PBS via the volume ratio of 1:9, then 1 ml of OTA standard solutions with the concentration of 10^2 fg ml^{-1}, 10^5 fg ml^{-1}, and 10^8 fg ml^{-1} were spiked respectively into 9 ml of the aforementioned extractions. As shown in **Table 3**, the recoveries of the three samples were in the range of 96.8–104.2% with the relative standard deviation (RSD) values of 3.0–5.9%. According to the result, the proposed aptasensing strategy was expected to become a powerful tool for OTA residue detection in real samples with enough precision and accuracy.

CONCLUSION

In conclusion, the AuNPs/ZIF-8 with a typical rhombic dodecahedron shape was prepared by *in situ* reduction method with $NaBH_4$. A highly sensitive OTA aptasensor was then designed by conducting an enzymatic signal amplification system, accompanying with ZIF-8 materials and the autonomously assembled hemin/G-quadruplex DNAzyme for further signal amplification. BET experiments revealed that the prepared ZIF-8 provided abundant available functional surface for subsequent modification of AuNPs, which is in favor of immobilization of HP1 on AuNPs/ZIF-8/ITO electrode. Owing to the specific ability of

DSN to identify and cleave DNA from DNA/RNA heteroduplex, ssDNA thus could be released and to open HP1 assembled on the electrode, which successfully triggered the HCR and further realized the pseudobienzyme electrocatalytic amplification. Catalytic results indicated that this constructed aptasensor exhibited a high sensitivity from 1 to 10^7 fg ml^{-1} and a low detection limit of 0.247 fg ml^{-1}. Furthermore, the aptasensor was proven to be applied in wheat samples, which demonstrated the potential prospects in practical detection.

DATA AVAILABILITY STATEMENT

The original contributions presented in the study are included in the article/Supplementary Material, further inquiries can be directed to the corresponding author.

AUTHOR CONTRIBUTIONS

XN: investigation, software, writing—original draft. YZ: methodology, data curation. CX: data curation. XC: funding acquisition, project administration, resources, validation, supervision. All authors discussed the results and commented on the article.

FUNDING

This work was financially supported by the National Key Research and Development Program (2017YFC1600604), National Natural Science Foundation of China (21575064), and the project fund of Jiangsu Key Laboratory of Molecular Biology for Skin Diseases and STIs (2021).

REFERENCES

Abrunhosa, L., Serra, R., and Venâncio, A. (2002). Biodegradation of Ochratoxin A by Fungi Isolated from Grapes. *J. Agric. Food Chem.* 50 (25), 7493–7496. doi:10.1021/jf025747i

Armstrong-Price, D. E., Deore, P. S., and Manderville, R. A. (2020). Intrinsic "Turn-On" Aptasensor Detection of Ochratoxin A Using Energy-Transfer Fluorescence. *J. Agric. Food Chem.* 68 (7), 2249–2255. doi:10.1021/acs.jafc.9b07391

Bai, Y., Zhang, H., Zhao, L., Wang, Y., Chen, X., Zhai, H., et al. (2021). A Novel Aptasensor Based on HCR and G-Quadruplex DNAzyme for Fluorescence Detection of Carcinoembryonic Antigen. *Talanta* 221, 121451. doi:10.1016/j.talanta.2020.121451

Bougrini, M., Baraket, A., Jamshaid, T., Aissari, A. E., Bausells, J., Zabala, M., et al. (2016). Development of A Novel Capacitance Electrochemical Biosensor Based on Silicon Nitride for Ochratoxin A Detection. *Sensors Actuators B: Chem.* 234, 446–452. doi:10.1016/j.snb.2016.03.166

Chen, J., Fang, Z., Liu, J., and Zeng, L. (2012). A Simple and Rapid Biosensor for Ochratoxin A Based on A Structure-Switching Signaling Aptamer. *Food Control* 25 (2), 555–560. doi:10.1016/j.foodcont.2011.11.039

Cheow, L. F., and Han, J. (2011). Continuous Signal Enhancement for Sensitive Aptamer Affinity Probe Electrophoresis Assay Using Electrokinetic Concentration. *Anal. Chem.* 83 (18), 7086–7093. doi:10.1021/ac201307d

Cho, Y.-J., Lee, D.-H., Kim, D.-O., Min, W.-K., Bong, K.-T., Lee, G.-G., et al. (2005). Production of A Monoclonal Antibody against Ochratoxin A and its Application to Immunochromatographic Assay. *J. Agric. Food Chem.* 53 (22), 8447–8451. doi:10.1021/jf051681q

Cruz-Aguado, J. A., and Penner, G. (2008). Determination of Ochratoxin A with A Dna Aptamer. *J. Agric. Food Chem.* 56 (22), 10456–10461. doi:10.1021/jf801957h

Duan, H., Huang, X., Shao, Y., Zheng, L., Guo, L., and Xiong, Y. (2017). Size-Dependent Immunochromatographic Assay with Quantum Dot Nanobeads for Sensitive and Quantitative Detection of Ochratoxin A in Corn. *Anal. Chem.* 89 (13), 7062–7068. doi:10.1021/acs.analchem.7b00869

Gao, L., Wu, Z., Ibrahim, A.-R., Zhou, S.-F., and Zhan, G. (2020). Fabrication of Folic Acid-Decorated Hollow ZIF-8/Au/CuS Nanocomposites for Enhanced and Selective Anticancer Therapy. *ACS Biomater. Sci. Eng.* 6 (11), 6095–6107. doi:10.1021/acsbiomaterials.0c01152

García-Campaña, A. M., Lombardo-Agüí, M., Arroyo-Manzanares, N., Gámiz-Gracia, L., and Cruces-Blanco, C. (2012). XV International Symposium on Luminescence Spectrometry-Biophysical and Analytical Aspects, Extended Abstracts, 19-22 June 2012, Barcelona, Spain-(ISLS 2012). *Luminescence* 27 (6), 534–572. doi:10.1002/bio.2432

Giovannoli, C., Passini, C., Di Nardo, F., Anfossi, L., and Baggiani, C. (2014). Determination of Ochratoxin A in Italian Red Wines by Molecularly Imprinted Solid Phase Extraction and HPLC Analysis. *J. Agric. Food Chem.* 62 (22), 5220–5225. doi:10.1021/jf5010995

Han, B., Zhao, C., Yin, J., and Wang, H. (2012). High Performance Aptamer Affinity Chromatography for Single-step Selective Extraction and Screening of Basic Protein Lysozyme. *J. Chromatogr. B* 903, 112–117. doi:10.1016/j.jchromb.2012.07.003

Hao, L., Wang, W., Shen, X., Wang, S., Li, Q., An, F., et al. (2020). A Fluorescent DNA Hydrogel Aptasensor Based on the Self-Assembly of Rolling Circle Amplification Products for Sensitive Detection of Ochratoxin A. *J. Agric. Food Chem.* 68 (1), 369–375. doi:10.1021/acs.jafc.9b06021

Hao, Y.-B., Shao, Z.-S., Cheng, C., Xie, X.-Y., Zhang, J., Song, W.-J., et al. (2019). Regulating Fluorescent Aptamer-Sensing Behavior of Zeolitic Imidazolate Framework (ZIF-8) Platform via Lanthanide Ion Doping. *ACS Appl. Mater. Inter.* 11 (35), 31755–31762. doi:10.1021/acsami.9b12253

Huang, X.-B., Wu, S.-H., Hu, H.-C., and Sun, J.-J. (2020). AuNanostar@4-MBA@Au Core-Shell Nanostructure Coupled with Exonuclease III-Assisted Cycling Amplification for Ultrasensitive SERS Detection of Ochratoxin A. *ACS Sens.* 5 (8), 2636–2643. doi:10.1021/acssensors.0c01162

Keskin, S. (2011). Atomistic Simulations for Adsorption, Diffusion, and Separation of Gas Mixtures in Zeolite Imidazolate Frameworks. *J. Phys. Chem. C* 115 (3), 800–807. doi:10.1021/jp109743e

Lee, H. J., and Ryu, D. (2015). Significance of Ochratoxin A in Breakfast Cereals from the United States. *J. Agric. Food Chem.* 63 (43), 9404–9409. doi:10.1021/jf505674v

Lee, H. J., and Ryu, D. (2017). Worldwide Occurrence of Mycotoxins in Cereals and Cereal-Derived Food Products: Public Health Perspectives of Their Co-occurrence. *J. Agric. Food Chem.* 65 (33), 7034–7051. doi:10.1021/acs.jafc.6b04847

Li, X., Ni, X., Cui, F., Qiu, Q., Chen, X., and Huang, H. (2021). A Logic Dual-Channel Detection of Hox Transcript Antisense Intergenic RNA Using Graphene Switch and Padlock Probe-Based Exponential Rolling Circle Amplification Assay. *Sensors Actuators B: Chem.* 340, 129931. doi:10.1016/j.snb.2021.129931

Li, Y., Li, S., Bao, M., Zhang, L., Carraro, C., Maboudian, R., et al. (2021). Pd Nanoclusters Confined in ZIF-8 Matrixes for Fluorescent Detection of Glucose and Cholesterol. *ACS Appl. Nano Mater.* 4 (9), 9132–9142. doi:10.1021/acsanm.1c01712

Manna, B., and Raj, C. R. (2018). Nanostructured Sulfur-Doped Porous Reduced Graphene Oxide for the Ultrasensitive Electrochemical Detection and Efficient Removal of Hg(II). *ACS Sust. Chem. Eng.* 6 (5), 6175–6182. doi:10.1021/acssuschemeng.7b04884

Park, K. S., Ni, Z., Cote, A. P., Choi, J. Y., Huang, R., Uribe-Romo, F. J., et al. (2006). Exceptional Chemical and Thermal Stability of Zeolitic Imidazolate Frameworks. *Proc. Natl. Acad. Sci.* 103 (27), 10186–10191. doi:10.1073/pnas.0602439103

Peng, G., Li, X., Cui, F., Qiu, Q., Chen, X., and Huang, H. (2018). Aflatoxin B1 Electrochemical Aptasensor Based on Tetrahedral DNA Nanostructures

Functionalized Three Dimensionally Ordered Macroporous MoS2-AuNPs Film. *ACS Appl. Mater. Inter.* 10 (21), 17551–17559. doi:10.1021/acsami.8b01693

Pittet, A., and Royer, D. (2002). Rapid, Low Cost Thin-Layer Chromatographic Screening Method for the Detection of Ochratoxin A in Green Coffee at a Control Level of 10 μg/kg. *J. Agric. Food Chem.* 50 (2), 243–247. doi:10.1021/jf010867w

Qiu, X., Zhang, H., Yu, H., Jiang, T., and Luo, Y. (2015). Duplex-Specific Nuclease-Mediated Bioanalysis. *Trends Biotechnol.* 33 (3), 180–188. doi:10.1016/j.tibtech.2014.12.008

Salandari-Jolge, N., Ensafi, A. A., and Rezaei, B. (2021). Ultra-Sensitive Electrochemical Aptasensor Based on Zeolitic Imidazolate Framework-8 Derived Ag/Au Core-Shell Nanoparticles for Mercury Detection in Water Samples. *Sensors Actuators B: Chem.* 331, 129426. doi:10.1016/j.snb.2020.129426

Shen, P., Li, W., Liu, Y., Ding, Z., Deng, Y., Zhu, X., et al. (2017). High-Throughput Low-Background G-Quadruplex Aptamer Chemiluminescence Assay for Ochratoxin A Using A Single Photonic Crystal Microsphere. *Anal. Chem.* 89 (21), 11862–11868. doi:10.1021/acs.analchem.7b03592

Suea-Ngam, A., Howes, P. D., Stanley, C. E., and DeMello, A. J. (2019). An Exonuclease I-Assisted Silver-Metallized Electrochemical Aptasensor for Ochratoxin A Detection. *ACS Sens.* 4 (6), 1560–1568. doi:10.1021/acssensors.9b00237

Sun, X., Chen, H., Wang, S., Zhang, Y., Tian, Y., and Zhou, N. (2018). Electrochemical Detection of Sequence-specific DNA Based on Formation of G-Quadruplex-Hemin through Continuous Hybridization Chain Reaction. *Analytica Chim. Acta* 1021, 121–128. doi:10.1016/j.aca.2018.02.076

Sun, Y., Shi, J., Zhang, S., Wu, Y., Mei, S., Qian, W., et al. (2019). Hierarchically Porous and Water-Tolerant Metal-Organic Frameworks for Enzyme Encapsulation. *Ind. Eng. Chem. Res.* 58 (28), 12835–12844. doi:10.1021/acs.iecr.9b02164

Sun, Z., Lv, J., Liu, X., Tang, Z., Wang, X., Xu, Y., et al. (2018). Development of A Nanobody-AviTag Fusion Protein and its Application in A Streptavidin-Biotin-Amplified Enzyme-Linked Immunosorbent Assay for Ochratoxin A in Cereal. *Anal. Chem.* 90 (17), 10628–10634. doi:10.1021/acs.analchem.8b03085

Torad, N. L., Hu, M., Kamachi, Y., Takai, K., Imura, M., Naito, M., et al. (2013). Facile Synthesis of Nanoporous Carbons with Controlled Particle Sizes by Direct Carbonization of Monodispersed ZIF-8 Crystals. *Chem. Commun.* 49 (25), 2521. doi:10.1039/c3cc38955c

Tuncel, D., and Ökte, A. N. (2021). Improved Adsorption Capacity and Photoactivity of ZnO-ZIF-8 Nanocomposites. *Catal. Today* 361, 191–197. doi:10.1016/j.cattod.2020.04.014

Wang, P.-L., Xie, L.-H., Joseph, E. A., Li, J.-R., Su, X.-O., and Zhou, H.-C. (2019a). Metal-Organic Frameworks for Food Safety. *Chem. Rev.* 119 (18), 10638–10690. doi:10.1021/acs.chemrev.9b00257

Wang, X., Shan, Y., Gong, M., Jin, X., Lv, L., Jiang, M., et al. (2019b). A Novel Electrochemical Sensor for Ochratoxin A Based on the Hairpin Aptamer and Double Report DNA via Multiple Signal Amplification Strategy. *Sensors Actuators B: Chem.* 281, 595–601. doi:10.1016/j.snb.2018.10.148

Wang, Y., Li, X., Waterhouse, G. I. N., Zhou, Y., Yin, H., and Ai, S. (2019c). Photoelectrochemical Biosensor for Protein Kinase A Detection Based on Carbon Microspheres, Peptide Functionalized Au-ZIF-8 and TiO2/g-C3n4. *Talanta* 196, 197–203. doi:10.1016/j.talanta.2018.12.035

Wang, Y., Song, W., Zhao, H., Ma, X., Yang, S., Qiao, X., et al. (2021). DNA Walker-Assisted Aptasensor for Highly Sensitive Determination of Ochratoxin A. *Biosens. Bioelectron.* 182, 113171. doi:10.1016/j.bios.2021.113171

Yang, J., Zhang, F., Lu, H., Hong, X., Jiang, H., Wu, Y., et al. (2015). Hollow Zn/Co ZIF Particles Derived from Core-Shell ZIF-67@ZIF-8 as Selective Catalyst for the Semi-hydrogenation of Acetylene. *Angew. Chem. Int. Ed.* 54 (37), 10889–10893. doi:10.1002/anie.201504242

Yang, Y.-J., Zhou, Y., Xing, Y., Zhang, G.-M., Zhang, Y., Zhang, C.-H., et al. (2019). A Label-free Aptasensor Based on Aptamer/NH2 Janus Particles for Ultrasensitive Electrochemical Detection of Ochratoxin A. *Talanta* 199, 310–316. doi:10.1016/j.talanta.2019.02.015

Ying, Z.-M., Xiao, H.-Y., Tang, H., Yu, R.-Q., and Jiang, J.-H. (2018). Light-up RNA Aptamer Enabled Label-free Protein Detection via A Proximity Induced Transcription Assay. *Chem. Commun.* 54 (64), 8877–8880. doi:10.1039/C8CC04498H

Yuan, Y., Gao, M., Liu, G., Chai, Y., Wei, S., and Yuan, R. (2014). Sensitive Pseudobienzyme Electrocatalytic DNA Biosensor for Mercury(II) Ion by Using the Autonomously Assembled Hemin/G-Quadruplex DNAzyme Nanowires for Signal Amplification. *Analytica Chim. Acta* 811, 23–28. doi:10.1016/j.aca.2013.11.051

Zhang, H., Fan, M., Jiang, J., Shen, Q., Cai, C., and Shen, J. (2019). Sensitive Electrochemical Biosensor for MicroRNAs Based on Duplex-specific Nuclease-Assisted Target Recycling Followed with Gold Nanoparticles and Enzymatic Signal Amplification. *Analytica Chim. Acta* 1064, 33–39. doi:10.1016/j.aca.2019.02.060

Zhang, J., Chen, J., Zhang, X., Zeng, Z., Chen, M., and Wang, S. (2012). An Electrochemical Biosensor Based on Hairpin-DNA Aptamer Probe and Restriction Endonuclease for Ochratoxin A Detection. *Electrochemistry Commun.* 25, 5–7. doi:10.1016/j.elecom.2012.09.006

Zhang, K., Kirlikovali, K. O., Varma, R. S., Jin, Z., Jang, H. W., Farha, O. K., et al. (2020). Covalent Organic Frameworks: Emerging Organic Solid Materials for Energy and Electrochemical Applications. *ACS Appl. Mater. Inter.* 12 (25), 27821–27852. doi:10.1021/acsami.0c06267

Zhang, K., Schaab, M. R., Southwood, G., Tor, E. R., Aston, L. S., Song, W., et al. (2017). A Collaborative Study: Determination of Mycotoxins in Corn, Peanut Butter, and Wheat Flour Using Stable Isotope Dilution Assay (SIDA) and Liquid Chromatography-Tandem Mass Spectrometry (LC-MS/MS). *J. Agric. Food Chem.* 65 (33), 7138–7152. doi:10.1021/acs.jafc.6b04872

Zhang, Y., Li, Q., Liu, C., Shan, X., Chen, X., Dai, W., et al. (2018). The Promoted Effect of a Metal-Organic Frameworks (ZIF-8) on Au/TiO2 for CO Oxidation at Room Temperature Both in Dark and under Visible Light Irradiation. *Appl. Catal. B: Environ.* 224, 283–294. doi:10.1016/j.apcatb.2017.10.027

Zhang, Z., Xian, S., Xi, H., Wang, H., and Li, Z. (2011). Improvement of CO2 Adsorption on ZIF-8 Crystals Modified by Enhancing Basicity of Surface. *Chem. Eng. Sci.* 66 (20), 4878–4888. doi:10.1016/j.ces.2011.06.051

Zhang, Z., Zhang, J., Liu, J., Xiong, Z., and Chen, X. (2016). Selective and Competitive Adsorption of Azo Dyes on the Metal-Organic Framework ZIF-67. *Water Air Soil Poll* 227 (12). doi:10.1007/s11270-016-3166-7

Conflict of Interest: The authors declare that the research was conducted in the absence of any commercial or financial relationships that could be construed as a potential conflict of interest.

Publisher's Note: All claims expressed in this article are solely those of the authors and do not necessarily represent those of their affiliated organizations, or those of the publisher, the editors, and the reviewers. Any product that may be evaluated in this article, or claim that may be made by its manufacturer, is not guaranteed or endorsed by the publisher.

frontiers | Frontiers in Chemistry

MINI REVIEW
published: 27 April 2022
doi: 10.3389/fchem.2022.882250

Recent Advances on DNAzyme-Based Biosensors for Detection of Uranyl

Yunlong Bai[1], Lechang Xu[1], Huining Chai[2], Lei Zhou[1], Guoping Jiang[1] and Guangyao Zhang[3]**

[1]Beijing Research Institute of Chemical Engineering and Metallurgy, China National Nuclear Corporation, Beijing, China, [2]School of Environmental and Municipal Engineering, Qingdao University of Technology, Qingdao, China, [3]Intelligent Wearable Engineering Research Center of Qingdao, Research Center for Intelligent and Wearable Technology, College of Textiles and Clothing, State Key Laboratory of Bio-Fibers and Eco-Textiles, Qingdao University, Qingdao, China

Nuclear facilities are widely used in fields such as national defense, industry, scientific research, and medicine, which play a huge role in military and civilian use. However, in the process of widespread application of nuclear technology, uranium and its compounds with high carcinogenic and biologically toxic cause a lot of environmental problems, such as pollutions of water, atmosphere, soil, or ecosystem. Bioensors with sensitivity and specificity for the detection of uranium are highly demand. Nucleic acid enzymes (DNAzyme) with merits of high sensitivity and selectivity for targets as excellent molecular recognition elements are commonly used for uranium sensor development. In this perspective review, we summarize DNAzyme-based biosensors for the quantitative detection of uranyl ions by integrating with diverse signal outputting strategies, such as fluorescent, colorimetry, surface-enhanced Raman scattering, and electrochemistry. Different design methods, limit of detection, and practical applications are fully discussed. Finally, the challenges, potential solutions, and future prospects of such DNAzyme-based sensors are also presented.

Keywords: uranyl sensor, DNAzyme, environmental monitoring, detection, spectrum, electrochemistry

OPEN ACCESS

Edited by:
Cheng Ma,
Yangzhou University, China

Reviewed by:
Taiping Qing,
Xiangtan University, China

****Correspondence:***
Lechang Xu
xu_lechang@163.com
Guangyao Zhang
gyzhang@qdu.edu.cn

Specialty section:
This article was submitted to Analytical Chemistry, a section of the journal Frontiers in Chemistry

Received: *23 February 2022*
Accepted: *22 March 2022*
Published: *27 April 2022*

Citation:
Bai Y, Xu L, Chai H, Zhou L, Jiang G and Zhang G (2022) Recent Advances on DNAzyme-Based Biosensors for Detection of Uranyl. Front. Chem. 10:882250. doi: 10.3389/fchem.2022.882250

INTRODUCTION

Uranium, a radioactive metal element, is a significant raw material for the nuclear industry including nuclear power, nuclear weapons, scientific research, and nuclear medicines. Uranium-based nuclear energy effectively reduces global environmental problems such as global warming and energy depletion caused by fossil energy. Economic, efficient, and clean nuclear energy has great development prospects. Whereas, with the development and application of nuclear technology, the radioactive wastes containing uranium will gradually infiltrate environmental media, such as water, soil, and atmosphere, and eventually enter the biosphere system, which will cause great damage to humans and ecosystems. Uranium with strong chemical toxicity and radiotoxicity will cause lasting disturbances and damage to the immune, reproduction, and hematopoietic systems of organisms (Domingo, 2001). The World Health Organization lists uranium as a priority environmental pollutant, stipulating that the concentration limit of uranium in drinking water is 30 ug/L (Ansoborlo et al., 2015). Uranium possesses a lot of forms under different conditions and the uranyl ion (UO_2^{2+}) is the most stable chemical form in aqueous solution. Many techniques have been developed for UO_2^{2+} detection, including X-ray fluorescence spectroscopy, atomic emission spectrometry, inductively coupled plasma mass spectrometry, and high-performance liquid chromatography (Jamali et al., 2006; Jaison et al., 2011; Boulyga et al., 2016; Sanyal et al., 2017).

TABLE 1 | DNAzyme-based biosensors for the detection of uranyl ion.

Sensor Type	Design Method	Detection Limit	Dynamic Range	Ref.
Fluorescence	DNAzyme-FAM-Quencher	45 pM	1–400 nM	Liu et al. (2007)
Fluorescence	DNAzyme-Cy3-BHQ	45 pM	45 pM–20 μM	Wu et al. (2013)
Fluorescence	DNAzyme-AuNPs-fluorophore	25 pM	0.1–60 nM	Xiong et al. (2020)
Fluorescence	DNAzyme-DNA-SG	0.06 ng/ml	0.2–200 ng/ml	Zhu et al. (2019)
Fluorescence	DNAzyme-FAM-AuNPs	13 pM	30 pM–5 nM	Yun et al. (2019)
Fluorescence	DNAzyme-HCA-AuNPs-fluorophore	0.1 pM	0.2–1,000 pM	Yun et al. (2018)
Fluorescence	DNAzyme-2-aminopurine	9.6 nM	5–400 nM	Wang et al. (2019)
Fluorescence	DNAzyme-C3 Spacer	0.19 nM	2–1,000 nM	Feng et al. (2019)
Fluorescence	DNAzyme-FAM-MoS_2	2.14 nM	5–100 nM	Zhang et al. (2015)
Fluorescence	DNAzyme-GO-NMM	86 pM	0.29–30 nM	Li et al. (2015)
Fluorescence	FAM-DNAzyme-DABCYL	0.6 nM	1–60 nM	Zhou et al. (2016)
Fluorescence	DNAzyme-SG-NMM	11.47 nM	10–1,000 nM	Yang et al. (2021)
Colorimetry	DNAzyme-SG-TMB-H_2O_2	0.08 μg/L	0.5–500 μg/L	Huang et al. (2018)
Colorimetry	MBs-DNAzyme-HCR-TMB-H_2O_2-HRP	0.33 nM	0.14–4.1 nM	Zhang et al. (2017)
Colorimetry	MBs-DNAzyme-RCA-TMB-H_2O_2	37 pM	74 pM–37 nM	Cheng et al. (2017)
Colorimetry	MBs-DNAzyme-AuNPs-TMB-H_2O_2	7 pM	74 pM–56 nM	Zhang et al. (2016)
Colorimetry	Hydrogel-DNAzyme-AuNPs	14 nM	50–800 nM	Huang et al. (2016)
Colorimetry	DNAzyme-AuNPs	4.09 μM	13.6–150 μM	Zhou et al. (2013)
Colorimetry	DNAzyme-litmus	15 μg/L	1.5–15 μg/L	Manochehry et al. (2018)
SERS	Rhodamine-DNAzyme-AuNPs	1.6 nM	2.5–100 nM	Jiang et al. (2013)
SERS	Cy5- DNAzyme-Au nanowire	1 pM	1 pM–100 nM	Gwak et al. (2016)
SERS	RhB -DNAzyme-ZnO-Ag	3.71 fM	0.1 pM–0.1 μM	He et al. (2019)
SERS	RhB -DNAzyme-ZnO-Ag	0.72 pM	1 pM–0.1 μM	He et al. (2020b)
SERS	DNAzyme -DNA Hydrogel- RhB	0.838 pM	1 pM–0.1 μM	He et al. (2020a)
Electrochemistry	DNAzyme-Ferrocene	1 nM	2–14 nM	Tang et al. (2013)
Electrochemistry	DNAzyme-AuNPs-Hexaammineruthenium (III)	5 pM	13 pM–0.15 nM	Ma et al. (2014)
Electrochemistry	DNAzyme-AuNPs-MB	8.1 pM	10–100 pM	Cao et al. (2020)
Electrochemistry	DNAzyme-HCR-MB	20 pM	0.05–4 nM	Yun et al. (2016b)
Electrochemistry	DNAzyme -CHA-MB	2 pM	10 pM–1 nM	Yun et al. (2016a)

BHQ: carboxylic acid; AuNPs: gold nanoparticles; SG: SYBR, green I; FAM: 6-carboxylfluorescein; HCA: hairpin catalytic assembly; MoS_2: molybdenum disulfide; GO: graphene oxide; NMM: N-methyl-mesoporphyrin IX; MB: methylene blue; CHA: catalyzed hairpin assembly; HCR: hybridization chain reaction; TMB: 3,3′,5,5′-Tetramethylbenzidine; RCA: rolling circle amplification; SERS: Surface-enhanced Raman scattering, RhB: Rhodamine B.

These methods with high selectivity and sensitivity are high cost, requiring sophisticated instrument and tedious pre-treating procedures, which are difficult to achieve the goal of real-time and onsite detection. Therefore, bioensors with high sensitivity and specificity for the detection of uranyl ion have become increasingly necessary.

Nucleic acid enzymes, also called DNAzymes, are isolated through *in vitro* selection (Liu et al., 2009). DNAzyme typically is composed of a substrate strand and an enzyme strand, and the two DNA strands are partially complementary hybridized by base pairing to form a double-stranded system. The presence of target ion activates the activity of DNAzyme and the ribo-adenosine (rA) on the substrate chain is cleavaged. The released target ion subsequently interacts with another DNAzyme, resulting in a signal-amplifying effect. DNAzymes with high metal-binding affinity and specificity show great promise as molecular tools in the design of diverse biosensors and nanodevices, benefiting from their unique characters, including low nonspecific adsorption, good stability, and easy preparation (Zhou et al., 2017; Jouha and Xiong, 2021). Moreover, the recycling of target molecule properties makes DNAzymes outstanding signal amplifiers for enzyme-free and highly sensitive detection of many different metal ions (Saidur et al., 2017; Jouha and Xiong, 2021; Khan et al., 2021). UO_2^{2+}-specific DNAzyme was firstly selected by Lu group and a fluorescent sensor was developed simultaneously (Liu et al., 2007). In the past few years, quite a few amplified sensing platforms had been established for the quantitative detection of UO_2^{2+} (Farzin et al., 2019; He and Hua, 2019; Wu et al., 2019; Wang et al., 2022). In this review, we only focused on the application of various types of DNAzymes-based methods with diverse signals outputting approaches to achieve quantitative detection of uranyl ion. Design strategies, detection limits, and detection ranges were comprehensively compared. Such DNAzymes based sensors are expected to show great potential in environmental monitoring and nuclear emergency.

APPLICATIONS OF DIFFERENT TYPES OF DNAZYME-BASED SENSORS

DNAzymes as the recognition element are suitable for the fabrication of uranyl sensors. Target molecules induced huge changes in structure and conformation of DNAzymes to produce diverse signal outputting including fluorescence, electrochemistry, colorimetry, and surface-enhanced Raman scattering (SERS). **Table 1** summarized the DNAzyme-based biosensors for the detection of UO_2^{2+} by integrating with different signal output types including fluorescent, electrochemistry, colorimetry, and SERS.

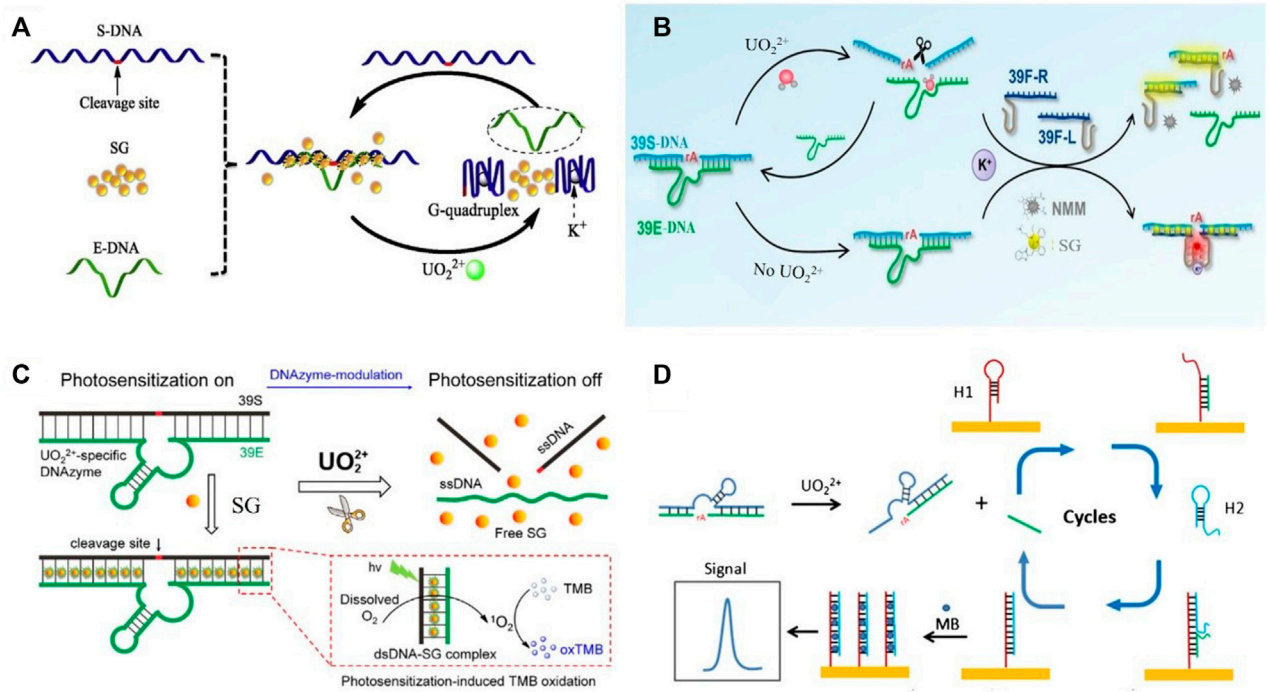

FIGURE 1 | DNAzyme-based biosensors for the detection of uranyl ions by integrating with diverse signal outputting strategies in previous reports **(A)** G-quadruplex-assisted enzyme strand recycling-based fluorescent uranyl ion sensor. Reprinted with permission (Zhu et al., 2019), Copyright 2019 Elsevier B.V. **(B)** Ratiometric fluorescent biosensor for uranyl detection. Reprinted with permission (Yang et al., 2021). Copyright 2021 Elsevier B.V. **(C)** Electrochemical biosensor for uranyl detection based on DNAzyme and CHA. Reprinted with permission (Yun et al., 2016a). Copyright 2017, Royal Society of Chemistry **(D)** DNAzyme-modulated SG photosensitization colorimetric sensor for detection of UO_2^{2+}. Reprinted with permission (Huang et al., 2018). Copyright 2017, Royal Society of Chemistry.

DNAzyme-Based Fluorescent Sensors for UO_2^{2+} Detection

Fluorescence techniques are commonly used for the detection of diverse targets by measuring the change of fluorescence emission. DNAzyme as affinity ligand was applied in fluorescence sensors. Lu group reported a DNAzyme-based gold nanoparticles (AuNPs) sensor for uranyl ion detection (Wu et al., 2013). AuNPs were functioned with uranyl-specific DNAzyme and the substrate strand was modified with a fluorophore/quencher at 5′ and 3′-end respectively. In the absence of UO_2^{2+}, the fluorescence of fluorophore was quenched by both quencher and AuNPs. Upon uranyl ion binding, the cleavage of rA resulted in the release of fluorophore and the enhanced fluorescence enabled the sensitive detection of UO_2^{2+} in living cells. Xiong et al. presented a DNA tweezer probe for the fluorescent detection of UO_2^{2+}. DNAzyme catalytic cleavage strategy was used for signal enhancement (Xiong et al., 2020). AuNPs and fluorophore were fixed at the ends of DNA tweezer. In the presence of target UO_2^{2+}, DNAzyme cleaved substrate linker DNA sequence, the enhanced fluorescent signal allowed the detection of target ions, and the limit of detection was 25 pM UO_2^{2+}.

Zhu et al. reported a G-quadruplex-assisted enzyme strand recycling strategy-based fluorescent sensor for detecting UO_2^{2+} as shown in **Figure 1A** (Zhu et al., 2019). Such approach contained enzyme strand (E-DNA), cleaved substrate strand (S-DNA), and SYBR green I (SG). In the presence of target UO_2^{2+}, DNAzyme was activated and further cleaved the S-DNA containing G-quadruplex sequence at the both ends. The formation of G-quadruplex helped the separation between E-DNA and S-DNA, which obviously improved the recycle utilization of E-DNA. The fluorescent signal of SG, a DNA intercalating dye, positively correlated with the amount of target UO_2^{2+}. The limit of detection was 200 pM UO_2^{2+}.

A variety of signal amplification strategies were also applied to the design of UO_2^{2+} sensor based on DNAzyme cleavage. Entropy-driven amplification and DNAzyme circular cleavage amplification-based fluorescent sensor was used for sensitive uranyl ion detection (Yun et al., 2019). The first amplification, entropy-driven amplification, was initiated by a DNA fragment coming from the cleavage of DNAzyme in the addition of target UO_2^{2+}. Two DNA sequences released from the entropy driven amplification were partly complementary, which was an E-DNA of Mg^2-specific DNAzyme. The second amplification, DNAzyme circular cleavage amplification, subsequently was activated. The formation of E-DNA circularly cleaved S-DNA-FAM probes decorated AuNPs. The following recovery of fluorescent signal enabled the sensitive detection of UO_2^{2+} and the limit of detection was as low as 13 pM. An enzyme-free dual amplification-based fluorescent sensor for ultra-sensitive detection of UO_2^{2+} was

reported by Huang et al. (Yun et al., 2018). The hairpin catalytic assembly (HCA) reaction and DNAzyme-strand recycling were used in such strategy. In the absence of UO_2^{2+}, dye-labeled hairpins absorbed on the surface of AuNPs and aggregation of AuNPs were prohibited. The addition of UO_2^{2+} triggered HCA reaction between the three hairpins. The formed rigid DNA triangles with negatively charged released from the negatively charged AuNPs. Turn-on fluorescent signal achieved the sensitive detection of UO_2^{2+} and the limit of detection was as low as 0.1 pM.

Wang et al. reported a fluorescent DNAzyme beacon probe for uranyl ion detection by embedding 2-aminopurine into the middle of S-DNA instead of labelling fluorescent dyes at the ends of S-DNA (Wang et al., 2019). 2-aminopurine, a fluorescent analog of adenosine, emitted fluorescence signals in a single-strand DNA (ssDNA); however, it was significantly quenched in the hybridized double-stranded DNA (dsDNA) due to the base-stacking interaction. In the presence of UO_2^{2+}, fluorescence signal recovered upon the cleavage of DNAzyme. Turn-on sensing process enabled the quantitative detection of UO_2^{2+}. The original catalytic activity of DNAzyme was hugely enhanced by inserting a C3 spacer. The length of flexible linkers and site of insertion were fully studied (Feng et al., 2019). Such modified DNAzyme was used in a fluorescent sensor and the detection limit was 0.19 nM UO_2^{2+}.

Nanosheets with merits of great adsorption of DNA probes and excellent fluorescence quenching effect were commonly used for the fabrication of fluorescence sensors. Fu group presented a fluorescent biosensor for the simple and rapid detection of UO_2^{2+} in aqueous environment (Zhang et al., 2015). Such an approach used DNAzyme as target recognition element and molybdenum disulfide (MoS_2) nanosheets as the fluorescence quencher. In the presence of UO_2^{2+}, the cleavage occurred and the released FAM-labeled ssDNA adsorbed on the surface of MoS_2 nanosheets, resulting in an obvious decreased fluorescence signal. The limit of detection of this turn-on sensor was 2.14 nM. Graphene oxide (GO) was used as a quencher to lower background fluorescence for amplified detection of UO_2^{2+} (Li et al., 2015). The presence of targets led to the cleavage of rA in DNAzyme, resulting in the formation of G-quadruplexes, which could interact with N-methyl-mesoporphyrin IX (NMM) to cause an enhanced fluorescence intensity. Free ssDNA and NMM were adsorbed by GO for background reduction. The limit of detection was as low as 86 pM.

DNAzyme nanostructures for UO_2^{2+} detection in living cells were developed (Zhou et al., 2016). The fluorescently quenched nanoprobes were decorated by ssDNAs containing the metal ion-dependent enzymatic and substrate sequences. The self-assembly formation nanostructure could specifically recognize target ions to recover fluorescent emissions. Increased fluorescent signals enabled the quantitative detection of uranyl ions. Yang et al. reported a ratiometric fluorescent DNAzyme sensor for UO_2^{2+} monitoring (Yang et al., 2021). The fluorescent biosensor contained DNAzyme probes (39E-DNA and 39S-DNA) and the split G-quadruplex probes (39F-R and 39F-L) as shown in **Figure 1B**. The presence of 39S-DNA leaded the proximity of 39F-R and 39F-L to form G-quadruplex. In the presence of target ions, DNAzyme-induced the cleavage of 39S-DNA splitted 39F-R and 39F-L. The decreased fluorescent of NMM was linear with uranyl ion concentration. Meanwhile, SG was used to monitor the hybridization of G-quadruplex probes and 39S-DNA. The ratiometric signal of NMM and SG enabled the robust detection of UO_2^{2+}.

DNAzyme-Based Colorimetric Sensors

Colorimetric technique was used to determine the concentration of targets in solution by measuring the absorbance of a specific wavelength, which could be performed by UV-vis spectrophotometry (Priyadarshini and Pradhan, 2017). The sensitivity of colorimetric technique was lower than that of fluorescence; however, the color change was easily captured by naked eyes, making it a facile and convenient method.

DNAzyme-based colorimetric sensors had been developed for UO_2^{2+} detection via DNAzyme modulated photosensitization as demonstrated in **Figure 1C** (Huang et al., 2018). The dsDNA structure allowed SG to be located in, which could activate the photosensitization of SG for TMB (3,3′,5,5′-tetramethylbenzidine) oxidation, and chromogenic reaction occurred subsequently. In the presence of target UO_2^{2+}, dsDNA structure of DNAzyme was cleaved and SG was released. Therefore, the color was weakened due to the reduced TMB oxidation from SG. This colorimetric sensor offered a detection limit of 0.08 μg/L (UV–vis detection) and 0.5 μg/L (naked eye).

Fu group reported magnetic beads (MBs) and HCR-based colorimetric biosensor for uranyl ion detection (Zhang et al., 2017). The addition of UO_2^{2+} cleaved DNAzymes immobilized on MBs surface to release ssDNA. The released ssDNA on MBs surface triggered HCR to capture a large amount of horseradish peroxidase (HRP). Upon the addition of TMB-H_2O_2 solution, the HRP-DNA-MBs conjugates could catalyze the H_2O_2-mediated oxidation of TMB, a color change from colorless to blue in solution was observed. This provided a sensitive and selective sensing platform for the visual or colorimetric detection of UO_2^{2+}. The proposed biosensor has high sensitivity and strong anti-interference capability. In addition, the same group described a UO_2^{2+} sensor in combination with rolling circle amplification (RCA) (Cheng et al., 2017). DNAzyme functionalized on MBs was selectively cleaved in the presence of UO_2^{2+}. The released DNA chains then triggered RCA, which increased the sensitivity of such biosensor. The detection limit was 37 pM. AuNPs-based enzymatic catalysis amplification was applied for UO_2^{2+} sensor development (Zhang et al., 2016).

DNAzyme-functionalized MBs was used for UO_2^{2+} recognition, released short ssDNA, then fixed HRP-functionalized AuNPs to the surface of MBs. H_2O_2-mediated oxidation of TMB occurred. The limit detection was 7 pM.

A smart hydrogel sensor was designed and synthesized for rapid, portable, sensitive detection of UO_2^{2+} (Huang et al., 2016). DNA-grafted polyacrylamide chains were utilized to crosslink with DNAzyme to form the DNA hydrogel. Colorimetric analysis was achieved by encapsulating AuNPs in the DNAzyme-

crosslinked hydrogel. The presence of UO_2^{2+} in the sample activated the cleavage of substrate strand from the enzyme strand, thereby decreasing the density of crosslinkers and destabilizing the hydrogel, which then released the encapsulated AuNPs. The dispersion of AuNPs would lead to the change of absorbance. The decreased signal value enabled the quantification of uranyl ion. DNAzyme-functionalized AuNPs were used for UO_2^{2+} detection (Zhou et al., 2013). The cleavage of the substrate strand of DNAzyme in the presence of targets resulted in releasing a shorter duplex, leading to the aggregation of AuNPs. The changed signal allowed the sensing of UO_2^{2+}. A litmus test-based assay for colorimetric uranyl biosensor was developed by Manochehry et al., The addition of target ions produced a pH-increasing enzyme, which was recognized by litmus paper. The changed signal was linear with uranyl ion concentration (Manochehry et al., 2018).

DNAzyme-Based SERS Sensors

SERS technique with advantages of rapid detection speed, high-throughput screening, and high sensitivity had great potential in the high-speed and sensitive detection of diverse targets molecules (Pilot et al., 2019; Fan et al., 2020). Jiang et al. showed a label-free DNAzyme-based SERS method for sensing uranyl ion (Jiang et al., 2013). Such an approach used rhodamine as the Raman signal probe. The addition of UO_2^{2+} induced the cleavage of DNAzyme and the released ssDNA was adsorbed on the surface of AuNPs to form a stable conjugate. Subsequently, the combination of rhodamine and AuNPs-ssDNA conjugate gave a strong SERS signal. Gwak et al. presented a DNAzyme-based plasmonic nanowire interstice sensor for uranyl ion detection (Gwak et al., 2016). The DNAzyme reacted with target UO_2^{2+} and released Cy5 labeled strand. The plasmonic nanowire interstice sensor sensitively captured the released strands, giving a strong Raman signal and the detection limit was 1pM.

He et al. described a reusable SERS-based microfluidic biosensor for rapid detection of UO_2^{2+}(He et al., 2019). When target ions were added to the solution, 5′-rhodamine B (RhB)-labeled DNAzymes were cleavaged in the microfluidic chip, ZnO-Ag nanosheet arrays modified with S-DNA, which was sequence-complementary with the RhB-labeled E-DNA. The hybridization of S-DNA and E-DNA fixed RhB close to the surface of ZnO-Ag. The increased Raman signal enabled the sensitive detection of UO_2^{2+}. In addition, the same group developed a recyclable SERS-microfluidic biosensor for UO_2^{2+} detection (He et al., 2020b). ZnO-Ag hybrids arrays were designed as the reaction substrates. In the absence of UO_2^{2+}, RhB-labeled dsDNA formed a rigid structure and weak Raman signal was detected. Addition of uranyl triggered DNAzyme-cleavage reaction. RhB was dropped down from the surface of SERS substrates, leading to the variation of Raman signals. The detection limit of uranyl was 0.72 pM. Flexible DNAzyme-based hydrogel SERS sensor for the detection of uranyl ions was also developed by Wang group (He et al., 2020a). The presence of UO_2^{2+} ions triggered the activity of DNAzyme to cleave the substrate strand; subsequently, the DNA hydrogel structure was destroyed to release RhB, leading to a changed Raman signal. The detection of limit of such approach was 0.84 pM.

DNAzyme-Based Electrochemical Sensors

Electrochemical biosensors had become increasingly popular due to its simplicity, portability, low cost, and high sensitivity (Wongkaew et al., 2019). DNAzymes were employed to achieve target recycling for signal amplification in electrochemical sensors. Tan et al. developed a DNAzyme-based electrochemical sensor for sensitive uranyl ion detection (Tang et al., 2013). A split uranyl-specific DNAzyme decorated with ferrocene unit was immobilized on the surface of a gold electrode. In the presence of uranyl, the cleavage of S-DNA induced the ferrocene release from the electrode. The measurement of changed electrochemical signal enabled the quantitative detection of UO_2^{2+}.

AuNPs with large surface areas had the ability to absorb large number of DNAzymes and electroactive indicator, which was suitable for electrochemical sensor fabrication. Ma et al. presented a DNAzymes- and AuNPs-based electrochemical biosensor for uranyl detection (Ma et al., 2014). The addition of UO_2^{2+} induced the cleavage of DNAzymes and electroactive indicators were removed from the electrode subsequently. Differential current signals were used for sensing uranyl. Cao et al. designed an electrochemical biosensor for UO_2^{2+} detection by the integration of DNAzyme and different DNA-modified AuNPs network structure (Cao et al., 2020). Such an approach effectively increased the amount of methylene blue (MB), a commonly used electrochemical indicator. The presence of UO_2^{2+} triggered the cleavage of DNAzyme. MB and DNA-AuNPs then released from the gold electrode. The detection of reduced electrochemical response allowed the sensitive uranyl sensing with a low detection limit of 8.1 pM.

Different amplification strategies, such as hybridization chain reaction (HCR) and catalyzed hairpin assembly (CHA), were used for electrochemical biosensor development. Yun et al. reported an ultrasensitive DNAzyme-based electrochemical sensor for uranyl detection (Yun et al., 2016b). DNAzyme was selectively cleaved in the presence of UO_2^{2+}. The released DNA chains triggered HCR, which increased the sensitivity of monitoring. The detection limit was 20 pM uranyl. An ultrasensitive electrochemical biosensor for uranyl detection based on DNAzyme and CHA was presented by Yun et al. (Yun et al., 2016a). As shown in **Figure 1D**, DNA was selectively cleaved in the presence of UO_2^{2+}. The released fragment hybridized with hairpin probe 1 (H1) immobilized on the gold electrode. The unfolding of H1 subsequently induced the hybridization with hairpin 2 (H2). The DNA fragment spontaneously dissociated from the surface and then initiated the next hybridization cycle. MB was added to intercalate into the dsDNA. Double magnification strategy enabled the sensitive detection of UO_2^{2+} and the detection limit was 2 pM.

CONCLUSION AND OUTLOOKS

In this review, the recent progresses of sensors functioned with DNAzymes for uranyl ion detection were summarized including the design strategies, limit of detection, and dynamic range. Sensitive sensing for uranyl ion had been achieved with different signal outputting approaches including fluorescent, electrochemistry, colorimetry, and SERS. Despite great progress has already been achieved in

this area, there are still many challenges to be overcome. Firstly, even though most DNAzyme-based uranyl sensors immune to the interference of commonly used metal ions, Th^{4+} can still affect the detection results. Hence, it is an important task in the future to improve the selectivity of such biosensor to tolerance the interfering ions. Secondly, in order to improve the limit of detection, complex construction strategies including using of functional nanomaterials and DNA recycle amplification (e.g., HCR, RCA and CHA) still need to be designed. Low-cost, portability, and onsite sensing platforms are of great promise in future uranyl sensor application. Thirdly, miniaturization and intellectualization are the trend of uranyl sensor in the future. Quantitative detection of uranium based on mobile phones is a very attractive direction (Chen et al., 2018), and chemical hybridization of carbon dots and CdTe QDs were used for the fabrication of ratiometric fluorescent probe. The addition of uranyl ions greatly quenched the red fluorescence of CdTe QDs, whereas the green fluorescence of carbon dots kept constant, leading to an obvious color change. A smartphone was used to analyze the content of uranyl on the basis of captured signals. Onsite and point-of-care detection of uranyl ions was achieved. Therefore, the sensitivity needed to be improved, which was mainly because the amplification strategy was not adopted.

Nowadays, the fabrication of high-quality DNAzyme-based sensors with merits of rapidness, low cost, sensitivity, and selectivity will become more active due to the widely used nuclear energy applications and the combined effects of its radioactive and biological toxicity during the uranium exploitation. Along with the great progress in the field of sensor design, we believe that DNAzyme-based sensors will play a vital role in various applications in environmental monitoring and nuclear environmental protection.

AUTHOR CONTRIBUTIONS

All authors have read and agreed to the published version of the manuscript. YB collected and analyzed data, completed pictures and spreadsheets, conceived and wrote the paper. HC, LZ and GJ collected and analyzed data; LX and GZ wrote and revised the paper.

FUNDING

This research was supported by the National Key Research and Development Program of China (No. 2019YFC1907700), the National Natural Science Foundation of China (No. 21801158), the Natural Science Foundation of Shandong Province (No. ZR2020QB092), the China Postdoctoral Science Foundation (No. 2021M691689), and the State Key Laboratory of Bio-Fibers and Eco-Textiles (Qingdao University, Nos. ZKT23, KF2020201, GZRC202025).

REFERENCES

Ansoborlo, E., Lebaron-Jacobs, L., and Prat, O. (2015). Uranium in Drinking-Water: A Unique Case of Guideline Value Increases and Discrepancies between Chemical and Radiochemical Guidelines. *Environ. Int.* 77, 1–4. doi:10.1016/j.envint.2014.12.011

Boulyga, S. F., Koepf, A., Konegger-Kappel, S., Macsik, Z., and Stadelmann, G. (2016). Uranium Isotope Analysis by MC-ICP-MS in Sub-ng Sized Samples. *J. Anal. Spectrom.* 31, 2272–2284. doi:10.1039/C6JA00238B

Cao, C., Liu, J., Tang, S., Dai, Z., Xiao, F., Rang, W., et al. (2020). Amplified Electrochemical Determination of UO_2^{2+} Based on the Cleavage of the DNAzyme and DNA-Modified Gold Nanoparticle Network Structure. *Microchim. Acta* 187, 311. doi:10.1007/s00604-020-04263-1

Chen, X., Mei, Q., Yu, L., Ge, H., Yue, J., Zhang, K., et al. (2018). Rapid and On-Site Detection of Uranyl Ions via Ratiometric Fluorescence Signals Based on a Smartphone Platform. *ACS Appl. Mater. Inter.* 10, 42225–42232. doi:10.1021/acsami.8b13765

Cheng, X., Yu, X., Chen, L., Zhang, H., Wu, Y., and Fu, F. (2017). Visual Detection of Ultra-Trace Levels of Uranyl Ions Using Magnetic Bead-Based Dnazyme Recognition in Combination with Rolling Circle Amplification. *Microchim. Acta* 184, 4259–4267. doi:10.1007/s00604-017-2472-0

Domingo, J. L. (2001). Reproductive and Developmental Toxicity of Natural and Depleted Uranium: A Review. *Reprod. Toxicol.* 15, 603–609. doi:10.1016/S0890-6238(01)00181-2

Fan, M., Andrade, G. F. S., and Brolo, A. G. (2020). A Review on Recent Advances in the Applications of Surface-Enhanced Raman Scattering in Analytical Chemistry. *Anal. Chim. Acta* 1097, 1–29. doi:10.1016/j.aca.2019.11.049

Farzin, L., Shamsipur, M., Sheibani, S., Samandari, L., and Hatami, Z. (2019). A Review on Nanomaterial-Based Electrochemical, Optical, Photoacoustic and Magnetoelastic Methods for Determination of Uranyl Cation. *Microchim. Acta* 186, 289. doi:10.1007/s00604-019-3426-5

Feng, M., Gu, C., Sun, Y., Zhang, S., Tong, A., and Xiang, Y. (2019). Enhancing Catalytic Activity of Uranyl-Dependent DNAzyme by Flexible Linker Insertion for More Sensitive Detection of Uranyl Ion. *Anal. Chem.* 91, 6608–6615. doi:10.1021/acs.analchem.9b00490

Gwak, R., Kim, H., Yoo, S. M., Lee, S. Y., Lee, G.-J., Lee, M.-K., et al. (2016). Precisely Determining Ultralow Level UO_2^{2+} in Natural Water with Plasmonic Nanowire Interstice Sensor. *Sci. Rep.* 6, 19646. doi:10.1038/srep19646

He, W., and Hua, D. (2019). Spectrographic Sensors for Uranyl Detection in the Environment. *Talanta* 201, 317–329. doi:10.1016/j.talanta.2019.04.018

He, X., Wang, S., Liu, Y., and Wang, X. (2019). Ultra-Sensitive Detection of Uranyl Ions with A Specially Designed High-Efficiency SERS-Based Microfluidic Device. *Sci. China Chem.* 62, 1064–1071. doi:10.1007/s11426-019-9468-x

He, X., Zhou, X., Liu, W., Liu, Y., and Wang, X. (2020a). Flexible DNA Hydrogel SERS Active Biofilms for Conformal Ultrasensitive Detection of Uranyl Ions from Aquatic Products. *Langmuir* 36, 2930–2936. doi:10.1021/acs.langmuir.9b03845

He, X., Zhou, X., Liu, Y., and Wang, X. (2020b). Ultrasensitive, Recyclable and Portable Microfluidic Surface-Enhanced Raman Scattering (SERS) Biosensor for Uranyl Ions Detection. *Sensors Actuators B: Chem.* 311, 127676. doi:10.1016/j.snb.2020.127676

Huang, Y., Fang, L., Zhu, Z., Ma, Y., Zhou, L., Chen, X., et al. (2016). Design and Synthesis of Target-Responsive Hydrogel for Portable Visual Quantitative Detection of Uranium with A Microfluidic Distance-Based Readout Device. *Biosens. Bioelectron.* 85, 496–502. doi:10.1016/j.bios.2016.05.008

Huang, C., Fan, X., Yuan, Q., Zhang, X., Hou, X., and Wu, P. (2018). Colorimetric Determination of Uranyl (UO_2^{2+}) in Seawater via Dnazyme-Modulated Photosensitization. *Talanta* 185, 258–263. doi:10.1016/j.talanta.2018.03.079

Jaison, P. G., Telmore, V. M., Kumar, P., and Aggarwal, S. K. (2011). Determination of Uranium in Seawater Samples by Liquid Chromatography Using Mandelic Acid as A Complexing Agent. *J. Chromatogr. Sci.* 49, 657–664. doi:10.1093/chrsci/49.9.657

Jamali, M. R., Assadi, Y., Shemirani, F., Hosseini, M. R. M., Kozani, R. R., Masteri-Farahani, M., et al. (2006). Synthesis of Salicylaldehyde-Modified Mesoporous Silica

and its Application as A New Sorbent for Separation, Preconcentration and Determination of Uranium by Inductively Coupled Plasma Atomic Emission Spectrometry. *Anal. Chim. Acta* 579, 68–73. doi:10.1016/j.aca.2006.07.006

Jiang, Z., Yao, D., Wen, G., Li, T., Chen, B., and Liang, A. (2013). A Label-Free Nanogold Dnazyme-Cleaved Surface-Enhanced Resonance Raman Scattering Method for Trace UO_2^{2+} Using Rhodamine 6G as Probe. *Plasmonics* 8, 803–810. doi:10.1007/s11468-012-9476-8

Jouha, J., and Xiong, H. (2021). DNAzyme-Functionalized Nanomaterials: Recent Preparation, Current Applications, and Future Challenges. *Small* 17, 2105439. doi:10.1002/smll.202105439

Khan, S., Burciu, B., Filipe, C. D. M., Li, Y., Dellinger, K., and Didar, T. F. (2021). DNAzyme-Based Biosensors: Immobilization Strategies, Applications, and Future Prospective. *Acs Nano* 15, 13943–13969. doi:10.1021/acsnano.1c04327

Li, M.-H., Wang, Y.-S., Cao, J.-X., Chen, S.-H., Tang, X., Wang, X.-F., et al. (2015). Ultrasensitive Detection of Uranyl by Graphene Oxide-Based Background Reduction and Rcdzyme-Based Enzyme Strand Recycling Signal Amplification. *Biosens. Bioelectron.* 72, 294–299. doi:10.1016/j.bios.2015.05.032

Liu, J., Brown, A. K., Meng, X., Cropek, D. M., Istok, J. D., Watson, D. B., et al. (2007). A Catalytic Beacon Sensor for Uranium with Parts-Per-Trillion Sensitivity and Millionfold Selectivity. *Proc. Natl. Acad. Sci. U.S.A.* 104, 2056–2061. doi:10.1073/pnas.0607875104

Liu, J., Cao, Z., and Lu, Y. (2009). Functional Nucleic Acid Sensors. *Chem. Rev.* 109, 1948–1998. doi:10.1021/cr030183i

Ma, D., Yuan, Y., Xiao, X., Gao, Y., Li, Y., Xu, W., et al. (2014). A Label-Free Electrochemical Biosensor for Trace Uranium Based on Dnazymes and Gold Nanoparticles. *J. Radioanal. Nucl. Chem.* 299, 1911–1919. doi:10.1007/s10967-013-2897-9

Manochehry, S., Mcconnell, E. M., Tram, K. Q., Macri, J., and Li, Y. (2018). Colorimetric Detection of Uranyl Using A Litmus Test. *Front. Chem.* 6, 332. doi:10.3389/fchem.2018.00332

Pilot, R., Signorini, R., Durante, C., Orian, L., Bhamidipati, M., and Fabris, L. (2019). A Review on Surface-Enhanced Raman Scattering. *Biosensors* 9, 57. doi:10.3390/bios9020057

Priyadarshini, E., and Pradhan, N. (2017). Gold Nanoparticles as Efficient Sensors in Colorimetric Detection of Toxic Metal Ions: A Review. *Sensors Actuators B: Chem.* 238, 888–902. doi:10.1016/j.snb.2016.06.081

Saidur, M. R., Aziz, A. R. A., and Basirun, W. J. (2017). Recent Advances in DNA-Based Electrochemical Biosensors for Heavy Metal Ion Detection: A Review. *Biosens. Bioelectron.* 90, 125–139. doi:10.1016/j.bios.2016.11.039

Sanyal, K., Khooha, A., Das, G., Tiwari, M. K., and Misra, N. L. (2017). Direct Determination of Oxidation States of Uranium in Mixed-Valent Uranium Oxides Using Total Reflection X-Ray Fluorescence X-Ray Absorption Near-Edge Spectroscopy. *Anal. Chem.* 89, 871–876. doi:10.1021/acs.analchem.6b03945

Tang, Q., Yuan, Y., Xiao, X., Guo, P., Hu, J., Ma, D., et al. (2013). DNAzyme Based Electrochemical Sensors for Trace Uranium. *Microchim. Acta* 180, 1059–1064. doi:10.1007/s00604-013-1021-8

Wang, X., Zeng, R., Chu, S., Tang, W., Lin, N., Fu, J., et al. (2019). A Quencher-free DNAzyme Beacon for Fluorescently Sensing Uranyl Ions via Embedding 2-Aminopurine. *Biosens. Bioelectron.* 135, 166–172. doi:10.1016/j.bios.2019.04.021

Wang, S., Jiang, J., He, X., Yang, S., Wu, H., Qin, Z., et al. (2022). Research Progress of SERS on Uranyl Ions and Uranyl Compounds: A Review. *J. Mater. Chem. C* 10, 4006–4018. doi:10.1039/d1tc05154g

Wongkaew, N., Simsek, M., Griesche, C., and Baeumner, A. J. (2019). Functional Nanomaterials and Nanostructures Enhancing Electrochemical Biosensors and Lab-On-A-Chip Performances: Recent Progress, Applications, and Future Perspective. *Chem. Rev.* 119, 120–194. doi:10.1021/acs.chemrev.8b00172

Wu, P., Hwang, K., Lan, T., and Lu, Y. (2013). A DNAzyme-Gold Nanoparticle Probe for Uranyl Ion in Living Cells. *J. Am. Chem. Soc.* 135, 5254–5257. doi:10.1021/ja400150v

Wu, X., Huang, Q., Mao, Y., Wang, X., Wang, Y., Hu, Q., et al. (2019). Sensors for Determination of Uranium: A Review. *Trac Trends Anal. Chem.* 118, 89–111. doi:10.1016/j.trac.2019.04.026

Xiong, Z., Wang, Q., Zhang, J., Yun, W., Wang, X., Ha, X., et al. (2020). A Simple and Programmed DNA Tweezer Probes for One-step and Amplified Detection of UO22+. *Spectrochimica Acta A: Mol. Biomol. Spectrosc.* 229, 118017. doi:10.1016/j.saa.2019.118017

Yang, Y., Yang, H., Wan, Y., Zhou, W., Deng, S., He, Y., et al. (2021). Temperature-robust and Ratiometric G-Quadruplex Proximate Dnazyme Assay for Robustly Monitoring of Uranium Pollution and its Microbial Biosorbents Screening. *J. Hazard. Mater.* 413, 125383. doi:10.1016/j.jhazmat.2021.125383

Yun, W., Cai, D., Jiang, J., Wang, X., Liao, J., Zhang, P., et al. (2016a). An Ultrasensitive Electrochemical Biosensor for Uranyl Detection Based on Dnazyme and Target-Catalyzed Hairpin Assembly. *Microchim. Acta* 183, 1425–1432. doi:10.1007/s00604-016-1778-7

Yun, W., Jiang, J., Cai, D., Wang, X., Sang, G., Liao, J., et al. (2016b). Ultrasensitive Electrochemical Detection of UO22+ Based on DNAzyme and Isothermal Enzyme-free Amplification. *RSC Adv.* 6, 3960–3966. doi:10.1039/c5ra22773a

Yun, W., Wu, H., Liu, X., Zhong, H., Fu, M., Yang, L., et al. (2018). Ultra-sensitive Fluorescent and Colorimetric Detection of UO22+ Based on Dual Enzyme-free Amplification Strategies. *Sensors Actuators B: Chem.* 255, 1920–1926. doi:10.1016/j.snb.2017.08.205

Yun, W., Wu, H., Yang, Z., Wang, R., Wang, C., Yang, L., et al. (2019). A Dynamic, Ultra-sensitive and "Turn-On" Strategy for Fluorescent Detection of Uranyl Based on Dnazyme and Entropy-Driven Amplification Initiated Circular Cleavage Amplification. *Anal. Chim. Acta* 1068, 104–110. doi:10.1016/j.aca.2019.04.018

Zhang, H., Ruan, Y., Lin, L., Lin, M., Zeng, X., Xi, Z., et al. (2015). A Turn-Off Fluorescent Biosensor for the Rapid and Sensitive Detection of Uranyl Ion Based on Molybdenum Disulfide Nanosheets and Specific DNAzyme. *Spectrochim. Acta Part A: Mol. Biomol. Spectrosc.* 146, 1–6. doi:10.1016/j.saa.2015.02.113

Zhang, H., Lin, L., Zeng, X., Ruan, Y., Wu, Y., Lin, M., et al. (2016). Magnetic Beads-Based DNAzyme Recognition and Aunps-Based Enzymatic Catalysis Amplification for Visual Detection of Trace Uranyl Ion in Aqueous Environment. *Biosens. Bioelectron.* 78, 73–79. doi:10.1016/j.bios.2015.11.024

Zhang, H., Cheng, X., Chen, L., Mo, F., Xu, L., and Fu, F. (2017). Magnetic Beads-Based DNA Hybridization Chain Reaction Amplification and Dnazyme Recognition for Colorimetric Detection of Uranyl Ion in Seafood. *Anal. Chim. Acta* 956, 63–69. doi:10.1016/j.aca.2016.12.021

Zhou, B., Shi, L.-F., Wang, Y.-S., Yang, H.-X., Xue, J.-H., Liu, L., et al. (2013). Resonance Light Scattering Determination of Uranyl Based on Labeled DNAzyme-Gold Nanoparticle System. *Spectrochim. Acta Part A: Mol. Biomol. Spectrosc.* 110, 419–424. doi:10.1016/j.saa.2013.03.036

Zhou, W., Liang, W., Li, D., Yuan, R., and Xiang, Y. (2016). Dual-color Encoded Dnazyme Nanostructures for Multiplexed Detection of Intracellular Metal Ions in Living Cells. *Biosens. Bioelectron.* 85, 573–579. doi:10.1016/j.bios.2016.05.058

Zhou, W., Saran, R., and Liu, J. (2017). Metal Sensing by DNA. *Chem. Rev.* 117, 8272–8325. doi:10.1021/acs.chemrev.7b00063

Zhu, P., Zhang, Y., Xu, S., and Zhang, X. (2019). G-quadruplex-assisted Enzyme Strand Recycling for Amplified Label-free Fluorescent Detection of UO_2^{2+}. *Chin. Chem. Lett.* 30, 58–62. doi:10.1016/j.cclet.2018.02.003

Conflict of Interest: The authors declare that the research was conducted in the absence of any commercial or financial relationships that could be construed as a potential conflict of interest.

Publisher's Note: All claims expressed in this article are solely those of the authors and do not necessarily represent those of their affiliated organizations, or those of the publisher, the editors, and the reviewers. Any product that may be evaluated in this article, or claim that may be made by its manufacturer, is not guaranteed or endorsed by the publisher.

frontiers | Frontiers in Chemistry

ORIGINAL RESEARCH
published: 11 May 2022
doi: 10.3389/fchem.2022.892919

Improved Performance for the Electrochemical Sensing of Acyclovir by Using the rGO–TiO_2–Au Nanocomposite-Modified Electrode

Xin-Yang Lu, Jing Li, Fen-Ying Kong, Mei-Jie Wei, Pei Zhang, Ying Li, Hai-Lin Fang and Wei Wang**

School of Chemistry and Chemical Engineering, Yancheng Institute of Technology, Yancheng, China

An electrochemical sensor for sensitive sensing of acyclovir (ACV) was designed by using the reduced graphene oxide–TiO_2–Au nanocomposite-modified glassy carbon electrode (rGO–TiO_2–Au/GCE). Transmission electron microscopy, X-ray diffractometer, and X-ray photoelectron spectroscopy were used to confirm morphology, structure, and composition properties of the rGO–TiO_2–Au nanocomposites. Cyclic voltammetry and linear sweep voltammetry were used to demonstrate the analytical performance of the rGO–TiO_2–Au/GCE for ACV. As a result, rGO–TiO_2–Au/GCE exerted the best response for the oxidation of ACV under the pH of 6.0 PB solution, accumulation time of 80 s at open-circuit, and modifier amount of 7 μl. The oxidation peak currents of ACV increased linearly with its concentration in the range of 1–100 μM, and the detection limit was calculated to be 0.3 μM (S/N = 3). The determination of ACV concentrations in tablet samples also demonstrated satisfactory results.

Keywords: acyclovir, electrochemical sensor, chemically modified electrode, metallic oxide, reduced graphene oxide

OPEN ACCESS

Edited by:
Junjie Zhu,
Nanjing University, China

Reviewed by:
Guifen Jie,
Qingdao University of Technology, China
Mani Govindasamy,
National Taipei University of Technology, Taiwan

****Correspondence:***
Fen-Ying Kong
kongfy@ycit.edu.cn
Wei Wang
wangw@ycit.edu.cn

Specialty section:
This article was submitted to Analytical Chemistry, a section of the journal Frontiers in Chemistry

Received: *09 March 2022*
Accepted: *29 March 2022*
Published: *11 May 2022*

Citation:
Lu X-Y, Li J, Kong F-Y, Wei M-J, Zhang P, Li Y, Fang H-L and Wang W (2022) Improved Performance for the Electrochemical Sensing of Acyclovir by Using the rGO–TiO_2–Au Nanocomposite-Modified Electrode. Front. Chem. 10:892919. doi: 10.3389/fchem.2022.892919

INTRODUCTION

Acyclovir (2-amino-9-[(2-hydroxyethoxy) methyl]-6,9-dihydro-3H-purin-6-one, ACV), an effective antiviral drug of synthetic deoxyguanosine analog, plays an important role in the therapy of viral diseases (Clercq, 2004). However, if ACV was used in an inappropriate and excessive manner, many other adverse reactions related to kidneys and certain neurotoxicity effects will occur (Lu et al., 2012). Therefore, measuring the concentration of ACV in pharmaceuticals and biological fluids appears very significant, and a number of analytical methods have already been developed for the analysis of ACV (Yu and Xiang, 2008; Long and Chen, 2012; Ajima and Onah, 2015; Liu et al., 2015; Mulabagal et al., 2020). Electrochemical sensors based on chemically modified electrodes are ideal candidates to more traditional methods, owing to their advantages of simplicity, sensitivity, rapidity, portability, and cheapness (Tarlekar et al., 2018; Bao et al., 2021; Kong et al., 2021). In addition, electrochemical methods can provide the drug-based electrode reaction mechanism, while the redox properties of drugs offer insight into their metabolism, *in vivo* redox processes, or pharmacological activity (Özkan et al., 2003; Özkan et al., 2004).

Reduced graphene oxide (rGO) is a promising candidate for the preparation of high-performance modified electrodes because of its unique 2D structures, interesting electrocatalytic activity, and excellent conductivity (Coros et al., 2020). Moreover, these characteristics can be tailored by making rGO as the

building blocks with metal oxide and metal nanoparticles (Chakraborty and Roychaudhuri, 2021). Metal oxide nanoparticles, such as TiO_2, have garnered extensive attention in the design of a potential sensing interface due to their non-toxicity, high surface area, exceptional chemical stability, and notable electrochemical properties (George et al., 2018). Meanwhile, noble metal nanoparticles such as Au and Ag possess outstanding conductivity, remarkable electrocatalytic properties, and good biocompatibility, which make them fit as modifiers for sensor fabrication (Xiao et al., 2020). All these alluring features endow the composite of rGO–TiO_2–Au with an improved sensing performance based on the excellent synergetic effect among them.

With regard to the aforementioned survey, we prepared the rGO–TiO_2–Au nanocomposite-modified glassy carbon electrode (GCE) for the sensitive sensing of ACV. On the rGO–TiO_2–Au/GCE, a significant improvement of the oxidation peak current of ACV was observed. It was endowed with the sensitive determination of ACV. On the basis of optimizing various experimental parameters, such as the pH of the supporting electrolyte, accumulation time and potential, and the modifier amount, the rGO-TiO_2-Au/GCE showed a wide linear range and low detection limit. The selectivity, repeatability, and stability of rGO–TiO_2–Au/GCE for the determination of ACV were also evaluated, and the results were acceptable. Finally, the rGO–TiO_2–Au/GCE was implemented for the estimation of ACV in tablet samples, which offered excellent recovery.

EXPERIMENTAL

Chemicals and Reagents

Graphite powder, chloroauric acid ($HAuCl_4{\cdot}4H_2O$), and the ACV standard powder were purchased from Aladdin Reagent Co. Ltd. Sodium citrate, NaH_2PO_4, Na_2HPO_4, H_3PO_4, NaOH, and other chemical reagents were purchased from Sinopharm Chemical Reagent Co., Ltd. ACV tablets (200 mg) were purchased from the local pharmacies. All other chemicals and reagents used in this work were of analytical grade and used directly. ACV stock solution (1.0 mM) was prepared by dissolving appropriate amounts of the ACV powder in ultrapure water. Before use, it was stored at 4°C in the dark to avoid any decomposition. The required concentration of ACV was made by diluting the stock solution. The supporting electrolyte was 0.1 M phosphate buffer (PB) solution. The pH varying from 5.5 to 8.0 was obtained by mixing NaH_2PO_4 and Na_2HPO_4, using H_3PO_4 and NaOH as reagents for pH adjusting. Ultrapure water (18 MΩ cm) obtained from a Milli-Q water purifying system was used for preparation of all the solutions.

Apparatus and Characterization

The structure and surface morphology of the prepared products were observed by transmission electron microscopy (TEM) (JEOL JEM-2100F) operated at 200 kV. The surface composition and chemical state of the rGO–TiO_2-–Au nanocomposites were examined by X-ray photoelectron spectroscopy (XPS) with a monochromatic Al Kα excitation source. The crystal phase of the materials was investigated by using a Bruker D8 Advance X-ray diffractometer at 40 kV with Cu Kα radiation (λ = 1.54 Å). The electrochemical performance of the nanocomposites was measured using a CHI 660E electrochemical workstation. A standard three-electrode system was engaged, which comprised a GC (bare or modified) working electrode with a diameter of 3 mm, a platinum wire counter electrode, and a 3-M KCl-saturated Ag/AgCl reference electrode. All the electrochemical experiments were carried out at room temperature with dissolved oxygen removed by a N_2 stream.

Synthesis of the rGO–TiO_2–Au Nanocomposites

GO, TiO_2, and Au nanoparticles were first prepared. GO was prepared by the oxidation of the graphite powder using a modified Hummer's method. Experimental details were given in the literature (Kong et al., 2015). TiO_2 nanoparticles were synthesized by the hydrothermal method using tetrabutyl titanate as the titanium source (Ya et al., 2015). Au nanoparticles were synthesized by the citrate reduction method. Details can be found in our previous work (Kong et al., 2019).

For the synthesis of rGO–TiO_2–Au nanocomposites, 10 mg of GO was dispersed in 20 ml ultrapure water and sonicated for 30 min to obtain a uniform dispersion. Then, 5.0 ml of GO dispersion was mixed with 100 µl TiO_2 and sonicated for 1.0 h. After adding 100 µl Au nanoparticles and ultrasonic treatment for another 0.5 h, the mixture was poured into a transparent vial and illuminated using a UV-LED spot lamp. After irradiation for 3 h, the product was collected by centrifugation and washed several times with ultrapure water.

Fabrication of the rGO–TiO_2–Au/GCE

The preparation process of rGO–TiO_2–Au/GCE was as follows: initially, the GCE was carefully polished with 0.3 and 0.05 µm alumina powder in sequence on a polishing cloth to obtain a mirror-like surface. After ultrasonic cleaning in 1:1 nitric acid, ethanol, and ultrapure water for 5 min, it was dried under N_2 flow. Then, 7 µl of rGO–TiO_2–Au dispersion was drop-cast on the surface of GCE using a microsyringe, and it was dried naturally under a closed vessel.

Electrochemical Measurements

The electrochemical measurements were performed in 10 ml of 0.1 M PB solution containing a certain concentration of ACV using cyclic voltammetry (CV) and linear sweep voltammetry (LSV). The accumulation step was performed at open-circuit for 80 s under stirring. After 5 s quiescence, LSV was recorded between +0.6 and +1.4 V. The oxidation peak currents were measured at 1.10 V for the quantification of ACV.

Analysis of the Sample

A total of ten tablets of ACV were finely powdered using the agate and a mortar, and a portion of this powder was accurately weighed and dissolved in ultrapure water with ultrasonic agitation for 10 min to ensure complete dissolution. Finally, it was filtered and diluted to volume with ultrapure water. A desired volume of the sample solution was transferred to the electrochemical cell and analyzed under optimal conditions using the LSV technique. The ACV content in the tablet was calculated using the standard addition method.

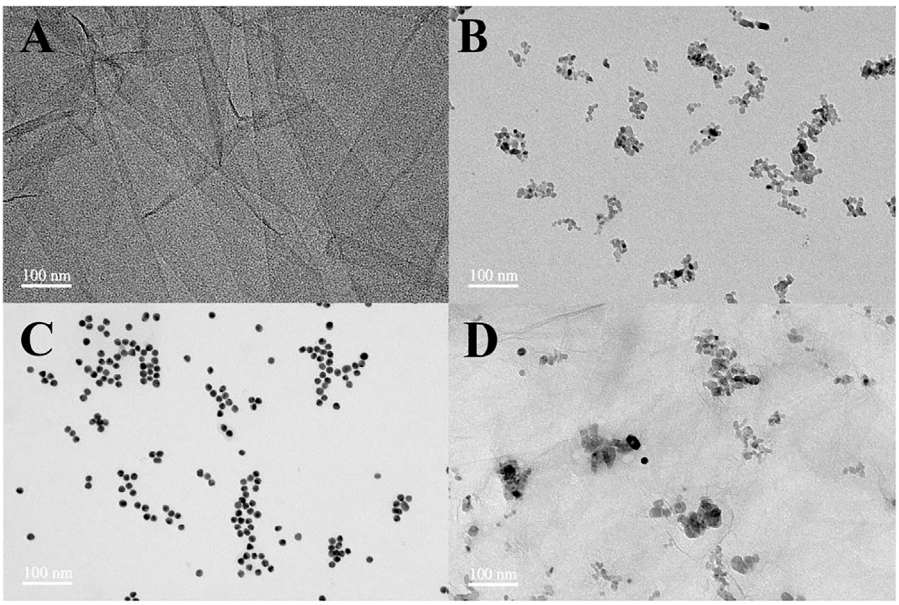

FIGURE 1 | TEM images of GO **(A)**, TiO_2 nanoparticles **(B)**, Au nanoparticles **(C)**, and rGO–TiO_2–Au nanocomposites **(D)**.

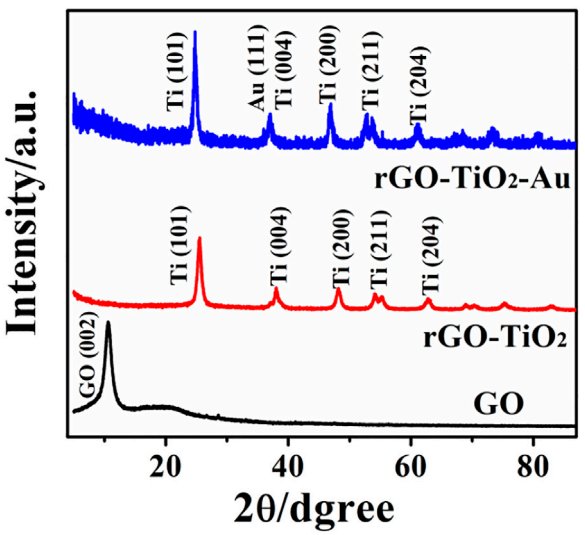

FIGURE 2 | XRD patterns of GO, rGO–TiO_2, and rGO–TiO_2–Au nanocomposites.

RESULTS AND DISCUSSION

Characterization of the rGO–TiO_2–Au Nanocomposites

The microstructure and morphology of the prepared nanomaterials are observed by TEM, and the obtained images are displayed in **Figure 1**. **Figure 1A** depicts the TEM micrograph of GO, in which an ultra-thin, wrinkled, and sheet-like structure is observed. The TEM image of TiO_2 exhibits a small amount of aggregation, which is composed of spheroid nanoparticles with a diameter of about 10 nm (**Figure 1B**). **Figure 1C** shows the well-monodispersed and spherical shape of Au nanoparticles with a mean size of about 15 nm. The obtained nanocomposites maintained the 2D sheet structure as shown in **Figure 1D**. TiO_2 and Au nanoparticles were loaded on the rGO sheet and accumulated along the wrinkles and edges.

XRD analysis was recorded to study crystalline characteristics of the nanocomposites, and the results are presented in **Figure 2**. As can be observed, GO reveals a sharp and intensive diffraction peak at 2θ of 11.0°, which corresponds to the (002) plane of the graphene sheets (Wang et al., 2008), indicating the formation of GO by the Hummers' method. The XRD pattern of rGO–TiO_2 shows the diffraction peaks at 25.3°, 37.8°, 48.0°, 55.1°, and 62.7°, which can be indexed to (101), (004), (200), (211), and (204) crystal planes of anatase TiO_2 (JCPDS card no.21-1272) (Li et al., 2007), respectively. Meanwhile, the characteristic diffraction peak of GO disappears, indicating the successful reduction of GO via UV irradiation. According to a previous report (Kong et al., 2016; Yang et al., 2016), when TiO_2 is exposed to UV light, the photo-induced electron–hole pairs are produced. The separated holes react with water to generate oxygen and H^+, whereas the electrons are effectively captured by the GO substrate to reduce functional groups. The XRD pattern of the rGO–TiO_2–Au nanocomposites is similar to rGO–TiO_2, suggesting that the introduction of Au nanoparticles did not alter their lattices.

The formation of rGO–TiO_2–Au nanocomposites and their surface features were examined by XPS, and the corresponding results are illustrated in **Figure 3**. The presence of major elements such as Au, C, Ti, and O from the survey spectrum conveys the successful preparation of rGO–TiO_2–Au nanocomposites (**Figure 3A**). For the Ti 2p spectrum, two main peaks appeared at 459.4 and 464.1 eV fit binding energy of Ti $2p_{3/2}$ and Ti $2p_{1/2}$ (**Figure 3B**), confirming Ti ions occur in the form of Ti^{4+} states. The

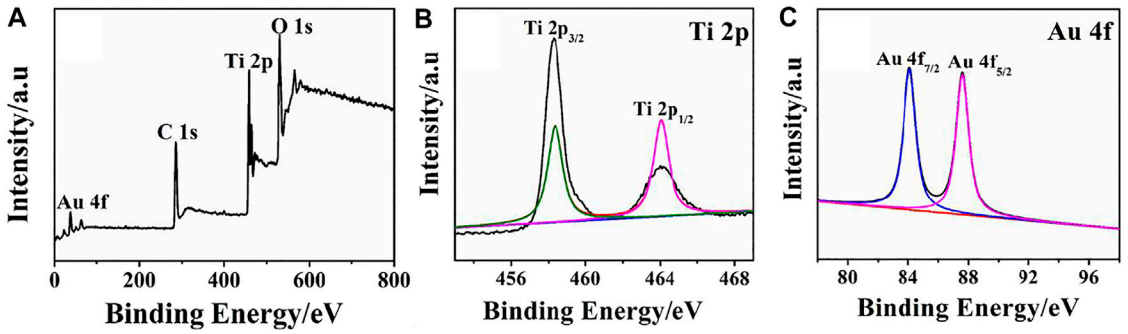

FIGURE 3 | XPS survey spectra **(A)** and high-resolution spectra of Ti 2p **(B)** and Au 4f **(C)** of the rGO–TiO_2–Au nanocomposites.

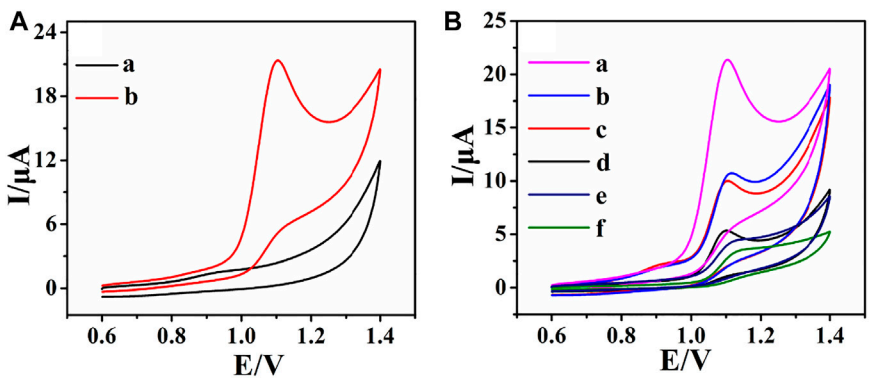

FIGURE 4 | CVs of rGO–TiO_2–Au/GCE in the absence (a) and presence (b) of 0.2 mM ACV in 0.1 M PB solution (pH 6.0) **(A)**; CVs of rGO–TiO_2–Au/GCE (a), rGO–Au/GCE (b), rGO–TiO_2/GCE (c), rGO/GCE (d), TiO_2/GCE (e), and bare GCE (f) in 0.1 M PB solution (pH 6.0) containing 0.2 mM ACV **(B)**. Scan rate: 100 mV s^{-1}.

result is consistent with the reported literature (Zhu et al., 2020). In **Figure 3C**, Au 4f displays two peaks located at a binding energy of 84.17 and 87.82 eV, which are assigned to Au $4f_{7/2}$ and Ag $4f_{5/2}$ of metallic Au, respectively (Shukla et al., 2018).

The Electrochemical Oxidation of Acyclovir at the rGO–TiO_2–Au/GCE

The electrochemical oxidation of ACV at the rGO–TiO_2–Au/GCE was investigated by the CV method (**Figure 4**). In the potential range from +0.6 to +1.4 V, the CV in the absence of ACV shows no observable redox peaks (**Figure 4A**, curve a). However, in the presence of ACV, a well-resolved oxidation peak is observed at about 1.10 V (**Figure 4A**, curve b), indicating that the oxidation peak is attributed to ACV. Furthermore, no reduction peaks are found in the reverse scan, suggesting that the electrochemical reaction is a totally irreversible process. Based on the aforementioned results and previously published literatures (Wang et al., 2013; Dorraji and Jalali, 2016; Ilager et al., 2021), a possible oxidation mechanism of ACV involves the two-electron and two-proton transfer process for the formation of 8-oxoacyclovir, which is structurally analogous to the preliminary oxidation product of guanine (**Supplementary Figure S1**).

The electrochemical behavior of ACV at various electrodes included rGO–TiO_2–Au/GCE (a), rGO–Au/GCE (b), rGO–TiO_2/GCE (c), rGO/GCE (d), TiO_2/GCE (e), and bare GCE (f) as illustrated in **Figure 4B**. As can be seen, the CV of ACV shows a broad peak and poor current response at bare GCE, revealing sluggish electron-transfer kinetics. At TiO_2/GCE and rGO/GCE, the peak current increases due to the huge surface area of nanomaterials. In great contrast, a well-defined and resolved oxidation peak of ACV can be observed at rGO–TiO_2/GCE, rGO–Au/GCE, and rGO–TiO_2–Au/GCE. Most notably, the rGO–TiO_2–Au/GCE shows the highest augmentation toward the determination of ACV. The outstanding electrochemical response may be due to the large surface area, excellent electrical conductivity, and remarkable electrocatalytic activity of rGO–TiO_2–Au nanocomposites, which provided the fastest electron transport at the electrode surface. These results clearly indicate that rGO–TiO_2–Au/GCE is very suitable for the determination of ACV.

Quantitative Analysis of Acyclovir by Using rGO–TiO_2–Au/GCE

Under optimized conditions (see Electronic **Supplementary Material**), LSV was recorded by varying the concentration of

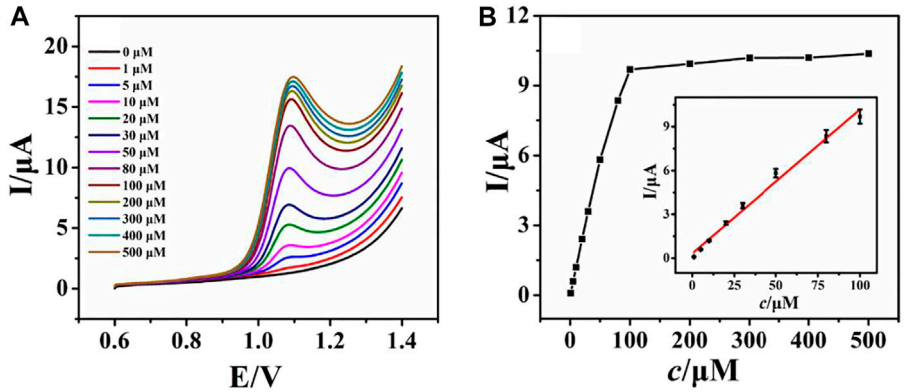

FIGURE 5 | LSV curves of various concentrations of ACV (0–500 μM, down to up) at rGO–TiO_2–Au/GCE in pH 6.0 PB solution **(A)**; plots of the peak current against the concentration of ACV **(B)**. Inset: the calibration plots for ACV.

ACV at the rGO–TiO_2–Au/GCE (**Figure 5**). **Figure 5A** shows the LSV responses of rGO–TiO_2–Au/GCE for varying the concentration of ACV from 0 to 500 μM in 0.1 M PB solution. As illustrated, the successive increase of the peak current is observed by raising the concentration of ACV. The plots of peak current responses against ACV concentrations are shown in **Figure 5B**. It can be seen that the peak current responses of ACV increased linearly with its concentrations from 1 to 100 μM. For higher concentrations, a deviation from linearity is observed, which is due to the adsorption of ACV or its oxidation product on the electrode surface. The linear regression equation is Ipa (μA) = 0.1403c + 2.1814 (μM) with a correlation coefficient of 0.996 (**Figure 5B** inset). The detection limit is 0.3 μM based on a signal-to-noise ratio of 3. The rGO–TiO_2–Au/GCE showed a comparable or better dynamic range and detection limit for ACV compared to other electrochemical sensors, such as Cu nanoparticle-modified carbon paste electrode (2.64 μM) (Heli et al., 2010), pencil graphite electrode (0.3 μM) (Dilgin and Karakaya, 2016), nanoporous nickel microsphere-modified carbon paste electrode (40 μM) (Heli et al., 2012), fluorine-doped SnO_2 electrode (1.25 μM) (Martínez-Rojas et al., 2017), and CdO/Fe_3O_4-modified carbon paste electrode (0.3 μM) (Naghian et al., 2020).

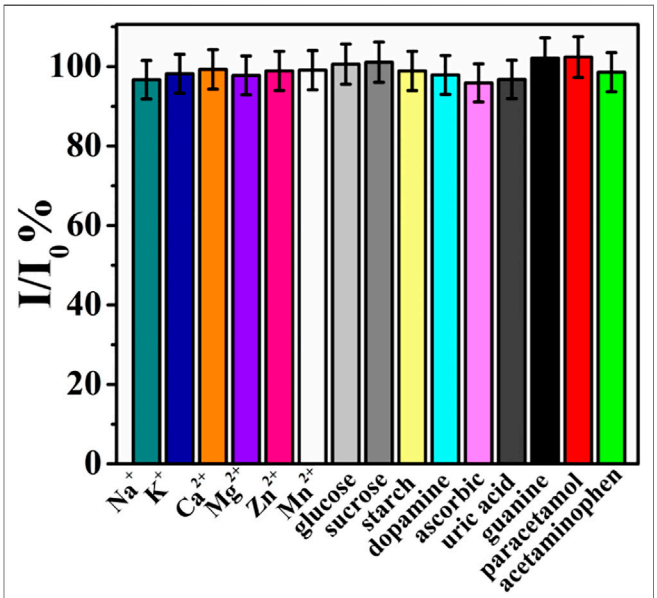

FIGURE 6 | Current ratio (I/I_0) of rGO–TiO_2–Au/GCE with 100 μM ACV in the presence of possible interfering species.

Reproducibility, Repeatability, Stability, and Selectivity of rGO–TiO_2–Au/GCE

To evaluate the reproducibility of rGO–TiO_2–Au/GCE for the analysis of ACV, five rGO–TiO_2–Au/GCEs were prepared independently with the same fabrication procedure, and their peak current values toward 100 μM ACV were compared. A relative standard deviation (RSD) of 3.18% was obtained, demonstrating the excellent reproducibility of the proposed sensor. The repeatability of rGO–TiO_2–Au/GCE was estimated by performing five successive measurements with the same rGO–TiO_2–Au/GCE in the same solution. It was observed that the oxidation peak current of ACV decreased continuously, which was due to the adsorption of an oxidative product of ACV on the electrode surface. In this case, rGO–TiO_2–Au/GCE can only be used for a single measurement. Meanwhile, the stability of TiO_2–Au–rGO/GCE was studied by storing the electrode in a refrigerator at 4°C. After two weeks, the peak current signal of the electrode remained at 90.2% of its initial response, suggesting the good storage stability of the modified electrode. The selectivity of rGO–TiO_2–Au/GCE toward the analysis of ACV was evaluated by testing some possible interfering species, including Na^+, K^+, Ca^{2+}, Mg^{2+}, Zn^{2+}, Mn^{2+}, glucose, sucrose, starch, dopamine, ascorbic acid, uric acid, guanine, paracetamol, and acetaminophen. As shown in **Figure 6**, a 100-fold concentration of each species had almost no influence on the peak current of ACV with deviations below 5%. These data revealed the good selectivity of rGO–TiO_2–Au/GCE toward the determination of ACV.

TABLE 1 | Determination of ACV in commercial ACV tablet samples (n = 3).

Sample	Added (μM)	Found (μM)	Recovery (%)	RSD (%)
1	20.00	19.19 ± 0.08	96.0	0.88
2	50.00	47.45 ± 0.15	94.9	0.29
3	80.00	85.67 ± 0.24	107.1	1.24

Analysis of a Real Sample

The practical application of rGO–TiO_2–Au/GCE in the analysis of real samples was studied by determination of ACV in commercial ACV tablet samples. The procedures for the analysis of tablets were followed as specified in *Analysis of the Sample*. The sample was spiked with three levels of ACV in the calibration range, and the content of ACV in the tablet samples was calculated by the standard addition method keeping the dilution factor in consideration. The result shows that the content of ACV was 196.2 mg per tablet, which was very close to the claimed value of 200 mg per tablet. Moreover, the recovery tests of ACV were performed, and the results are presented in **Table 1**. The satisfactory sample recoveries indicated the validity of the developed sensor for the determination of ACV in pharmaceutical formulations.

CONCLUSION

In this work, the sensitive determination of ACV was achieved by using the rGO–TiO_2–Au/GCE. The formation of rGO–TiO_2–Au nanocomposites was verified by TEM, XRD, and XPS techniques. The electrochemical experiments demonstrated that the rGO–TiO_2–Au/GCE showed outstanding electrocatalytic activity for the oxidation of ACV in pH 6.0 PB solution. Based on the unique properties of rGO, TiO_2, Au, and their synergistic effects, a good linear detection range and low detection limit for ACV were achieved. The rGO–TiO_2–Au/GCE also represented acceptable selectivity, repeatability, and stability and offered satisfactory recovery when applied for the analysis of ACV in the real samples.

DATA AVAILABILITY STATEMENT

The original contributions presented in the study are included in the article/**Supplementary Material**, further inquiries can be directed to the corresponding authors.

AUTHOR CONTRIBUTIONS

X-YL: methodology, data curation, formal analysis, validation, and writing–original draft. JL: methodology, data curation, formal analysis, validation, and writing–original draft. F-YK: conceptualization, methodology, data curation, formal analysis, validation, writing–original draft, funding acquisition, and project administration. M-JW: writing–review and editing. PZ: methodology, data curation, formal analysis, and validation. YL: methodology, data curation, formal analysis, and validation. H-LF: writing–review and editing. WW: writing–review and editing, funding acquisition, and project administration.

FUNDING

This work was supported by the National Natural Science Foundation of China, 21876144, 22176166 WW.

SUPPLEMENTARY MATERIAL

The Supplementary Material for this article can be found online at: https://www.frontiersin.org/articles/10.3389/fchem.2022.892919/full#supplementary-material

REFERENCES

Ajima, U., and Onah, J. O. (2015). Spectrophotometric Determination of Acyclovir After Its Reaction with Ninhydrin and Ascorbic Acid. *J. Appl. Pharm. Sci.* 5, 65–69. doi:10.7324/japs.2015.50411

Bao, Z.-l., Zhong, H., Li, X.-r., Zhang, A.-r., Liu, Y.-x., Chen, P., et al. (2021). Core-Shell Au@Ag Nanoparticles on Carboxylated Graphene for Simultaneous Electrochemical Sensing of Iodide and Nitrite. *Sensors Actuators B: Chem.* 345, 130319. doi:10.1016/j.snb.2021.130319

Chakraborty, B., and Roychaudhuri, C. (2021). Metal/Metal Oxide Modified Graphene Nanostructures for Electrical Biosensing Applications: A Review. *IEEE Sensors J.* 21, 17629–17642. doi:10.1109/jsen.2021.3082554

Clercq, E. D. (2004). Antivirals and Antiviral Strategies. *Nat. Rev. Microbiol.* 2, 704–720. doi:10.1038/nrmicro975

Coros, M., Pruneanu, S., and Stefan-van Staden, R. I. (2020). Review-Recent Progress in the Graphene-Based Electrochemical Sensors and Biosensors. *J. Electrochem. Soc.* 167, 037528. doi:10.1149/2.0282003JES

Dilgin, D. G., and Karakaya, S. (2016). Differential Pulse Voltammetric Determination of Acyclovir in Pharmaceutical Preparations Using a Pencil Graphite Electrode. *Mater. Sci. Eng. C* 63, 570–576. doi:10.1016/j.msec.2016.02.079

Dorraji, P. S., and Jalali, F. (2016). Differential Pulse Voltammetric Determination of Nanomolar Concentrations of Antiviral Drug Acyclovir at Polymer Film Modified Glassy Carbon Electrode. *Mater. Sci. Eng. C* 61, 858–864. doi:10.1016/j.msec.2016.01.030

George, J. M., Antony, A., and Mathew, B. (2018). Metal Oxide Nanoparticles in Electrochemical Sensing and Biosensing: A Review. *Microchim. Acta* 185, 358. doi:10.1007/s00604-018-2894-3

Heli, H., Zarghan, M., Jabbari, A., Parsaei, A., and Moosavi-Movahedi, A. A. (2010). Electrocatalytic Oxidation of the Antiviral Drug Acyclovir on a Copper Nanoparticles-Modified Carbon Paste Electrode. *J. Solid State. Electrochem.* 14, 787–795. doi:10.1007/s10008-009-0846-x

Heli, H., Pourbahman, F., and Sattarahmady, N. (2012). Nanoporous Nickel Microspheres: Synthesis and Application for the Electrocatalytic Oxidation and Determination of Acyclovir. *Anal. Sci.* 28, 503–510. doi:10.2116/analsci.28.503

Ilager, D., Shetti, N. P., Malladi, R. S., Shetty, N. S., Reddy, K. R., and Aminabhavi, T. M. (2021). Synthesis of Ca-Doped ZnO Nanoparticles and its Application as Highly Efficient Electrochemical Sensor for the Determination of Anti-Viral Drug, Acyclovir. *J. Mol. Liquids* 322, 114552. doi:10.1016/j.molliq.2020.114552

Kong, F.-Y., Li, W.-W., Wang, J.-Y., and Wang, W. (2015). UV-Assisted Photocatalytic Synthesis of Highly Dispersed Ag Nanoparticles Supported on DNA Decorated Graphene for Quantitative Iodide Analysis. *Biosens. Bioelectron.* 69, 206–212. doi:10.1016/j.bios.2015.02.029

Kong, F.-Y., Chen, T.-T., Wang, J.-Y., Fang, H.-L., Fan, D.-H., and Wang, W. (2016). UV-Assisted Synthesis of Tetrapods-Like Titanium Nitride-Reduced

Graphene Oxide Nanohybrids for Electrochemical Determination of Chloramphenicol. *Sensors Actuators B: Chem.* 225, 298–304. doi:10.1016/j.snb.2015.11.041

Kong, F.-Y., Li, R.-F., Yao, L., Wang, Z.-X., Li, H.-Y., Wang, W.-J., et al. (2019). A Novel Electrochemical Sensor Based on Au Nanoparticles/8-Aminoquinoline Functionalized Graphene Oxide Nanocomposite for Paraquat Detection. *Nanotechnology* 30, 285502. doi:10.1088/1361-6528/ab10ac

Kong, F.-Y., Li, R.-F., Zhang, S.-F., Wang, Z.-X., Li, H.-Y., Fang, H.-L., et al. (2021). Nitrogen and Sulfur Co-Doped Reduced Graphene Oxide-Gold Nanoparticle Composites for Electrochemical Sensing of Rutin. *Microchem. J.* 160, 105684. doi:10.1016/j.microc.2020.105684

Li, J., Tang, S., Lu, L., and Zeng, H. C. (2007). Preparation of Nanocomposites of Metals, Metal Oxides, and Carbon Nanotubes via Self-Assembly. *J. Am. Chem. Soc.* 129, 9401–9409. doi:10.1021/ja071122v

Liu, Z., Yang, F., Yao, M., Lin, Y., and Su, Z. (2015). Simultaneous Determination of Antiviral Drugs in Chicken Tissues by Ultra High Performance Liquid Chromatography with Tandem Mass Spectrometry. *J. Sep. Sci.* 38, 1784–1793. doi:10.1002/jssc.201401461

Long, X., and Chen, F. (2012). Flow Injection-Chemiluminescence Determination of Acyclovir. *Luminescence* 27, 478–481. doi:10.1002/bio.1378

Lu, Y., Celum, C., Wald, A., Baeten, J. M., Cowan, F., Delany-Moretlwe, S., et al. (2012). Acyclovir Achieves a Lower Concentration in African HIV-Seronegative, Herpes Simplex Virus 2-Seropositive Women Than in Non-African Populations. *Antimicrob. Agents Chemother.* 56, 2777–2779. doi:10.1128/aac.06160-11

Martínez-Rojas, F., Del Valle, M. A., Isaacs, M., Ramírez, G., and Armijo, F. (2017). Electrochemical Behaviour Study and Determination of Guanine, 6-thioguanine, Acyclovir and Gancyclovir on Fluorine-Doped SnO_2 Electrode. Application in Pharmaceutical Preparations. *Electroanalysis* 29, 2888–2895. doi:10.1002/elan.201700516

Mulabagal, V., Annaji, M., Kurapati, S., Dash, R. P., Srinivas, N. R., Tiwari, A. K., et al. (2020). Stability-Indicating HPLC Method for Acyclovir and Lidocaine in Topical Formulations. *Biomed. Chromatogr.* 34, 4751. doi:10.1002/bmc.4751

Naghian, E., Marzi Khosrowshahi, E., Sohouli, E., Pazoki-Toroudi, H. R., Sobhani-Nasab, A., Rahimi-Nasrabadi, M., et al. (2020). Electrochemical Oxidation and Determination of Antiviral Drug Acyclovir by Modified Carbon Paste Electrode with Magnetic CdO Nanoparticles. *Front. Chem.* 8, 689. doi:10.3389/fchem.2020.00689

Özkan, S. A., Uslu, B., and Aboul-Enein, H. Y. (2003). Analysis of Pharmaceuticals and Biological Fluids Using Modern Electroanalytical Techniques. *Crit. Rev. Anal. Chem.* 33, 155–181. doi:10.1080/713609162

Özkan, S. A., Uslu, B., and Sentürk, Z. (2004). Electroanalytical Characteristics of Amisulpride and Voltammetric Determination of the Drug in Pharmaceuticals and Biological media. *Electroanalysis* 16, 231–237. doi:10.1002/elan.200402828

Shukla, S., Haldorai, Y., Bajpai, V. K., Rengaraj, A., Hwang, S. K., Song, X., et al. (2018). Electrochemical Coupled Immunosensing Platform Based on Graphene Oxide/Gold Nanocomposite for Sensitive Detection of Cronobacter Sakazakii in Powdered Infant Formula. *Biosens. Bioelectron.* 109, 139–149. doi:10.1016/j.bios.2018.03.010

Tarlekar, P., Khan, A., and Chatterjee, S. (2018). Nanoscale Determination of Antiviral Drug Acyclovir Engaging Bifunctionality of Single Walled Carbon Nanotubes - Nafion Film. *J. Pharm. Biomed. Anal.* 151, 1–9. doi:10.1016/j.jpba.2017.12.006

Wang, G., Yang, J., Park, J., Gou, X., Wang, B., Liu, H., et al. (2008). Facile Synthesis and Characterization of Graphene Nanosheets. *J. Phys. Chem. C* 112, 8192–8195. doi:10.1021/jp710931h

Wang, P., Gan, T., Zhang, J., Luo, J., and Zhang, S. (2013). Polyvinylpyrrolidone-Enhanced Electrochemical Oxidation and Detection of Acyclovir. *J. Mol. Liquids* 177, 129–132. doi:10.1016/j.molliq.2012.11.009

Xiao, T., Huang, J., Wang, D., Meng, T., and Yang, X. (2020). Au and Au-Based Nanomaterials: Synthesis and Recent Progress in Electrochemical Sensor Applications. *Talanta* 206, 120210. doi:10.1016/j.talanta.2019.120210

Ya, J., Yang, N., Hu, F., Liu, Z., and E, L. (2015). Preparation and Activity Evaluation of TiO_2/Cu-TiO_2 Composite Catalysts. *J. Sol Gel. Sci. Technol.* 73, 322–331. doi:10.1007/s10971-014-3535-x

Yang, W.-D., Li, Y.-R., and Lee, Y.-C. (2016). Synthesis of R-GO/TiO_2 Composites via the UV-Assisted Photocatalytic Reduction of Graphene Oxide. *Appl. Surf. Sci.* 380, 249–256. doi:10.1016/j.apsusc.2016.01.118

Yu, L., and Xiang, B. (2008). Quantitative Determination of Acyclovir in Plasma by Near Infrared Spectroscopy. *Microchem. J.* 90, 63–66. doi:10.1016/j.microc.2008.03.006

Zhu, L., Wu, M., Van der Bruggen, B., Lei, L., and Zhu, L. (2020). Effect of TiO_2 Content on the Properties of Polysulfone Nanofiltration Membranes Modified with a Layer of TiO_2-Graphene Oxide. *Separat. Purif. Techn.* 242, 116770–116781. doi:10.1016/j.seppur.2020.116770

Conflict of Interest: The authors declare that the research was conducted in the absence of any commercial or financial relationships that could be construed as a potential conflict of interest.

Publisher's Note: All claims expressed in this article are solely those of the authors and do not necessarily represent those of their affiliated organizations or those of the publisher, the editors, and the reviewers. Any product that may be evaluated in this article, or claim that may be made by its manufacturer, is not guaranteed or endorsed by the publisher.

frontiers | Frontiers in Chemistry

MINI REVIEW
published: 13 May 2022
doi: 10.3389/fchem.2022.909110

Metal Graphitic Nanocapsules for Theranostics in Harsh Conditions

Yanxia Yang[1†], Shengkai Li[1†], Hongxiu Bu[1], Xin Xia[1], Long Chen[2], Yiting Xu[3] and Zhuo Chen[1]*

[1]*Aptamer Engineering Center of Hunan Province, Molecular Science and Biomedicine Laboratory (MBL), State Key Laboratory of Chemo/Bio–Sensing and Chemometrics, Hunan Provincial Key Laboratory of Biomacromolecular Chemical Biology, College of Chemistry and Chemical Engineering, Hunan University, Changsha, China,* [2]*Faculty of Science and Technology, University of Macau, Macau, China,* [3]*Key Laboratory of Theoretical Organic Chemistry and Function Molecule, Ministry of Education, School of Chemistry and Chemical Engineering, Hunan University of Science and Technology, Xiangtan, China*

Metal nanoparticles (NPs) with superior physicochemical properties and biocompatibility have shown great potential in theranostics. However, metal NPs show poor stability in some harsh conditions such as strong acid, oxidation, corrosion and high-temperature conditions, which limits their extensive bioapplications. To address such issue, a variety of superstable metal graphitic nanocapsules with the metal cores confined in the nanospace of few-layer graphitic shell have been developed for biodetection and therapy in harsh conditions. In this mini-review, we summarize the recent advances in metal graphitic nanocapsules for bioapplications in harsh conditions. Firstly, their theranostic performance in non-intrinsic physiological harsh environment, including oxidation, corrosion and high-temperature conditions, is systematically discussed. Then, we highlight their theranostic performance in the harsh stomach condition that is strong acidic and pepsin-rich. It is expected that this review will offer inspiration to facilitate the exploitation of novel theranostic agents that are stable in harsh conditions.

Keywords: metal graphitic nanocapsules, theranostics, harsh condition, gastric environment, stability

OPEN ACCESS

Edited by:
Junjie Zhu,
Nanjing University, China

Reviewed by:
Zhimei He,
Nanjing University of Posts and Telecommunications, China
Wei Chen,
Hefei University of Technology, China

***Correspondence:**
Zhuo Chen
zhuochen@hnu.edu.cn

†These authors have contributed equally to this work

Specialty section:
This article was submitted to Analytical Chemistry, a section of the journal Frontiers in Chemistry

Received: *31 March 2022*
Accepted: *21 April 2022*
Published: *13 May 2022*

Citation:
Yang Y, Li S, Bu H, Xia X, Chen L, Xu Y and Chen Z (2022) Metal Graphitic Nanocapsules for Theranostics in Harsh Conditions. Front. Chem. 10:909110. doi: 10.3389/fchem.2022.909110

INTRODUCTION

Metal nanoparticles (NPs) with different compositions and unique physicochemical properties are powerful tools for various biodetection and therapy (Azharuddin et al., 2019; Kim et al., 2019; Ma et al., 2021b). However, metal NPs show unsatisfactory stability in some non-intrinsic physiological harsh conditions (including strong oxidation, corrosion and high-temperature conditions) as well as harsh stomach condition (including strong acid (pH 0.9-1.5) and pepsin-rich conditions), and these harsh conditions hinder their broad applications in biomedicine. Hence, it is of great significance to develop effective strategies to improve the stability of metal NPs for reliable disease diagnosis and treatment in harsh conditions. The encapsulation of metal NPs is one of the most effective strategies to promote their stability (Gao et al., 2021). Currently, inert inorganic coating (such as silica (Li et al., 2010; Żygieło et al., 2021), titanium dioxide (Jin et al., 2021; Perumal et al., 2021) and graphene oxide (Xu et al., 2020; Kasztelan et al., 2021)) protection and organic coating (such as polyvinylpyrrolidone (Mirzaei et al., 2017)and lipids (Hsu et al., 2018)) functionalization strategies have been widely used to prevent the metal NPs from damage under external environments. However, these strategies make it difficult to completely isolate metal NPs from harsh conditions without affecting their inherent properties and functions.

Metal graphitic nanocapsules, a new type of nanomaterials with metal cores confined in the nanospace of few-layer graphitic shell prepared by the chemical vapor deposition method, show

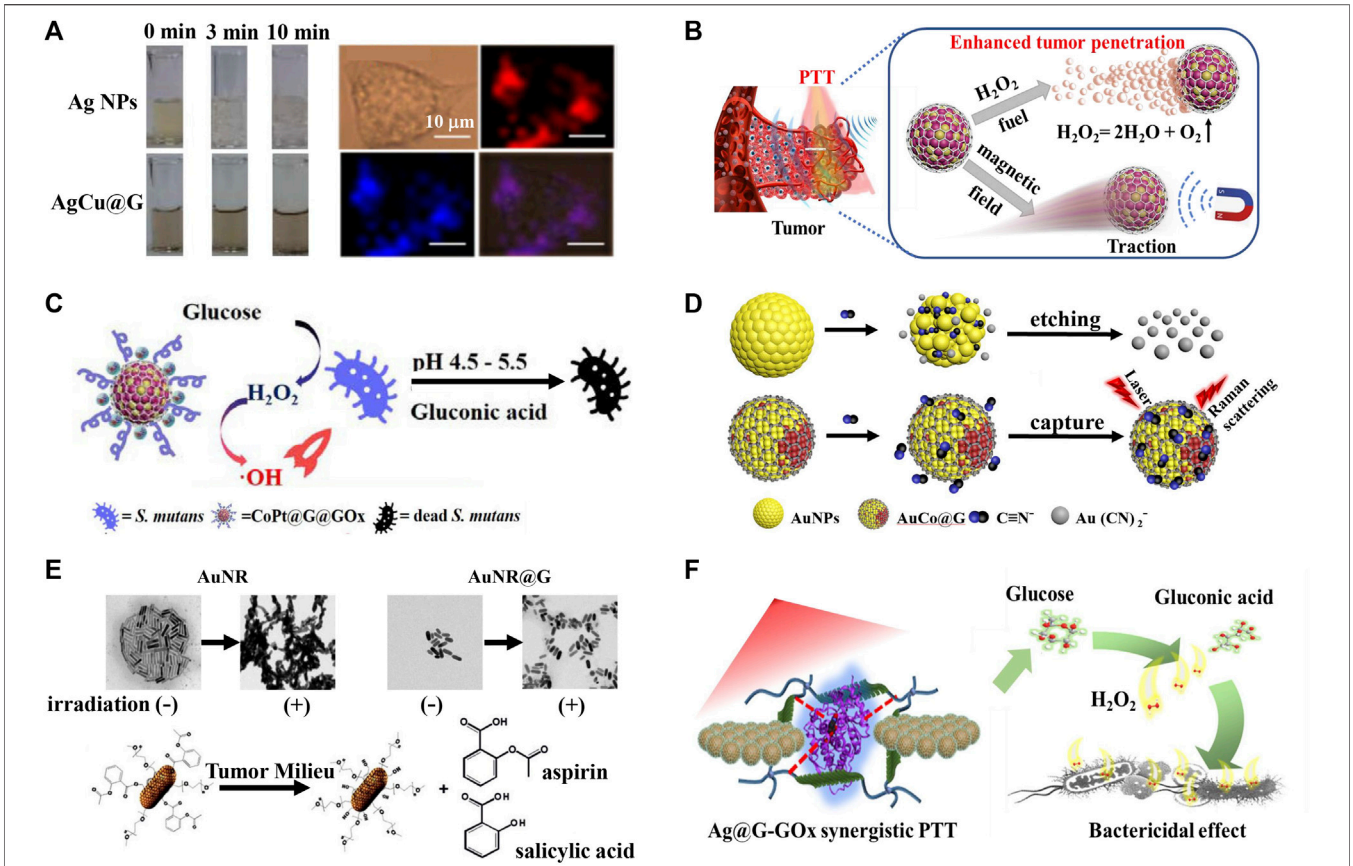

FIGURE 1 | Metal graphitic nanocapsules-based theranostics in non-intrinsic physiological harsh conditions. **(A)** Oxidation resistance of AgCu@G and AgCu@G for multimodal cellular Raman imaging (Song et al., 2014). **(B)** Illustration of the CoPt@G propelled navigator to enhance penetration and PTT action against tumor cells (Zhang et al., 2021a). **(C)** Illustration of the CoPt@G@GOx with magneto-actuated cascade catalytic activity for the therapy of *Streptococcus mutans* biofilm (Dong et al., 2022). **(D)** AuCo@G with corrosion resistance for direct capture and SERS analysis of the CN^- (Zhang et al., 2019). **(E)** AuNR@G-P-aspirin for enhanced NIR-mediated PTT of solid tumor and simultaneously inhibit PTT-induced inflammatory response (Dong et al., 2018). **(F)** Thermostable Ag@G-GOx synergistic PTT platform for bacterial elimination (Liu et al., 2022).

superior stability in harsh conditions (Li et al., 2019, 2022; Liu et al., 2020; Tang et al., 2021; Zhu et al., 2021). The graphitic shell acts as an inert layer to protect the unique physicochemical properties and intact functions of the metal core. Moreover, the graphitic shell with a large specific surface area and delocalized π electronic structure offers a robust platform for targeted molecules or drugs loading, and it also acts as a stable Raman label or internal standard molecule for reliable Raman bioanalysis. Benefiting from the ultra-high stability of graphitic layer and versatility of metal cores, a variety of theranostic applications in harsh conditions have been implemented by metal graphitic nanocapsules in the past few years. In this mini-review, we first introduce the theranostic advances of the metal graphitic nanocapsules in non-intrinsic physiological harsh environment, including oxidation, corrosion and high-temperature conditions. Then, we highlight the theranostic performance of the metal graphitic nanocapsules in the strong acid (pH 0.9-1.5) and pepsin-rich stomach conditions. Finally, the potential challenge and development direction of their theranostic applications in harsh conditions are further discussed. We expect this review will attract readers to facilitate the exploitation of novel theranostic agents that are stable in harsh conditions.

Theranostics in Non-intrinsic Physiological Harsh Conditions

Metal NPs-based theranostic agents are commonly subjected to a variety of non-intrinsic physiological harsh conditions, including strong oxidation, corrosion and high temperature conditions that exists during the occurrence, development and theranostics of diseases. These harsh conditions affect the stability of metal NPs to a certain extent, making direct biodetection and therapy challenging. Core-shell structured metal graphitic nanocapsules that integrated the multifunctional metal core in the nanospace of inert graphitic shell demonstrate exceptional theranostic potential in harsh conditions.

Oxidation conditions are able to affect the stability and property of metal NPs, especially the plasmonic-active Ag NPs that are prone to oxidation in air (Han et al., 2011). With the goal

of protecting Ag NPs from oxidation, Song et al. (2014) prepared a highly surface enhanced Raman scattering (SERS)-active AgCu graphitic nanocapsules (AgCu@G). Using the intrinsic characteristic Raman bands from the graphitic shell of AgCu@G as the stable Raman label, high-resolution multimodal cellular Raman imaging was achieved (**Figure 1A**). Latterly, Li et al. (2021) reported a novel AuAg graphitic nanocapsules (AuAg@G) with superior anti-oxidation property and realized SERS quantitative analysis in homogeneous system and multimodal Raman imaging of MCF-7 cells.

Endogenous/exogenous H^+ and H_2O_2 are other kinds corrosive substances that influence the stability and function of metal NPs (Mabilleau et al., 2006). Zhang et al. (2021a) constructed the catalase-like CoPt graphitic nanocapsules (CoPt@G) with superior corrosion resistance to H_2O_2, and it catalyzed H_2O_2 to produce O_2, offering a driving force for enhanced tumor penetration. Coupled with the magnetic and photothermal properties of CoPt@G, enhanced penetration and efficient photothermal therapy (PTT) of solid tumors have been achieved with the assistance of H_2O_2 and an external magnetic field (**Figure 1B**). Based on the superior corrosion resistance to H_2O_2 of CoPt@G, Dong et al. (2022) further proposed a glucose oxidase loaded CoPt@G (CoPt@G@GOx) platform with cascade reaction activity for *Streptococcus mutans* biofilms treatment. GOx firstly oxidized glucose to generate H_2O_2 and gluconic acid in the presence of endogenous glucose. The lower pH of the local microenvironment caused by gluconic acid could enhance the peroxidase-like activity of CoPt@G, and catalyze H_2O_2 to produce a large amount of highly toxic •OH, thereby achieving efficient inhibition of bacteria (**Figure 1C**). Recently, Keoingthong et al. (2021) fabricated a novel peroxidase active Ru graphitic nanocapsules (Ru@G) with superior corrosion resistance to H_2O_2 for sensitive colorimetric detection of glutathione (GSH) at near-physiological pH. In the presence of H_2O_2, Ru@G could catalyze colorimetric probe 3,3′,5,5′-tetramethylbenzydine (TMB) into blue-colored products, which was inhibited in the presence of GSH, building a simple and sensitive method for the colorimetric detection of GSH. In addition to H^+ and H_2O_2, CN^- is also a common corrosive substance that could influence the stability and function of metal NPs-based bioanalytical platform (Wang et al., 2009). Zhang et al. (2019) developed a versatile AuCo graphitic nanocapsules (AuCo@G) with superior SERS activity, magnetic properties and corrosion resistance to CN^-, and direct SERS analysis of the biomarker of CN^- in *Pseudomonas aeruginosa* was achieved (**Figure 1D**). The superstable AuCo@G proposed a robust platform for detecting *Pseudomonas aeruginosa* infection.

High temperature produced in the PTT process tends to affect the stability of photothermal reagents, meaning the development of stable photothermal reagents is of great significance (Gao et al., 2015). Metal graphitic nanocapsules present excellent thermostability and the graphitic layer has superior spectral absorption properties, thus showing extensive prospects in PTT applications. Dong et al. (2018) found that gold nanorod graphitic nanocapsules (AuNR@G) had superior near-infrared (NIR) light absorption property and had a better thermostability than AuNR. They further integrated AuNR@G with anti-inflammatory prodrugs (AuNR@G-P-aspirin) to realize enhanced NIR-mediated PTT of solid tumor and simultaneously inhibit PTT-induced inflammatory response (**Figure 1E**). Based on the superior thermostability and photothermal property of AuNR@G, Xu et al. (2019) reported a AuNR@G-doped hydrogel system for highly efficient photothermal antibacterial therapy for both Gram-negative *Escherichia coli* and Gram-positive *Staphylococcus aureus*. Recently, Liu et al. (2022) reported a GOx and Ag graphitic nanocapsules (Ag@G) co-loaded silk membrane theranostic system, the silk membrane enabled GOx to maintain good antibacterial activity during the photothermal antibacterial therapy process, the inert graphitic shell enabled Ag@G to keep excellent SERS performance and photothermal performance under high temperature and GOx-catalyzed production of large amounts of H_2O_2, SERS identification of bacteria in the bacteria-infected wound model and efficient synergistic treatment of bacteria were eventually achieved (**Figure 1F**).

Theranostics in Harsh Stomach Conditions

Gastric environment is a harsh condition with extremely low pH (0.9-1.5) and abundant pepsin. Among these, H^+ is a corrosive substance that affects the stability of theranostic reagents, and pepsin in gastric fluid can degrade or bind to theranostic reagents nonspecifically, resulting in instability and inefficiency of theranostics (Huang et al., 2015). Metal graphitic nanocapsules have excellent corrosion resistance to H^+ and degradation resistance to pepsin, providing a robust platform for the theranostic of gastric diseases.

Helicobacter pylori (*H. pylori*) infection is implicated in the aetiology of many diseases (Sanders and Peura, 2002). Although a series of methods for the detection of *H. pylori* infection have been developed, researchers have never stopped exploring safer and more efficient *in situ* diagnostic methods (Abu Shady et al., 2015; Celik et al., 2021; Jain et al., 2021). Magnetic resonance imaging (MRI), a powerful technique with superior penetration depth, noninvasiveness, high spatial and temporal resolution, shows great promises for the *in situ* detection of *H. pylori* infection (Hsieh et al., 2019). However, the harsh gastric acid environment affects the application of conventional contrast agent such as Gd^{3+} complexes and superparamagnetic iron oxide (Stephen et al., 2011; Li and Meade, 2019). Previous works reported that the FeCo graphitic nanocapsules (FeCo@G) showed superior stability and magnetic properties in solutions with extensive pH range, including the 1 M HCl solution (Chen et al., 2012; Nie et al., 2014). Based on the unique properties of FeCo@G, Li et al. (2017) used the FeCo@G as a robust contrast agent, and further prepared the benzeneboronic acid-PEG (B-PEG, a molecule that could specifically bind to peptidoglycan in bacterial cells) modified FeCo@G system for *in situ* targeted MRI imaging detection of *H. pylori* in mice (**Figure 2A**). Triple therapy (a proton pump inhibitor and two antibiotics) is used as the standard first-line therapy in the clinical treatment of *H. pylori* infection, but its efficacy is greatly limited by the rapid degradation of antibiotics in gastric acid, the emergence of drug-resistant bacteria and the side effect to the

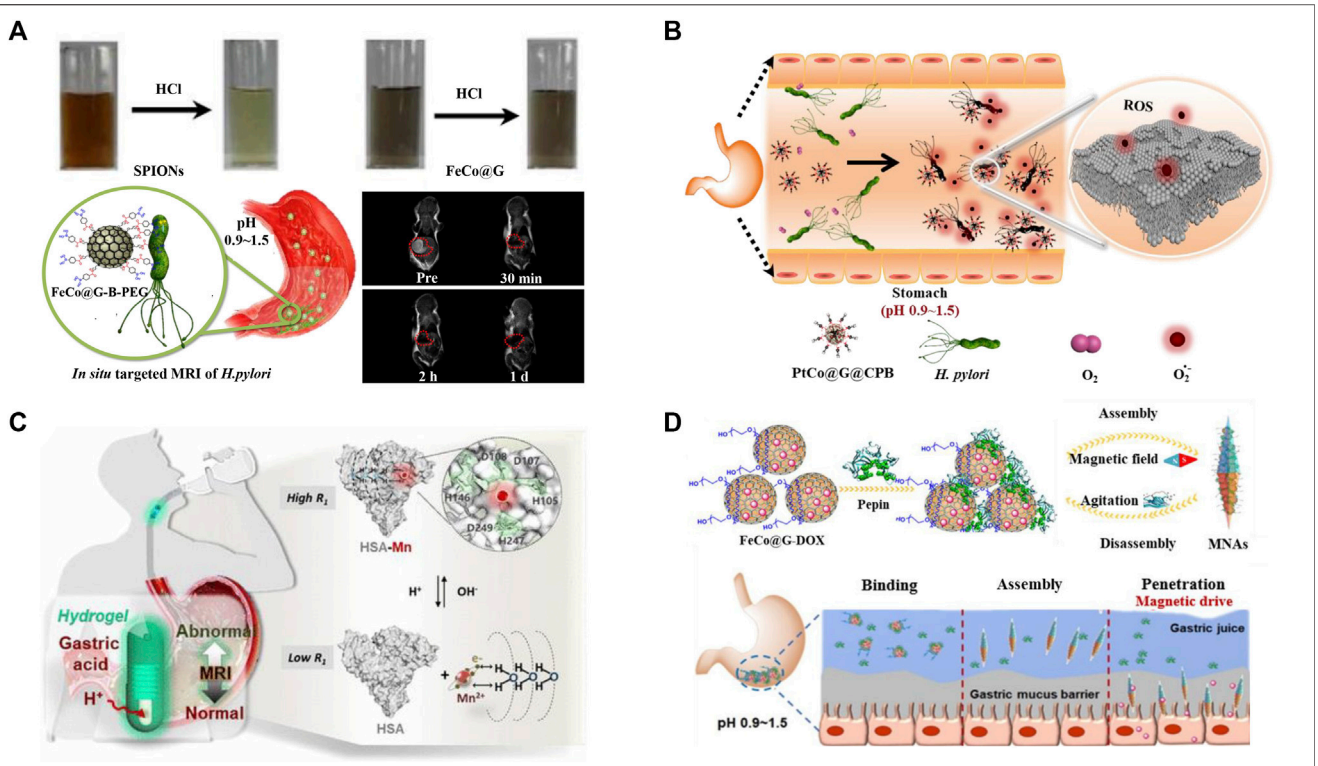

FIGURE 2 | Metal graphitic nanocapsules-based theranostics in harsh stomach conditions. **(A)** Stability of FeCo@G in 1 M HCl and FeCo@G-B-PEG for *in situ* MRI images of *H. pylori* (Li et al., 2017). **(B)** CoPt@G@CPB platform for targeted and selective combating *H. pylori* infection *in vivo* (Zhang et al., 2021b). **(C)** Hydrogel isolated HSA-Mn system for MRI monitoring of gastric pH (Xu et al., 2021). **(D)** Pepsin-assisted assembly of FeCo@G for enhanced mucosal penetration depth and prolonged drug retention (Cai et al., 2021).

intestinal flora (Wu et al., 2012; Brestoff and Artis, 2013). Nanozyme-based bacterial therapy has been developed rapidly in recent years, and it is expected to provide new options for the treatment of *H. pylori* (Huang et al., 2019; Jiang et al., 2019). Zhang et al. (2021b) developed a bacteria-targeting molecule C_{18}-PEG_n-benzeneboronic acid-functionalized CoPt graphitic nanocapsules (CoPt@G@CPB) platform for targeting and selective combating *H. pylori* infection *in vivo*. The CoPt@G showed superior corrosion resistance in acidic conditions and its oxidase-like activity was activated to catalyze the generation of superoxide radical species for antibacterial applications (**Figure 2B**). Meanwhile, its oxidase-like activity was suppressed under intestinal neutral conditions, showing minimal side effects. In addition, MRI and Raman imaging was used for monitoring the distribution of CoPt@G@CPB to guide further treatment.

Abundant pepsin in the gastric fluid can also affect the theranostics of gastric diseases because it tends to degrade or bind to the theranostic reagents nonspecifically. Many gastric diseases are highly correlated with abnormal pH, and *in situ* pH monitoring is therefore indispensable for prevention and treatment of gastric diseases (Ma et al., 2021a). To realize accurate and interference-free MRI detection of gastric pH, Xu et al. (2021) developed an orally administrated hydrogel capsule isolated human serum albumin–manganese (HSA-Mn) complex system, which could shield the interference of the pepsin in gastric fluid without severely hindering the penetration of H^+, for sensitive MRI monitoring of gastric pH *in vivo* (**Figure 2C**). Magnetic nanomaterials show huge potential for enhanced targeted drug delivery, the FeCo@G with superior corrosion resistance to gastric fluid is therefore expected to be a robust tool for targeted drug delivery in the stomach (Yang et al., 2014; Xu et al., 2018). Cai et al. (2021) surprisingly discovered FeCo@G could not only avoid the interference, but also use the pepsin as a "bridge" to realize the self-assembly of FeCo@G under an external magnetic field, and enhanced mucosal penetration depth and prolonged drug retention time were finally achieved *in vivo* (**Figure 2D**). This magnetic field-mediated *in situ* self-assembly platform without the interference of extremely acidic and pepsin-rich stomach conditions provided new ideas for the delivery of oral drugs and site-selective treatment of gastric diseases.

DISCUSSION AND PERSPECTIVES

Versatile metal graphitic nanocapsules have been widely used for theranostics in harsh conditions due to their excellent stability, good biocompatibility and unique physicochemical properties. In this mini-review, we have summarized the recent advances in

metal graphitic nanocapsules for theranostics in different harsh conditions. Firstly, plasmonic metal graphitic nanocapsues that can resist corrosion and high temperature damage have been constructed for reliable SERS bioanalysis, efficient photothermal anticancer and photothermal antibacterial applications in harsh conditions. Secondly, metal graphitic nanocapsules with robust MRI contrast ability and nanozyme activity under strong acid conditions have shown superior performance in the theranostics of gastric diseases. Finally, magnetic and magnetocatalytic propelled metal graphitic nanocapsules that can be stabilized in harsh conditions have been developed as delivery platforms for enhanced gastric mucus penetration and tumor penetration.

Despite great progress has been made in metal graphitic nanocapsules for theranostics in harsh conditions, some critical issues are still needed to be resolved. Firstly, novel multifunctional metal graphitic nanocapsules should be developed to broaden their scope of disease theranostics applications in harsh conditions. Secondly, long-term toxicity of metal graphitic nanocapsules *in vivo* should be systematically explored for promoting expected clinical applications. Finally, the integration of metal graphitic nanocapsules with some advanced technology like Raman endoscope should be considered to acquire more accurate and abundant information for the theranostics of grastric diseases. We expect the superstable metal graphitic nanocapsules will offer robust nanoplatforms for future clinical theranostics without the interference of harsh conditions.

AUTHOR CONTRIBUTIONS

YY and SL wrote the original draft of the manuscript. HB and XX edited the manuscript. ZC and YX discussed the scope and content of this review. ZC and LC reviewed the final version of the review.

FUNDING

This work was financially supported by the National Key Research and Development Program of China (2020YFA0210800), the National Natural Science Foundation of China (No. 21522501), the Science and Technology Innovation Program of Hunan Province (No. 2020RC4017), and the Hunan Provincial Education Office General Project of China (No. 21CO349).

REFERENCES

Abu Shady, M. M., Fathy, H. A., Ali, A., Galal, E. M., Fathy, G. A., and Sibaii, H. (2015). Comparison of Serum IgG Antibody Test with Gastric Biopsy for the Detection of *Helicobacter pylori* Infection Among Egyptian Children. *Open Access Maced. J. Med. Sci.* 3, 303–306. doi:10.3889/oamjms.2015.062

Azharuddin, M., Zhu, G. H., Das, D., Ozgur, E., Uzun, L., Turner, A. P. F., et al. (2019). A Repertoire of Biomedical Applications of Noble Metal Nanoparticles. *Chem. Commun.* 55, 6964–6996. doi:10.1039/c9cc01741k

Brestoff, J. R., and Artis, D. (2013). Commensal Bacteria at the Interface of Host Metabolism and the Immune System. *Nat. Immunol.* 14, 676–684. doi:10.1038/ni.2640

Cai, X., Xu, Y., Zhao, L., Xu, J., Li, S., Wen, C., et al. (2021). *In Situ* pepsin-assisted Needle Assembly of Magnetic-Graphitic-Nanocapsules for Enhanced Gastric Retention and Mucus Penetration. *Nano Today* 36, 101032. doi:10.1016/j.nantod.2020.101032

Celik, C., Can Sezgin, G., Kocabas, U. G., Gursoy, S., Ildiz, N., Tan, W., et al. (2021). Novel Anthocyanin-Based Colorimetric Assay for the Rapid, Sensitive, and Quantitative Detection of *Helicobacter pylori*. *Anal. Chem.* 93, 6246–6253. doi:10.1021/acs.analchem.1c00663

Chen, Z., Hong, G., Wang, H., Welsher, K., Tabakman, S. M., Sherlock, S. P., et al. (2012). Graphite-coated Magnetic Nanoparticle Microarray for Few-Cells Enrichment and Detection. *ACS Nano* 6, 1094–1101. doi:10.1021/nn2034692

Dong, Q., Wang, X., Hu, X., Xiao, L., Zhang, L., Song, L., et al. (2018). Simultaneous Application of Photothermal Therapy and an Anti-inflammatory Prodrug Using Pyrene-Aspirin-Loaded Gold Nanorod Graphitic Nanocapsules. *Angew. Chem.* 130, 183–187. doi:10.1002/ange.201709648

Dong, Q., Li, Z., Xu, J., Yuan, Q., Chen, L., and Chen, Z. (2022). Versatile Graphitic Nanozymes for Magneto Actuated Cascade Reaction-Enhanced Treatment of S. Mutans Biofilms. *Nano Res.* doi:10.1007/s12274-022-4258-x

Gao, W., Wang, X., Fan, H., Song, Z., Lai, X., Chen, Z., et al. (2015). Fabrication of Superstable Gold Nanorod-Carbon Nanocapsule as a Molecule Loading Material. *Sci. Bull.* 60, 1101–1107. doi:10.1007/s11434-015-0814-z

Gao, C., Lyu, F., and Yin, Y. (2021). Encapsulated Metal Nanoparticles for Catalysis. *Chem. Rev.* 121, 834–881. doi:10.1021/acs.chemrev.0c00237

Han, Y., Lupitskyy, R., Chou, T.-M., Stafford, C. M., Du, H., and Sukhishvili, S. (2011). Effect of Oxidation on Surface-Enhanced Raman Scattering Activity of Silver Nanoparticles: a Quantitative Correlation. *Anal. Chem.* 83, 5873–5880. doi:10.1021/ac2005839

Hsieh, V., Okada, S., Wei, H., García-Álvarez, I., Barandov, A., Alvarado, S. R., et al. (2019). Neurotransmitter-responsive Nanosensors for T2-Weighted Magnetic Resonance Imaging. *J. Am. Chem. Soc.* 141, 15751–15754. doi:10.1021/jacs.9b08744

Hsu, J. C., Naha, P. C., Lau, K. C., Chhour, P., Hastings, R., Moon, B. F., et al. (2018). An All-In-One Nanoparticle (AION) Contrast Agent for Breast Cancer Screening with DEM-CT-MRI-NIRF Imaging. *Nanoscale* 10, 17236–17248. doi:10.1039/c8nr03741h

Huang, J., Shu, Q., Wang, L., Wu, H., Wang, A. Y., and Mao, H. (2015). Layer-by-layer Assembled Milk Protein Coated Magnetic Nanoparticle Enabled Oral Drug Delivery with High Stability in Stomach and Enzyme-Responsive Release in Small Intestine. *Biomaterials* 39, 105–113. doi:10.1016/j.biomaterials.2014.10.059

Huang, Y., Ren, J., and Qu, X. (2019). Nanozymes: Classification, Catalytic Mechanisms, Activity Regulation, and Applications. *Chem. Rev.* 119, 4357–4412. doi:10.1021/acs.chemrev.8b00672

Jain, U., Saxena, K., and Chauhan, N. (2021). *Helicobacter pylori* Induced Reactive Oxygen Species: a New and Developing Platform for Detection. *Helicobacter* 26, e12796. doi:10.1111/hel.12796

Jiang, D., Ni, D., Rosenkrans, Z. T., Huang, P., Yan, X., and Cai, W. (2019). Nanozyme: New Horizons for Responsive Biomedical Applications. *Chem. Soc. Rev.* 48, 3683–3704. doi:10.1039/c8cs00718g

Jin, L., Shaaban, E., Bamonte, S., Cintron, D., Shuster, S., Zhang, L., et al. (2021). Surface Basicity of Metal@TiO2 to Enhance Photocatalytic Efficiency for CO2 Reduction. *ACS Appl. Mat. Interfaces* 13, 38595–38603. doi:10.1021/acsami.1c09119

Kasztelan, M., Studzinska, A., Żukowska, G. Z., and Pałys, B. (2021). Silver-Graphene Oxide Nanohybrids for Highly Sensitive, Stable SERS Platforms. *Front. Chem.* 9, 665205. doi:10.3389/fchem.2021.665205

Keoingthong, P., Hao, Q., Li, S., Zhang, L., Xu, J., Wang, S., et al. (2021). Graphene Encapsuled Ru Nanocrystal with Highly-Efficient Peroxidase-like Activity for Glutathione Detection at Near-Physiological pH. *Chem. Commun.* 57, 7669–7672. doi:10.1039/d1cc02953c

Kim, M., Lee, J. H., and Nam, J. M. (2019). Plasmonic Photothermal Nanoparticles for Biomedical Applications. *Adv. Sci.* 6, 1900471. doi:10.1002/advs.201900471

Li, H., and Meade, T. J. (2019). Molecular Magnetic Resonance Imaging with Gd(III)-based Contrast Agents: Challenges and Key Advances. *J. Am. Chem. Soc.* 141, 17025–17041. doi:10.1021/jacs.9b09149

Li, J. F., Huang, Y. F., Ding, Y., Yang, Z. L., Li, S. B., Zhou, X. S., et al. (2010). Shell-isolated Nanoparticle-Enhanced Raman Spectroscopy. *Nature* 464, 392–395. doi:10.1038/nature08907

Li, Y., Hu, X., Ding, D., Zou, Y., Xu, Y., Wang, X., et al. (2017). *In Situ* targeted MRI Detection of *Helicobacter pylori* with Stable Magnetic Graphitic Nanocapsules. *Nat. Commun.* 8, 1–12. doi:10.1038/ncomms15653

Li, S., Xu, J., Wang, S., Xia, X., Chen, L., and Chen, Z. (2019). Versatile Metal Graphitic Nanocapsules for SERS Bioanalysis. *Chin. Chem. Lett.* 30, 1581–1592. doi:10.1016/j.cclet.2019.05.049

Li, S., Zhu, Z., Cai, X., Song, M., Wang, S., Hao, Q., et al. (2021). Versatile Graphene-Isolated AuAg-Nanocrystal for Multiphase Analysis and Multimodal Cellular Raman Imaging †. *Chin. J. Chem.* 39, 1491–1497. doi:10.1002/cjoc.202000734

Li, S., Yang, Y., Wang, S., Gao, Y., Song, Z., Chen, L., et al. (2022). Advances in Metal Graphitic Nanocapsules for Biomedicine. *Exploration*, 20210223. doi:10.1002/EXP.20210223

Liu, Z., Li, S., Xia, X., Zhu, Z., Chen, L., and Chen, Z. (2020). Recent Advances in Multifunctional Graphitic Nanocapsules for Raman Detection, Imaging, and Therapy. *Small Methods* 4, 1900440. doi:10.1002/smtd.201900440

Liu, Z., Li, S., Yin, Z., Zhu, Z., Chen, L., Tan, W., et al. (2022). Stabilizing Enzymes in Plasmonic Silk Film for Synergistic Therapy of *In Situ* SERS Identified Bacteria. *Adv. Sci.* 9, 2104576. doi:10.1002/advs.202104576

Mabilleau, G., Bourdon, S., Joly-Guillou, M. L., Filmon, R., Baslé, M. F., and Chappard, D. (2006). Influence of Fluoride, Hydrogen Peroxide and Lactic Acid on the Corrosion Resistance of Commercially Pure Titanium. *Acta Biomater.* 2, 121–129. doi:10.1016/j.actbio.2005.09.004

Ma, Y., Liu, Y., Jiang, Z., Lv, H., Wang, J., Wang, T., et al. (2021a). Visualization of the pH-Fluctuations in Gastric Ulcer Living Mice by the *In Situ* Near-Infrared Imaging. *Sensors Actuators B Chem.* 349, 130747. doi:10.1016/j.snb.2021.130747

Ma, Z., Mohapatra, J., Wei, K., Liu, J. P., and Sun, S. (2021b). Magnetic Nanoparticles: Synthesis, Anisotropy, and Applications. *Chem. Rev.* doi:10.1021/acs.chemrev.1c00860

Mirzaei, A., Janghorban, K., Hashemi, B., Bonyani, M., Leonardi, S. G., and Neri, G. (2017). Characterization and Optical Studies of PVP-Capped Silver Nanoparticles. *J. Nanostruct Chem.* 7, 37–46. doi:10.1007/s40097-016-0212-3

Nie, X. K., Xu, Y. T., Song, Z. L., Ding, D., Gao, F., Liang, H., et al. (2014). Magnetic-graphitic-nanocapsule Templated Diacetylene Assembly and Photopolymerization for Sensing and Multicoded Anti-counterfeiting. *Nanoscale* 6, 13097–13103. doi:10.1039/c4nr03837a

Perumal, A., Kannan, S., and Nallaiyan, R. (2021). Silver Nanoparticles Incorporated Polyaniline on TiO2 Nanotube Arrays: A Nanocomposite Platform to Enhance the Biocompatibility and Antibiofilm. *Surfaces Interfaces* 22, 100892. doi:10.1016/j.surfin.2020.100892

Sanders, M. K., and Peura, D. A. (2002). *Helicobacter Pylori*-Associated Diseases. *Curr. Gastroenterol. Rep.* 4, 448–454. doi:10.1007/s11894-002-0019-x

Song, Z. L., Chen, Z., Bian, X., Zhou, L. Y., Ding, D., Liang, H., et al. (2014). Alkyne-functionalized Superstable Graphitic Silver Nanoparticles for Raman Imaging. *J. Am. Chem. Soc.* 136, 13558–13561. doi:10.1021/ja507368z

Stephen, Z. R., Kievit, F. M., and Zhang, M. (2011). Magnetite Nanoparticles for Medical MR Imaging. *Mater. Today* 14, 330–338. doi:10.1016/S1369-7021(11)70163-8

Tang, W., Li, S., Wang, S., Chen, L., and Chen, Z. (2021). Laser-mediated Enrichment Based Surface Enhanced Raman Analysis. *Chem. J. Chin. Univ.* 42, 3054–3061. doi:10.7503/cjcu20210153

Wang, X.-B., Wang, Y.-L., Yang, J., Xing, X.-P., Li, J., and Wang, L.-S. (2009). Evidence of Significant Covalent Bonding in Au(CN)2−. *J. Am. Chem. Soc.* 131, 16368–16370. doi:10.1021/ja908106e

Wu, W., Yang, Y., and Sun, G. (2012). Recent Insights into Antibiotic Resistance inHelicobacter pyloriEradication. *Gastroenterology Res. Pract.* 2012, 1–8. doi:10.1155/2012/723183

Xu, X., Hou, S., Wattanatorn, N., Wang, F., Yang, Q., Zhao, C., et al. (2018). Precision-guided Nanospears for Targeted and High-Throughput Intracellular Gene Delivery. *ACS Nano* 12, 4503–4511. doi:10.1021/acsnano.8b00763

Xu, M.-L., Guan, L.-Y., Li, S.-K., Chen, L., and Chen, Z. (2019). Stable Gold Graphitic Nanocapsule Doped Hydrogels for Efficient Photothermal Antibacterial Applications. *Chem. Commun.* 55, 5359–5362. doi:10.1039/c9cc01933b

Xu, L., Zhang, H., Tian, Y., Jiao, A., Li, S., Tan, Y., et al. (2020). Modified Photochemical Strategy to Support Highly-Purity, Dense and Monodisperse Au Nanospheres on Graphene Oxide for Optimizing SERS Detection. *Talanta* 209, 120535. doi:10.1016/j.talanta.2019.120535

Xu, Y., Yang, Y., Yin, Z., Cai, X., Xia, X., Donovan, M. J., et al. (2021). *In Situ* gastric pH Imaging with Hydrogel Capsule Isolated Paramagnetic Metallo-Albumin Complexes. *Anal. Chem.* 93, 5939–5946. doi:10.1021/acs.analchem.1c00538

Yang, Z., Deng, L., Lan, Y., Zhang, X., Gao, Z., Chu, C.-W., et al. (2014). Molecular Extraction in Single Live Cells by Sneaking in and Out Magnetic Nanomaterials. *Proc. Natl. Acad. Sci. U.S.A.* 111, 10966–10971. doi:10.1073/pnas.1411802111

Zhang, L., Zhang, J., Zheng, Z., Liao, Y., Xu, Y., Li, Z., et al. (2019). Interaction-transferable Graphene-Isolated Superstable AuCo Nanocrystal-Enabled Direct Cyanide Capture. *Anal. Chem.* 91, 8762–8766. doi:10.1021/acs.analchem.9b01811

Zhang, L., Dong, Q., Zhang, H., Xu, J., Wang, S., Zhang, L., et al. (2021a). A Magnetocatalytic Propelled Cobalt-Platinum@Graphene Navigator for Enhanced Tumor Penetration and Theranostics. *CCS Chem.* 3, 2382–2395. doi:10.31635/ccschem.021.202101219

Zhang, L., Zhang, L., Deng, H., Li, H., Tang, W., Guan, L., et al. (2021b). *In Vivo* activation of pH-Responsive Oxidase-like Graphitic Nanozymes for Selective Killing of *Helicobacter pylori*. *Nat. Commun.* 12, 1–10. doi:10.1038/s41467-021-22286-x

Zhu, Z., Li, S., Song, M., Cai, X., Song, Z., Chen, L., et al. (2021). Recent Progress of Versatile Metal Graphitic Nanocapsules in Biomedical Applications. *Chem. J. Chin. Univ.* 42, 2701–2716. doi:10.7503/cjcu20210118

Żygieło, M., Piotrowski, P., Witkowski, M., Cichowicz, G., Szczytko, J., and Królikowska, A. (2021). Reduced Self-Aggregation and Improved Stability of Silica-Coated Fe3O4/Ag SERS-Active Nanotags Functionalized with 2-Mercaptoethanesulfonate. *Front. Chem.* 9, 697595. doi:10.3389/fchem.2021.697595

Conflict of Interest: The authors declare that the research was conducted in the absence of any commercial or financial relationships that could be construed as a potential conflict of interest.

Publisher's Note: All claims expressed in this article are solely those of the authors and do not necessarily represent those of their affiliated organizations, or those of the publisher, the editors and the reviewers. Any product that may be evaluated in this article, or claim that may be made by its manufacturer, is not guaranteed or endorsed by the publisher.

frontiers | Frontiers in Chemistry

ORIGINAL RESEARCH
published: 17 May 2022
doi: 10.3389/fchem.2022.907777

Simple Synthesis of CeO_2 Nanoparticle Composites *In Situ* Grown on Carbon Nanotubes for Phenol Detection

Chao Hu[1], *Haiping Huang*[1,2]*, *Yu Yan*[1], *Yongmei Hu*[2], *Sui-Jun Liu*[1] *and He-Rui Wen*[1]

[1]*Jiangxi Provincial Key Laboratory of Functional Molecular Materials Chemistry, School of Chemistry and Chemical Engineering, Jiangxi University of Science and Technology, Ganzhou, China,* [2]*Key Laboratory of Testing and Tracing of Rare Earth Products for State Market Regulation, Jiangxi University of Science and Technology, Ganzhou, China*

via simple hydrothermal method, CeO_2 was *in-situ* grown onto the CNTs to form CeO_2/CNTs nanocomposites were synthesized with cerium nitrate as Ce resource. The morphology and structure were characterized by transmission electron microscopy and X-ray diffraction. The characterizations reveal that CeO_2 nanoparticles are uniformly dispersed onto the surface of the pre-acidified CNTs. The electrochemical property of the synthesized nanocomposite was investigated in 0.1 M KCl electrolyte containing 2 mM $[Fe(CN)_6]^{3-/4-}$. The nanocomposites were employed to fabricate electrochemical sensor for phenol detection. The linear range for phenol detection measured by the differential pulse voltammetry method is 1–500 μM. The sensor also exhibits good selectivity, reproducibility and stability. When applied for the river and tap water analysis, it shows good recovery rate.

Keywords: carbon nanotube, phenol, electrochemical sensor, nanocomposites, cerium dioxide

OPEN ACCESS

Edited by:
Cheng Ma,
Yangzhou University, China

Reviewed by:
Hongcheng Pan,
Guilin University of Technology, China
Chang-Jie Mao,
Anhui University, China

****Correspondence:***
Haiping Huang
huanghp@jxust.edu.cn

Specialty section:
This article was submitted to Analytical Chemistry, a section of the journal Frontiers in Chemistry

Received: *30 March 2022*
Accepted: *27 April 2022*
Published: *17 May 2022*

Citation:
Hu C, Huang H, Yan Y, Hu Y, Liu S-J and Wen H-R (2022) Simple Synthesis of CeO_2 Nanoparticle Composites In Situ Grown on Carbon Nanotubes for Phenol Detection. Front. Chem. 10:907777. doi: 10.3389/fchem.2022.907777

INTRODUCTION

At present, human life is inseparable from chemical products. As the chemical industry brings great convenience to our daily lives, it also damages our environment, making the global water pollution problem more and more serious (Lopez-Pacheco et al., 2019; Liu J. et al., 2021). Phenol is such a common pollutant in the chemical industrial wastewater, which can cause pollution to water bodies and the atmosphere, and also has strong chemical toxicity to human beings (Gruzdev et al., 2015; Singh and Chandra, 2019; Wang and Chen, 2020). Excessive exposure to water containing phenol can cause damage to the skin and eyes, and it also causes nerve damage and increases the risk of cancer (Singh and Chandra, 2019). Not only the World Health Organization (WHO) lists it as the third category of carcinogens, the European Union (EU) and the US Environmental Protection Agency also list it as an important environmental pollutant (Diaz-Gonzalez et al., 2016). What's more, because phenol is difficult to degrade in the natural environment, its environmental pollution will eventually destroy the ecology system. Therefore, it is urgent to develop a technology that can quickly detect the phenol content in river water. At present, the main methods for detecting phenol includes spectrophotometry, gas chromatography-mass spectrometry, liquid/solid phase extraction/microextraction, high-performance liquid chromatography, etc (Alcudia-Leon et al., 2011; Jaworek, 2018; Liu W. et al., 2021) However, the operations for these methods are relatively complex, and the instruments are expensive, which limit their rapid and wide detection. Compared with the previous analysis methods, electrochemical analysis has the advantages of good stability, high sensitivity, low

cost, and easy operation (Curulli, 2020; Tajik et al., 2020). Owing to these advantages, it is widely employed for the electrochemical detection of inorganic ions, small organic molecules and bio-molecules, etc.

One key factor in improving the performance of electrochemical sensors is to find suitable materials for modifying working electrodes (Ferrier and Honeychurch, 2021). So far, scientists have done a lot of research on this, and many materials with excellent electrochemical properties have been used to improve the performance of sensors (Abbas and Amin, 2022; Shao et al., 2022). Among them, the carbon nanotube is treated as an ideal material for the chemical modified electrode owing to excellent performance (Zhang and Du, 2020; Billing, 2021). Carbon nanotubes are composed of pure carbon atoms that interact through strong sp^2 carbon-carbon bonds. They exhibit the unique carbon network geometry of tubular structures in nanoscale diameters and microscale lengths. The strong chemical bonds in the carbon network make CNTs the most fascinating nanomaterials. Because of the unique physical and chemical properties such as high mechanical strength, large surface area and electrical conductivity, it is widely utilized in the electrochemical fields such as electrochemical sensor (Wang J. et al., 2018), electrochemical catalyst (Tafete et al., 2022), supercapacitor (Yang et al., 2020), etc.

Due to the unique electronic configuration, rare earth elements are currently the hot-topic research materials (Huang and Zhu, 2019). Take Cerium (Ce) as an example, Ce is a member of the lanthanide family of metals, and it is the most abundant element of the rare earth metals found in the earth crust (Algethami et al., 2018). It is easy to lose outer electrons to form compounds of different valence states, thus making its chemical properties very active. The oxide of cerium, called ceria, is a rare earth semiconductor material with a low price and a wide range of applications. CeO_2 has a cubic fluorite structure, in which the Ce element has two oxidation states Ce^{4+} and Ce^{3+}. It is widely used in luminescent materials (Huang et al., 2021) catalysts (Zhu et al., 2019), electrode materials (Xiao et al., 2018; Huang et al., 2019), and so on. For the purpose of further exploring the electrochemical application of CeO_2, in this study, a simple hydrothermal route was used to *in situ* grow CeO_2 nanoparticles on the surface of carbon nanotubes. The synthesized CeO_2/CNTs composites were employed to construct a phenol electrochemical sensor. The experimental results show that the CeO_2/CNTs modified electrode has a good detection effect on phenol.

EXPERIMENTAL

Preparation of CeO_2/CNTs

First, the CNTs were acidified with a mixed acid solution ($V_{98\%\ \text{concentrated sulfuric acid}}$: $V_{68\%\ \text{concentrated nitric acid}}$ = 3:1) at 90°C for 4 h under stirring and refluxing. $Ce(NO_3)_3{\cdot}6H_2O$ was used as the cerium source to synthesize CeO_2/CNTs composite material in one step by hydrothermal method. Dissolve 1.2 g $Ce(NO_3)_3{\cdot}6H_2O$ and 0.1 g treated CNTs into 60 ml deionized water. After adjust the solution to pH = 9.0 with 0.5 M NaOH and stir for 1 h, it was then transferred into the autoclave and reacted at 160°C for 24 h. After that, it was allowed to cool naturally, and the product was centrifuged, washed, dried under vacuum, and ground. The similar route was used to prepare CeO_2 nanoparticles without the addition of treated CNT at the beginning.

Preparation of Electrochemical Sensor

The modified glassy carbon electrodes (GCE, Φ = 4 mm) of CeO_2/CNTs/GCE, CeO_2/GCE and CNTs/GCE were used as working electrode. All the cyclic voltammetric (CV) and differential pulse voltammetric (DPV) responses were recorded on electrochemical workstation.

Other detailed experimental procedures and apparatus parameters are provided in the Supplementary Material.

RESULTS AND DISCUSSION

Material Characterization

TEM and XRD technologies were employed for the purpose of intuitively observing the morphology and structure of the nanomaterials. Shown in **Figures 1A,B** is the TEM image of CeO_2 nanoparticles and CeO_2/CNTs nanocomposites. It can be seen that CeO_2 nanoparticles are grown uniformly on the surface of CNTs. In the XRD spectra of **Figure 1C**, the diffraction peak at 26° in the curve 1) is the characteristic peak of CNTs. For CeO_2, it can be seen from curve b in **Figure 1C** that a series of sharp diffraction peaks appear at 28.3°, 33.1°, 47.5°, 58.2°, which are correspond to the (111), (200), (220), (311) planes of CeO_2 (Xiao et al., 2019). This is also consistent with the standard XRD spectrum of CeO_2 (curve d, JCPDS card No. 34–0,394). And all these peaks are appeared in the CeO_2/CNTs nanocomposite (curve c), proving the successful preparation of CeO_2/CNTs composite.

Cyclic Voltammetric Response of Different Electrodes

To study the electrochemical property of the nanocomposites, the CV responses of different nanocomposites modified electrode were recorded in 0.1 M KCl electrolyte containing 2 mM $[Fe(CN)_6]^{3-/4-}$, which are shown in **Figure 2A**. Compared with bare GCE (curve a), CeO_2/GCE (curve b) shows a little bigger CV response. This confirms that as a rare earth semiconductor material, CeO_2 can still promote the electron transfer between the electrode and the electrolyte. Nevertheless, the peak current is dramatically enlarged after CNTs are modified onto the GCE as CNTs/GCE (curve c), due to the excellent conductivity of CNTs. And the peak current is further enlarged for CeO_2/CNTs/GCE (curve d). This proves that the binary composite of CeO_2/CNTs owes the best electrochemical performance than single CNT or CeO_2.

In order to investigate the electrochemical catalytic effect of the different nanomaterial towards oxidation of phenol, CV

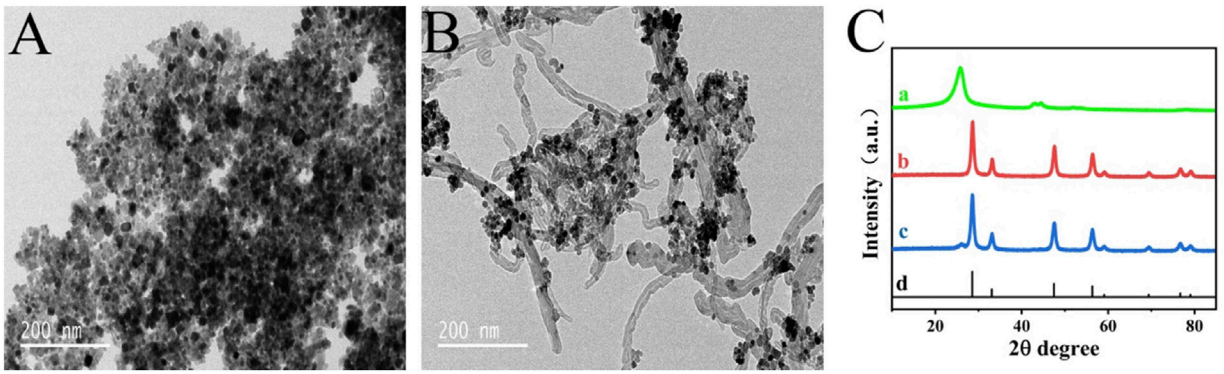

FIGURE 1 | TEM images of CeO_2 **(A)**, CeO_2/CNTs **(B)**, and XRD patterns **(C)** of CNTs (a), CeO_2 (b), CeO_2/CNTs (c) and standard spectrum of CeO_2 (d).

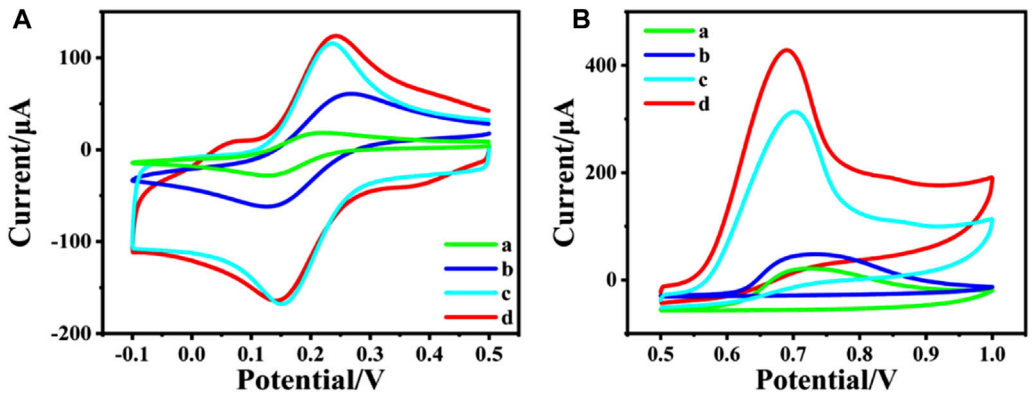

FIGURE 2 | CVs of different electrode in 2 mM $[Fe(CN)_6]^{3-/4-}$ + 0.1 M KCl **(A)** and in phosphate buffer (pH = 5.0, 0.1 M) containing 2 mM phenol **(B)**. (a) bare GCE, (b) CeO_2/GCE, (c) CNTs/GCE and (d) CeO_2/CNTs/GCE. Scan rate: 50 mV s^{-1}.

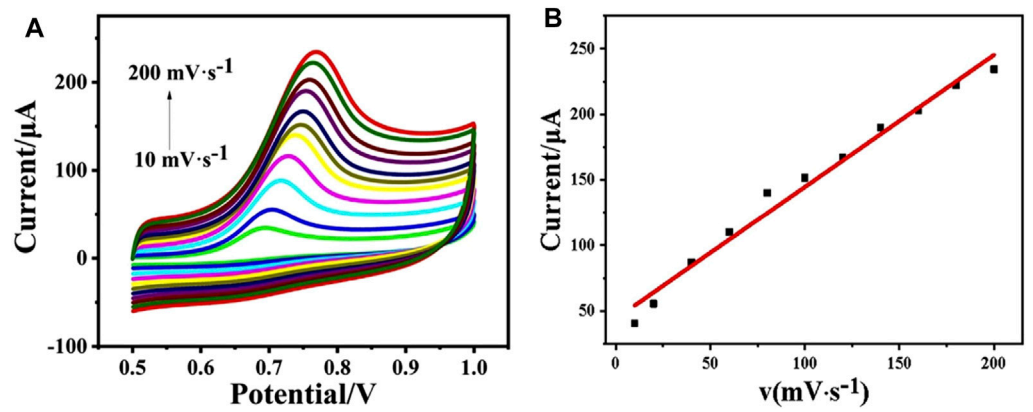

FIGURE 3 | CVs of CeO_2/CNTs/GCE in phosphate buffer (pH = 5.0, 0.1 M) with 1 mM phenol at different scan rates (10–200) mV·s^{-1} **(A)**, and the linear curve of the peak current *vs.* the scan rate **(B)**.

tests were performed on different modified electrodes in 0.1 M phosphate buffer containing 2 mM phenol in **Figure 2B**. It can be found that both CeO_2/GCE (curve b in **Figure 2B**) and CNTs/GCE (curve c in **Figure 2B**) responses are better than the bare GCE (curve a in **Figure 2B**), which means both CeO_2 nanoparticles and carbon nanotubes have a certain catalytic

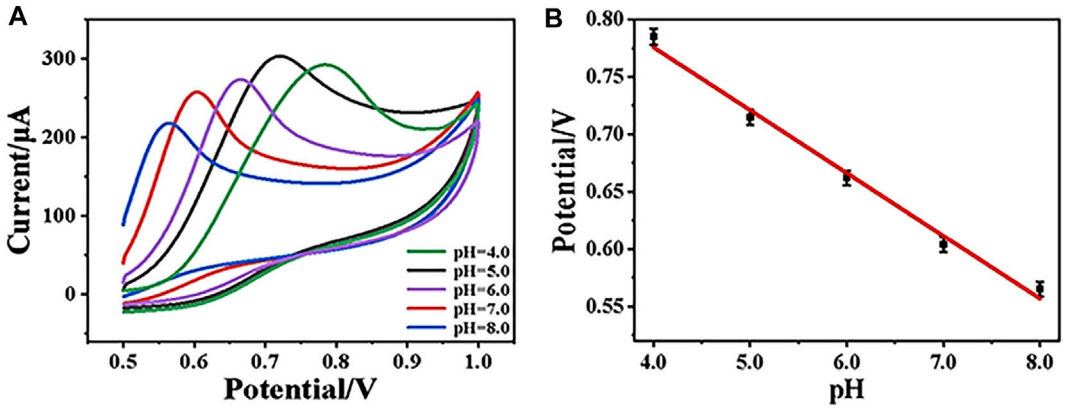

FIGURE 4 | CVs of CeO_2/CNTs/GCE in electrolyte with pH from 4.0 to 8.0 **(A)**, and the linear curve of peak potential *vs*. pH **(B)**.

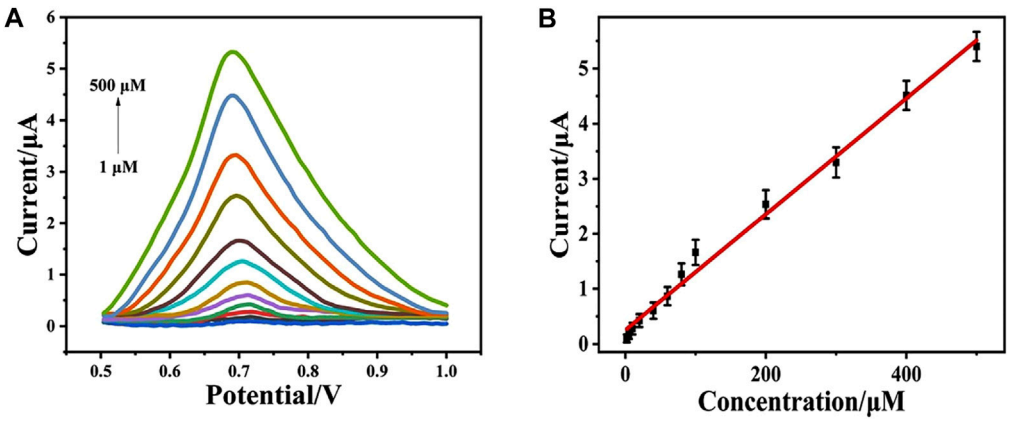

FIGURE 5 | DPVs for CeO_2/CNTs in phosphate buffer (pH = 5.0, 0.1 M) with different concentrations of phenol (1–500 μM) **(A)** and the corresponding plots of the oxidation peak currents at peak potentials *vs*. the concentrations of phenol **(B)**.

TABLE 1 | Comparison of different sensor performance.

Electrodes	Method	Linear Range (μM)	Detection Limit (μM)	Ref
Ni/MWCNT/GCE	CV	10–480	7.07	Yajing Wang et al. (2018)
Pt/g-C_3N_4/GCE	DPV	2–20	0.667	Song et al. (2019)
Na^+-doped g-C_3N_4/CP	CV	1–110	0.23	Yin et al. (2020)
Fe_3O_4/AGO[a]/GCE	DPV	0.45–56, 156–456	0.4	Meng et al. (2019)
Fe_3O_4/MWCNT/GCE	DPV	5–235	4.83	Jiankang Wang et al. (2018)
CeO_2/CNTs/GCE	DPV	1–500	0.3	This work

[a]*AGO, for Amino-Functional Graphene.*

effect toward the electrochemical oxidation of phenol. And CeO_2/CNTs/GCE (curve d in **Figure 2B**) has the largest oxidation peak compared to other modified electrodes. This shows that CeO_2/CNTs nanomaterials have the best electrochemical catalytic effect on phenol. This is due to the synergistic catalysis effect between CeO_2 nanoparticles and CNTs.

Effect of Scan Rate

The electrochemical kinetic behavior of the as-prepared electrode was studied by CV in phosphate buffer (pH = 5.0, 0.1 M) containing 1 mM phenol (**Figure 3**). When the scan rate enlarges from 10 to 200 mV s^{-1}, the oxidation peak current increases accordingly (**Figure 3A**). **Figure 3B** shows the linear curve of peak current value *vs*. the scan rate, where I_p (μA) =

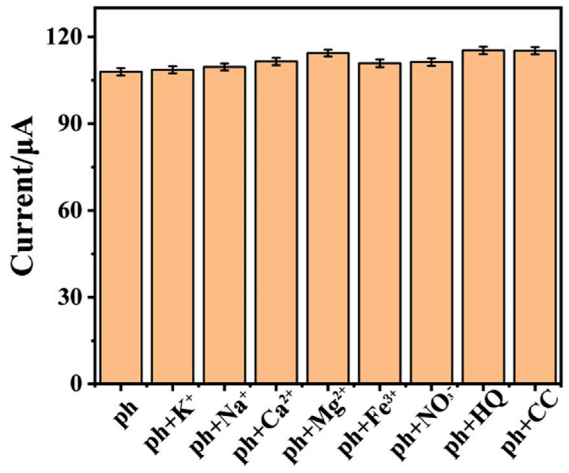

FIGURE 6 | The selectivity study of CeO_2/CNTs/GCE upon addition of different interferences.

44.00961 + 1.00644 v ($mV{\cdot}s^{-1}$) with R^2 = 0.98044. It confirms the kinetic behavior of CeO_2/CNTs/GCE is a surface-controlled process.

Effect of the pH Value

During electrochemical analysis, the pH value of the solution plays an important role for the target determination. Herein, in order to study the effect of pH on the electrochemical performance of CeO_2/CNTs/GCE, the CV behaviors of CeO_2/CNTs/GCE in electrolytes with different pH values were recorded. As shown in **Figure 4A**, when the pH value increases from 4.0 to 8.0, the oxidation peak potential obviously shifts to the lower voltage direction. **Figure 4B** is the linear curve between the pH value of the solution and the oxidation peak potential of phenol, where E_p(V) = 0.99462–0.05473pH with R^2 = 0.98843. Through calculation, the ratio value between the involved number of protons and electrons in the reaction is approximately 1. This is consistent with the transfer number of protons and electrons in the phenol oxidation reaction. At the same time, it is observed in **Figure 4A** that the electrode has the largest response current at pH = 5.0, so subsequent electrochemical experiments are carried out under the optimal pH value of 5.0.

Determination of Phenol

Under the optimal condition, the DPV response of CeO_2/CNTs/GCE upon the addition of different concentration of phenol was recorded. **Figure 5A** is the DPV signals recorded in a phosphate buffer (pH = 5.0) with different phenol concentrations in the range of 1–500 μM. It can be seen from **Figure 5A** that as phenol concentration gradually increases, the corresponding oxidation peak current also increases. Drawn from the DPV curves, the linear equation (**Figure 5B**) between the DPV peak current (I_p) and the phenol concentration (c_{phenol}) is I_p(μA) = 0.252 + 0.105 c_{phenol} (μM) with R^2 = 0.992. The detection limit for phenol is 0.3 μM. In contrast to other published electrochemical sensors, as shown in **Table 1**, CeO_2/CNTs/GCE has a lower detection limit and a wide detection range. It shows that the sensor in this system exhibits satisfied performance.

Selectivity and Reproducibility

In order to study the selectivity of the electrochemical sensor, other common substances are added into 0.1 M phosphate buffer (pH = 5.0) with 1 mM phenol, so as to record interfere effect for the electrochemical response of phenol. Based on the previous report about the anti-interference investigation for phenol detection, potassium chloride, calcium chloride, sodium chloride, iron chloride, sodium nitrate, magnesium chloride, hydroquinone (HQ) and catechol (CC) are chosen for anti-interference research. The result is shown in **Figure 6**. After adding different interferences (0.1 mM) into electrolyte, the electrochemical signal almost remains unchanged as compared to solo phenol detection. This illustrates that the prepared sensor has good selectivity. To investigate the repeatability of the sensor modification, five CeO_2/CNTs modified electrodes were fabricated under the same conditions to measure 100 μM phenol solution. The calculated relative standard deviation (RSD) is 5.76%, which shows that the sensor has good reproducibility. And the stability is studied by measuring the CV response of the sensor in 100 μM phenol solution after stored in a

TABLE 2 | Real sample detection in river water and tap water.

River Water					
Specimen	**Concentration**	**Addition (μM)**	**Found (μM)**	**Recovery (%)**	**RSD (%)**
1	ND[a]	60.0	60.87	101.4	5.4
2	ND	100.0	101.28	101.28	6.5
3	ND	300.0	302.7	100.9	7.8
tap water					
4	ND	60.0	60.6	101.0	5.3
5	ND	100.0	101.2	101.2	6.1
6	ND	300.0	301.9	100.6	7.4

[a]*ND, for Not Detected.*

desiccator for 1 week. Its signal value was 98.6% of the initial value.

Real Sample Detection

DPV determinations of phenol in real samples of river and tap water were estimated using standard addition method to assess the possibility for real sample detection. **Table 2** shows the actual sample detection results. The results show that the sensor in this system has good recovery rate and RSD in both river and tap water analysis. This proves that CeO_2/CNTs/GCE is a reliable and effective platform for phenol detection in real sample.

CONCLUSION

CeO_2/CNTs nanocomposites were synthesized by hydrothermal method. CeO_2 nanoparticles are obtained with cerium nitrate as Ce resource. TEM images reveal that CeO_2 nanoparticles are uniformly dispersed onto the surface of the pre-acidified CNTs. XRD spectra show that all the characteristic peaks of CNT and CeO_2 are appeared in the CeO_2/CNT nanocomposite. The CV responses in 0.1 M KCl electrolyte containing 2 mM $[Fe(CN)_6]^{3-/4-}$ prove that, as compared to the bare CNTs and CeO_2, the CeO_2/CNTs/GCE owes the best electrochemical performance. When applied for the electrochemical catalytic effect towards oxidation of phenol, CeO_2/CNTs nanomaterials have the best catalytic effect on phenol oxidation. The CeO_2/CNTs nanocomposites based electrochemical sensor displays wide linear range, good selectivity, reproducibility and stability, as well as the potential application for real sample detection.

DATA AVAILABILITY STATEMENT

The original contributions presented in the study are included in the article/**Supplementary Material**, further inquiries can be directed to the corresponding author.

AUTHOR CONTRIBUTIONS

CH was responsible for experimental studies and the draft preparation. HH was responsible for the submission, final revision, and financial support to this research. YY and YH were responsible for experiments and characterization. S-JL and H-RW contributed to reviewing and supervising the project. All authors contributed to the article and approved the submitted version.

FUNDING

This work thanks for financial support from the National Natural Science Foundation of China (Grant Nos. 22061019), Jiangxi Provincial Key Laboratory of Functional Molecular Materials Chemistry (20212BCD42018), the Youth Jinggang Scholars Program in Jiangxi Province and Qingjiang Excellent Young Talents Program of Jiangxi University of Science and Technology.

SUPPLEMENTARY MATERIAL

The Supplementary Material for this article can be found online at: https://www.frontiersin.org/articles/10.3389/fchem.2022.907777/full#supplementary-material

REFERENCES

Abbas, A., and Amin, H. M. A. (2022). Silver Nanoparticles Modified Electrodes for Electroanalysis: An Updated Review and a Perspective. *Microchem. J.* 175, 107166. doi:10.1016/j.microc.2021.107166

Alcudia-León, M. C., Lucena, R., Cárdenas, S., and Valcárcel, M. (2011). Determination of Phenols in Waters by Stir Membrane Liquid-Liquid-Liquid Microextraction Coupled to Liquid Chromatography with Ultraviolet Detection. *J. Chromatogr. A* 1218 (16), 2176–2181. doi:10.1016/j.chroma.2011.02.033

Algethami, F. K., Marwani, H. M., Asiri, A. M., and Rahman, M. M. (2018). Comparative Performances of Phenolic Sensors Based on Various CeO2-Carbon Material Nanocomposites for Environmental Safety. *Sr* 38 (4), 467–477. doi:10.1108/sr-11-2017-0235

Billing, B. K. (2021). Carbon Nanotubes and its Potential Application in Sensing. *Chemistryselect* 6 (36), 9571–9590. doi:10.1002/slct.202102636

Curulli, A. (2020). Nanomaterials in Electrochemical Sensing Area: Applications and Challenges in Food Analysis. *Molecules* 25 (23), 5759. doi:10.3390/molecules25235759

Díaz-González, M., Gutiérrez-Capitán, M., Niu, P., Baldi, A., Jiménez-Jorquera, C., and Fernández-Sánchez, C. (2016). Electrochemical Devices for the Detection of Priority Pollutants Listed in the EU Water Framework Directive. *TrAC Trends Anal. Chem.* 77, 186–202. doi:10.1016/j.trac.2015.11.023

Ferrier, D. C., and Honeychurch, K. C. (2021). Carbon Nanotube (CNT)-Based Biosensors. *Biosensors* 11 (12), 486. doi:10.3390/bios11120486

Gruzdev, I. V., Zenkevich, I. G., and Kondratenok, B. M. (2015). Derivatization in Gas Chromatographic Determination of Phenol and Aniline Traces in Aqueous Media. *Russ. Chem. Rev.* 84 (6), 653–664. doi:10.1070/rcr4553

Huang, H., Chen, Y., Chen, Z., Chen, J., Hu, Y., and Zhu, J.-J. (2021). Electrochemical Sensor Based on Ce-MOF/carbon Nanotube Composite for the Simultaneous Discrimination of Hydroquinone and Catechol. *J. Hazard. Mater.* 416, 125895. doi:10.1016/j.jhazmat.2021.125895

Huang, H., and Zhu, J.-J. (2019). The Electrochemical Applications of Rare Earth-Based Nanomaterials. *Analyst* 144 (23), 6789–6811. doi:10.1039/c9an01562k

Huang, W., Tan, Y., Li, D., Du, H., Hu, X., Li, G., et al. (2019). Improved Photo-Luminescence by Co-doped Lithium in the Phosphor System CeO2:Eu3+. *J. Luminescence* 206, 432–439. doi:10.1016/j.jlumin.2018.10.072

Jaworek, K. (2018). Determination of Aromatic Hydrocarbons, Phenols, and Polycyclic Aromatic Hydrocarbons in Water by Stir Bar Sorptive Extraction and Gas Chromatography-Mass Spectrometry. *Anal. Lett.* 51 (4), 469–482. doi:10.1080/00032719.2017.1338712

Liu, J., Zhang, L., Lu, G., Jiang, R., Yan, Z., and Li, Y. (2021). Occurrence, Toxicity and Ecological Risk of Bisphenol A Analogues in Aquatic Environment - A Review. *Ecotoxicol. Environ. Saf.* 208, 111481. doi:10.1016/j.ecoenv.2020.111481

Liu, W., Xie, M., Hao, X., Xu, Q., Jiang, X., Liu, T., et al. (2021). Rapid Synergistic Cloud Point Extraction for Simultaneous Determination of Five Polar Phenols in Environmental Water Samples via High Performance Liquid Chromatography with Fluorescence Detection. *Microchem. J.* 164, 105963. doi:10.1016/j.microc.2021.105963

López-Pacheco, I. Y., Silva-Núñez, A., Salinas-Salazar, C., Arévalo-Gallegos, A., Lizarazo-Holguin, L. A., Barceló, D., et al. (2019). Anthropogenic Contaminants of High

Concern: Existence in Water Resources and Their Adverse Effects. *Sci. Total Environ.* 690, 1068–1088. doi:10.1016/j.scitotenv.2019.07.052

Meng, Z., Li, M., Li, C., Liu, X., and Lei, Z. (2019). A Sensitive Phenol Electrochemical Sensor Based on Magnetic Oxide/Amino-Functional Graphene Nanocomposite. *Int. J. Electrochem. Sci.* 14 (3), 3126–3137. doi:10.20964/2019.03.25

Shao, J., Wang, C., Shen, Y., Shi, J., and Ding, D. (2022). Electrochemical Sensors and Biosensors for the Analysis of Tea Components: A Bibliometric Review. *Front. Chem.* 9, 818461. doi:10.3389/fchem.2021.818461

Singh, A. K., and Chandra, R. (2019). Pollutants Released from the Pulp Paper Industry: Aquatic Toxicity and Their Health Hazards. *Aquat. Toxicol.* 211, 202–216. doi:10.1016/j.aquatox.2019.04.007

Song, B. B., Zhen, Y. F., Yin, H. Y., and Song, X. C. (2019). Electrochemical Sensor Based on Platinum Nanoparticles Modified Graphite-like Carbon Nitride for Detection of Phenol. *J. Nanosci. Nanotechnol.* 19 (7), 4020–4025. doi:10.1166/jnn.2019.16297

Tafete, G. A., Thothadri, G., and Abera, M. K. (2022). "A Review on Carbon Nanotube-Based Composites for Electrocatalyst Applications," in *Fullerenes, Nanotubes and Carbon Nanostructures*, 1–9. doi:10.1080/1536383x.2022.2028278

Tajik, S., Beitollahi, H., Nejad, F. G., Zhang, K., Le, Q. V., Jang, H. W., et al. (2020). Recent Advances in Electrochemical Sensors and Biosensors for Detecting Bisphenol A. *Sensors* 20 (12), 3364. doi:10.3390/s20123364

Wang, J., and Chen, H. (2020). Catalytic Ozonation for Water and Wastewater Treatment: Recent Advances and Perspective. *Sci. Total Environ.* 704, 135249. doi:10.1016/j.scitotenv.2019.135249

Wang, J., Wang, Y., Yao, Z., Liu, C., Xu, Y., and Jiang, Z. (2018). Preparation of Fe3O4/MWCNT Nano-Hybrid and its Application as Phenol Sensor. *Mat. Res. Express* 5 (7), 075003. doi:10.1088/2053-1591/aace38

Wang, Y., Wang, J., Yao, Z., Liu, C., Xie, T., Deng, Q., et al. (2018). Ni Nanoparticle Anchored on MWCNT as a Novel Electrochemical Sensor for Detection of Phenol. *Nano* 13 (11), 1850134. doi:10.1142/s1793292018501345

Xiao, X., Wang, Y., Zhang, D., Gong, J., Ma, J., Yang, T., et al. (2019). Synthesis of Pumpkin-like CeO2 Microstructures and Electrochemical Detection for Phenol. *Inorg. Nano-Metal Chem.* 49 (10), 349–353. doi:10.1080/24701556.2019.1661438

Xiao, X., Wang, Y., Zhang, D., Gong, J., Zhang, Y., Ma, J., et al. (2018). Synthesis of Columnar-shaped CeO 2 and Electrochemical Sensor for Detecting Phenol. *Micro & Nano Lett.* 13 (10), 1382–1385. doi:10.1049/mnl.2018.5163

Yang, X., Li, J., Hou, C., Zhang, Q., Li, Y., and Wang, H. (2020). Skeleton-Structure WS2@CNT Thin-Film Hybrid Electrodes for High-Performance Quasi-Solid-State Flexible Supercapacitors. *Front. Chem.* 8, 442. doi:10.3389/fchem.2020.00442

Yin, H. Y., Zheng, Y. F., and Wang, L. (2020). Electrochemical sensor based on Na^+-doped g-C_3 N_4 for detection of phenol. *Bull. Mat. Sci.* 43 (1), 110. doi:10.1007/s12034-020-2081-0

Zhang, C., and Du, X. (2020). Electrochemical Sensors Based on Carbon Nanomaterial Used in Diagnosing Metabolic Disease. *Front. Chem.* 8, 651. doi:10.3389/fchem.2020.00651

Zhu, J., Zhang, G., Xian, G., Zhang, N., and Li, J. (2019). A High-Efficiency CuO/CeO2 Catalyst for Diclofenac Degradation in Fenton-Like System. *Front. Chem.* 7, 796. doi:10.3389/fchem.2019.00796

Conflict of Interest: The authors declare that the research was conducted in the absence of any commercial or financial relationships that could be construed as a potential conflict of interest.

Publisher's Note: All claims expressed in this article are solely those of the authors and do not necessarily represent those of their affiliated organizations, or those of the publisher, the editors and the reviewers. Any product that may be evaluated in this article, or claim that may be made by its manufacturer, is not guaranteed or endorsed by the publisher.

frontiers | Frontiers in Chemistry

ORIGINAL RESEARCH
published: 18 May 2022
doi: 10.3389/fchem.2022.845617

In Situ Formation of Bi_2MoO_6-Bi_2S_3 Heterostructure: A Proof-Of-Concept Study for Photoelectrochemical Bioassay of L-Cysteine

Hui-Jin Xiao [1], Xiao-Jing Liao [1], Hui Wang [1], Shu-Wei Ren [2], Jun-Tao Cao [1] and Yan-Ming Liu [1]**

[1]Xinyang Key Laboratory of Functional Nanomaterials for Bioanalysis, College of Chemistry and Chemical Engineering, Xinyang Normal University, Xinyang, China, [2]Xinyang Central Hospital, Xinyang, China

A novel signal-increased photoelectrochemical (PEC) biosensor for L-cysteine (L-Cys) was proposed based on the Bi_2MoO_6–Bi_2S_3 heterostructure formed *in situ* on the indium–tin oxide (ITO) electrode. To fabricate the PEC biosensor, Bi_2MoO_6 nanoparticles were prepared by a hydrothermal method and coated on a bare ITO electrode. When L-Cys existed, Bi_2S_3 was formed *in situ* on the interface of the Bi_2MoO_6/ITO electrode by a chemical displacement reaction. Under the visible light irradiation, the Bi_2MoO_6–Bi_2S_3/ITO electrode exhibited evident enhancement in photocurrent response compared with the Bi_2MoO_6/ITO electrode, owing to the signal-increased sensing system and the excellent property of the formed Bi_2MoO_6–Bi_2S_3 heterostructure such as the widened light absorption range and efficient separation of photo-induced electron–hole pairs. Under the optimal conditions, the sensor for L-Cys detection has a linear range from 5.0×10^{-11} to 1.0×10^{-4} mol L^{-1} and a detection limit of 5.0×10^{-12} mol L^{-1}. The recoveries ranging from 90.0% to 110.0% for determining L-Cys in human serum samples validated the applicability of the biosensor. This strategy not only provides a method for L-Cys detection but also broadens the application of the PEC bioanalysis based on *in situ* formation of photoactive materials.

Keywords: photoelectrochemical sensor, Bi_2MoO_6–Bi_2S_3 heterostructure, L-cysteine, *in situ* formation reaction, ion exchange reaction

OPEN ACCESS

Edited by:
Junjie Zhu,
Nanjing University, China

Reviewed by:
Jing Qian,
Jiangsu University, China
Wei Chen,
Fujian Medical University, China

***Correspondence:**
Jun-Tao Cao
jtcao11@163.com
Yan-Ming Liu
liuym9518@sina.com

Specialty section:
This article was submitted to Analytical Chemistry, a section of the journal Frontiers in Chemistry

Received: *30 December 2021*
Accepted: *24 March 2022*
Published: *18 May 2022*

Citation:
Xiao H-J, Liao X-J, Wang H, Ren S-W, Cao J-T and Liu Y-M (2022) In Situ Formation of Bi_2MoO_6-Bi_2S_3 Heterostructure: A Proof-Of-Concept Study for Photoelectrochemical Bioassay of L-Cysteine. Front. Chem. 10:845617. doi: 10.3389/fchem.2022.845617

INTRODUCTION

L-Cysteine (L-Cys), which is involved in the process of protein synthesis, affects the function of protein and plays an important role in the life system (Palego et al., 2015). Its abnormal levels in human serum are associated with lots of diseases, and thus it is considered a significant biomarker. For instance, people with heart disease and liver injury often have low levels of L-Cys in their blood (Wu et al., 2016), whereas people with Alzheimer's disease and cancer often have high levels of L-Cys (Li et al., 2014b; Huang et al., 2018). Therefore, monitoring the content of L-Cys in human body is meaningful. Currently, some analytical methods such as high-performance liquid chromatography (Deáková et al., 2015), mass spectrometry (Li et al., 2014a), fluorescence (Li et al., 2019), colorimetry (Song et al., 2018), and photoelectrochemistry (PEC) (Peng et al., 2020) have been developed for L-Cys detection.

PEC analysis, a fast, efficient, and low background analytical method, has attracted great attention in recent years (Cao et al., 2021; Lv et al., 2021; Zhu et al., 2021). Until now, many sensing principles

have been exploited and adopted for the PEC bioanalysis, such as steric hindrance effect (Wang et al., 2019c; Meng et al., 2020), electron donor/acceptor reaction (Li et al., 2017; Wang et al., 2019b), exciton–plasmon interactions (Ma et al., 2016; Dong et al., 2017), plasmon-enhanced effect (Li et al., 2016; Qiu et al., 2018), and *in situ* growth reaction (Qiu and Tang, 2020). Of these, the signaling mechanism based on the *in situ* growth reaction that acts directly on the electrode is not only simple to operate but also with a low background signal (Hou et al., 2016). For example, on the basis of the reaction between L-Cys and copper compounds, Zhu et al. (2017) constructed a PEC bioassay of L-Cys using a CuO–Cu_2O heterojunction as a photoactive material. By using the reaction between Cu^{2+} and S^{2-} from the WO_3–Au–CdS nanocomposite, Zhang et al. (2019) designed a PEC immunoassay for the prostate-specific antigen. However, these works have always quantified the targets based on the signal decrease, which limits the sensitivity to some extent. By the reaction between Ag^+ and BiOI/Ni electrode, Yu et al. (2019a) constructed a signal-increased biosensing system. In this system, the AgI–Ag–BiOI Z-scheme heterojunction formed *in situ* greatly enhanced the PEC response, achieving satisfied detection sensitivity and stability. Considering the good performance and the few reports of such strategy, exploiting the new *in situ* growth reaction to construct signal-increased sensing systems and extending their applications in PEC bioanalysis are urgent and necessary.

Among various semiconductor materials, bismuth-based semiconductors possess advantages of good biocompatibility and highly visible light response (Chen et al., 2016; Zhou et al., 2017; Yu et al., 2019b). Bi_2MoO_6, featuring non-toxic, good stability, and adjustable morphology (Li et al., 2020), has attracted wide attention. In addition, Bi_2MoO_6 has a layered structure with a $[Bi_2O_2]^{2+}$ layer stuck between two MoO_4^{2-} slabs, which makes it have lots of active surfaces (Wu et al., 2018), while the PEC performance of Bi_2MoO_6 leaves much to be desired due to the rapid recombination between holes and electrons. In order to restrain such recombination, constructing heterostructures is one of the most effective strategies (Wang et al., 2019a; Liao et al., 2021). As a method to form heterojunctions, ion exchange can be excited by the differences in solubility of different substances and helps maintain their original state to a large extent (Wang et al., 2017). Intelligently, both Bi_2MoO_6 and Bi_2S_3 contain bismuth element, and the solubility of Bi_2S_3 is far less than that of Bi_2MoO_6. Based on this, whether the principle of the ion exchange reaction can be used for *in situ* generation of Bi_2MoO_6–Bi_2S_3 heterostructure and construction of a PEC biosensor?

A signal-increased PEC biosensor for L-Cys detection was proposed based on the *in situ* formation of a Bi_2MoO_6–Bi_2S_3 heterostructure on the indium–tin oxide (ITO) electrode. As illustrated in **Scheme 1**, Bi_2MoO_6 nanoparticles were initially coated on a bare ITO electrode. In the existence of L-Cys, Bi_2S_3 was generated *in situ* on the interface of Bi_2MoO_6/ITO by a chemical displacement reaction between sulfur ions from L-Cys and MoO_6^{6-} from Bi_2MoO_6. The compact contact and the matchable band-edge levels of Bi_2MoO_6 and Bi_2S_3 formed a heterostructure, which broadens the light absorption range and effectively restrains the electron–hole recombination, producing an improved photocurrent response. The increased concentrations of L-Cys could generate more amount of Bi_2S_3 on the Bi_2MoO_6/ITO interface, thereby boosting the photocurrent response. By this means, a signal-increased PEC system to quantitatively detect L-Cys was established by measuring the photocurrent change of the photoelectrode.

EXPERIMENTAL

Chemicals and Reagents

Bismuth nitrate ($Bi(NO_3)_3{\cdot}5H_2O$), ethylene glycol (EG), and sodium molybdate ($Na_2MoO_4{\cdot}2H_2O$) were purchased from Macklin Biochemical Co., Ltd. (Shanghai, China). L-Serine (L-Ser), glycine (Gly), and L-tyrosine (L-Tyr) were purchased from Sinopharm Chemical Reagent Co., Ltd. (China). L-Cys and glutathione (GSH) were obtained from Aladdin Reagent Inc. (Shanghai, China). Ascorbic acid (AA), sodium sulfate (Na_2SO_4), and sodium sulfite (Na_2SO_3) were purchased from Sinopharm Chemical Reagent Co., Ltd. (China). Phosphate buffer solution of 0.01 M (PBS, pH 7.4) was prepared with $NaH_2PO_4.2H_2O$, $K_2HPO_4.3H_2O$, and KCl. All chemical reagents were of analytical grade, and all aqueous solutions were prepared with ultrapure water (18.2 MΩ cm).

Apparatus

The PEC system consists of a CHI660E electrochemical workstation (Shanghai Chenhua Apparatus Corporation, China) and a PEAC 200A PEC reaction instrument (Tianjin Aidahengsheng Science-Technology Development Co., Ltd., China). PEC experiments and linear sweep voltammetry (LSV) curves were conducted on the PEC system using a three-electrode system: an ITO electrode with a geometric area of 0.25 cm^2 as the working electrode, a saturated Ag/AgCl electrode as the reference electrode, and a Pt wire as the counter electrode. The electrochemical impedance spectra (EIS) were implemented on a CHI660E electrochemical workstation in 5.0 mM K_3 $[Fe(CN)_6]$/K_4 $[Fe(CN)_6]$ solution containing 0.1 M KCl. The scanning electron microscope (SEM) images were acquired from the Hitachi S-4800 SEM (Tokyo, Japan). UV-visible diffuse reflection spectra were recorded using a PerkinElmer Lambda 950 UV-visible spectrophotometer (United States). X-ray photoelectron spectroscopy (XPS) images were recorded on a K-Alpha X-ray photoelectron spectrometer (Thermo Fisher Scientific Co., Waltham, MA, United States). Fourier transform infrared (FT-IR) spectra were acquired from the Bruker TENZOR 27 spectrophotometer (Bruker Optics, Germany).

Synthesis of Bi_2MoO_6 Nanoparticles

Bi_2MoO_6 was synthesized by a hydrothermal method (Dai et al., 2018). First, 0.4210 g of $Na_2MoO_4{\cdot}2H_2O$ was dissolved in 5 ml of EG under stirring for 0.5 h, and 1.6866 g of $Bi(NO_3)_3{\cdot}5H_2O$ solution was prepared in the same way. After mixing them together, 20 ml of ethanol was added dropwise under stirring. Second, the resulted solution was transferred into the Teflon-lined stainless steel

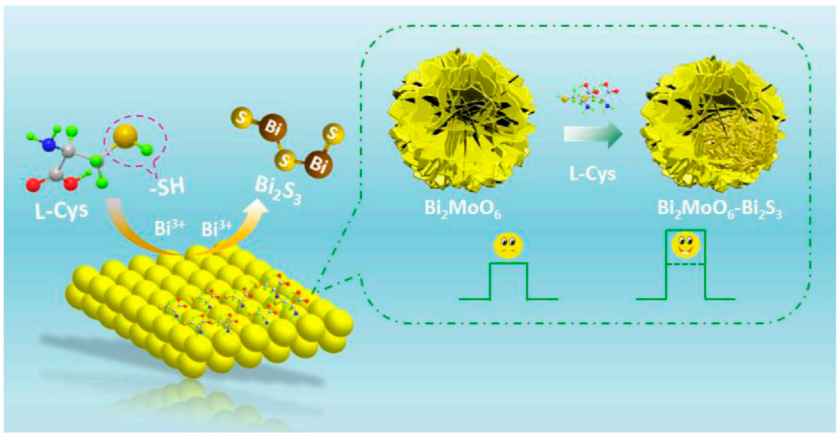

SCHEME 1 | Illustration of the proposed PEC sensor.

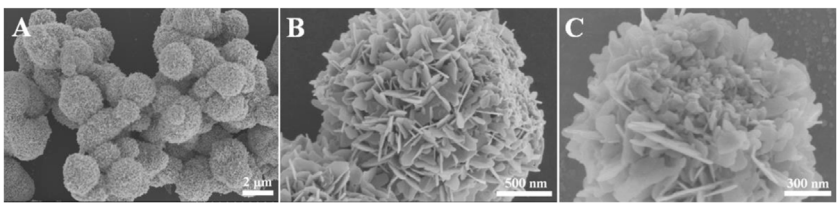

FIGURE 1 | SEM images of Bi_2MoO_6 **(A,B)** and Bi_2MoO_6 after reacting with L-Cys **(C)**.

autoclave, heated to 160°C for 12 h, and cooled to room temperature. Finally, the resultant product collected by centrifugation was washed three times with ethanol as well as water, dried overnight at 80°C, and then annealed at 400°C for 3 h to obtain Bi_2MoO_6 nanoparticles.

Fabrication of the Photoelectrochemical Biosensor

Bi_2MoO_6 suspension of 20 microliters with a concentration of 3 mg ml^{-1} was evenly dropped onto the cleaned ITO electrode and dried at 60°C for 20 min. Afterward, 20 μL of L-Cys solution was cast onto the surface of Bi_2MoO_6/ITO gently. After the reaction at 37°C for 0.5 h, the electrode was washed with water and then immersed in 0.01 M PBS (pH 7.4) containing 0.1 M AA for PEC measurement.

RESULTS AND DISCUSSION

Material Characterization

The morphology of Bi_2MoO_6 was characterized using the SEM. **Figures 1A,B** depicted that Bi_2MoO_6 possessed a nanosheet-assembled spherical structure, and the diameters of the microsphere were less than 3 μm. The stacked sheet structure makes the material have a large specific surface area, which benefits for the subsequent ion exchange reaction and the PEC detection. After incubated with L-Cys, parts of nanosheets granulated on the microsphere of Bi_2MoO_6 (**Figure 1C**), indicating the interaction between Bi_2MoO_6 and L-Cys. Additionally, the elemental mapping images in **Supplementary Figure S1** suggested that Bi, Mo, O, and S elements existed in the material, indicating the reaction between Bi_2MoO_6 and L-Cys.

To characterize the chemical composition and chemical state of Bi_2MoO_6 before and after reacting with L-Cys, XPS analysis was performed. As shown in **Figure 2A**, the elements of Bi, Mo, and O exist in Bi_2MoO_6 samples, whereas a new element of sulfur appeared after the reaction between Bi_2MoO_6 and L-Cys. Peaks in Bi 4f spectra in **Figure 2B** showed that two main peaks at 159.0 and 164.3 eV belong to Bi $4f_{5/2}$ and Bi $4f_{7/2}$ in Bi_2MoO_6 (Jia et al., 2018), shifted to 159.3 and 164.6 eV after the chemical reaction. This chemical shift originated from the formation of new bonds between bismuth and sulfur which changed the original chemical environment of bismuth atoms. The high-resolution XPS spectra of Mo 3d, S 2p, and O 1s of Bi_2MoO_6 after reacting with L-Cys were also conducted. The binding energy at 232.3, 235.4, 159.2, 164.4, and 531.1 eV pictured in **Figures 2C–E** were ascribed to Mo $3d_{5/2}$, Mo $3d_{3/2}$, S $2p_{3/2}$, S $2p_{1/2}$, and O 1 s, respectively. The result further witnessed the *in situ* formation of Bi_2S_3 on Bi_2MoO_6 (Li et al., 2020).

The optical property of Bi_2MoO_6 before and after reacting with L-Cys was studied by FT-IR spectroscopy and UV-vis DRS. As can be seen from **Figure 3A**, the characteristic peak at 712 cm^{-1} existed both in the FT-IR spectrum of Bi_2MoO_6 and

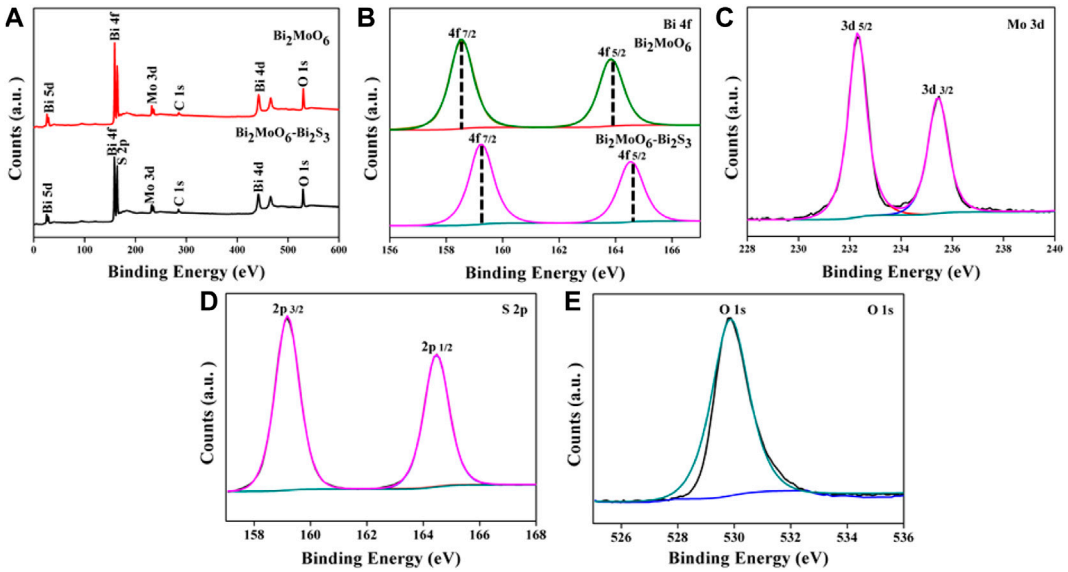

FIGURE 2 | XPS survey spectra of Bi_2MoO_6 before and after reacting with L-Cys **(A)**; high-resolution XPS spectra of Bi 4f **(B)**, Mo 3d **(C)**, S 2p **(D)**, and O 1s **(E)**.

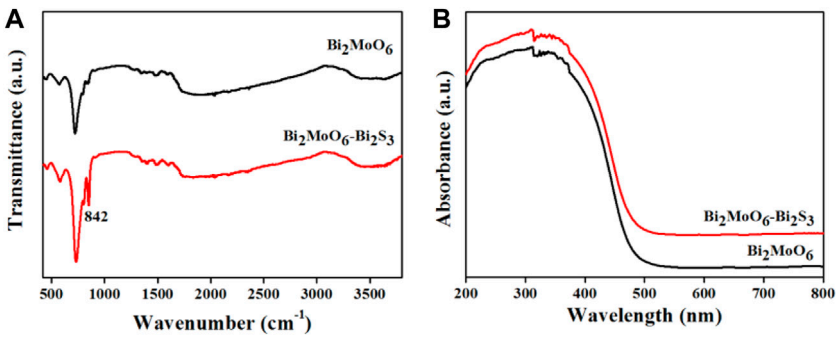

FIGURE 3 | FT-IR spectra of Bi_2MoO_6 and Bi_2MoO_6–Bi_2S_3 **(A)**; UV-vis DRS of Bi_2MoO_6 and Bi_2MoO_6–Bi_2S_3 **(B)**.

that after reacting with L-Cys, attributing to the symmetrical tensile vibration of the top oxygen atom of MoO_6^{6-} (Zhang et al., 2010; Li et al., 2014a; Tian et al., 2015). Compared with the FT-IR spectrum of Bi_2MoO_6, a new peak at 842 cm^{-1} appeared in the chart of Bi_2MoO_6 after the reaction with L-Cys. This new peak corresponds to the stretching vibration of Bi–S, indicative of the formation of Bi_2S_3 through the reaction between Bi_2MoO_6 and L-Cys (Zhao et al., 2017). The UV-vis DRS in **Figure 3B** suggested that the formation of Bi_2MoO_6–Bi_2S_3 widened the absorption range of the light irradiation and thus is benefit for the subsequent PEC analysis.

Condition Optimizations

As a photoactive material to construct the photoelectrode, the concentration of Bi_2MoO_6 plays a crucial effect on the PEC performance of the sensor. The photocurrent signal of the Bi_2MoO_6/ITO electrode constructed with varied concentration of Bi_2MoO_6 was recorded, and the photocurrent response reached a maximum value when the concentration of Bi_2MoO_6 was 3 mg ml^{-1} (**Supplementary Figure S2**). So, 3 mg ml^{-1} Bi_2MoO_6 was used for the subsequent experiments. In addition, the reaction time of Bi_2MoO_6 with L-Cys was optimized. According to **Supplementary Figure S3**, the photocurrent response gradually enhanced with the increase of reaction time, but the signal tended to stabilize when the reaction time reached 30 min. Therefore, 30 min was used as the reaction time.

Electrochemical and Photoelectrochemical Characterizations

To explore the interfacial electrochemical behavior of the biosensor, EIS analysis was conducted. As seen from **Figure 4A**, the bared ITO electrode displayed a small electron-transfer resistance (R_{et}), whereas the Bi_2MoO_6/ITO electrode gave an increased R_{et} because the coating of the semiconductor impedes the electron transfer. After Bi_2MoO_6/ITO

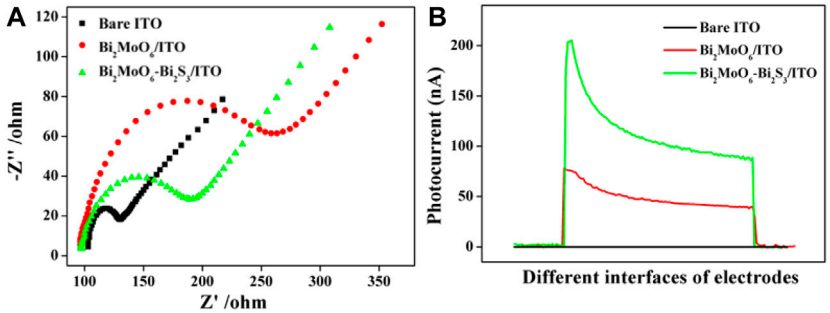

FIGURE 4 | EIS **(A)** and photocurrent intensity **(B)** of bare ITO, Bi_2MoO_6/ITO, and Bi_2MoO_6/ITO after reacting with L-Cys.

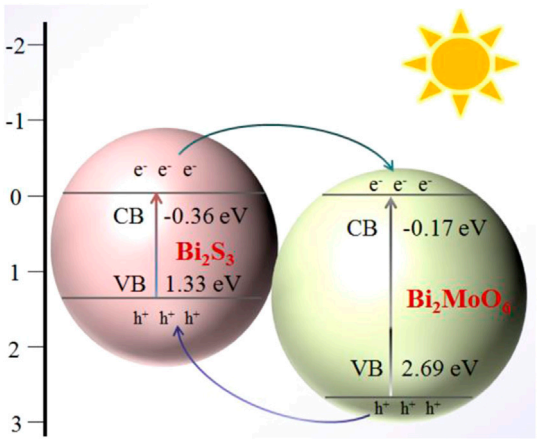

SCHEME 2 | Charge transfer of Bi_2MoO_6–Bi_2S_3 under visible light irradiation.

was incubated with L-Cys, the R_{et} declined. This result may be because the *in situ* formation of Bi_2S_3 on the interface of Bi_2MoO_6/ITO improved the electrical conductivity of the electrode. The photocurrent responses of the sensor at different modification stages were also investigated. As illustrated in **Figure 4B**, almost no PEC response was shown on the bare ITO electrode, while an evident photocurrent response was observed when Bi_2MoO_6 was immobilized on the electrode. After reacting with L-Cys (10 μmol L^{-1}), the Bi_2MoO_6/ITO electrode gave a much stronger photocurrent response. This is because the compact heterostructure formed between Bi_2S_3 and Bi_2MoO_6 by *in situ* formation of Bi_2S_3 on Bi_2MoO_6 and the matchable band-edge levels of Bi_2MoO_6 and Bi_2S_3 could effectively accelerate the transfer of the photo-excited charge carriers. The valence band (VB) and conduction band (CB) energy levels of Bi_2MoO_6 and Bi_2S_3 were determined by the electrochemical method (**Supplementary Figure S4**), and the charge transfer in Bi_2MoO_6–Bi_2S_3 heterostructure is illustrated in **Scheme 2**. Under the light irradiation, the photo-generated electrons in the CB of Bi_2S_3 (−0.36 eV) easily transferred to the CB of Bi_2MoO_6 (−0.17 eV), whereas the holes in the VB of Bi_2MoO_6 (2.69 eV) moved to the VB of Bi_2S_3 (1.33 eV).

Analytical Performance

The PEC response of the Bi_2MoO_6/ITO electrode toward L-Cys was explored. As depicted in **Figure 5A**, the photocurrent intensity enhanced along with the increase in L-Cys concentration. The reason of this variation trend may be that more L-Cys increased the amount of Bi_2S_3 *in situ* formed on the Bi_2MoO_6/ITO electrode, thus facilitating the charge transfer and boosting the photocurrent enhancement. As demonstrated in **Figure 5B**, the photocurrent intensity of the sensor showed a linear relationship with the logarithm of L-Cys concentrations when the concentrations varied in the range of 5.0×10^{-11}–1.0×10^{-4} mol L^{-1}. The linear equation is $I = 128.7 + 8.1 \log C_{L\text{-}Cys}$ ($R^2 = 0.997$). The limit of detection is 5.0×10^{-12} mol L^{-1}. Compared with some reported methods, this method demonstrates high detection sensitivity and a wide linear range for L-Cys (**Table 1**). The excellent performance of the sensor can be attributed to the *in situ* formation of Bi_2MoO_6–Bi_2S_3 heterostructure, which possesses an excellent photoelectric response under light irradiation.

Selectivity, Reproducibility, and Stability

The selectivity of the sensor was evaluated by testing the PEC response of Bi_2MoO_6/ITO toward Gly, L-Tyr, L-Lys, GSH, L-Ser, SO_3^{2-}, and SO_4^{2-} and the mixture of the aforementioned substances with L-Cys (all the aforementioned solutions have a concentration of 5 μmol L^{-1}). As pictured in **Figure 6A**, the PEC responses of Bi_2MoO_6/ITO to Gly, L-Tyr, L-Lys, GSH, and L-Ser showed no obvious change compared with the blank solution, whereas the response of L-Cys as well as the mixture of the aforementioned interferents with L-Cys exhibited an obvious enhancement, thus demonstrating good selectivity. The reproducibility of the sensor was studied by intra-assay and inter-assay of 10 μmol L^{-1} L-Cys. The relative standard deviations (RSDs) of intra-assay by using five Bi_2MoO_6/ITO electrodes in the same batch and inter-assay of the electrodes in different batches were 3.0 and 4.2%, respectively, indicating good reproducibility of the sensor. In addition, the photocurrent response of Bi_2MoO_6/ITO for 100 nmol L^{-1} L-Cys within 4 weeks of storage was investigated to study the stability of the sensor. As shown in **Figure 6B**, the photocurrents show negligible change with RSDs less than 5.1%. The signal of this system for 15 cycles was monitored. In **Supplementary Figure S5**, the photocurrent

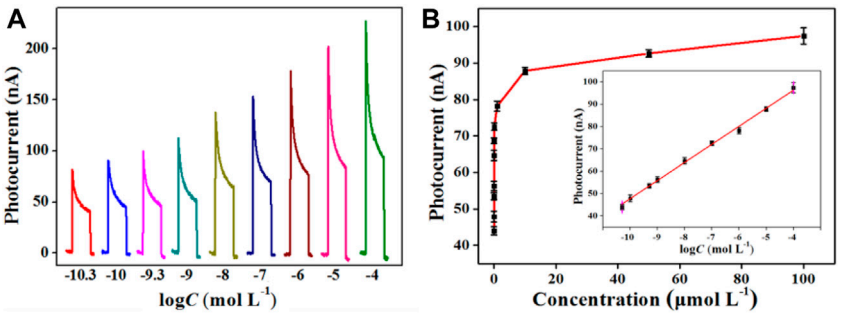

FIGURE 5 | Photocurrent responses of Bi_2MoO_6/ITO corresponding to L-Cys with varied concentrations **(A)**; relationship between photocurrent changes and L-Cys concentrations **(B)**; insert of part B, calibration curve between photocurrents and the logarithm of the L-Cys concentrations.

TABLE 1 | Comparison between this method and the reported methods for L-Cys detection.

Method	Material	Linear range (mol L^{-1})	LOD (mol L^{-1})	Reference
Amperometry	Y_2O_3NPs/N-rGO	1.3×10^{-6}–7.2×10^{-4}	8.0×10^{-7}	Yang et al. (2016)
Fluorescence	Carbon dots	0.0–3.0×10^{-5}	3.4×10^{-10}	Zong et al. (2014)
Colorimetry	CuNPs	0.0–2.5×10^{-5}	1.0×10^{-7}	Ahmed et al. (2016)
Electrochemiluminescence	PtNPs–RubRMs	1.0×10^{-9}–5.0×10^{-4}	3.3×10^{-10}	Wu et al. (2019)
Ratiometric absorption	AuNPs–CS/PLNPs-IBA	1.0×10^{-8}–5.5×10^{-6}	2.2×10^{-9}	Li et al. (2018)
Chronoamperometry	PB–AuNPs–Pd	3.0×10^{-7}–4.0×10^{-4}	1.8×10^{-7}	Pandey et al. (2012)
Cyclic voltammetry	PPy/GQDs@PB	2.0×10^{-7}–1.0×10^{-3}	1.50×10^{-7}	Wang et al. (2016)
PEC	Cu_2SnS_3@SnS_2	1.0×10^{-10}–3.0×10^{-4} 1.0×10^{-8}–1.0×10^{-4}	6.8×10^{-11} 8.5×10^{-9}	Wang et al. (2020)
PEC	Bi_2MoO_6	5.0×10^{-11}–1.0×10^{-4}	5.0×10^{-12}	This work

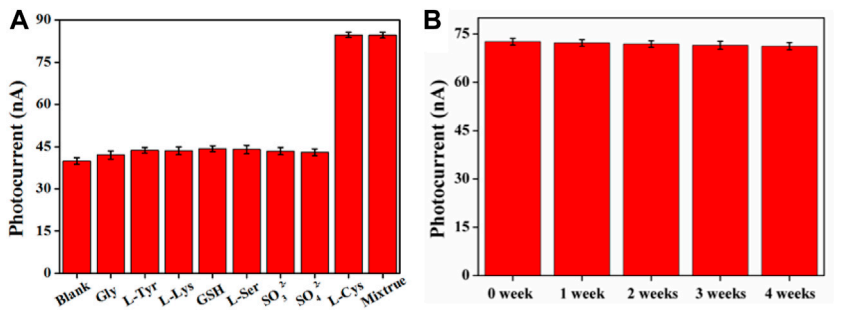

FIGURE 6 | Selectivity **(A)** and stability **(B)** of the PEC sensor.

was stable with a RSD of 3.2%. The data indicate the good stability of the sensor.

Applications

To explore the practical application of the sensor, seven undiluted human serum samples from Xinyang Central Hospital were measured. As listed in **Supplementary Table S1**, compared with the reference method (enzymatic cycling) used by the hospital, the relative errors between the reference method and this method are less than 6.1%, and the RSDs are no more than 6.2%. In addition, the standard addition test results suggest that the recoveries of L-Cys are in the range of 90.0–110.0% with RSDs less than 6.8%, as shown in **Supplementary Table S2**. The aforementioned results show that this method has good accuracy and feasibility.

CONCLUSION

In summary, a facile and signal-increased PEC sensor for L-Cys detection was developed based on the *in situ* formation of Bi_2MoO_6–Bi_2S_3 heterostructure. In virtue of the chemical reaction between L-Cys and Bi_2MoO_6, Bi_2S_3 was formed *in situ*

on the surface of Bi_2MoO_6, and the signal-increased sensing system endowed the sensor with high sensitivity. The Bi_2MoO_6–Bi_2S_3 heterostructure showed effective photoelectric conversion efficiency and thus demonstrated sensitive photocurrent response under light irradiation. Thanks to the fine performance of the Bi_2MoO_6–Bi_2S_3 heterostructure, the sensor for L-Cys achieved excellent performance in sensitivity, selectivity, and stability. The proposed method based on the *in situ* growth reaction not only proposes a new strategy for L-Cys detection but also opens up a new perspective for PEC bioanalysis.

DATA AVAILABILITY STATEMENT

The original contributions presented in the study are included in the article/**Supplementary Material**; further inquiries can be directed to the corresponding authors.

AUTHOR CONTRIBUTIONS

H-JX: conceptualization, methodology, investigation, and writing–original draft. X-JL: investigation. HW: investigation. S-WR: validation. J-TC: conceptualization, methodology, project administration, writing–original draft, and writing–review and editing. Y-ML: conceptualization, methodology, supervision, project administration, writing–original draft, and writing–review and editing.

FUNDING

This work was supported by the National Natural Science Foundation of China (Grant Nos. 21874115 and 21675136), Zhongyuan Thousand Talents Program of Henan Province (Nos. ZYQR201912127 and ZYQR201912177), Key Scientific Research Project of Higher Education Institutions in Henan Province (No. 22A150022), and Nanhu Young Scholar Supporting Program of XYNU.

SUPPLEMENTARY MATERIAL

The Supplementary Material for this article can be found online at: https://www.frontiersin.org/articles/10.3389/fchem.2022.845617/full#supplementary-material

REFERENCES

Ayaz Ahmed, K. B., Sengan, M., P., S. K., and Veerappan, A. (2016). Highly Selective Colorimetric Cysteine Sensor Based on the Formation of Cysteine Layer on Copper Nanoparticles. *Sensors Actuators B: Chem.* 233 (10), 431–437. doi:10.1016/j.snb.2016.04.125

Cao, J.-T., Lv, J.-L., Liao, X.-J., Ma, S.-H., and Liu, Y.-M. (2021). Photogenerated Hole-Induced Chemical-Chemical Redox Cycling Strategy on a Direct Z-Scheme Bi_2S_3/Bi_2MoO_6 Heterostructure Photoelectrode: Toward an Ultrasensitive Photoelectrochemical Immunoassay. *Anal. Chem.* 93 (28), 9920–9926. doi:10.1021/acs.analchem.1c02175

Chen, L., He, J., Liu, Y., Chen, P., Au, C.-T., and Yin, S.-F. (2016). Recent Advances in Bismuth-Containing Photocatalysts with Heterojunctions. *Chin. J. Catal.* 37 (6), 780–791. doi:10.1016/S1872-2067(15)61061-0

Dai, W., Hu, X., Wang, T., Xiong, W., Luo, X., and Zou, J. (2018). Hierarchical CeO_2/Bi_2MoO_6 Heterostructured Nanocomposites for Photoreduction of CO_2 into Hydrocarbons under Visible Light Irradiation. *Appl. Surf. Sci.* 434, 481–491. doi:10.1016/j.apsusc.2017.10.207

Deáková, Z., Ďuračková, Z., Armstrong, D. W., and Lehotay, J. (2015). Two-Dimensional High Performance Liquid Chromatography for Determination of Homocysteine, Methionine and Cysteine Enantiomers in Human Serum. *J. Chromatogr. A* 1408, 118–124. doi:10.1016/j.chroma.2015.07.009

Dong, Y.-X., Cao, J.-T., Wang, B., Ma, S.-H., and Liu, Y.-M. (2017). Exciton-Plasmon Interactions Between CdS@g-C_3N_4 Heterojunction and Au@Ag Nanoparticles Coupled with DNAase-Triggered Signal Amplification: Toward Highly Sensitive Photoelectrochemical Bioanalysis of MicroRNA. *ACS Sustain. Chem. Eng.* 5 (11), 10840–10848. doi:10.1021/acssuschemeng.7b02774

Hou, T., Zhang, L., Sun, X., and Li, F. (2016). Biphasic Photoelectrochemical Sensing Strategy Based on *In Situ* Formation of CdS Quantum Dots for Highly Sensitive Detection of Acetylcholinesterase Activity and Inhibition. *Biosens. Bioelectron.* 75, 359–364. doi:10.1016/j.bios.2015.08.063

Huang, Z., Yang, Y., Long, Y., and Zheng, H. (2018). A Colorimetric Method for Cysteine Determination Based on the Peroxidase-Like Activity of Ficin. *Anal. Methods* 10 (54), 2676–2680. doi:10.1039/C8AY00707A

Jia, Y., Ma, Y., Tang, J., and Shi, W. (2018). Hierarchical Nanosheet-Based Bi_2MoO_6 Microboxes for Efficient Photocatalytic Performance. *Dalton Trans.* 47 (16), 5542–5547. doi:10.1039/C8DT00061A

Laura Betti, L. P., Betti, L., and Giannaccini, G. (2015). Sulfur Metabolism and Sulfur-Containing Amino Acids: I-Molecular Effectors. *Biochem. Pharmacol. (Los Angel)* 04 (7), 1–8. doi:10.4172/2167-0501.1000158

Li, H., Liu, J., Hou, W., Du, N., Zhang, R., and Tao, X. (2014a). Synthesis and Characterization of G-C_3N_4/Bi_2MoO_6 Heterojunctions with Enhanced Visible Light Photocatalytic Activity. *Appl. Catal. B: Environ.* 160-161, 89–97. doi:10.1016/j.apcatb.2014.05.019

Li, J.-J., Qiao, D., Zhao, J., Weng, G.-J., Zhu, J., and Zhao, J.-W. (2019). Fluorescence Turn-On Sensing of L-Cysteine Based on FRET Between Au-Ag Nanoclusters and Au Nanorods. *Spectrochimica Acta A: Mol. Biomol. Spectrosc.* 217, 247–255. doi:10.1016/j.saa.2019.03.092

Li, J., Yang, C., Wang, W.-L., and Yan, X.-P. (2018). Functionalized Gold and Persistent Luminescence Nanoparticle-Based Ratiometric Absorption and TR-FRET Nanoplatform for High-Throughput Sequential Detection of L-Cysteine and Insulin. *Nanoscale* 10 (31), 14931–14937. doi:10.1039/C8NR04414G

Li, R., Yan, R., Bao, J., Tu, W., and Dai, Z. (2016). A Localized Surface Plasmon Resonance-Enhanced Photoelectrochemical Biosensing Strategy for Highly Sensitive and Scatheless Cell Assay Under Red Light Excitation. *Chem. Commun.* 52 (79), 11799–11802. doi:10.1039/C6CC05964C

Li, R., Zhang, Y., Tu, W., and Dai, Z. (2017). Photoelectrochemical Bioanalysis Platform for Cells Monitoring Based on Dual Signal Amplification Using *In Situ* Generation of Electron Acceptor Coupled with Heterojunction. *ACS Appl. Mater. Inter.* 9 (27), 22289–22297. doi:10.1021/acsami.7b06107

Li, W., Xie, P., Chen, J., He, J., Guo, X., Yu, D., et al. (2014b). Quantitative Liquid Chromatography-Tandem Mass Spectrometry Method for Determination of Microcystin-RR and its Glutathione and Cysteine Conjugates in Fish Plasma and Bile. *J. Chromatogr. B* 963, 113–118. doi:10.1016/j.jchromb.2014.05.057

Li, X., Chen, D., Li, N., Xu, Q., Li, H., He, J., et al. (2020). Efficient Reduction of Cr(VI) by a BMO/Bi_2S_3 Heterojunction via Synergistic Adsorption and Photocatalysis Under Visible Light. *J. Hazard. Mater.* 400, 123243. doi:10.1016/j.jhazmat.2020.123243

Liao, X.-J., Xiao, H.-J., Cao, J.-T., Ren, S.-W., and Liu, Y.-M. (2021). A Novel Split-Type Photoelectrochemical Immunosensor Based on Chemical Redox Cycling Amplification for Sensitive Detection of Cardiac Troponin I. *Talanta* 233, 122564. doi:10.1016/j.talanta.2021.122564

Lv, J.-L., Wang, B., Liao, X.-J., Ren, S.-W., Cao, J.-T., and Liu, Y.-M. (2021). Chemical-Chemical Redox Cycling Amplification Strategy in a Self-Powered Photoelectrochemical System: A Proof of Concept for Signal Amplified

Photocathodic Immunoassay. *Chem. Commun.* 57 (15), 1883–1886. doi:10.1039/D0CC08240F

Ma, Z.-Y., Xu, F., Qin, Y., Zhao, W.-W., Xu, J.-J., and Chen, H.-Y. (2016). Invoking Direct Exciton-Plasmon Interactions by Catalytic Ag Deposition on Au Nanoparticles: Photoelectrochemical Bioanalysis with High Efficiency. *Anal. Chem.* 88 (8), 4183–4187. doi:10.1021/acs.analchem.6b00503

Meng, L., Xiao, K., Zhang, X., Du, C., and Chen, J. (2020). A Novel Signal-Off Photoelectrochemical Biosensor for M.SssI MTase Activity Assay Based on GQDs@ZIF-8 Polyhedra as Signal Quencher. *Biosens. Bioelectron.* 150, 111861. doi:10.1016/j.bios.2019.111861

Pandey, P. C., Pandey, A. K., and Chauhan, D. S. (2012). Nanocomposite of Prussian Blue Based Sensor for L-Cysteine: Synergetic Effect of Nanostructured Gold and Palladium on Electrocatalysis. *Electrochimica Acta* 74, 23–31. doi:10.1016/j.electacta.2012.03.179

Peng, J., Huang, Q., Liu, Y., Huang, Y., Zhang, C., and Xiang, G. (2020). Photoelectrochemical Detection of L-Cysteine with a Covalently Grafted ZnTAPc-Gr-based Probe. *Electroanalysis* 32 (6), 1237–1242. doi:10.1002/elan.201900505

Qiu, Z., Shu, J., and Tang, D. (2018). Plasmonic Resonance Enhanced Photoelectrochemical Aptasensors Based on g-C_3N_4/Bi_2MoO_6. *Chem. Commun.* 54 (52), 7199–7202. doi:10.1039/C8CC04211J

Qiu, Z., and Tang, D. (2020). Nanostructure-Based Photoelectrochemical Sensing Platforms for Biomedical Applications. *J. Mater. Chem. B* 8 (13), 2541–2561. doi:10.1039/C9TB02844G

Song, N., Zhu, Y., Ma, F., Wang, C., and Lu, X. (2018). Facile Preparation of Prussian Blue/Polypyrrole Hybrid Nanofibers as Robust Peroxidase Mimics for Colorimetric Detection of L-Cysteine. *Mater. Chem. Front.* 2 (4), 768–774. doi:10.1039/C7QM00571G

Tian, J., Hao, P., Wei, N., Cui, H., and Liu, H. (2015). 3D Bi_2MoO_6 Nanosheet/TiO_2 Nanobelt Heterostructure: Enhanced Photocatalytic Activities and Photoelectochemistry Performance. *ACS Catal.* 5 (8), 4530–4536. doi:10.1021/acscatal.5b00560

Wang, B., Xu, Y.-T., Lv, J.-L., Xue, T.-Y., Ren, S.-W., Cao, J.-T., et al. (2019a). $Ru(NH_3)_6^{3+}$/$Ru(NH_3)_6^{2+}$-Mediated Redox Cycling: Toward Enhanced Triple Signal Amplification for Photoelectrochemical Immunoassay. *Anal. Chem.* 91 (6), 3768–3772. doi:10.1021/acs.analchem.8b05129

Wang, H., Yuan, F., Wu, X., Dong, Y., and Wang, G.-L. (2019b). Enzymatic *In Situ* Generation of Covalently Conjugated Electron Acceptor of PbSe Quantum Dots for High Throughput and Versatile Photoelectrochemical Bioanalysis. *Analytica Chim. Acta* 1058, 1–8. doi:10.1016/j.aca.2019.01.057

Wang, H., Zhang, B., Xi, J., Zhao, F., and Zeng, B. (2019c). Z-Scheme I-BiOCl/CdS with Abundant Oxygen Vacancies as Highly Effective Cathodic Material for Photocathodic Immunoassay. *Biosens. Bioelectron.* 141, 111443. doi:10.1016/j.bios.2019.111443

Wang, L., Liu, Z., Wang, D., Ni, S., Han, D., Wang, W., et al. (2017). Tailoring Heterostructured Bi_2MoO_6/Bi_2S_3 Nanobelts for Highly Selective Photoelectrochemical Analysis of Gallic Acid at Drug Level. *Biosens. Bioelectron.* 94, 107–114. doi:10.1016/j.bios.2017.02.045

Wang, L., Tricard, S., Yue, P., Zhao, J., Fang, J., and Shen, W. (2016). Polypyrrole and Graphene Quantum Dots @ Prussian Blue Hybrid Film on Graphite Felt Electrodes: Application for Amperometric Determination of L-cysteine. *Biosens. Bioelectron.* 77, 1112–1118. doi:10.1016/j.bios.2015.10.088

Wang, Q., Zhou, M., and Zhang, L. (2020). A Dual Mode Photoelectrochemical Sensor for Nitrobenzene and L-Cysteine Based on 3D Flower-Like Cu_2SnS_3@SnS_2 Double Interfacial Heterojunction Photoelectrode. *J. Hazard. Mater.* 382, 121026. doi:10.1016/j.jhazmat.2019.121026

Wu, J., Ran, P., Zhu, S., Mo, F., Wang, C., and Fu, Y. (2019). A Highly Sensitive Electrochemiluminescence Sensor for the Detection of L-Cysteine Based on the Rhombus-Shaped Rubrene Microsheets and Platinum Nanoparticles. *Sensors Actuators B: Chem.* 278, 97–102. doi:10.1016/j.snb.2018.09.066

Wu, L.-L., Wang, L.-Y., Xie, Z.-J., Pan, N., and Peng, C.-F. (2016). Colorimetric Assay of L-Cysteine Based on Peroxidase-Mimicking DNA-Ag/Pt Nanoclusters. *Sensors Actuators B: Chem.* 235, 110–116. doi:10.1016/j.snb.2016.05.069

Wu, Y., Song, M., Wang, Q., Wang, T., and Wang, X. (2018). A Highly Selective Conversion of Toxic Nitrobenzene to Nontoxic Aminobenzene by Cu_2O/Bi/Bi_2MoO_6. *Dalton Trans.* 47 (26), 8794–8800. doi:10.1039/C8DT01536H

Yang, S., Li, G., Wang, Y., Wang, G., and Qu, L. (2016). Amperometric L-Cysteine Sensor Based on a Carbon Paste Electrode Modified with Y_2O_3 Nanoparticles Supported on Nitrogen-Doped Reduced Graphene Oxide. *Microchim. Acta* 183 (4), 1351–1357. doi:10.1007/s00604-015-1737-8

Yu, S.-Y., Mei, L.-P., Xu, Y.-T., Xue, T.-Y., Fan, G.-C., Han, D.-M., et al. (2019a). Liposome-Mediated *In Situ* Formation of AgI/Ag/BiOI Z-Scheme Heterojunction on Foamed Nickel Electrode: A Proof-Of-Concept Study for Cathodic Liposomal Photoelectrochemical Bioanalysis. *Anal. Chem.* 91 (6), 3800–3804. doi:10.1021/acs.analchem.9b00352

Yu, S.-Y., Zhang, L., Zhu, L.-B., Gao, Y., Fan, G.-C., Han, D.-M., et al. (2019b). Bismuth-Containing Semiconductors for Photoelectrochemical Sensing and Biosensing. *Coord. Chem. Rev.* 393, 9–20. doi:10.1016/j.ccr.2019.05.008

Zhang, L., Luo, Z., Zeng, R., Zhou, Q., and Tang, D. (2019). All-Solid-State Metal-Mediated Z-Scheme Photoelectrochemical Immunoassay with Enhanced Photoexcited Charge-Separation for Monitoring of Prostate-Specific Antigen. *Biosens. Bioelectron.* 134, 1–7. doi:10.1016/j.bios.2019.03.052

Zhang, L., Xu, T., Zhao, X., and Zhu, Y. (2010). Controllable Synthesis of Bi_2MoO_6 and Effect of Morphology and Variation in Local Structure on Photocatalytic Activities. *Appl. Catal. B: Environ.* 98 (3–4), 138–146. doi:10.1016/j.apcatb.2010.05.022

Zhao, G., Zhang, D., Yu, J., Xie, Y., Hu, W., and Jiao, F. (2017). Multi-Walled Carbon Nanotubes Modified Bi_2S_3 Microspheres for Enhanced Photocatalytic Decomposition Efficiency. *Ceramics Int.* 43 (17), 15080–15088. doi:10.1016/j.ceramint.2017.08.036

Zhou, Q., Lin, Y., Lu, M., and Tang, D. (2017). Bismuth Ferrite-Based Photoactive Materials for the Photoelectrochemical Detection of Disease Biomarkers Coupled with Multifunctional Mesoporous Silica Nanoparticles. *J. Mater. Chem. B* 5 (48), 9600–9607. doi:10.1039/C7TB02354E

Zhu, J.-H., Feng, Y.-G., Wang, A.-J., Mei, L.-P., Luo, X., and Feng, J.-J. (2021). A Signal-On Photoelectrochemical Aptasensor for Chloramphenicol Assay Based on 3D Self-Supporting AgI/Ag/BiOI Z-Scheme Heterojunction Arrays. *Biosens. Bioelectron.* 181, 113158. doi:10.1016/j.bios.2021.113158

Zhu, Y., Xu, Z., Yan, K., Zhao, H., and Zhang, J. (2017). One-Step Synthesis of CuO-Cu_2O Heterojunction by Flame Spray Pyrolysis for Cathodic Photoelectrochemical Sensing of L-Cysteine. *ACS Appl. Mater. Inter.* 9 (46), 40452–40460. doi:10.1021/acsami.7b13020

Zong, J., Yang, X., Trinchi, A., Hardin, S., and Cole, I. (2014). Carbon Dots as Fluorescent Probes for "Off-On" Detection of Cu^{2+} and L-Cysteine in Aqueous Solution. *Biosens. Bioelectron.* 51, 330–335. doi:10.1016/j.bios.2013.07.042

Conflict of Interest: The authors declare that the research was conducted in the absence of any commercial or financial relationships that could be construed as a potential conflict of interest.

Publisher's Note: All claims expressed in this article are solely those of the authors and do not necessarily represent those of their affiliated organizations, or those of the publisher, the editors, and the reviewers. Any product that may be evaluated in this article, or claim that may be made by its manufacturer, is not guaranteed or endorsed by the publisher.

frontiers | Frontiers in Chemistry

ORIGINAL RESEARCH
published: 09 June 2022
doi: 10.3389/fchem.2022.909670

Mitochondrial-Targeted Ratiometric Fluorescent Probe to Monitor ClO^- Induced by Ferroptosis in Living Cells

*Beidou Feng[1], Kui Wang[1], Zhe Wang[1], Huiyu Niu[1], Ge Wang[2], Yuehua Chen[1] and Hua Zhang[1]**

[1]School of Chemistry and Chemical Engineering, Henan Normal University, Xinxiang, China, [2]School of Basic Medical Sciences, Xinxiang Medical University, Xinxiang, China

Ferroptosis is a type of iron-dependent programmed cell death. Once such kind of death occurs, an individual cell would undergo a series of changes related to reactive oxygen species (ROS) in mitochondria. A mitochondrial-targeted ratiometric fluorescent probe (**MBI-OMe**) was developed to specifically detect ferroptosis-induced ClO^-, whose recognition group is *p*-methoxyphenol, and the mitochondrial-targeted group is benzimidazole. The fluorescence of **MBI-OMe** was first quenched by 30 μM of Fe^{3+}, and then **MBI-OMe** appeared as a ratiometric signal at 477 nm and 392 nm in response to ferroptosis-induced ClO^- in living cells. **MBI-OMe** was successfully used to evaluate changes in ClO^- induced by ferroptosis.

Keywords: fluorescent probe, ClO^-, ratio fluorescence, mitochondria, ferroptosis

OPEN ACCESS

Edited by:
Tingting Zheng,
East China Normal University, China

Reviewed by:
Lin Yuan,
Hunan University, China
Duanping Sun,
Guangdong Pharmaceutical University, China

****Correspondence:***
Hua Zhang
zhanghua1106@163.com

Specialty section:
This article was submitted to Analytical Chemistry, a section of the journal Frontiers in Chemistry

Received: *31 March 2022*
Accepted: *02 May 2022*
Published: *09 June 2022*

Citation:
Feng B, Wang K, Wang Z, Niu H, Wang G, Chen Y and Zhang H (2022) Mitochondrial-Targeted Ratiometric Fluorescent Probe to Monitor ClO^- Induced by Ferroptosis in Living Cells. Front. Chem. 10:909670. doi: 10.3389/fchem.2022.909670

INTRODUCTION

Ferroptosis is a kind of programmed cell death that mainly results from the imbalance between the generation and degradation of intracellular reactive oxygen species (ROS) caused by iron accumulation (Chen et al., 2021; Cheshchevik et al., 2021; Dietrich and Hofmann, 2021). Mitochondria, the centers of energy metabolism in cells, are important sites for ROS generation (Yin et al., 2011; Li et al., 2019). Ferroptosis is frequently accompanied by the accumulation of ROS in mitochondria and is involved in many other pathophysiological processes (Gao et al., 2019; Floros et al., 2021). For example, iron homeostasis plays an important role in the nervous system, and the occurrence of ferroptosis induces neurodegenerative diseases, causing the degradation of mitochondrial activity (Wu et al., 1999; Torti et al., 2013; Zhou et al., 2022). In theory, real-time monitoring of ferroptosis could provide us with necessary information for disease diagnosis. Therefore, it is crucial to develop a selective and sensitive assay for ferroptosis-induced ROS at the solution and cellular levels, which is extremely helpful to understand the physiological and pathological roles of ferroptosis for the living organisms.

Hypochlorous acid, a kind of ROS, usually exists in the form—ClO^- in physiological pH (Li et al., 2012; Ren et al., 2019; Zhang et al., 2020a). Due to its oxidative properties, ClO^- is used in the immune defense system and plays an important role in a variety of physiological and pathological processes. Iron-dependent ferroptosis leads to the accumulation of ClO^- concentrations which can reach the values of 20–400 μM, leading to oxidative damage to mitochondria (Tang et al., 2021; Yan et al., 2021). Fluorescent probes are becoming more and more popular in the detection of biological objects, such as ClO^-, because of their simplicity, high temporal and spatial resolution, and real-time and non-destructive biological imaging. To date, fluorescent probes based on the

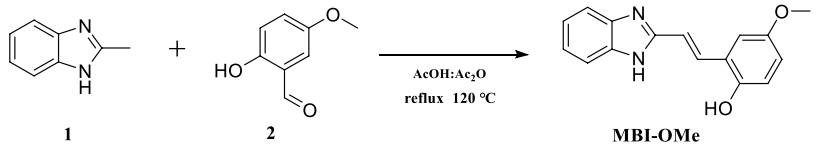

SCHEME 1 | Synthesis of the fluorescent probe MBI-OMe.

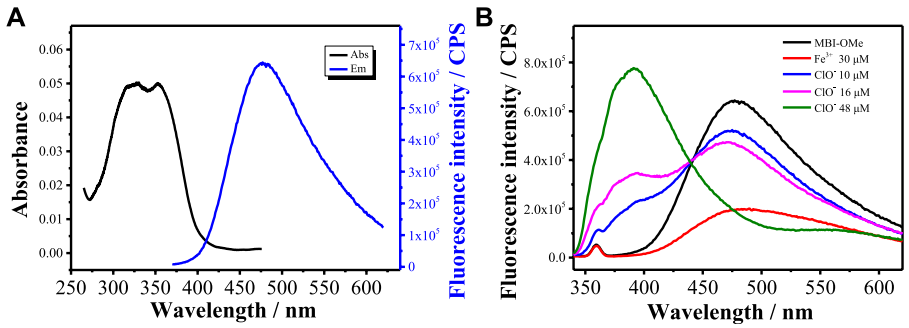

FIGURE 1 | (A) Absorption and emission spectra of MBI-OMe (2.0 μM) in PBS buffer (pH = 7.4). **(B)** Emission spectra of MBI-OMe in response to Fe^{3+} (30 μM) and ClO^- (10, 16, and 48 μM).

detection of ClO^- targeting different organelles have been designed (Wang et al., 2019; Li et al., 2020; Zhang et al., 2020b). In addition, a number of fluorescent probes have been prepared that specifically monitor ClO^- changes in different disease models, such as sepsis, pneumonia, and cancer (Zhang et al., 2018; Long et al., 2020; Wang et al., 2021; Yang et al., 2021). Although these probes can achieve specific, fast, and sensitive responses to ClO^-, these probes cannot be used to detect ClO^- content changes in suborganelles during ferroptosis. This is mainly because the concentration of ClO^- produced by iron death is larger than that in normal cells, so it is impossible to determine whether ferroptosis has occurred. Therefore, it is necessary to develop related reactive oxygen species probes to selectively detect ClO^- and perform fluorescence imaging during ferroptosis.

With this in mind, we developed a mitochondrial-targeted fluorescent probe (**MBI-OMe**) for monitoring the changing behavior of ClO^- that was induced by ferroptosis in this work. **MBI-OMe** was synthesized by linking *p*-methoxyphenol with a fluorophore benzimidazole via a conjugated vinyl bond. *p*-Methoxyphenol can enhance the fluorescence intensity of the probe and act as a selective recognition site for ClO^- (Hu et al., 2014). **MBI-OMe** could coordinate with iron ions to quench fluorescence. When encountering ClO^- induced by ferroptosis, **MBI-OMe** could produce a ratiometric fluorescence signal. More importantly, **MBI-OMe** with a high fidelity signal can be used to monitor ClO^- production that accompanies ferroptosis, suggesting that mitochondrial ClO^- levels may play an important role in ferroptotic cancer cells. Therefore, **MBI-OMe** is considered to be instructive to study the detection of ClO^- in ferroptosis.

MATERIALS AND METHODS

Instruments and Reagents

All chemicals and solvents used in synthesis are commercially purchased, and no further purification is performed unless otherwise stated. The structures were characterized by AVANCE III HD 600MHZ (600 MHz ^{1}H, 151 MHz ^{13}C) NMR spectroscopy. The solvent was DMSO (TMS as an internal standard). An ultrahigh resolution electrospray time-of-flight mass spectrometry system was used to determine the molecular weight of compounds. Fluorescence spectra were determined using the HORIBA FluoroMax-Plus spectrophotometer. The UV spectrum was determined by the Cintra 2020 spectrophotometer of GBC. Fluorescence images were collected using an Olympus FV1200 confocal laser fluorescence microscope.

Synthesis of Probe MBI-OMe

Here, 2-methylbenzimidazole (1.5 mmol, 200.0 mg) and 2-hydroxy-5-methoxybenzaldehyde (1.8 mmol, 276.3 mg) were added to a mixed solution of acetic acid (6.0 ml) and acetic anhydride (12.0 ml). The mixture was obtained after reacting at 120°C for 6 h. The solution was cooled with water; 5 ml of concentrated hydrochloric acid was added overnight, and a solid was obtained by filtration. The yellow solid MBI-OMe was obtained by column chromatography. The yield of the probe MBI-OMe was 64%. ^{1}H NMR (600 MHz, DMSO-d6) δ 12.76 (s, 1H), 9.66 (s, 1H), 7.86 (d, *J* = 16.6 Hz, 1H), 7.52 (dd, *J* = 5.9, 3.2 Hz, 2H), 7.27 (d, *J* = 16.6 Hz, 1H), 7.20–7.10 (m, 3H), 6.85 (d, *J* = 8.8 Hz, 1H), 6.80 (dd, *J* = 8.8, 2.9 Hz, 1H), and 3.75 (s, 3H). ^{13}C NMR (151 MHz, DMSO-d6) δ 152.81, 151.99, 150.39, 130.86,

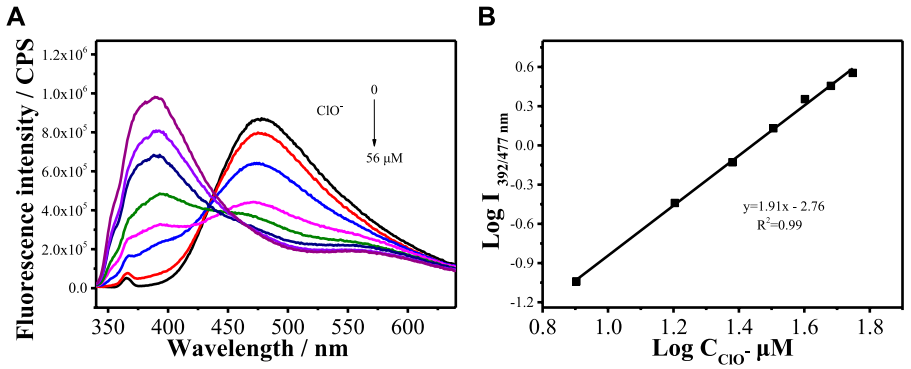

FIGURE 2 | (A) Fluorescence spectra of MBI-OMe (2.0 μM) in PBS buffer (pH = 7.4) containing different concentrations of ClO^- (0–56 μM). **(B)** Linear relationship between MBI-OMe fluorescence intensity and ClO^- concentration.

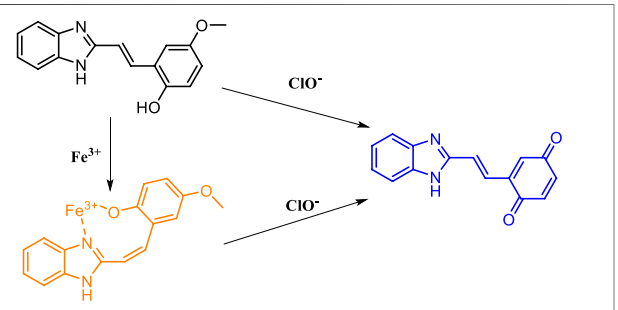

SCHEME 2 | Molecular structure of MBI-OMe and the proposed sensing mechanism.

123.29, 122.49, 117.55, 117.34, 116.86, 111.74, and 55.91. High-resolution mass spectrometry (HRMS) m/z calcd for $C_{16}H_{14}N_2O_2$ $(M + H)^+$: 267.1128; found 267.1156.

Cell Imaging

HL-7702 cells and HepG 2 cells were cultured in Dulbecco's modified Eagle's medium (Corning) containing 10% fetal bovine serum (Sigma Aldrich) and 1% penicillin/streptomycin (Corning). Cell culture conditions were 37°C and 5% CO_2.

For the imaging experiment of exogenous ClO^-, HepG 2 cells were incubated with ClO^- solution of different concentrations for 30 min, and then the probe **MBI-OMe** was added for further incubation for 30 min. In the endogenous ClO^- imaging experiment, lipopolysaccharides (LPSs) were added to HepG 2 cells and incubated for 12 h; phorbol-12-myristate-13-acetate (PMA) was added for further incubation for 90 min, and then the probe was added for 30 min for imaging. The cells treated with LPS and PMA were incubated with N-acetylcysteine (NAC) and 4-azidobenzohydrazide (ABH) for 1 h and then incubated with **MBI-OMe** for 30 min for imaging. The HepG 2 cells were incubated with erastin for 6 h to construct the ferroptosis cell model and then incubated with the probe for 30 min for imaging. Deferoxamine was added and incubated for 6 h, and **MBI-OMe** was added and incubated for 30 min before imaging.

RESULTS AND DISCUSSIONS

Design and Synthesis of MBI-OMe

In order to monitor the changing behavior of ClO^- during ferroptosis, a ClO^- responsive fluorescent probe (**MBI-OMe**) was designed. In molecular design, the *p*-methoxyphenol group was selected as the recognition site because it can produce benzoquinone through ClO^- oxidation. In order to realize the detection of ClO^- in the process of ferroptosis, imidazole and hydroxyl groups, which can complex with Fe^{3+}, were introduced into the probe as the turn-on signal for the detection of ferroptosis. To form the typical intramolecular charge transfer (ICT) molecular system, **MBI-OMe** was synthesized by connecting *p*-methoxyphenol as the electron-donor group, benzimidazole compound as the electron-acceptor group, and vinyl as the conjugated bridge. When the probe is complexed with Fe^{3+}, the ICT effect of the probe is weakened, and the fluorescence is quenched. When the system encounters ClO^-, the complex system is destroyed and the fluorescence is recovered. As the ClO^- concentration increased, methoxyphenol was oxidized to benzoquinone, thereby exhibiting a proportional fluorescence signal.

As shown in **Scheme 1**, the synthetic route of **MBI-OMe** is simple, and **MBI-OMe** is obtained by the Knoevenagel condensation reaction of 2-methylbenzimidazole (compound 1) and 2-hydroxy-5-methoxy-benzaldehyde (compound 2) directly. The chemical structure of **MBI-OMe** was characterized by ^1H NMR, ^{13}C NMR, and ESI-TOF-MS.

SPECTRAL PROPERTIES

The optical properties of the **MBI-OMe** (2.0 μM) were investigated by UV-vis absorption and fluorescence spectroscopy in PBS buffer (pH = 7.4). As shown in **Figure 1A**, **MBI-OMe** showed bright fluorescence at 477 nm that was excited by the one-photon light source ($\lambda_{ex}^{\text{one-photon}}$ = 325 nm, Φ = 0.28) and the two-photon light source ($\lambda_{ex}^{\text{two-photon}}$ = 750 nm, **Supplementary Figure S1**). When **MBI-OMe** encountered 30 μM of Fe^{3+} in PBS buffer (pH = 7.4), the

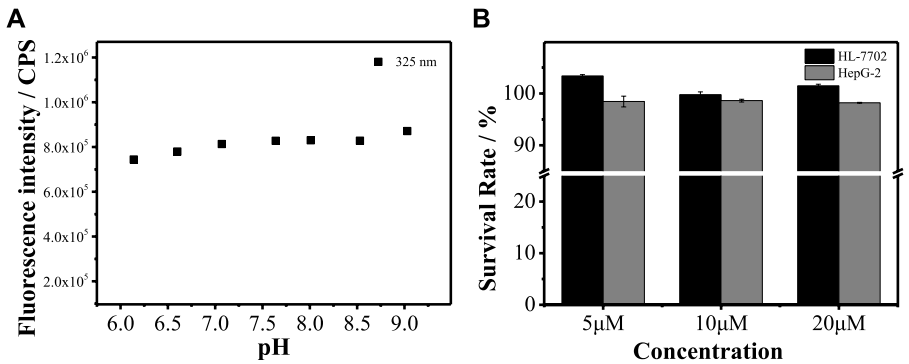

FIGURE 3 | (A) Fluorescence signal changes of MBI-OMe (2.0 μM) at different pH (6.0–9.0). **(B)** Cytotoxicity of MBI-OMe at different concentrations (5, 10, and 20 μM).

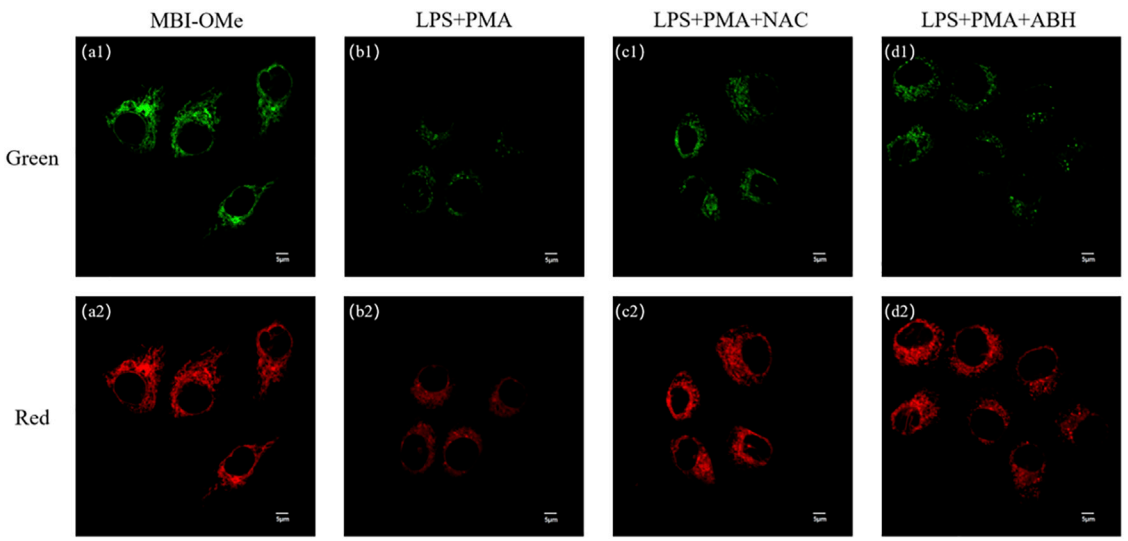

FIGURE 4 | (A) Imaging of MBI-OMe in HepG 2 cells. **(B)** Cell imaging of MBI-OMe performed after LPS (1.0 μg/ml, 12 h) and PMA (10 mg/ml, 90 min) were added to the cells. **(C)** Cell imaging of MBI-OMe after incubation with NAC (2.0 mM, 1 h) under the condition of **(B)**. **(D)** Cell imaging of MBI-OMe after incubation with ABH (200 μM, 1 h) under the condition of **(B)**. Green: 415–450 nm; Red: 460–560 nm; MBI-OMe: 30 μM.

fluorescence decreased to 1.5×10^5 at 477 nm (Φ = 0.015) within 1 min (**Supplementary Figure S2**). Also, the dosage of Fe^{3+} for the **MBI-OMe** is 30 μM, which is far greater than the endogenous amount of Fe^{3+} in living organisms. Therefore, the Fe^{3+} concentration increased to 30 μM when ferroptosis occurred (Hentze et al., 2010). Due to the complexation of a large amount of Fe^{3+} with **MBI-OMe**, resulting in the change of the intramolecular conjugated system, the fluorescence intensity is quenched (Zhao et al., 2016). After that, by adding ClO^- into the system, the fluorescence of **MBI-OMe** at 477 nm (Φ = 0.25) was recovered within 1 min (**Supplementary Figure S2**). When ClO^- was continually added into the system, fluorescence strength at 477 nm decreased and was accompanied by another increase at a new emission peak (392 nm, **Figure 1B**).

Figure 2A shows the fluorescence spectra of **MBI-OMe** in PBS buffer (pH = 7.4) containing different concentrations of ClO^- (0–56 μM) at an excitation wavelength of 325 nm. With the increase of ClO^- concentration, the fluorescence at 477 nm gradually weakened, a new fluorescence emission peak appeared at 392 nm, and the fluorescence intensity gradually increased with the increase of ClO^- concentration. The emission peak at 392 nm increased 40-fold after the addition of 56 μM ClO^-. As can be seen in **Figure 2B**, the fluorescence intensity has a good linear relationship with the concentration of ClO^- in the range of 8–56 μM. The detection limit of **MBI-OMe** for ClO^- is 1.2 μM. The results showed that the probe could interact with ClO^- with good sensitivity.

To evaluate the selectivity of **MBI-OMe** for ClO^-, the fluorescence responses to various analytes, including

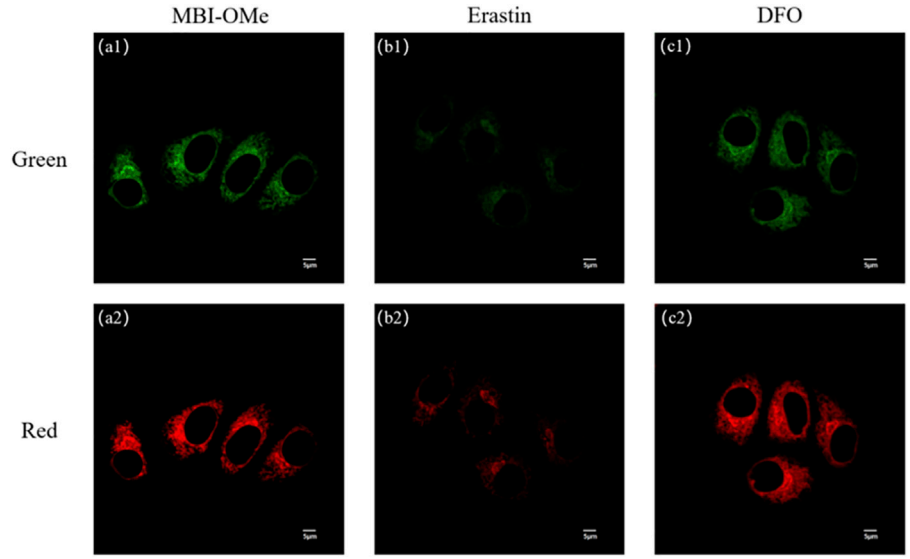

FIGURE 5 | (A) Imaging of MBI-OMe in HepG 2 cells. **(B)** Cell imaging of MBI-OMe performed after erastin (10 μM, 6 h) was added to the cells. **(C)** Cell imaging of MBI-OMe after incubation with DFO (100 μM, 6 h) under the condition of **(B)**. Green: 415–450 nm; Red: 460–560 nm; MBI-OMe: 30 μM.

biologically reactive oxygen species, amino acids, and cationic and anionic species, were investigated in PBS buffer (pH = 7.4). As shown in **Supplementary Figure S4**, there were no significant changes in other bioactive species, except for the ClO^--induced spectra change. Meanwhile, in order to prove that **MBI-OMe** can have good photostability *in vivo*, the fluorescence intensity of the PBS solution containing **MBI-OMe** after illumination at different times was recorded. **Supplementary Figure S5** shows that the fluorescence intensity decreases slightly with the increase of time, but the intensity remains above 80% after 5 h, which indicates that **MBI-OMe** has good photostability. The results showed that **MBI-OMe** has a good fluorescence response to ClO^-, which is very suitable for biological applications.

SENSING MECHANISM

Based on the aforementioned spectroscopic evidence, a possible mechanism for the detection of ClO^- and Fe^{3+} by **MBI-OMe** was proposed (**Scheme 2**). The sensing mechanism was detected by adding ClO^- and Fe^{3+} to the **MBI-OMe** probe solution. The reaction solution was detected by high-resolution mass spectrometry (HRMS). When Fe^{3+} (30 μM) was added into **MBI-OMe** (2.0 μM), the mass spectrum showed a peak at 267.1126 M/z [M + H^+]. This indicated that the probe only complexed with Fe^{3+} without changing the molecular structure. When ClO^- (20 μM) was added into it, there were two peaks showed by the mass spectrum at 267.1121 M/z [M + H^+] and 249.0663 M/z [M-H^+]. This indicated that with the addition of ClO^-, the phenolic hydroxyl and methoxy groups in the probe were oxidized to benzoquinone. In addition, mass spectrometry analysis showed 251.0790 M/z [M + H^+] after adding amounts of ClO^- to the probe-containing solution (**Supplementary Figure S6**). It was further proved that *p*-methoxyphenol was oxidized to benzoquinone in the probe, and a proportional fluorescence signal was generated.

Chemical Stability and Biological Toxicity

To verify whether **MBI-OMe** can be used for bioimaging detection, the chemical stability of **MBI-OMe** in the physiological pH range was first investigated. As shown in **Figure 3A**, it can be seen that the fluorescence intensity of **MBI-OMe** remains almost unchanged with the change of pH 6.0–9.0. This indicates that **MBI-OMe** has good chemical stability and can be used for testing in a physiological environment. To further illustrate the feasibility of the probe for the imaging detection in living cells, the cytotoxicity was measured by MTT assay in HL-7702 cells and HepG 2 cells. **Figure 3B** showed that the cell viability was maintained above 95% under incubation by different concentrations of **MBI-OMe**, showing good cell viability. **MBI-OMe** proved to be a potential tool for detecting and imaging in living cells.

Ratiometric Fluorescence Detection and Imaging of ClO^-

We first explored whether this probe could be used for imaging (**Supplementary Figure S7A**) in living cells. When HepG 2 cells were incubated with **MBI-OMe**, there appeared a distinct fluorescence and presented good regional characteristics. The colocalization experiments demonstrated that **MBI-OMe** was able to localize in the mitochondria (**Supplementary Figure S7**). In addition, two-photon imaging in cells showed that the probe had a good two-photon effect (**Supplementary Figure S8**). These results suggested that **MBI-OMe** can be used to image intracellular mitochondria. By adding ClO^- to cells, it was

demonstrated that the probe could detect and image ClO^- in cells (**Supplementary Figure S9**). Subsequently, the endogenous ClO^- production was induced in cells by adding lipopolysaccharide and phorbol, as shown in **Figures 4A,B**. The fluorescence of **MBI-OMe** in both the red channel (460–560 nm) and green channel (415–450 nm) was weakened. This may be due to the fact that the excitation wavelength is not optimal (Ex = 405 nm, the best excitation wavelength is 325 nm), which leads to the decreased fluorescence intensity of the probe in the green channel. In order to verify whether endogenous ClO^- responded to the probe, NAC and ABH were added to cells, as shown in **Figures 4C,D**. When ClO^- was removed from cells, the probe was added for incubation, and the fluorescence intensity was basically the same as that of the probe alone. The aforementioned experiments indicate that **MBI-OMe** may be an effective tool for detecting and imaging ClO^- in mitochondria of ferroptosis cells.

Changes of ClO^- During Cell Ferroptosis

Ferroptosis is a novel mode of cell death distinct from apoptosis, necrosis, and autophagy (Dixon et al., 2012; Li, 2020). The most characteristic feature of ferroptosis is the need for iron, and some iron chelators can inhibit this process. Studies have shown that the production of ROS is observed during ferroptosis (Li et al., 2019; Chen et al., 2020; Zhang et al., 2020a). Here, the ability of **MBI-OMe** to image ClO^- during ferroptosis in HepG 2 cells was further investigated by constructing a cellular ferroptosis model. As shown in **Figure 5**, the fluorescence intensity of the green and red channels was significantly attenuated after treatment of cells with erastin, a classic iron ion inducer (Dixon et al., 2012), for 6 h, compared with untreated HepG 2 cells. Deferoxamine (DFO, an inhibitor of ferroptosis) significantly inhibits the onset of ferroptosis (Dixon et al., 2012). When DFO was added to the treated cells and incubated, the fluorescence intensity of the probe was basically the same as that of the probe only, which was the same as that of the *in vitro* spectroscopic experiment and intracellular ClO^- imaging experiment. The aforementioned results suggest that the probe **MBI-OMe** can be used as an imaging sensor for ClO^- changes during ferroptosis in cancer cells.

CONCLUSION

In summary, **MBI-OMe** based on benzimidazole was developed for selective detection of ClO^- in mitochondria during ferroptosis. The *p*-methoxyphenol group is used as the specific reaction site of ClO^-, and methylbenzimidazole is used for the mitochondrial targeting. **MBI-OMe** appears as a fluorescence at 477 nm. **MBI-OMe** can form a complex with Fe^{3+}, and its fluorescence also was quenched (Φ = 0.015). More importantly, **MBI-OMe** can not only complex with Fe^{3+} for fluorescence quenching but also show a good ratiometric fluorescence signal to ClO^- that was caused by ferroptosis stimulation. The fluorescence intensity ratio (I_{392} nm/I_{477} nm) was linearly related to the concentration of ClO^- with a detection limit of 1.2 μM. This can mainly be attributed to the formation of benzoquinone through the redox reaction between ClO^- and *p*-methoxyphenol. **MBI-OMe** has good two-photon properties, which is beneficial to the detection and imaging of ClO^- in ferroptosis. This work provides an effective tool for the detection of ferroptosis and its ClO^--related diseases. In this work, the probe was able to achieve a proportional fluorescence signal *in vitro* to detect ClO^-. However, the excitation light wavelength is in the range of 275–400 nm in one-photon mode. Although the probe has two-photon properties, in order to broaden the application of this type of probe in biological detection and imaging, it is still necessary to improve the wavelength of the probe under single-photon excitation. Therefore, more long-wavelength fluorescent probes need to be designed for the diagnosis of biological diseases.

DATA AVAILABILITY STATEMENT

The original contributions presented in the study are included in the article/**Supplementary Material**; further inquiries can be directed to the corresponding author.

AUTHOR CONTRIBUTIONS

All the authors listed have made a substantial, direct, and intellectual contribution to the work and approved it for publication.

FUNDING

This work was supported by the National Natural Science Foundation of China (U21A20314, 22107089, 21722501, and 21803018), National Natural Science Foundation of Henan Province (222300420207), and Postdoctoral Research Funding (5101219470256).

ACKNOWLEDGMENTS

HZ wishes to thank the Zhongyuan High Level Talents Special Support Plan-Science and Technology Innovation Leading Talents (204200510006); GW wishes to thank the National Natural Science Foundation of Henan Province (212300410226).

SUPPLEMENTARY MATERIAL

The Supplementary Material for this article can be found online at: https://www.frontiersin.org/articles/10.3389/fchem.2022.909670/full#supplementary-material

REFERENCES

Chen, X., Yu, C., Kang, R., Kroemer, G., and Tang, D. (2021). Cellular Degradation Systems in Ferroptosis. *Cell Death Differ.* 28, 1135–1148. doi:10.1038/s41418-020-00728-1

Chen, Y.-C., Oses-Prieto, J. A., Pope, L. E., Burlingame, A. L., Dixon, S. J., and Renslo, A. R. (2020). Reactivity-based Probe of the Iron(II)-dependent Interactome Identifies New Cellular Modulators of Ferroptosis. *J. Am. Chem. Soc.* 142, 19085–19093. doi:10.1021/jacs.0c06710.1021/jacs.0c06709

Cheshchevik, V. T., Krylova, N. G., Cheshchevik, N. G., Lapshina, E. A., Semenkova, G. N., and Zavodnik, I. B. (2021). Role of Mitochondrial Calcium in Hypochlorite Induced Oxidative Damage of Cells. *Biochimie* 184, 104–115. doi:10.1016/j.biochi.2021.02.009

Dietrich, C., and Hofmann, T. G. (2021). Ferroptosis Meets Cell-Cell Contacts. *Cells* 10, 2462. doi:10.3390/cells10092462

Dixon, S. J., Lemberg, K. M., Lamprecht, M. R., Skouta, R., Zaitsev, E. M., Gleason, C. E., et al. (2012). Ferroptosis: an Iron-dependent Form of Nonapoptotic Cell Death. *Cell* 149, 1060–1072. doi:10.1016/j.cell.2012.03.042

Floros, K. V., Cai, J., Jacob, S., Kurupi, R., Fairchild, C. K., Shende, M., et al. (2021). MYCN-amplified Neuroblastoma Is Addicted to Iron and Vulnerable to Inhibition of the System Xc-/glutathione axis. *Cancer Res.* 81, 1896–1908. doi:10.1158/0008-5472.CAN-20-1641

Gao, M., Yi, J., Zhu, J., Minikes, A. M., Monian, P., Thompson, C. B., et al. (2019). Role of Mitochondria in Ferroptosis. *Mol. Cell* 73, 354–363. doi:10.1016/j.molcel.2018.10.042

Hentze, M. W., Muckenthaler, M. U., Galy, B., and Camaschella, C. (2010). Two to Tango: Regulation of Mammalian Iron Metabolism. *Cell* 142, 24–38. doi:10.1016/j.cell.2010.06.028

Hu, J. J., Wong, N.-K., Gu, Q., Bai, X., Ye, S., and Yang, D. (2014). HKOCl-2 Series of Green BODIPY-Based Fluorescent Probes for Hypochlorous Acid Detection and Imaging in Live Cells. *Org. Lett.* 16, 3544–3547. doi:10.1021/ol501496n

Li, H., Cao, Z., Moore, D. R., Jackson, P. L., Barnes, S., Lambeth, J. D., et al. (2012). Microbicidal Activity of Vascular Peroxidase 1 in Human Plasma via Generation of Hypochlorous Acid. *Infect. Immun.* 80, 2528–2537. doi:10.1128/IAI.06337-11

Li, H., Shi, W., Li, X., Hu, Y., Fang, Y., and Ma, H. (2019). Ferroptosis Accompanied by OH Generation and Cytoplasmic Viscosity Increase Revealed via Dual-Functional Fluorescence Probe. *J. Am. Chem. Soc.* 141, 18301–18307. doi:10.1021/jacs.9b09722

Li, M.-Y., Li, K., Liu, Y.-H., Zhang, H., Yu, K.-K., Liu, X., et al. (2020). Mitochondria-immobilized Fluorescent Probe for the Detection of Hypochlorite in Living Cells, Tissues, and Zebrafishes. *Anal. Chem.* 92, 3262–3269. doi:10.1021/acs.analchem.9b05102

Li, Z. (2020). Imaging of Hydrogen Peroxide (H2O2) during the Ferroptosis Process in Living Cancer Cells with a Practical Fluorescence Probe. *Talanta* 212, 120804. doi:10.1016/j.talanta.2020.120804

Long, L., Han, Y., Liu, W., Chen, Q., Yin, D., Li, L., et al. (2020). Simultaneous Discrimination of Hypochlorite and Single Oxygen during Sepsis by a Dual-Functional Fluorescent Probe. *Anal. Chem.* 92, 6072–6080. doi:10.1021/acs.analchem.0c00492

Ren, M., Li, Z., Deng, B., Wang, L., and Lin, W. (2019). Single Fluorescent Probe Separately and Continuously Visualize H2S and HClO in Lysosomes with Different Fluorescence Signals. *Anal. Chem.* 91, 2932–2938. doi:10.1021/acs.analchem.8b05116

Tang, D., Chen, X., Kang, R., and Kroemer, G. (2021). Ferroptosis: Molecular Mechanisms and Health Implications. *Cell Res.* 31, 107–125. doi:10.1038/s41422-020-00441-1

Torti, S. V., and Torti, F. M. (2013). Iron and Cancer: More Ore to Be Mined. *Nat. Rev. Cancer* 13, 342–355. doi:10.1038/nrc3495

Wang, L., Liu, J., Zhang, H., and Guo, W. (2021). Discrimination between Cancerous and Normal Cells/tissues Enabled by a Near-Infrared Fluorescent HClO Probe. *Sensors Actuators B Chem.* 334, 129602. doi:10.1016/j.snb.2021.129602

Wang, Z., Zhang, Q., Liu, J., Sui, R., Li, Y., Li, Y., et al. (2019). A Twist Six-Membered Rhodamine-Based Fluorescent Probe for Hypochlorite Detection in Water and Lysosomes of Living Cells. *Anal. Chim. Acta* 1082, 116–125. doi:10.1016/j.aca.2019.07.046

Wu, K.-J., Polack, A., and Dalla-Favera, R. (1999). Coordinated Regulation of Iron-Controlling Genes, H-Ferritin and IRP2 , by C-MYC. *Science* 283, 676–679. doi:10.1126/science.283.5402.676

Yan, H.-f., Zou, T., Tuo, Q.-z., Xu, S., Li, H., Belaidi, A. A., et al. (2021). Ferroptosis: Mechanisms and Links with Diseases. *Sig Transduct. Target Ther.* 6, 49. doi:10.1038/s41392-020-00428-9

Yang, X., Liu, J., Xie, P., Han, X., Zhang, D., Ye, Y., et al. (2021). Visualization of Biothiols and HClO in Cancer Therapy via a Multi-Responsive Fluorescent Probe. *Sensors Actuators B Chem.* 347, 130620. doi:10.1016/j.snb.2021.130620

Yin, H., Xu, L., and Porter, N. A. (2011). Free Radical Lipid Peroxidation: Mechanisms and Analysis. *Chem. Rev.* 111, 5944–5972. doi:10.1021/cr200084z

Zhang, H.-C., Tian, D.-H., Zheng, Y.-L., Dai, F., and Zhou, B. (2021). Designing an ESIPT-Based Fluorescent Probe for Imaging of Hydrogen Peroxide during the Ferroptosis Process. *Spectrochimica Acta Part A Mol. Biomol. Spectrosc.* 248, 119264. doi:10.1016/j.saa.2020.119264

Zhang, X., Zhao, W., Li, B., Li, W., Zhang, C., Hou, X., et al. (2018). Ratiometric Fluorescent Probes for Capturing Endogenous Hypochlorous Acid in the Lungs of Mice. *Chem. Sci.* 9, 8207–8212. doi:10.1039/c8sc03226b

Zhang, M.-M., Ma, Y.-H., Li, P., Jia, Y., and Han, K.-L. (2020a). Detection of Atherosclerosis-Related Hypochlorous Acid Produced in Foam Cells with a Localized Endoplasmic Reticulum Probe. *Chem. Commun.* 56, 2610–2613. doi:10.1039/D0CC00090F

Zhang, W., Wang, H., Li, F., Chen, Y., Kwok, R. T. K., Huang, Y., et al. (2020b). A Ratiometric Fluorescent Probe Based on AIEgen for Detecting HClO in Living Cells. *Chem. Commun.* 56, 14613–14616. doi:10.1039/D0CC06582J

Zhao, J., Gao, Q., Zhang, F., Sun, W., and Bai, Y. (2016). Two Colorimetric Fluorescent Probes for Detection Fe3+: Synthesis, Characterization and Theoretical Calculations. *J. Luminescence* 180, 278–286. doi:10.1016/j.jlumin.2016.07.037

Zhou, Y., Lin, W., Rao, T., Zheng, J., Zhang, T., Zhang, M., et al. (2022). Ferroptosis and its Potential Role in the Nervous System Diseases. *Jir* 15, 1555–1574. doi:10.2147/JIR.S351799

Conflict of Interest: The authors declare that the research was conducted in the absence of any commercial or financial relationships that could be construed as a potential conflict of interest.

frontiers | Frontiers in Chemistry

ORIGINAL RESEARCH
published: 22 June 2022
doi: 10.3389/fchem.2022.920123

Fluorescence Detection of Cancer Stem Cell Markers Using a Sensitive Nano-Aptamer Sensor

Jie Ding[1,2†], Weiqiang Xu[2†], Jing Tan[2], Zhifang Liu[2], Guoliang Huang[1,2], Shoushan Wang[3*] and Zhiwei He[4*]*

[1]Guangdong Provincial Key Laboratory of Medical Molecular Diagnostics, The First Dongguan Affiliated Hospital, Guangdong Medical University, Dongguan, China, [2]Key Laboratory for Epigenetics of Dongguan City, China-America Cancer Research Institute, Guangdong Medical University, Dongguan, China, [3]Guangdong Engineering and Technology Research Center for Advanced Nanomaterials, School of Environment and Civil Engineering, Dongguan University of Technology, Dongguan, China, [4]The First Dongguan Affiliated Hospital, School of Basic Medical Science, Guangdong Medical University, Dongguan, China

Antigen CD133 is a glycoprotein present on the surface of cancer stem cells (CSCs), which is a key molecule to regulate the fate of stem cells and a functional marker of stem cells. Herein, a novel fluorescence "turn-on" nano-aptamer sensor for quantifying CD133 was designed using hybridization between CD133-targeted aptamers and partially complementary paired RNA (ssRNA), which were modified on the surface of quantum dots (QDs) and gold nanoparticles (AuNPs), respectively. Owing to the hybridization of aptamers and ssRNA, the distance between QDs and AuNPs was shortened, which caused fluorescence resonance energy transfer (FRET) between them, and the florescence of QDs was quenched by AuNPs. When CD133 competitively replaced ssRNA and was bound to aptamers, AuNPs-ssRNA could be released, which led to a recovery of fluorescent signals of QDs. The increase in the relative value of fluorescence intensity was investigated to linearly correlate with the CD133 concentration in the range of 0–1.539 μM, and the detection limit was 6.99 nM. In confocal images of A549 cells, the CD133 aptamer sensor was further proved applicable in lung cancer cell samples with specificity, precision, and accuracy. Compared with complicated methods, this study provided a fresh approach to develop a highly sensitive and selective detection sensor for CSC markers.

Keywords: cancer stem cell, CD133, aptamer sensor, CdSe/ZnS QDs, AuNPs

OPEN ACCESS

Edited by:
Cheng Ma,
Yangzhou University, China

Reviewed by:
Huachao Chen,
China Pharmaceutical University, China
Yingshu Guo,
Qilu University of Technology, China

****Correspondence:***
Jie Ding
wenqiong_1979@163.com
Shoushan Wang
wangshsh@dgut.edu.cn
Zhiwei He
hezhiwei@gdmu.edu.cn

†These authors have contributed equally to this work

Specialty section:
This article was submitted to Analytical Chemistry, a section of the journal Frontiers in Chemistry

Received: *14 April 2022*
Accepted: *18 May 2022*
Published: *22 June 2022*

Citation:
Ding J, Xu W, Tan J, Liu Z, Huang G, Wang S and He Z (2022) Fluorescence Detection of Cancer Stem Cell Markers Using a Sensitive Nano-Aptamer Sensor. Front. Chem. 10:920123. doi: 10.3389/fchem.2022.920123

INTRODUCTION

Cancer stem cells (CSC) refer to cancer cells with stem cell properties, which have the ability of self-renewal and multi-cell differentiation (Dick, 2008; Batlle and Clevers, 2017). CSCs are considered to have the potential to form tumors that develop into cancer, with it specifically being the source of formation of other cancer lesions during cancer metastases (Fidler, 2003; Kreso and Dick, 2014). In functional experiments, CSCs are defined as self-renewal cells and a source of formation of tumors when transplanted to immunodeficient mice (Lapidot et al., 1994). If CSCs are not completely eliminated in the treatment of cancer, cancer is easy to relapse and metastasize (Vlashi and Pajonk, 2015). Therefore, CSCs must be accurately detected and eradicated in the process of cancer treatment (Baum et al., 1992). Currently, multiple specific CSC-related markers have been identified and used to distinguish CSCs from the bulk of tumor cells (Hilbe et al., 2004; Phillips et al., 2006). The first marker was antigen CD133 (also known as promini-1), which was a CSC surface transmembrane

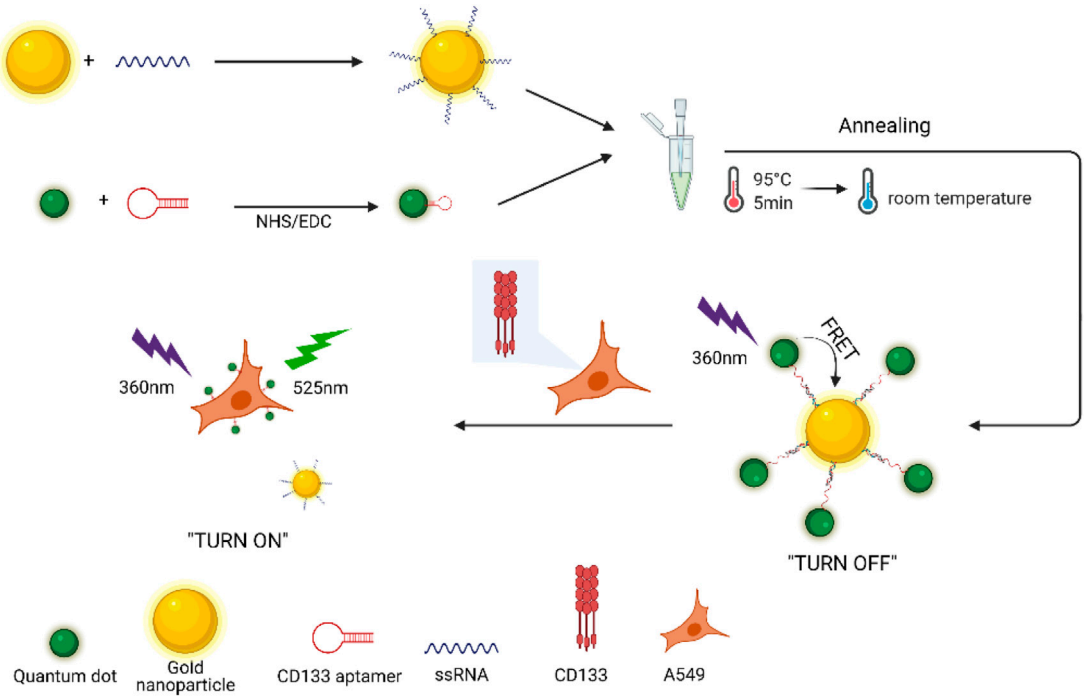

SCHEME 1 | Fluorescence detection of CD133 based on the "turn-on" FRET nano-aptamer sensor.

glycoprotein that contained five transmembrane segments, two large extracellular loops, and two small intracellular loops (Singh et al., 2004; Miki et al., 2007). The protein is now widely adopted for the detection and isolation of CSCs in several cancers, such as breast cancer (Al-Hajj et al., 2003), brain cancer (Jin et al., 2010), lung cancer (Wu and Wu, 2009), and liver cancer (Suetsugu et al., 2006). In the past, the detection of the $CD133^{pos}$ (CD133 overexpression) CSC had mostly relied on using immunehistochemical methods and flow cytometry, which required the participation of antibodies for accurate identification of CD133 (Kemper et al., 2010; Hermansen et al., 2011). Nevertheless, protein structure analysis showed that multiple N-glycan structures in CD133 could influence antibody binding due to their high sensitivity to glycosylation modification (Bidlingmaier et al., 2008). For overcoming the limitations of antibodies in the identification of CD133, researchers screened CD133-targeted aptamers by systematic evolution of ligands by exponential enrichment (SELEX) to substitute antibodies (Shigdar et al., 2013; Alibolandi et al., 2018). Aptamers are small single-stranded RNA or DNA oligonucleotides (~20–60 nucleotides) that are easier to bind to targets and have the advantages of non-immunogenicity, low cost, high specificity, and strong affinity (Lakhin et al., 2013). In order to obtain a sensitive detection signal, aptamers were usually combined with fluorescence materials to form aptasensors or aptamer probes, which could provide powerful tools for the detection of targets.

The design mechanism of many fluorescence aptasensors utilized the FRET (Förster resonance energy transfer) principle, which is a photophysical process of non-radiative energy transfer between an excited donor and an acceptor by long-range dipole–dipole interactions (Xu et al., 2014). The efficiency of FRET is primarily dependent on the spectral overlap between the donor emission and acceptor absorption spectra. The effective distance between the donor and the acceptor in FRET is of order of 1–10 nm (Liu et al., 2011). In the past, organic dyes as the energy donor or the acceptor were the major components of FRET sensors. However, these sensors suffered some drawbacks, such as low resistance to photo-bleaching and chemicals, spectral cross-talk, and small Stokes shifts, which might cause wrong transmission signals and a high detection limit. With development of research, it has been shown that nanostructured particles could be particularly suited for FRET systems due to the high efficiency of energy transfer (Jennings et al., 2006; Rakshit et al., 2017). Quantum dots (QDs), also known as nanocrystals, are a kind of nanoparticles composed of II–VI or III–V elements, which have abundant energy electrons and holes limited by quantum (Oh et al., 2005). The continuous energy band structure becomes a discrete energy level structure with molecular characteristics, which can emit excellent fluorescence after excitation (Huang and Ren, 2012). Based on well-known advantages, QDs had been extensively exploited as energy donors for FRET systems (Chang et al., 2017; Wang et al., 2017). As an energy receptor frequently paired with QDs in FRET, gold nanoparticles (AuNPs) have unique physical and chemical properties, mainly including the broad absorption spectra in the visible region, good biocompatibility, easy surface modification, etc. (Ling and Huang, 2010; Quintiliani et al., 2014). In addition, AuNPs are ready for labeling by RNA via the sulfhydryl group (Nie and Emory, 1997). The FRET sensor system constructed by QDs and AuNPs could be divided into two types according to the quenching or recovery of fluorescence: the "turn-off" mode and the "turn-on"

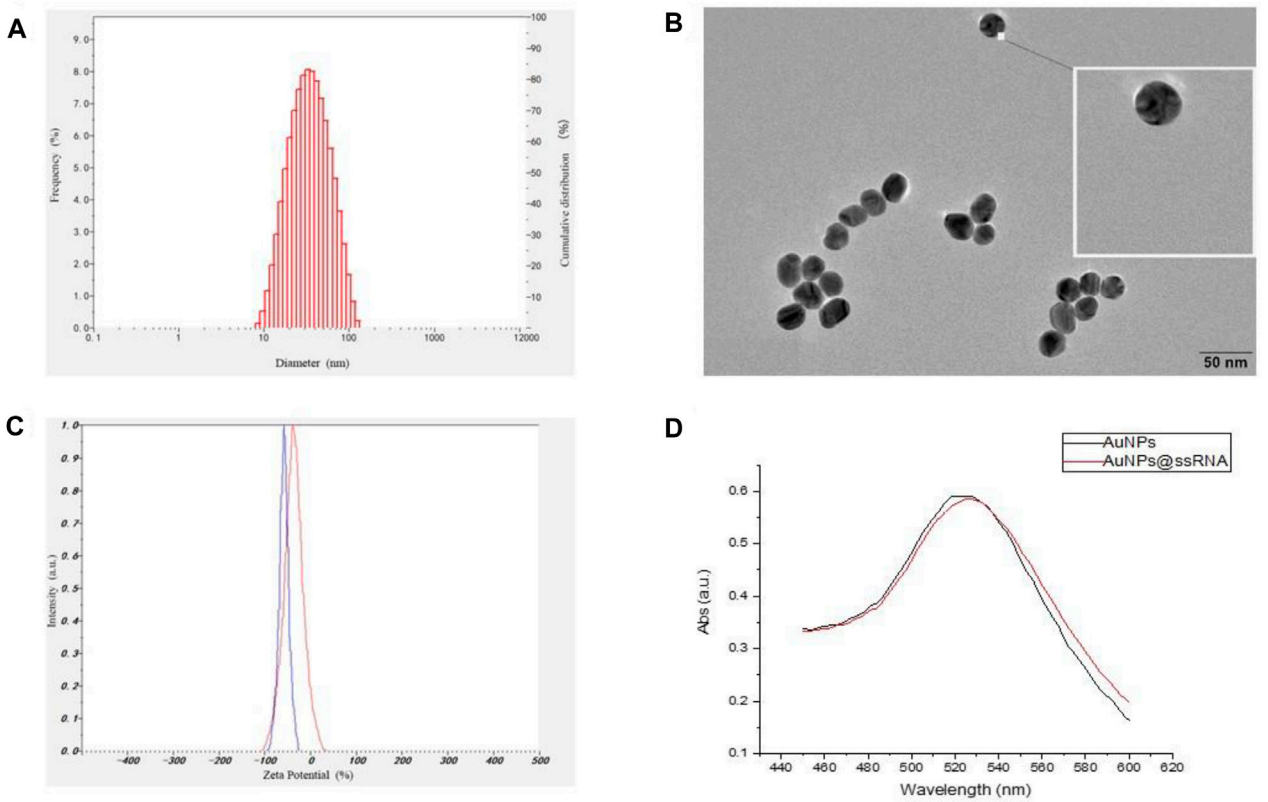

FIGURE 1 | (A) The hydrodynamic size distribution of AuNPs by DLS measurement. **(B)** TEM image of AuNPs. **(C)** The zeta potentials of AuNPs and AuNPs-ssRNA. **(D)** The UV–Vis spectra of the AuNPs and AuNPs-ssRNA.

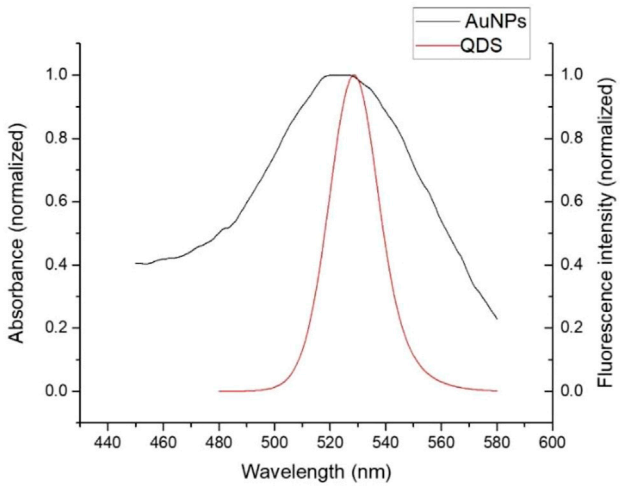

FIGURE 2 | After normalization, the QDs' fluorescence peak overlapped with the AuNPs' absorption peak.

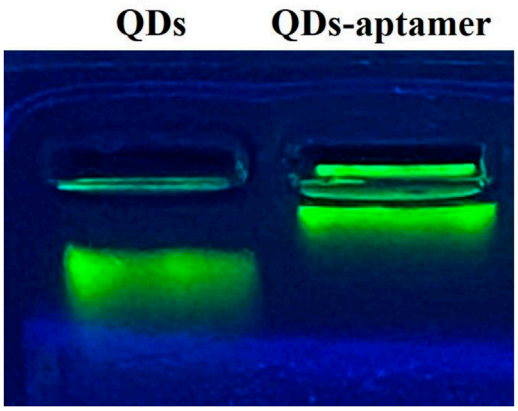

FIGURE 3 | The agarose gel electrophoresis of QDs and QD-aptamers showed that QDs without a conjugated aptamer ran faster in agarose gel.

mode. In the past, most of the fluorescence nanosensors were designed with the "turn-off" mode, where many factors could influence the detection effect and detection limit (Xia et al., 2012). By comparison, the fluorescence "turn-on" nanosensors employed in FRET-based systems could reduce the probability of false positives (Wang et al., 2012). Therefore, in this article, a nano-aptamer sensor composed of classical CdSe/ZnS QDs and AuNPs with a size of 25 nm was designed to detect CD133 in the fluorescent "turn-on" mode.

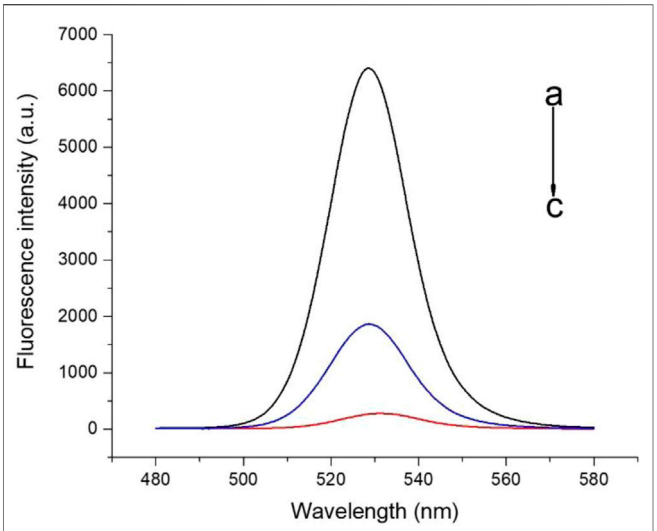

FIGURE 4 | The fluorescence spectra of a) QD-aptamers, b) the mixture of QD-aptamers and AuNPs, and c) the hybridization of QD-aptamers and AuNPs-ssRNA (aptamer sensor).

In this study, a novel "turn-on" FRET nano-aptamer sensor with CdSe/ZnS QDs and AuNPs as the energy donor–acceptor pairs was developed for detecting CD133, a CSC-related marker. Initially, the CD133-targeted aptamer and partially complementary paired RNA (ssRNA) were screened based on the sequence specific for CD133 and conjugated to QDs and AuNPs, respectively. As shown in **Scheme 1**, FRET occurred when the CD133 aptamer was hybridized with ssRNA, allowing one to bring QDs and AuNPs into close proximity; then the fluorescence of QDs was quenched by AuNPs. In principle, the fluorescence recovery of QDs was related to the ability of CD133 to competitively replace ssRNA and bind it to the CD133-targeted aptamer. Based on the standard curve obtained by fluorescence recovery of QDs, the detection limit (LOD) of the nano-aptamer sensor was calculated to be around 6.99 nM for CD133 detection. Meanwhile, the specificity, precision, and accuracy of the nano-aptamer sensor were examined, and its applicability in lung cancer cell samples was also validated. It was believed that this simple "turn-on" FRET nano-aptamer sensor would offer a promising approach for CSC marker detection with a low LOD and good selectivity.

RESULTS AND DISCUSSION

Synthesis and Characterization of AuNPs-ssRNA

The synthetic approach of the fluorescence "turn-on" nano-aptamer sensor is summarized in **Scheme 1**. First, AuNPs with a size of 25 nm were synthesized according to the method reported by Wang et al. (2019). The dynamic light scattering (DLS) results showed that AuNPs were well-dispersed with an average hydrodynamic size of 30 nm (**Figure 1A**). At the same time, the TEM image of AuNPs is exhibited in **Figure 1B**, where AuNPs are of a round shape and well-dispersed. Subsequently, the ssRNA with the endpoint modified sulfhydryl group was directly bound to the surface of AuNPs through coordination bonds. After the modification of ssRNA, the zeta potential of AuNPs dramatically increased from −58 mV to −36 mV (**Figure 1D**), indicating the successful modification of ssRNA on AuNPs. In **Figure 1D**, the UV–Vis spectra of AuNPs and AuNPs-ssRNA showed that the adsorption peak of AuNPs was at 523 nm while that of AuNPs-ssRNA was at 525 nm. The red-shift in the adsorption spectra further demonstrated that ssRNA was successfully conjugated onto the AuNPs' surface. Since RNA hybridization required annealing, agglomeration would occur in subsequent experiments if the concentration ratio of AuNPs to ssRNA was greater than or less than 1:200 (molar concentration ratio). Thus, the optimum concentration ratio of AuNPs to ssRNA was chosen to be 1:200.

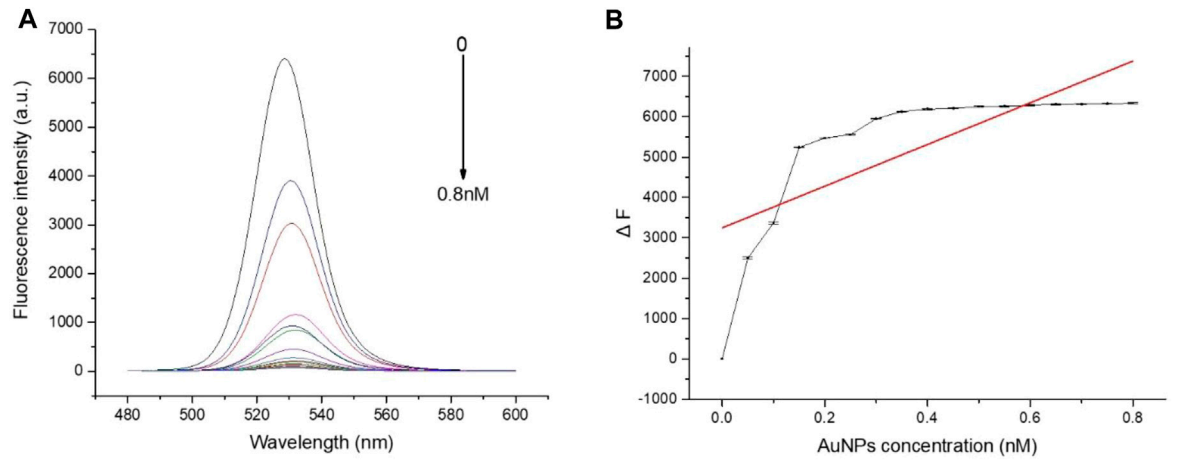

FIGURE 5 | (A) The fluorescence spectra of QD-aptamers hybridized with different concentrations of AuNPs-ssRNA; **(B)** When the hybridization concentration ratio of QD-aptamers to AuNPs-ssRNA was 10:1, the fluorescence intensity of QDs reached the plateau stage. The aptamer sensor for the detection of targeted CSC markers.

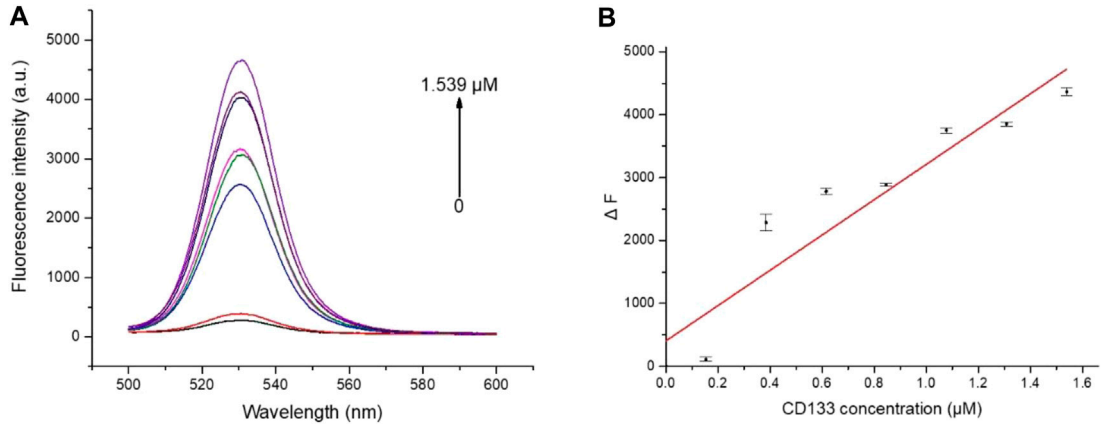

FIGURE 6 | (A) The fluorescence spectra of the aptamer sensor treated with different concentrations of CD133. **(B)** The plot of ΔF as a function of CD133 concentration.

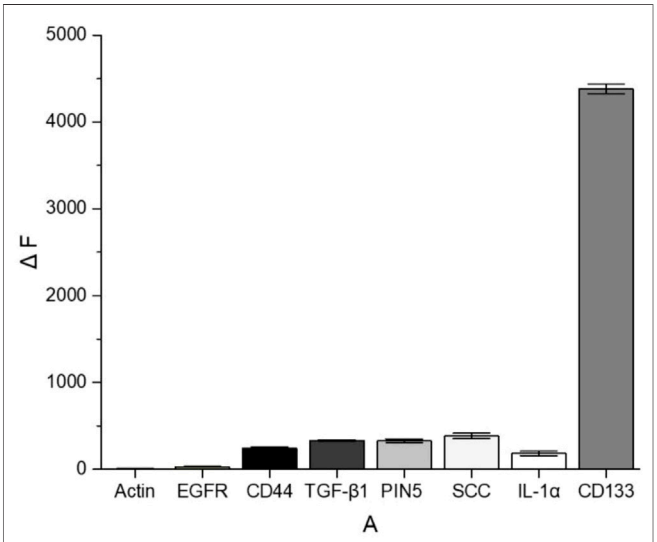

FIGURE 7 | ΔF comparison between CD133 and other common cancer-associated proteins.

Synthesis and Characterization of QD-Aptamers

The fluorescence spectra in **Figure 2** showed that the emission peak was 525 nm for CdSe/ZnS QDs; there was an overlap between the emission spectrum of QDs and the absorption spectrum of AuNPs around 525 nm, indicating that the QDs and AuNPs could work as a FRET donor–acceptor pair. Then, the CD133-targeted aptamer was conjugated onto CdSe/ZnS QDs by an ammonia carboxylation reaction, and the ratio between aptamer and QDs was optimized. Due to the large surface area of QDs, there were multiple binding sites on the surface of QDs to couple with aptamers. After the overdose aptamer reacted with QDs, the unbound aptamer was removed using an ultrafiltration tube. For proving the aptamer conjugation, QDs and QD-aptamers were monitored by agarose gel electrophoresis (**Figure 3**), which implied that the conjugation efficiency reached a plateau when the aptamer concentration exceeded 7 times the molar concentration of QDs. Herein, 7:1 was chosen as the optimal concentration ratio of aptamer-bound QDs.

Synthesis and Characterization of Fluorescence "Turn-On" Nano-Aptamer Sensors

To evaluate whether FRET occurred in our design, these fluorescence spectra were measured, including QD-aptamers, the mixture of QD-aptamer and AuNPs, and the hybridization of QD-aptamers and AuNPs-ssRNA (aptamer sensor) (**Figure 4**). The fluorescence spectrum for free QDs showed a maximum peak at 525 nm, which was close to the maximum of absorption measured for AuNPs. It suggested that CdSe/ZnS QDs and AuNPs could serve as a suitable donor–acceptor pair. It could also be seen that the fluorescence band (the full width at half-maximum fluorescence intensity, FWHM) was relative narrow and symmetric, which suggested that both QDs and the aptamer sensor were homogenous and monodisperse. According to the past studies, FRET could operate when an energy donor to an acceptor was in close proximity (≤10 nm). The chain length of the CD133-targeted aptamer indicated that the distance between the donor and the acceptor was definitely achieved in the studied system. As could be seen in **Figure 4C**, when the hybridization between QD-aptamers and AuNPs-ssRNA is driven by the specific pairing of aptamers and partial complementary ssRNA, the fluorescence signal of QDs was quenched dramatically by AuNPs due to the occurrence of FRET. However, when there was no ssRNA conjugated to AuNPs (**Figure 4B**), the hybridization was not in operation, and the fluorescence intensity of QDs was only partially reduced. The spectra results indicated that the efficiency of FRET was significantly improved by linking QDs and AuNPs through aptamer–ssRNA hybridization. To ensure adequate hybridization between the aptamer and ssRNA, the hybridization time was fixed at 90 min (annealing time). As

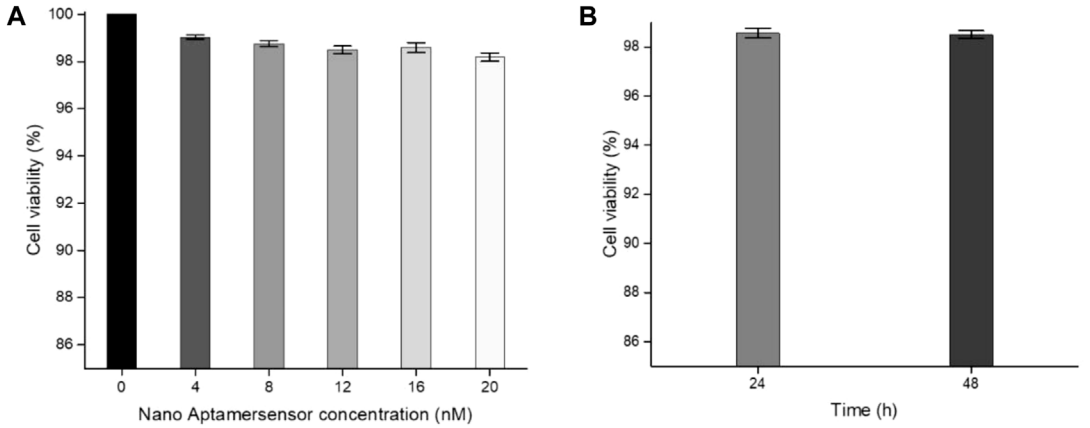

FIGURE 8 | (A) Cell viability of A549 cells incubated with different concentrations of the aptamer sensor for 24 h. **(B)** Cell viability of A549 cells incubated with a 20 nM aptamer sensor for 24 or 48 h.

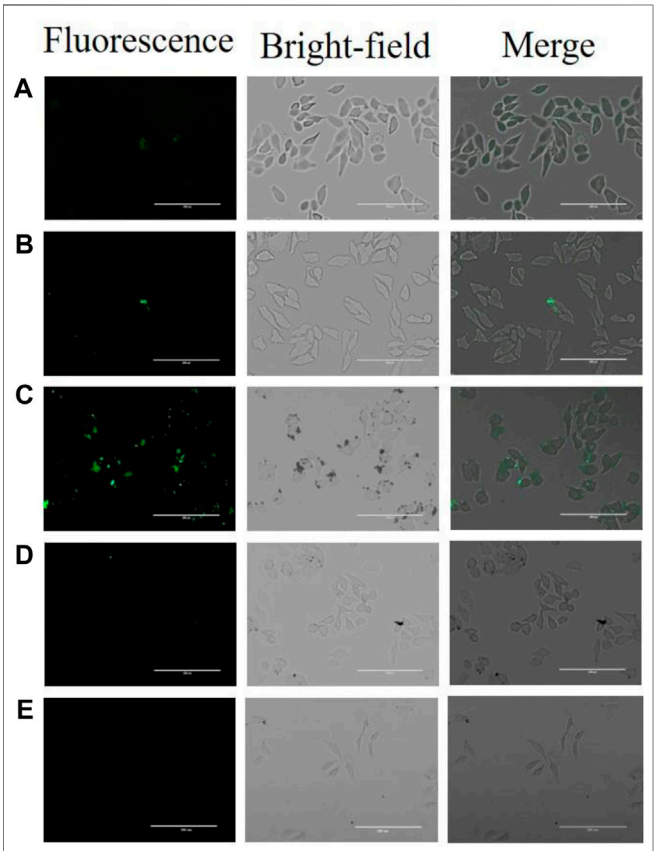

FIGURE 9 | Confocal microscopy images of A549 cells or HuH-7 cells following treatment of **(A)** QDs, **(B)** QD-aptamers, **(C)** aptamer sensors, and **(D)** pretreated cells with CD133-targeted aptamers for 24 h and then incubated with the aptamer sensor. **(E)** HuH-7 cells were treated with the aptamer sensor.

shown in **Figure 5A**, the fluorescence signal intensity of QDs decreased with the increase in AuNPs and reached quench equilibrium when the molar concentration ratio of QDs to AuNPs was 10:1 (**Figure 5B**). Finally, the synthesis conditions of the aptamer sensor were determined where the hybridization reaction time was 90 min and the concentration ratio was 10:1.

To explore the fluorescence "turn-on" efficiency of this FRET aptamer sensor, a series of concentrations of CD133 were tested from 0 to 1.539 μM. Herein, a fixed number of QD-aptamers (5 nM) was used. As a result of competitive replacement of ssRNA by CD133, the distance between QDs and AuNPs increased significantly, and fluorescence recovery was realized. The recovery efficiency was expressed by $\Delta F = F_C - F_0$, where Fc is the fluorescence intensity of QDs after recovery and F_0 is the original fluorescence intensity of the aptamer sensor. As shown in **Figure 6A**, the recovery efficiency gradually increased with the increase in CD133 and reached a maximum of 68% with 1.539 μM CD133, and then the recovery efficiency was almost unchanged when the concentration of CD133 further increased. **Figure 6B** indicated the fluorescence signal recovery ($F_C - F_0$) versus a series of CD133 concentrations. Then the detection limit (LOD) was determined by the standard curve, which was around 6.99 nM.

The Specificity of the Aptamer Sensor

To evaluate the specificity, the aptamer sensor was treated with multiple common cancer-associated proteins and compared with CD133. All the experiments used the same concentration (2 μM) of proteins for comparison. As shown in **Figure 7**, these interfering proteins hardly recovered the fluorescence of QDs. For example, the recovery efficiency of CD133 was around 68%, while that of SCC was merely around 5%. The results indicated that this FRET "turn-on" nano-aptamer sensor exhibited high selectivity.

In Vitro Imaging of Cell Response to the Aptamer Sensor

In order to study the biocompatibility of the nano-aptamer sensor, CCK-8 assays were used to evaluate the cytotoxicity of the aptamer sensor. The results indicated that A549 cells still

maintained high viability after incubating for 24 h with the aptamer sensor up to 20 nM (**Figure 8A**). Even if the incubation time was prolonged to 48 h, it would not affect the cell viability (**Figure 8B**). In other words, if the concentration of the aptamer sensor was not more than 20 nM, then the aptamer sensor had low toxicity to cells and could be used for cellular imaging. Furthermore, to demonstrate the capacity of the fluorescence "turn-on" FRET aptamer sensor in selectively detecting $CD133^{pos}$ cells, the lung cancer cell A549 ($CD133^{pos}$ cell) was treated with the aptamer sensor. After incubation with QD-aptamers or the aptamer sensor for 8 h, strong fluorescence signals were detected from A549 cells by confocal microscopy imaging (**Figures 9B,C**), while the control experiment using QDs without the aptamer at the same concentration showed weak fluorescence (**Figure 9A**). For verifying that this "turn-on" phenomenon was ascribed to the competitive release of AuNPs-ssRNA, the binding site of A549 cells was saturated with the CD133-targeted aptamer for 24 h before incubation with the aptamer sensor. It turned out that the fluorescence signal from A549 cells was negligible, as shown in **Figure 9D**. A negative control experiment performed with CD133-negative HuH-7 human hepatoma cells showed that the fluorescence recovery of the aptamer sensor was not observed (**Figure 9E**), further indicating that the release of AuNPs-ssRNA was from the specific binding between the aptamer and CD133.

EXPERIMENTAL SECTION

Materials and Equipment

Chloroauric acid ($HAuCl_4$) and sodium citrate were purchased from Shanghai Aladdin Biochemical Technology Co. Ltd. Carboxyl-modified quantum dots (-COOH QDs) were obtained from Suzhou Xingshuo Nanotechnology Co. Ltd. 1-ethyl-(3-dimethylaminopropyl) carboimide (EDC) and N-hydroxysuccinimide (NHS) were purchased from Shanghai Macklin Biochemical Co. Ltd. The amino-modified CD133 aptamer (5′-NH_2-CCCUCCUACAUAGGG-3′) and CD133 aptamer partial complementary pairing part (ssRNA, 5′-SH-CCCUAUG-3′) were synthesized by Shanghai Generay Biotech Co. Ltd. All buffers were prepared with ultrapure water, which was purified to a resistivity of 18.2 MΩ*cm by a milli-Q system (Merck Millipore, United States). A dynamic light scattering particle size analyzer (SZ-100, Horiba, Japan) was used for measuring the zeta potential and particle size. The morphology of nanoparticles was characterized by transmission electron microscopy (JEOL JEM-2100 F, JEOL Ltd., Japan). The UV–Vis absorption spectra were recorded on a microspectrophotometer (NanoDrop ND-1000, Thermo Scientific, United States). Fluorescence spectra were obtained using a fluorescence spectrophotometer (F-7000, Hitachi, Japan). Fluorescence images were recorded using a confocal laser scanning microscope (TCS SP8 Leica, United States).

The Synthesis of Gold Nanoparticles

All reaction instruments needed to be soaked in aqua regia or concentrated alkali and washed with ultrapure water 3 to 4 times. Then 250 μl of 0.4 M chloroauric acid ($HAuCl_4$) and 50 ml of ultrapure water were added to a round bottom flask, continuously stirred, and heated to boiling. After boiling, 10 ml of 38 mM sodium citrate solution was quickly injected, and then the solution was heated to boiling again. The color of the solution gradually changed from light yellow to wine red; the solution was boiled for another 15 min until the reaction was complete. After cooling, it was filtered by an ultrafiltration membrane and stored at 4°C.

AuNP-Coupled Nucleotide Single Strand (AuNPs-ssRNA)

The prepared AuNPs were incubated with a sulfhydryl nucleotide single chain (ssRNA) in a ratio of 1:200 for 24 h, and then 1 M sodium phosphate buffer (PBS, 1 M NaCl, 100 mM Na_2HPO_4 and NaH_2PO_4, pH = 7.4) was added step by step. At least for 30 min between each step, the final concentration of PBS reached 0.1 M. The solution was incubated at room temperature for 40 h. Finally, the excess ssRNA was removed by centrifugation (13,800 rpm, 20 min) and redispersed in 0.1 M PBS.

The Characterization of AuNPs-ssRNA

Since coupling nucleotides with AuNPs would reduce the anions on their surface, the salt solution was added to resist the cations on the surface of AuNPs in order to prevent agglomeration and maintain stability, while uncoupled or incompletely coupled AuNPs would agglomerate and change color. Therefore, salt solution of the same concentration and volume could be added to the reaction mixture of AuNPs and ssRNA to observe whether it changes color and agglomerates, and the reaction degree between AuNPs and ssRNA is judged.

QD-Coupled Aptamers (QD-Aptamers)

Carboxyl CdSe/ZnS QDs (40 μl, 0.6 nM) were activated with 60 μl (50 mM) EDC and 30 μl (25 mM) NHS under mild stirring for 15 min. The activated QDs were incubated with an amino aptamer at different mass ratios for 24 h, and then the unreacted aptamer was separated using an ultrafiltration centrifuge tube. The obtained QD-aptamers were redispersed in PBS.

The Detection of Fluorescence Change After Hybridization Between QD-Aptamers and AuNPs-ssRNA

The obtained QD-aptamers were divided into two groups. One group was added with the stock solution of AuNPs, and the other was added with AuNPs-ssRNA. The nucleotide chains were complementary paired by annealing (adding the annealing buffer at 95°C for 5 min and gradually reducing to room temperature), and then the fluorescence value of the mixture was measured at the same time to verify that the strong fluorescence quenching effect was due to the complementary pairing of the nucleotide chains, shortening the distance between the energy donor and the acceptor. Based on the fluorescence change in QDs, the reaction time and the molar ratio of AuNPs to

QDs were determined. The final fluorescence "turn-on" nano-aptamer sensor was obtained.

Highly Selective Detection of CD133 by Aptamer Sensors

After the aptamer sensor reacted with CD133 and other interfering proteins (actin, EGFR, CD44, TGF-β1, PIN 5, SCC, and IL-1α), the fluorescence value of the reaction solution was measured to verify that CD133 could specifically bind to the CD133-targeted aptamer on the surface of QDs by replacing AuNPs-ssRNA. The aptamer did not respond to other interfering proteins, which proved its specificity.

Fluorescence Imaging of $CD133^{pos}$ CSCs Using the Aptamer Sensor

After passage, lung cancer cells A549 were inoculated into confocal dishes and divided into four groups for different experimental operations. The first group was incubated with single QDs for 8 h. The second group was incubated with QD-aptamers for 8 h. The third group was incubated with aptamer sensors for 8 h. The last group was incubated with a single aptamer for 24 h and then with the aptamer sensor for 8 h. The concentration of QDs in the four groups was the same. After incubation, the solution in the dishes was washed with PBS twice, and the fluorescence imaging of the cells was observed under a confocal laser scanning microscope. As control, HuH-7 cells were incubated with an aptamer sensor for 8 h to detect the fluorescence of QDs.

CONCLUSION

In summary, a novel aptamer sensor was designed to detect CD133 that consisted of QDs modified with a CD133-targeted aptamer and AuNPs conjugated with partially complementary paired RNA (ssRNA). The hybridization between the aptamer and ssRNA brought QDs and AuNPs into close proximity to trigger FRET, where the change in fluorescence intensity of QDs was recorded using a fluorescence spectrophotometer. CD133, a CSC marker, competitively replaced ssRNA, resulting in the decrease in the FRET effect between QDs and AuNPs and the recovery of QD fluorescence. The experiments demonstrated the feasibility of this "turn-on" FRET nano-aptamer sensor for CD133 detection with an LOD of 6.99 nM. Moreover, the aptamer sensor was able to detect CD133 on the surface of A549 cells by displaying the fluorescence of QDs through confocal images. These results suggested that the aptamer sensor is a sensitive and reliable sensor for the detection of CD133 and offers a simple yet promising testing tool for CSC marker detection.

DATA AVAILABILITY STATEMENT

The original contributions presented in the study are included in the article/Supplementary Material; further inquiries can be directed to the corresponding authors.

AUTHOR CONTRIBUTIONS

All authors listed have made a substantial, direct, and intellectual contribution to the work and approved it for publication.

FUNDING

We acknowledge the financial support of the Natural Science Foundation of Guangdong Province (2021A1515012320), the Discipline Construction Project of Guangdong Medical University (4SG22005G), the Dongguan Science and Technology Commissioner Project (20201800500172), the National Natural Science Foundation of China (81772982), and the Special Innovation Fund of the Department of Education of Guangdong Province (2019KTSCX049).

REFERENCES

Al-Hajj, M., Wicha, M. S., Benito-Hernandez, A., Morrison, S. J., and Clarke, M. F. (2003). Prospective Identification of Tumorigenic Breast Cancer Cells. *Proc. Natl. Acad. Sci. U.S.A.* 100, 3983–3988. doi:10.1073/pnas.0530291100

Alibolandi, M., Abnous, K., Anvari, S., Mohammadi, M., Ramezani, M., and Taghdisi, S. M. (2018). CD133-targeted Delivery of Self-Assembled PEGylated Carboxymethylcellulose-SN38 Nanoparticles to Colorectal Cancer. *Artif. Cells Nanomed. Biotechnol.* 46, 1159–1169. doi:10.1080/21691401.2018.1446969

Batlle, E., and Clevers, H. (2017). Cancer Stem Cells Revisited. *Nat. Med.* 23, 1124–1134. doi:10.1038/nm.4409

Baum, C. M., Weissman, I. L., Tsukamoto, A. S., Buckle, A. M., and Peault, B. (1992). Isolation of a Candidate Human Hematopoietic Stem-Cell Population. *Proc. Natl. Acad. Sci. U.S.A.* 89, 2804–2808. doi:10.1073/pnas.89.7.2804

Bidlingmaier, S., Zhu, X., and Liu, B. (2008). The Utility and Limitations of Glycosylated Human CD133 Epitopes in Defining Cancer Stem Cells. *J. Mol. Med.* 86, 1025–1032. doi:10.1007/s00109-008-0357-8

Chang, L., He, X., Chen, L., and Zhang, Y. (2017). A Novel Fluorescent Turn-On Biosensor Based on QDs@GSH-GO Fluorescence Resonance Energy Transfer for Sensitive Glutathione S-Transferase Sensing and Cellular Imaging. *Nanoscale* 9, 3881–3888. doi:10.1039/c6nr09944k

Dick, J. E. (2008). Stem Cell Concepts Renew Cancer Research. *Blood* 112, 4793–4807. doi:10.1182/blood-2008-08-077941

Fidler, I. J. (2003). The Pathogenesis of Cancer Metastasis: the 'seed and Soil' Hypothesis Revisited. *Nat. Rev. Cancer* 3, 453–458. doi:10.1038/nrc1098

Hermansen, S. K., Christensen, K. G., Jensen, S. S., and Kristensen, B. W. (2011). Inconsistent Immunohistochemical Expression Patterns of Four Different CD133 Antibody Clones in Glioblastoma. *J. Histochem Cytochem.* 59, 391–407. doi:10.1369/0022155411400867

Hilbe, W., Dirnhofer, S., Oberwasserlechner, F., Schmid, T., Gunsilius, E., Hilbe, G., et al. (2004). CD133 Positive Endothelial Progenitor Cells Contribute to the Tumour Vasculature in Non-small Cell Lung Cancer. *J. Clin. Pathology* 57, 965–969. doi:10.1136/jcp.2004.016444

Huang, X., and Ren, J. (2012). Nanomaterial-based Chemiluminescence Resonance Energy Transfer: A Strategy to Develop New Analytical Methods. *TrAC Trends Anal. Chem.* 40, 77–89. doi:10.1016/j.trac.2012.07.014

Jennings, T. L., Singh, M. P., and Strouse, G. F. (2006). Fluorescent Lifetime Quenching Near D = 1.5 Nm Gold Nanoparticles: Probing NSET Validity. *J. Am. Chem. Soc.* 128, 5462–5467. doi:10.1021/ja0583665

Jin, F., Zhao, L., Guo, Y.-J., Zhao, W.-J., Zhang, H., Wang, H.-T., et al. (2010). Influence of Etoposide on Anti-apoptotic and Multidrug Resistance-Associated Protein Genes in CD133 Positive U251 Glioblastoma Stem-like Cells. *Brain Res.* 1336, 103–111. doi:10.1016/j.brainres.2010.04.005

Kemper, K., Sprick, M. R., de Bree, M., Scopelliti, A., Vermeulen, L., Hoek, M., et al. (2010). The AC133 Epitope, but Not the CD133 Protein, Is Lost upon Cancer Stem Cell Differentiation. *Cancer Res.* 70, 719–729. doi:10.1158/0008-5472.can-09-1820

Kreso, A., and Dick, J. E. (2014). Evolution of the Cancer Stem Cell Model. *Cell Stem Cell* 14, 275–291. doi:10.1016/j.stem.2014.02.006

Lakhin, A. V., Tarantul, V. Z., and Gening, L. V. (2013). Aptamers: Problems, Solutions and Prospects. *Acta Naturae* 5, 34–43. doi:10.32607/20758251-2013-5-4-34-43

Lapidot, T., Sirard, C., Vormoor, J., Murdoch, B., Hoang, T., Caceres-Cortes, J., et al. (1994). A Cell Initiating Human Acute Myeloid Leukaemia after Transplantation into SCID Mice. *Nature* 367, 645–648. doi:10.1038/367645a0

Ling, J., and Huang, C. Z. (2010). Energy Transfer with Gold Nanoparticles for Analytical Applications in the Fields of Biochemical and Pharmaceutical Sciences. *Anal. Methods* 2, 1439–1447. doi:10.1039/c0ay00452a

Liu, X., Freeman, R., Golub, E., and Willner, I. (2011). Chemiluminescence and Chemiluminescence Resonance Energy Transfer (CRET) Aptamer Sensors Using Catalytic hemin/G-Quadruplexes. *ACS Nano* 5, 7648–7655. doi:10.1021/nn202799d

Miki, J., Furusato, B., Li, H., Gu, Y., Takahashi, H., Egawa, S., et al. (2007). Identification of Putative Stem Cell Markers, CD133 and CXCR4, in hTERT-Immortalized Primary Nonmalignant and Malignant Tumor-Derived Human Prostate Epithelial Cell Lines and in Prostate Cancer Specimens. *Cancer Res.* 67, 3153–3161. doi:10.1158/0008-5472.can-06-4429

Nie, S., and Emory, S. R. (1997). Probing Single Molecules and Single Nanoparticles by Surface-Enhanced Raman Scattering. *Science* 275, 1102–1106. doi:10.1126/science.275.5303.1102

Oh, E., Hong, M.-Y., Lee, D., Nam, S.-H., Yoon, H. C., and Kim, H.-S. (2005). Inhibition Assay of Biomolecules Based on Fluorescence Resonance Energy Transfer (FRET) between Quantum Dots and Gold Nanoparticles. *J. Am. Chem. Soc.* 127, 3270–3271. doi:10.1021/ja0433323

Phillips, T. M., McBride, W. H., and Pajonk, F. (2006). The Response of CD24 (−/low)/CD44+ Breast Cancer-Initiating Cells to Radiation. *J. Natl. Cancer Inst.* 98, 1777–1785. doi:10.1093/jnci/djj495

Quintiliani, M., Bassetti, M., Pasquini, C., Battocchio, C., Rossi, M., Mura, F., et al. (2014). Network Assembly of Gold Nanoparticles Linked through Fluorenyl Dithiol Bridges. *J. Mat. Chem. C* 2, 2517–2527. doi:10.1039/c3tc32567a

Rakshit, S., Moulik, S. P., and Bhattacharya, S. C. (2017). Understanding the Effect of Size and Shape of Gold Nanomaterials on Nanometal Surface Energy Transfer. *J. Colloid Interface Sci.* 491, 349–357. doi:10.1016/j.jcis.2016.12.052

Shigdar, S., Qiao, L., Zhou, S.-F., Xiang, D., Wang, T., Li, Y., et al. (2013). RNA Aptamers Targeting Cancer Stem Cell Marker CD133. *Cancer Lett.* 330, 84–95. doi:10.1016/j.canlet.2012.11.032

Singh, S. K., Hawkins, C., Clarke, I. D., Squire, J. A., Bayani, J., Hide, T., et al. (2004). Identification of Human Brain Tumour Initiating Cells. *Nature* 432, 396–401. doi:10.1038/nature03128

Suetsugu, A., Nagaki, M., Aoki, H., Motohashi, T., Kunisada, T., and Moriwaki, H. (2006). Characterization of CD133+ Hepatocellular Carcinoma Cells as Cancer Stem/progenitor Cells. *Biochem. Biophysical Res. Commun.* 351, 820–824. doi:10.1016/j.bbrc.2006.10.128

Vlashi, E., and Pajonk, F. (2015). Cancer Stem Cells, Cancer Cell Plasticity and Radiation Therapy. *Seminars Cancer Biol.* 31, 28–35. doi:10.1016/j.semcancer.2014.07.001

Wang, G.-L., Jiao, H.-J., Zhu, X.-Y., Dong, Y.-M., and Li, Z.-J. (2012). Enhanced Fluorescence Sensing of Melamine Based on Thioglycolic Acid-Capped CdS Quantum Dots. *Talanta* 93, 398–403. doi:10.1016/j.talanta.2012.02.062

Wang, X., Xu, G., Wei, F., Ma, Y., Ma, Y., Song, Y., et al. (2017). Highly Sensitive and Selective Aptasensor for Detection of Adenosine Based on Fluorescence Resonance Energy Transfer from Carbon Dots to Nano-Graphite. *J. Colloid Interface Sci.* 508, 455–461. doi:10.1016/j.jcis.2017.07.028

Wang, Y., Rao, Z., Zhou, J., Zheng, L., and Fu, L. (2019). A Chiral Assembly of Gold Nanoparticle Trimer-Based Biosensors for Ultrasensitive Detection of the Major Allergen Tropomyosin in Shellfish. *Biosens. Bioelectron.* 132, 84–89. doi:10.1016/j.bios.2019.02.038

Wu, Y., and Wu, P. Y. (2009). CD133 as a Marker for Cancer Stem Cells: Progresses and Concerns. *Stem Cells Dev.* 18, 1127–1134. doi:10.1089/scd.2008.0338

Xia, Y., Wang, J., Zhang, Y., Song, L., Ye, J., Yang, G., et al. (2012). Quantum Dot Based Turn-On Fluorescent Probes for Anion Sensing. *Nanoscale* 4, 5954–5959. doi:10.1039/c2nr31809a

Xu, S., Xu, S., Zhu, Y., Xu, W., Zhou, P., Zhou, C., et al. (2014). A Novel Upconversion, Fluorescence Resonance Energy Transfer Biosensor (FRET) for Sensitive Detection of Lead Ions in Human Serum. *Nanoscale* 6, 12573–12579. doi:10.1039/c4nr03092c

Conflict of Interest: The authors declare that the research was conducted in the absence of any commercial or financial relationships that could be construed as a potential conflict of interest.

Publisher's Note: All claims expressed in this article are solely those of the authors and do not necessarily represent those of their affiliated organizations, or those of the publisher, the editors, and the reviewers. Any product that may be evaluated in this article, or claim that may be made by its manufacturer, is not guaranteed or endorsed by the publisher.

frontiers | Frontiers in Chemistry

ORIGINAL RESEARCH
published: 08 July 2022
doi: 10.3389/fchem.2022.928607

Gold Nanocluster-Encapsulated Hyperbranched Polyethyleneimine for Selective and Ratiometric Dopamine Analyses by Enhanced Self-Polymerization

Jing Zhang[1], *Ying Liu*[1], *Yang Liu*[1], *Wencai Liu*[1], *Fengniu Lu*[2], *Zhiqin Yuan*[1,3]* *and Chao Lu*[1,4]*

[1]State Key Laboratory of Chemical Resource Engineering, College of Chemistry, Beijing University of Chemical Technology, Beijing, China, [2]Department of Chemistry and Chemical Engineering, Beijing Institute of Technology, Beijing, China, [3]Beijing Key Laboratory of Plant Resources Research and Development, Beijing Technology and Business University, Beijing, China, [4]Green Catalysis Center, College of Chemistry, Zhengzhou University, Zhengzhou, China

The exploitation of selective and sensitive dopamine (DA) sensors is essential to more deeply understand its biological function and diagnosis of related diseases. In this study, gold nanocluster-encapsulated hyperbranched polyethyleneimine (hPEI-Au NCs) has been explored as the specific and ratiometric DA nanoprobe through hPEI-assisted DA self-polymerization reactions. The Au NCs encapsulation not only provides a fluorescent internal reference but also enhances the DA self-polymerization by weakening the proton sponge effect of the hPEI layer. Rapid and sensitive DA detection is realized through the proposed hPEI-Au NC nanoprobe with a limit of detection of 10 nM. The favorable selectivity over other possible interferents including amino acids, sugars, and salts is due to the specific self-polymerization reaction. The DA analysis in urine samples with small relative standard deviations has been accomplished with an hPEI-Au NC nanoprobe.

Keywords: hyperbranched polyethyleneimine, gold nanoclusters, dopamine analysis, self-polymerization, ratiometric fluorescence

OPEN ACCESS

Edited by:
Junjie Zhu,
Nanjing University, China

Reviewed by:
Wei Wen,
Hubei University, China
Jiu-Ju Feng,
Zhejiang Normal University, China

***Correspondence:**
Zhiqin Yuan
yuanzq@mail.buct.edu.cn
Chao Lu
luchao@mail.buct.edu.cn

Specialty section:
This article was submitted to Analytical Chemistry, a section of the journal Frontiers in Chemistry

Received: *26 April 2022*
Accepted: *17 May 2022*
Published: *08 July 2022*

Citation:
Zhang J, Liu Y, Liu Y, Liu W, Lu F, Yuan Z and Lu C (2022) Gold Nanocluster-Encapsulated Hyperbranched Polyethyleneimine for Selective and Ratiometric Dopamine Analyses by Enhanced Self-Polymerization. Front. Chem. 10:928607. doi: 10.3389/fchem.2022.928607

INTRODUCTION

Catecholamines with specific structures can act as neurotransmitters, which are associated with neuron communication and affect brain functions (Fuxe et al., 2012). Among these catecholamines, dopamine (DA) regulates numerous biological processes and plays vital roles in the nervous, cardiovascular, and renal systems (Bucolo et al., 2019). Thus, its abnormality usually reflects the physiologic condition and is related to many diseases. For example, aprosexia related to lack of muscle control and Parkinson's diseases are reported to be associated with DA deficiency (Kim et al., 2002). Meanwhile, energy metabolism disorder-induced Huntington's disease is caused by the overexpression of DA (Cepeda et al., 2014). In this case, the development of sensitive and accurate analytical methods for DA quantification is significant for a deeper understanding of its biological function and early diagnosis of relevant diseases.

So far, a number of DA detection methods based on UV–vis spectroscopy, fluorimetry, Raman, electrochemical technique, and nuclear magnetic resonance imaging have been reported (Li et al., 2013; Mao et al., 2018; Ling et al., 2020; Senel et al., 2020; Ren et al., 2021). In particular, fluorescence-based DA detection approaches attract growing attention because of their low background, high

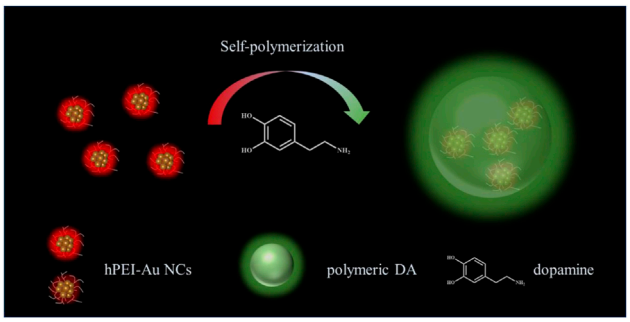

FIGURE 1 | Schematic illustration of ratiometric DA detection with the hPEI-Au NC nanoprobe.

sensitivity, and strong interference rejection (Qu et al., 2019; Yu et al., 2021). The commonly used mechanisms for fluorescent DA sensing can be divided into four categories: aptamer–DA binding-mediated conformation change, o-diquinone-induced fluorescence quenching, resorcinol–DA coupling-mediated formation of azamonardine, and polydopamine-regulated energy transfer (Zhang et al., 2016; He et al., 2018; Zeng et al., 2020; Ma et al., 2021). Oxidation of DA-induced production of o-diquinone is primarily applied to DA sensing with inorganic fluorophores as the references (Zhang et al., 2015; Diaz-Diestra et al., 2017). This strategy, however, is difficult to distinguish DA from other catechols. Therefore, it is appealing to explore a simple and direct strategy for selective DA perception. It is reported that hyperbranched polyethyleneimine (hPEI) can induce the spontaneous formation of polymeric DA nanoparticles with strong green fluorescence through DA self-polymerization reaction (Liu et al., 2015). This reaction is also capable to discriminate DA analogs by integrating the linear discrimination analysis technique (Sun et al., 2019). However, such a discrimination approach can only differentiate DA analogs at the μM level. Notice that ratiometric sensing systems with built-in correction characters usually display high sensitivity (Li et al., 2017; Huang et al., 2018; Yang et al., 2020a); this specific reaction, in combination with a fluorescent internal reference, may be able to construct a sensitive and selective DA sensor, which is theoretically feasible.

Gold nanoclusters (Au NCs) consist of several gold atoms and show unique chemical/physical properties and usually bright fluorescence (Liang et al., 2022; Liu et al., 2022). The ultrasmall size and bright emission make them potential reporters in chemo/biosensing and imaging (Chen et al., 2015; Xiao et al., 2021). Notably, the surface protecting layers largely decide the stability and application of Au NCs (Tseng et al., 2014; Lu et al., 2020). As indicated in our previous reports, hPEI with branched molecular structure and abundant amine groups can act as a good template for yielding fluorescent gold nanoclusters (Au NCs), and the emission of Au NCs is tunable by regulating hPEI/thiolate molar ratio (Yuan et al., 2017; Lu et al., 2019; Yang et al., 2020b). It is thus conjectured that Au NCs-encapsulated hPEI (hPEI-Au NCs) might endow selective and sensitive DA sensing by integrating specific reaction and ratiometric response.

In this study, we tried our attempt to explore the selective and sensitive DA detection system by utilizing red-emissive hPEI-Au NCs as the reporters. The addition of DA caused an increase in green fluorescence and a decrease in red emission by DA self-polymerization–mediated formation of polymeric DA nanoparticles and alteration of the hPEI-Au NCs charge transfer pathway, which achieved selective and ratiometric DA. The schematic illustration of the DA detection mechanism using hPEI-Au NCs is shown in **Figure 1**. The proposed DA nanoprobes exhibited a rapid response toward DA with a limit of detection (LOD) of 10 nM (S/N = 3). The selectivity toward DA over other amino acids, small molecules, and ions was also inspected. In addition, the practical application of the proposed hPEI-Au NC nanoprobe was verified by reproducible and accurate DA analysis in urine samples.

METHODS

Materials, Reagents, and Instruments

Chloroauric acid tetrahydrate ($HAuCl_4{\cdot}4H_2O$) was purchased from damas-beta (Shanghai, China). Polyethyleneimine (25,000, branched) was purchased from Shanghai Macklin Biochemical Co., Ltd. (Shanghai, China). 11-Mercaptoundecanoic acid (MUA) was purchased from Shanghai Yuanye Bio-Technology Co., Ltd. (Shanghai, China). Dopamine (DA) and anthocyanidins (Anthos) were purchased from Aladdin Industrial Corporation (Shanghai, China). Uric acid (UA) was purchased from TCI (Shanghai, China). Urea and potassium nitrate (KNO_3) were purchased from Xilong Scientific (Guangdong, China). Potassium chloride (KCl), sodium chloride (NaCl), and sodium sulfate (Na_2SO_4) were purchased from Fuchen (Tianjin, China). L-Alanine (Ala), L-lysine (Lys), and L-threonine (Thr) were purchased from Solarbio (Beijing, China). L-serine (Ser), L-arginine (Arg), and saccharose (Sac) were purchased from J&K Chemical Ltd (Beijing, China). L-ascorbic acid (AA) and catechin (Cat) were obtained from Hunan Intellijoy Biotechnology Co., Ltd. (Changsha, China). Quercetin (Que) was purchased from TCI (Shanghai, China). Anhydrous calcium chloride ($CaCl_2$), glucose (Glu), hydrochloric acid (HCl), sodium hydroxide (NaOH), ethanol, disodium hydrogen phosphate (Na_2HPO_4), potassium dihydrogen phosphate (KH_2PO_4), sodium carbonate (Na_2CO_3), and sodium bicarbonate ($NaHCO_3$) were purchased from Beijing Chemical Reagent Company (Beijing, China). All chemicals used were of the analytical-reagent grade and used without further purification. All solutions were freshly prepared with deionized water (18.2 MΩ cm, Milli-Q, Millipore, Barnstead, CA, United States).

The UV–vis absorption spectra were collected using a UV–3900H spectrophotometer (Shimadzu, Japan). Fluorescence spectra were obtained using an F-7000 fluorescence spectrophotometer (Hitachi, Japan) at a slit of 5.0 nm with a scanning rate of 2,400 nm/min. Zeta potential and hydrodynamic diameter were determined using a Malvern Zetasizer 3000HS nano-granularity analyzer (Malvern, United Kingdom). The transmission electron microscopy

(TEM) images were collected using an HT7700 transmission electron microscope (HITACHI, Japan). The time-resolved fluorescence decay curve was performed on an FLS 980 (Edinburgh, United Kingdom). The pH values were measured using a benchtop pH meter (Orion plus, Thermo Fisher, United States).

Synthesis of Red-Emissive hPEI-Au NCs

Red-emissive hPEI-Au NCs were prepared according to our previous report with slight modifications (Yuan et al., 2017). Typically, 1.1 ml hPEI (10 mM) dissolved in ultrapure water was first mixed with 50 μl $HAuCl_4$ (0.1 M) to make a final solution volume of 4 ml. After 10 min stirring, 50 μl AA (0.1 M) was added. Fifteen minutes later, 100 μl MUA ethanol solution (0.1 M) was introduced into the colorless solution. The solution was stirred at room temperature for another 6 h. Finally, the resulted light yellow solution with red emission was obtained and stored at room temperature before further characterization and application.

Sensitivity and Selectivity Measurement

First, DA stock solution (500 μM) was prepared and then diluted with ultrapure water to obtain a series of DA with a concentration gradient. To detect DA, 50 μl of DA solution with various concentrations were mixed with 50 μl of hPEI-Au NCs and 900 μl of ultrapure water to make the final volume 1 ml. After 25 min of reaction at UV light (365 nm) and 30°C, the fluorescence emission spectra were collected by an F-7000 fluorescence spectrophotometer at the excitation wavelength of 320 nm. In order to evaluate the specificity of the probe, the specificity of the metal ions, amino acids, and small molecules, including Ca^{2+}, K^{+}, Na^{+}, Cl^{-}, NO^{3-}, SO_4^{2-}, urea, UA, Glu, Sac, Lys, Ala, Ser, Thr, Arg, AA, Cat, Anthos, and Que were considered. To investigate the inference, interferents were added to hPEI-Au NCs working solutions in the absence or presence of 10 μM DA. The concentrations for metal ions, small molecules, and amino acids were also 10 μM. After 25 min of reaction at UV light (365 nm) and 30°C, the fluorescence emission spectra were collected by an F-7000 fluorescence spectrophotometer at the excitation wavelength of 320 nm.

Urine Sample Analysis

Human urine samples were obtained from a healthy volunteer who had not taken any drug/DA in the past 3 months. Urine samples were first filtered by a filter membrane with a pore size of 0.22 μm and were then ultrafiltered twice with an ultrafiltration tube with a molecular weight of 3,000 at 5,000 rpm for 8 minutes. For DA detection, 50 μl urine samples were added into a 1.5 ml centrifuge tube containing 50 μl of hPEI-Au NCs probe, and then 900 μl of ultrapure water was added to make the final volume 1 ml. After 25 min of reaction at UV light (365 nm) and 30°C, the fluorescence emission spectra were collected by an F-7000 fluorescence spectrophotometer at the excitation wavelength of 320 nm. For conducting standard addition experiments, 50 μl DA with different concentrations were firstly mixed with 50 μl of urine sample, then 50 μl hPEI-Au NCs was added immediately, and, finally, 850 μl water was added to make the final volume 1 ml. The final concentrations of added DA were 2 μM, 3 μM, and 4 μM respectively. After 25 min of reaction at UV light (365 nm) and 30°C, the fluorescence emission spectra were collected by an F-7000 fluorescence spectrophotometer at the excitation wavelength of 320 nm.

RESULTS AND DISCUSSION

DA-Mediated Fluorescence Response of hPEI-Au NCs

At the starting point, the red-emissive hPEI-Au NCs were synthesized based on the previous report. As indicated in **Figure 2A**, the fluorescence excitation and emission maxima were centered at 280 and 595 nm, respectively. In addition, the fluorescence excitation and emission spectra were consistent with the reported work (**Supplementary Figure S1**) (Yang et al., 2020a). These results indicate that red-emissive hPEI-Au NCs were successfully produced. To investigate the interaction between hPEI-Au NCs and DA, the 3D fluorescence emission spectra of hPEI-Au NCs solution with the addition of DA were obtained. As displayed in **Figures 2A,B**, new emissive species with excitation/emission maxima located at 380/520 nm appeared, while the corresponding emission intensity of hPEI-Au NCs decreased, indicating DA can interact with hPEI-Au NCs and regulate the fluorescence behavior. The newly generated fluorescent species as well as the weakened emission of hPEI-Au NCs make hPEI-Au NCs possible for ratiometric DA sensing in aqueous media and urine.

Mechanism of DA-Induced Ratiometric Fluorescence Variation

It is well-known that hPEI could induce the self-polymerization of DA, which forms fluorescent indole intermediate and finally polymeric DA nanoparticles (Liu et al., 2015). To understand the generation of new fluorescent species, 3D fluorescence emission spectra of hPEI solution after adding DA were acquired. As shown in **Figure 3A**, fluorescent components with maximum excitation and emission wavelengths of 380 and 520 nm appeared, respectively, which is comparable to the product of DA/hPEI-Au NCs mixture, suggesting that the newly produced species are polymeric DA nanoparticles (Sun et al., 2019). After adding DA, a new absorption peak around 380 nm appeared, which is similar to the absorption spectra of polymeric DA nanoparticles (**Figure 3B**). The similar absorption profiles also demonstrated the generation of polymeric DA nanoparticles. It was seen that the hydrodynamic diameter of hPEI-Au NCs solution showed a dramatic increase after the addition of DA (**Figure 3C**), from 2.4 to 39.0 nm, indicating the formation of large nanoparticles. According to the TEM image of hPEI-Au NCs/DA mixture, nanoparticles with a size around 90 nm were observed (**Figure 3D**), further proving the formation of polymeric DA nanoparticles (Sun et al., 2019). According to the TEM, hPEI-Au NCs were not observed nearby polymeric DA nanoparticles. In addition, hPEI is involved in the DA self-polymerization process. Thus, a possible reason is that

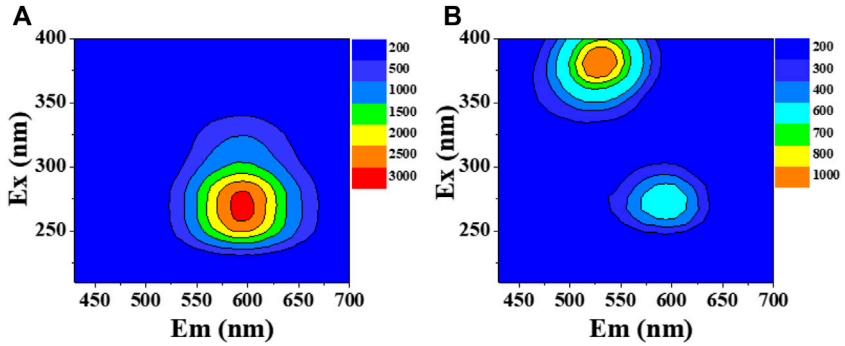

FIGURE 2 | 3D fluorescence emission spectra of hPEI-Au NCs in the absence **(A)** and presence of **(B)** DA.

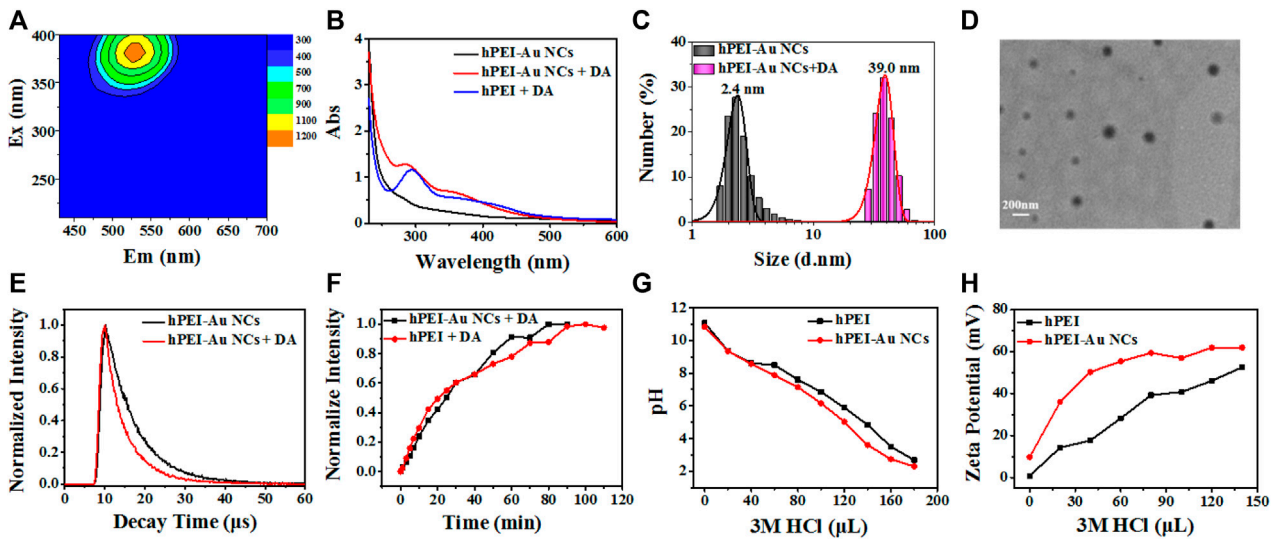

FIGURE 3 | (A) 3D fluorescence emission spectra of hPEI solution after adding DA. **(B)** UV–vis absorption spectra of hPEI-Au NCs (black line), hPEI-Au NCs-DA mixture (red line), and hPEI-DA mixture (blue line). **(C)** Hydrodynamic diameter of hPEI-Au NCs without (gray histogram) and with (purple histogram) the addition of DA. **(D)** TEM image of hPEI-Au NCs-DA mixture. **(E)** Time-resolved fluorescence emission spectra of hPEI-Au NCs in the absence (black line) and presence (red line) of DA. **(F)** Time-dependent fluorescence variation of I_{520} of hPEI-Au NCs-DA mixture (black line) and hPEI-DA mixture (red line). **(G)** pH variation of hPEI (black line) and hPEI-Au NCs (red line) upon adding HCl. **(H)** Surface charge variation of hPEI (black line) and hPEI-Au NCs (red line) upon adding HCl.

hPEI-Au NCs were embedded into polymeric DA nanoparticles during the self-polymerization process, as indicated in **Figure 1**. Moreover, it can be seen from **Supplementary Figure S2** that the polymeric DA nanoparticles coated with Au NCs are much larger than the polymeric DA nanoparticles induced by hPEI alone, which also proves our conjecture. As mentioned earlier, the introduction of DA also led to the decrease in red emission of hPEI-Au NCs. To gain insights into the DA-induced fluorescence inhibition mechanism, the time-resolved fluorescence spectra of hPEI-Au NCs without and with the addition of DA were collected. It was seen that the fluorescence lifetime curve of hPEI-Au NCs showed an obvious decrease after reaction with DA (**Figure 3E**), indicating the alternation of the emission pathway of Au NCs (Lu et al., 2020). Through three components simulation (**Supplementary Table S1**), the fluorescence lifetime of hPEI-Au NCs decreased from 5.71 to 3.19 μs. As reported in Chang's work, the fluorescence of thiolate-capped Au NCs originates from ligand-to-metal–metal charge transfer (S→Au ··· Au, LMMCT), and the rotation of thiolate ligands easily affect the LMMCT pathway and decreases the lifetime (Shiang et al., 2011). Such a phenomenon has also been observed by Zheng and Xie et al. (Sun et al., 2016; Wu et al., 2020). In this case, the formation of polymeric DA nanoparticles leads to the conformation change. However, the emission of Au NCs is largely decided by the MUA ligand and subsequent LMMCT, which is related to the steric structure. The self-polymerization induced conformation change not only alters the steric structure but also regulates the LMMT efficiency. On the basis of our previous work (Zhou et al., 2022), hPEI also contributed to the fluorescence. The conformation change of

hPEI may also weaken the interaction and diminish the red fluorescence. As a consequence, the red fluorescence from Au NCs decreased as the DA concentration increased.

It is usually accepted that the reactivity of organic molecules on the nanostructure surface usually exhibits a slight decrease due to the steric effect. To understand whether the hPEI-mediated DA self-polymerization reaction is restricted by Au NCs, the time-dependent fluorescence emission of hPEI and hPEI-Au NCs solutions upon adding DA were investigated. To rule out the concentration-related fluorescence differences, the concentrations of hPEI in both solutions were set to the same. As illustrated in **Supplementary Figure S3**, the green emission of polymeric DA nanoparticles around 520 nm in both systems gradually increased with the increasing reaction time, and the fluorescence intensity did not show a large difference, indicating the Au NCs encapsulation has no suppression toward DA self-polymerization. It should be noticed that the relative green fluorescence intensity (I_{520}) in hPEI-Au NCs solution grew faster than that of hPEI solution (**Figure 3F**). DA self-polymerization reaction easily occurs under alkaline conditions, and the electron density/nucleophilicity of hPEI plays an important role to enhance the polymerization reaction. In view of these factors, we hypothesized that the accelerated reaction rate may be attributed to the enhanced electron density of the hPEI layer. It is well-known that hPEI can act as a strong proton sponge, which adsorbs abundant protons to primary and secondary amine groups (Wojnilowicz et al., 2019). The strong proton sponge effect makes hPEI a promising candidate for gene/drug delivery. To ensure stable Au NCs encapsulation, strong binding affinity between the amine group in hPEI and the carboxylic group of MUA may exist. This interaction may hinder the adsorption of protons and enhance the electron density of hPEI; as a result, the DA polymerization reaction is boosted. To reveal this assumption, the proton sponge effects of hPEI and hPEI-Au NCs were tested by adding HCl. As shown in **Figure 3G**, the pH decrease rate of hPEI-Au NCs upon adding HCl was faster than that of hPEI, indicating the decrement of the proton sponge effect after Au NCs encapsulation (Richard et al., 2013). In addition, the surface potential increase rate of hPEI-Au NCs upon adding HCl was also higher than that of hPEI (**Figure 3H**), further demonstrating the Au NCs encapsulation-induced decrease of the proton sponge effect. Moreover, the slightly increased surface potential may also facilitate the approaching of DA. Thus, Au NCs encapsulation would assist the DA self-polymerization reaction by reducing the proton sponge effect. Taken together, hPEI-assisted DA polymerization not only generates polymeric DA nanoparticles with green emission but also suppresses the red emission of Au NCs by changing the LMMCT pathway, which endows ratiometric and sensitive fluorescence response toward DA.

DA Sensing in Aqueous Media

Since the introduction of DA into hPEI-Au NCs solution caused dramatic fluorescence variation, such a response might be able to be utilized for fluorimetric DA detection by using hPEI-Au NCs as the optical reporters. As mentioned in our previous report, the self-polymerization reaction of DA in hPEI solution could be affected by several parameters, including pH, solution temperature, and reaction time. To achieve sensitive DA detection, the sensing condition of these factors was optimized. As shown in **Supplementary Figure S4A**, the formation of polymeric DA nanoparticles was related to solution pH and preferred at pH 10–11. Interestingly, the fluorescence intensity ratio (I_{520}/I_{595}) of hPEI-Au NCs solution after adding DA was also proportional to pH values (**Supplementary Figure S4B**). It should be noticed that the pH of hPEI-Au NCs solution was close to 11, thus the following experiments were conducted without further pH adjustment. With Au NCs encapsulation, the temperature-dependent intensity ratio (I_{520}/I_{595}) showed sine function-like curve (**Supplementary Figure S5**), which is different from previous studies. It was seen that the red emission from Au NCs displayed a visible decrease under high temperature; the enhanced intensity ratio (I_{520}/I_{595}) at high temperature should be assigned to the change of Au NCs but not the generation of polymeric DA nanoparticles. As a result, 30°C was chosen as the optimal reaction temperature. In addition, we optimized the reaction time at this temperature. According to the previous works (Du et al., 2014; Li et al., 2021), UV light irradiation can induce the release of reactive oxygen species and thus promote the oxidative polymerization of DA. Therefore, the reaction kinetics was conducted in the absence and presence of UV light radiation (365 nm). As manifested in **Supplementary Figure S6**, conventional self-polymerization was completed after 50 min reaction, while it became 20 min after UV light radiation, and thus, 20 min reaction window with 365 nm UV light irradiation.

For conducting ratiometric DA sensing, the sensitivity evaluation was first investigated. After the addition of DA with various concentrations, the fluorescence emission spectra of hPEI-Au NCs solution were obtained. As shown in **Figure 4A**, the red fluorescence intensity (595 nm) of Au NCs gradually decreased with the increasing DA concentration while without obvious change in the spectral shape. The maintained emission profile indicates the destruction of Au NCs rather than the formation of a new Au NC component. In contrast, green fluorescence steadily increased, yielding an increased fluorescence intensity ratio (I_{520}/I_{595}). As manifested in **Figure 4B**, the plots of the intensity ratio (I_{520}/I_{595}) showed a linear response vs. DA concentration range from 0 to 25 μM. The fluorescence intensity ratio (I_{520}/I_{595}) can be expressed with a linear equation: $y = 0.07 + K[Q]$ ($R^2 = 0.997$), where y is the I_{520}/I_{595} value, K is the corresponding fluorescence response constant, and [Q] is the concentration of DA. Through the linear regression of the plots, K was calculated to be $1.5 \times 10^4\ M^{-1}$. To further understand the stability of DA analysis, fifteen repeated measurements of hPEI-Au NCs upon adding certain DA were conducted. As illustrated in **Supplementary Figure S7**, the fluorescence intensity ratio (I_{520}/I_{595}) showed only slight variation and a low relative standard deviation (RSD, 1.2%) value, indicating the good reproducibility of the hPEI-Au NC nanoprobe. In addition, four hPEI-Au NC nanoprobes from different batches also displayed small RSD values (2.6%, **Supplementary Figure S8**), further suggesting the high

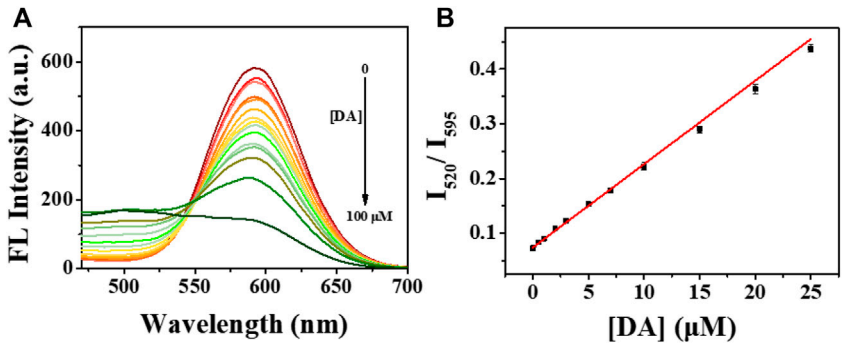

FIGURE 4 | (A) Fluorescence emission spectra of hPEI-Au NCs solution upon adding DA with various concentrations. **(B)** Plots of fluorescence intensity ratio (I_{520}/I_{595}) of hPEI-Au NCs solution vs. DA concentrations.

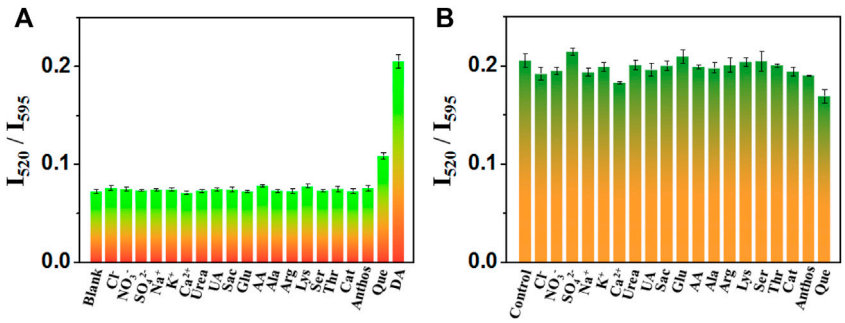

FIGURE 5 | Fluorescence intensity ratio (I_{520}/I_{595}) of hPEI-Au NCs upon adding DA in the absence **(A)** and presence **(B)** of various interferents.

reproducibility. As a result, the hPEI-Au NC nanoprobe is reproducible for ratiometric DA sensing. Moreover, the LOD toward DA by spectroscopic analysis was determined to be 10 nM (S/N = 3). This LOD is comparable to many reported methods (**Supplementary Table S2**) (Yu et al., 2014; Guo et al., 2018; Ling et al., 2018; Wang et al., 2018; Naik et al., 2019; Ding et al., 2020; Huang et al., 2020; Liu et al., 2020; Teng et al., 2020; Yao et al., 2020; Baluchova et al., 2021; Chen et al., 2021; Sun et al., 2021; Amara et al., 2022).

The selectivity of nanoprobe is also an important character that evaluates its performance. In order to inspect whether the ratiometric fluorescence variation induced by DA is specific, the fluorescence emission spectra of the hPEI-Au NCs nanoprobe after adding possible interferents were recorded. In this work, ions, small molecules, and amino acids, including Cl^-, NO^{3-}, SO_4^{2-}, Na^+, K^+, Ca^{2+}, urea, Sac, Glu, UA, AA, Ala, Arg, Lys, Ser, Thr, Cat, Anthos, and Que were chosen for specificity evaluation. The concentrations of DA and other interferents were 10 μM. As displayed in **Figure 5A**, none of these interferents, even Cat and Anthos, could generate a conspicuous increment of the intensity ratio (I_{520}/I_{595}) as DA did, indicating the DA-induced ratiometric change is specific. Although Que showed a slight response, the increased ratio was assigned to its self-florescence around 500 nm. In addition, the change of fluorescence caused by DA is not affected by the addition of various interferents (**Figure 5B**), which indicates that the proposed nanoprobe has strong interference inhibition. The favorable selectivity is probably attributed to the unique self-polymerization reaction of DA in the presence of hPEI. The hPEI-induced fluorescence response toward these interferents was also recorded. As shown in **Supplementary Figure S9**, the selectivity and anti-interference were generally the same as the proposed nanoprobe, revealing the unchanged specificity of DA analysis with our system. As a result, for ratiometric DA detection, the hPEI-Au NC nanoprobe is simple, reproducible, and with comparable or better sensing performance in comparison with other reported nanomaterials or fluorophores.

TABLE 1 | DA detection in urine samples with the proposed hPEI-Au NCs nanoprobe.

Sample	Spiked DA (μM)	Found (μM)	Recovery (%)	RSD (%,*n* = 3)
Urine	2.00	2.27	113.5	1.1
	3.00	2.75	91.7	1.9
	4.00	3.84	96.0	1.6

DA Analysis in Urine Samples

The satisfying selectivity and sensitivity of the hPEI-Au NC nanoprobe suggest a high feasibility of DA detection in real

samples. Thus, to further demonstrate the practical application of the proposed nanoprobe, we tried to detect DA in urine samples. In consideration of containing protein and other components, urine samples were centrifuged and filtered to reduce unexpected interference. However, DA in urine samples was not detected, indicating a very low concentration of DA, which is consistent with previous reports. In addition, the detection accuracy was validated by the standard addition method. As summarized in **Table 1**, the recovery rate was around 100% (91.7–113.5%), proving the practical capability of DA analysis in urine samples. Moreover, the small RSD values ($\leqq$ 1.9%, n = 3) revealed high reliability for the proposed hPEI-Au NC nanoprobe. In a word, the proposed hPEI-Au NC-based ratiometric platform is capable of DA sensing in complicated biological media.

CONCLUSION

In conclusion, we have explored a ratiometric DA sensing platform using the hPEI-Au NC nanoprobe, which integrates DA self-polymerization and Au NC internal reference. With a self-calibration character, the proposed platform shows high accuracy and sensitivity. In addition, other interferents including ions, small molecules, and amino acids have no visible influence due to the hPEI-mediated specific self-polymerization reaction of DA. By using the hPEI-Au NC nanoprobe, rapid DA detection with an LOD of 10 nM is achieved under the optimized condition. In addition, the practical application is verified by the accurate DA analysis in urine samples. Our study not only develops a ratiometric neurotransmitter sensing system but also demonstrates the exploration of selective nanosensor by involving specific ligand-target reactions. Thus, new protocols for the design of versatile nanosensors for the rapid and selective detection of bioanalytes and other targets by integrating functional nanomaterials and unique chemical reactions are now possible in life science or environment-related fields.

DATA AVAILABILITY STATEMENT

The original contributions presented in the study are included in the article/**Supplementary Material**; further inquiries can be directed to the corresponding authors.

AUTHOR CONTRIBUTIONS

JZ and ZY conceived the experiments. JZ carried out the experiments. JZ and ZY contributed to the data analysis and writing of this manuscript. All the authors have reviewed the manuscript and agreed to its publication.

FUNDING

This work was supported by the Natural Science Foundation of Beijing Municipality (2202038), the National Natural Science Foundation of China (22074005 and 21974008), and the Open Research Fund Program of Beijing Key Lab of Plant Resource Research and Development, Beijing Technology and Business University (PRRD-2021-YB6).

SUPPLEMENTARY MATERIAL

The Supplementary Material for this article can be found online at: https://www.frontiersin.org/articles/10.3389/fchem.2022.928607/full#supplementary-material

REFERENCES

Amara, U., Sarfraz, B., Mahmood, K., Mehran, M. T., Muhammad, N., Hayat, A., et al. (2022). Fabrication of Ionic Liquid Stabilized MXene Interface for Electrochemical Dopamine Detection. *Microchim. Acta* 189, 64. doi:10.1007/s00604-022-05162-3

Baluchová, S., Brycht, M., Taylor, A., Mortet, V., KrůšekIvan, J. D., Dittert, I., et al. (2021). Enhancing Electroanalytical Performance of Porous Boron-Doped Diamond Electrodes by Increasing Thickness for Dopamine Detection. *Anal. Chim. Acta* 1182, 338949. doi:10.1016/j.aca.2021.338949

Bucolo, C., Leggio, G. M., Drago, F., and Salomone, S. (2019). Dopamine outside the Brain: The Eye, Cardiovascular System and Endocrine Pancreas. *Pharmacol. Ther.* 203, 107392. doi:10.1016/j.pharmthera.2019.07.003

Cepeda, C., Murphy, K. P. S., Parent, M., and Levine, M. S. (2014). The Role of Dopamine in Huntington's Disease. *Prog. Brain Res.* 211, 235–254. doi:10.1016/B978-0-444-63425-2.00010-6

Chen, L.-Y., Wang, C.-W., Yuan, Z., and Chang, H.-T. (2015). Fluorescent Gold Nanoclusters: Recent Advances in Sensing and Imaging. *Anal. Chem.* 87, 216–229. doi:10.1021/ac503636j

Chen, S., Song, N., Mu, M., Wang, C., and Lu, X. (2021). Sacrificial Template Synthesis of Ultrathin Polyaniline Nanosheets and Their Application in Highly Sensitive Electrochemical Dopamine Detection. *Mater. Today Chem.* 20, 100479. doi:10.1016/j.mtchem.2021.100479

Diaz-Diestra, D., Thapa, B., Beltran-Huarac, J., Weiner, B. R., and Morell, G. (2017). L-cysteine Capped ZnS:Mn Quantum Dots for Room-Temperature Detection of Dopamine with High Sensitivity and Selectivity. *Biosens. Bioelectron.* 87, 693–700. doi:10.1016/j.bios.2016.09.022

Ding, H., Guo, W., Zhou, P., and Su, B. (2020). Nanocage-confined Electrochemiluminescence for the Detection of Dopamine Released from Living Cells. *Chem. Commun.* 56, 8249–8252. doi:10.1039/d0cc03370g

Du, X., Li, L., Li, J., Yang, C., Frenkel, N., Welle, A., et al. (2014). UV-triggered Dopamine Polymerization: Control of Polymerization, Surface Coating, and Photopatterning. *Adv. Mat.* 26, 8029–8033. doi:10.1002/adma.201403709

Fuxe, K., Borroto-Escuela, D. O., Romero-Fernandez, W., Ciruela, F., Manger, P., Leo, G., et al. (2012). On the Role of Volume Transmission and Receptor-Receptor Interactions in Social Behaviour: Focus on Central Catecholamine and Oxytocin Neurons. *Brain Res.* 1476, 119–131. doi:10.1016/j.brainres.2012.01.062

Guo, Y., Lu, J., Kang, Q., Fang, M., and Yu, L. (2018). Fabrication of Biocompatible, Luminescent Supramolecular Structures and Their Applications in the Detection of Dopamine. *Langmuir* 34, 9195–9202. doi:10.1021/acs.langmuir.8b01548

He, Y.-S., Pan, C.-G., Cao, H.-X., Yue, M.-Z., Wang, L., and Liang, G.-X. (2018). Highly Sensitive and Selective Dual-Emission Ratiometric Fluorescence Detection of Dopamine Based on Carbon Dots-Gold Nanoclusters Hybrid. *Sensors Actuators B Chem.* 265, 371–377. doi:10.1016/j.snb.2018.03.080

Huang, H., Bai, J., Li, J., Lei, L., Zhang, W., Yan, S., et al. (2020). Fluorescence Detection of Dopamine Based on the Polyphenol Oxidase-Mimicking Enzyme. *Anal. Bioanal. Chem.* 412, 5291–5297. doi:10.1007/s00216-020-02742-1

Huang, X., Song, J., Yung, B. C., Huang, X., Xiong, Y., and Chen, X. (2018). Ratiometric Optical Nanoprobes Enable Accurate Molecular Detection and Imaging. *Chem. Soc. Rev.* 47, 2873–2920. doi:10.1039/c7cs00612h

Kim, J.-H., Auerbach, J. M., Rodríguez-Gómez, J. A., Velasco, I., Gavin, D., Lumelsky, N., et al. (2002). Dopamine Neurons Derived from Embryonic Stem Cells Function in an Animal Model of Parkinson's Disease. *Nature* 418, 50–56. doi:10.1038/nature00900

Li, B.-R., Hsieh, Y.-J., Chen, Y.-X., Chung, Y.-T., Pan, C.-Y., and Chen, Y.-T. (2013). An Ultrasensitive Nanowire-Transistor Biosensor for Detecting Dopamine Release from Living PC12 Cells under Hypoxic Stimulation. *J. Am. Chem. Soc.* 135, 16034–16037. doi:10.1021/ja408485m

Li, R., Li, J., Rao, L., Lin, H., Shen, L., Xu, Y., et al. (2021). Inkjet Printing of Dopamine Followed by UV Light Irradiation to Modify Mussel-Inspired PVDF Membrane for Efficient Oil-Water Separation. *J. Membr. Sci.* 619, 118790. doi:10.1016/j.memsci.2020.118790

Li, Z., Guo, S., Yuan, Z., and Lu, C. (2017). Carbon Quantum Dot-Gold Nanocluster Nanosatellite for Ratiometric Fluorescence Probe and Imaging for Hydrogen Peroxide in Living Cells. *Sensors Actuators B Chem.* 241, 821–827. doi:10.1016/j.snb.2016.10.134

Liang, Z., Hao, C., Chen, C., Ma, W., Sun, M., Xu, L., et al. (2022). Ratiometric FRET Encoded Hierarchical ZrMOF @ Au Cluster for Ultrasensitive Quantifying microRNA *In Vivo*. *Adv. Mater.* 34, 2107449. doi:10.1002/adma.202107449

Ling, X., Shi, R., Zhang, J., Liu, D., Weng, M., Zhang, C., et al. (2018). Dual-signal Luminescent Detection of Dopamine by a Single Type of Lanthanide-Doped Nanoparticles. *ACS Sens.* 3, 1683–1689. doi:10.1021/acssensors.8b00368

Ling, Y., Wang, L., Zhang, X. Y., Wang, X. H., Zhou, J., Sun, Z., et al. (2020). Ratiometric Fluorescence Detection of Dopamine Based on Effect of Ligand on the Emission of Ag Nanoclusters and Aggregation-Induced Emission Enhancement. *Sensors Actuators B Chem.* 310, 127858. doi:10.1016/j.snb.2020.127858

Liu, M., Ji, J., Zhang, X., Zhang, X., Yang, B., Deng, F., et al. (2015). Self-polymerization of Dopamine and Polyethyleneimine: Novel Fluorescent Organic Nanoprobes for Biological Imaging Applications. *J. Mat. Chem. B* 3, 3476–3482. doi:10.1039/C4TB02067G

Liu, Y., He, X., Ma, P., Huang, Y., Li, X., Sun, Y., et al. (2020). Fluorometric Detection of Dopamine Based on 3-aminophenylboronic Acid-Functionalized AgInZnS QDs and Cells Imaging. *Talanta* 217, 121081. doi:10.1016/j.talanta.2020.121081

Liu, Y., Liu, Y., Zhang, J., Zheng, J., Yuan, Z., and Lu, C. (2022). Catechin-inspired Gold Nanocluster Nanoprobe for Selective and Ratiometric Dopamine Detection via Forming Azamonardine. *Spectrochimica Acta Part A Mol. Biomol. Spectrosc.* 274, 121142. doi:10.1016/j.saa.2022.121142

Lu, F., Yang, H., Tang, Y., Yu, C.-J., Wang, G., Yuan, Z., et al. (2020). 11-Mercaptoundecanoic Acid Capped Gold Nanoclusters with Unusual Aggregation-Enhanced Emission for Selective Fluorometric Hydrogen Sulfide Determination. *Microchim. Acta* 187, 200. doi:10.1007/s00604-020-4159-1

Lu, F., Yang, H., Yuan, Z., Nakanishi, T., Lu, C., and He, Y. (2019). Highly Fluorescent Polyethyleneimine Protected Au8 Nanoclusters: One-Pot Synthesis and Application in Hemoglobin Detection. *Sensors Actuators B Chem.* 291, 170–176. doi:10.1016/j.snb.2019.04.067

Ma, Z., Xu, Y., Li, P., Cheng, D., Zhu, X., Liu, M., et al. (2021). Self-Catalyzed Surface Reaction-Induced Fluorescence Resonance Energy Transfer on Cysteine-Stabilized MnO2 Quantum Dots for Selective Detection of Dopamine. *Anal. Chem.* 93, 3586–3593. doi:10.1021/acs.analchem.0c05102

Mao, G., Du, M., Wang, X., Ji, X., and He, Z. (2018). Simple Construction of Ratiometric Fluorescent Probe for the Detection of Dopamine and Tyrosinase by the Naked Eye. *Analyst* 143, 5295–5301. doi:10.1039/c8an01640b

Naik, V., Zantye, P., Gunjal, D., Gore, A., Anbhule, P., Kowshik, M., et al. (2019). Nitrogen-Doped Carbon Dots via Hydrothermal Synthesis: Naked Eye Fluorescent Sensor for Dopamine and Used for Multicolor Cell Imaging. *ACS Appl. Bio Mat.* 2, 2069–2077. doi:10.1021/acsabm.9b00101

Qu, Z., Yu, T., and Bi, L. (2019). A Dual-Channel Ratiometric Fluorescent Probe for Determination of the Activity of Tyrosinase Using Nitrogen-Doped Graphene Quantum Dots and Dopamine-Modified CdTe Quantum Dots. *Microchim. Acta* 186, 635. doi:10.1007/s00604-019-3733-x

Ren, X., Zhang, Q., Yang, J., Zhang, X., Zhang, X., Zhang, Y., et al. (2021). Dopamine Imaging in Living Cells and Retina by Surface-Enhanced Raman Scattering Based on Functionalized Gold Nanoparticles. *Anal. Chem.* 93, 10841–10849. doi:10.1021/acs.analchem.1c01108

Richard, I., Thibault, M., De Crescenzo, G., Buschmann, M. D., and Lavertu, M. (2013). Ionization Behavior of Chitosan and Chitosan-DNA Polyplexes Indicate that Chitosan Has a Similar Capability to Induce a Proton-Sponge Effect as PEI. *Biomacromolecules* 14, 1732–1740. doi:10.1021/bm4000713

Senel, M., Dervisevic, E., Alhassen, S., Dervisevic, M., Alachkar, A., Cadarso, V. J., et al. (2020). Microfluidic Electrochemical Sensor for Cerebrospinal Fluid and Blood Dopamine Detection in a Mouse Model of Parkinson's Disease. *Anal. Chem.* 92, 12347–12355. doi:10.1021/acs.analchem.0c02032

Shiang, Y.-C., Lin, C.-A., Huang, C.-C., and Chang, H.-T. (2011). Protein A-Conjugated Luminescent Gold Nanodots as a Label-free Assay for Immunoglobulin G in Plasma. *Analyst* 136, 1177–1182. doi:10.1039/c0an00889c

Sun, S., Ning, X., Zhang, G., Wang, Y.-C., Peng, C., and Zheng, J. (2016). Dimerization of Organic Dyes on Luminescent Gold Nanoparticles for Ratiometric pH Sensing. *Angew. Chem. Int. Ed.* 55, 2421–2424. doi:10.1002/anie.201509515

Sun, Y., Lu, F., Yang, H., Ding, C., Yuan, Z., and Lu, C. (2019). Fluorescent Sensor Array for Separation-free Dopamine Analogue Discrimination via Polyethyleneimine-Mediated Self-Polymerization Reaction. *Nanoscale* 11, 12889–12897. doi:10.1039/c9nr03643a

Sun, Y., Song, Z., Ni, X., Dramou, P., and He, H. (2021). A Boric Acid-Functionalized Lanthanide Metal-Organic Gel: A Ratiometric Fluorescence Probe with Rapid and Sensitive Detection of Dopamine. *Microchem. J.* 169, 106579. doi:10.1016/j.microc.2021.106579

Teng, H., Song, J., Xu, G., Gao, F., and Luo, X. (2020). Nitrogen-doped Graphene and Conducting Polymer PEDOT Hybrids for Flexible Supercapacitor and Electrochemical Sensor. *Electrochimica Acta* 355, 136772. doi:10.1016/j.electacta.2020.136772

Tseng, Y.-T., Yuan, Z., Yang, Y.-Y., Huang, C.-C., and Chang, H.-T. (2014). Photoluminescent Gold Nanodots: Role of the Accessing Ligands. *RSC Adv.* 4, 33629–33635. doi:10.1039/C4RA04774E

Wang, H., Ye, H., Zhang, B., Zhao, F., and Zeng, B. (2018). Synthesis of ZnIn2S4/CdS Heterostructure Based on Electrostatic Interaction Mechanism for Indirect Photoelectrochemical Detection of Dopamine. *J. Phys. Chem. C* 122, 20329–20336. doi:10.1021/acs.jpcc.8b05287

Wojnilowicz, M., Glab, A., Bertucci, A., Caruso, F., and Cavalieri, F. (2019). Super-resolution Imaging of Proton Sponge-Triggered Rupture of Endosomes and Cytosolic Release of Small Interfering RNA. *ACS Nano* 13, 187–202. doi:10.1021/acsnano.8b05151

Wu, Z., Yao, Q., Chai, O. J. H., Ding, N., Xu, W., Zang, S., et al. (2020). Unraveling the Impact of Gold(I)-Thiolate Motifs on the Aggregation-Induced Emission of Gold Nanoclusters. *Angew. Chem. Int. Ed.* 59, 9934–9939. doi:10.1002/anie.201916675

Xiao, Y., Wu, Z., Yao, Q., and Xie, J. (2021). Luminescent Metal Nanoclusters: Biosensing Strategies and Bioimaging Applications. *Aggregate* 2, 114–132. doi:10.1002/agt2.11

Yang, H., Lu, F., Zhan, X., Tian, M., Yuan, Z., and Lu, C. (2020a). A Eu3+-Inspired Fluorescent Carbon Nanodot Probe for the Sensitive Visualization of Anthrax Biomarker by Integrating EDTA Chelation. *Talanta* 208, 120368. doi:10.1016/j.talanta.2019.120368

Yang, H., Yang, Y., Liu, S., Zhan, X., Zhou, H., Li, X., et al. (2020b). Ratiometric and Sensitive Cyanide Sensing Using Dual-Emissive Gold Nanoclusters. *Anal. Bioanal. Chem.* 412, 5819–5826. doi:10.1007/s00216-020-02806-2

Yao, K., Tan, X., Dai, B., Bai, J., Sun, Q., Cao, W., et al. (2020). Au Nanospheres Modified Boron-Doped Diamond Microelectrode Grown via Hydrogen Plasma Etching Solid Doping Source for Dopamine Detection. *J. Mater. Sci. Technol.* 49, 42–46. doi:10.1016/j.jmst.2020.02.003

Yu, L., Feng, L., Xiong, L., Li, S., Xu, Q., Pan, X., et al. (2021). Multifunctional Nanoscale Lanthanide Metal-Organic Framework Based Ratiometric Fluorescence Paper Microchip for Visual Dopamine Assay. *Nanoscale* 13, 11188–11196. doi:10.1039/d1nr02036f

Yu, X., Sheng, K., and Shi, G. (2014). A Three-Dimensional Interpenetrating Electrode of Reduced Graphene Oxide for Selective Detection of Dopamine. *Analyst* 139, 4525–4531. doi:10.1039/c4an00604f

Yuan, Z., Du, Y., and He, Y. (2017). Hyperbranched Polyamine Assisted Synthesis of Dual-Luminescent Gold Composite with pH Responsive Character. *Methods Appl. Fluoresc.* 5, 014011. doi:10.1088/2050-6120/aa625d

Zeng, S., Wang, S., Xie, X., Yang, S.-h., Fan, J.-h., Nie, Z., et al. (2020). Live-Cell Imaging of Neurotransmitter Release with a Cell-Surface-Anchored DNA-Nanoprism Fluorescent Sensor. *Anal. Chem.* 92, 15194–15201. doi:10.1021/acs.analchem.0c03764

Zhang, X., Chen, X., Kai, S., Wang, H.-Y., Yang, J., Wu, F.-G., et al. (2015). Highly Sensitive and Selective Detection of Dopamine Using One-Pot Synthesized Highly Photoluminescent Silicon Nanoparticles. *Anal. Chem.* 87, 3360–3365. doi:10.1021/ac504520g

Zhang, X., Zhu, Y., Li, X., Guo, X., Zhang, B., Jia, X., et al. (2016). A Simple, Fast and Low-Cost Turn-On Fluorescence Method for Dopamine Detection Using *In Situ* Reaction. *Anal. Chim. Acta* 944, 51–56. doi:10.1016/j.aca.2016.09.023

Conflict of Interest: The authors declare that the research was conducted in the absence of any commercial or financial relationships that could be construed as a potential conflict of interest.

Advantages of publishing in Frontiers

OPEN ACCESS
Articles are free to read for greatest visibility and readership

FAST PUBLICATION
Around 90 days from submission to decision

HIGH QUALITY PEER-REVIEW
Rigorous, collaborative, and constructive peer-review

TRANSPARENT PEER-REVIEW
Editors and reviewers acknowledged by name on published articles

Frontiers
Avenue du Tribunal-Fédéral 34
1005 Lausanne | Switzerland

Visit us: www.frontiersin.org
Contact us: frontiersin.org/about/contact

REPRODUCIBILITY OF RESEARCH
Support open data and methods to enhance research reproducibility

DIGITAL PUBLISHING
Articles designed for optimal readership across devices

FOLLOW US
@frontiersin

IMPACT METRICS
Advanced article metrics track visibility across digital media

EXTENSIVE PROMOTION
Marketing and promotion of impactful research

LOOP RESEARCH NETWORK
Our network increases your article's readership